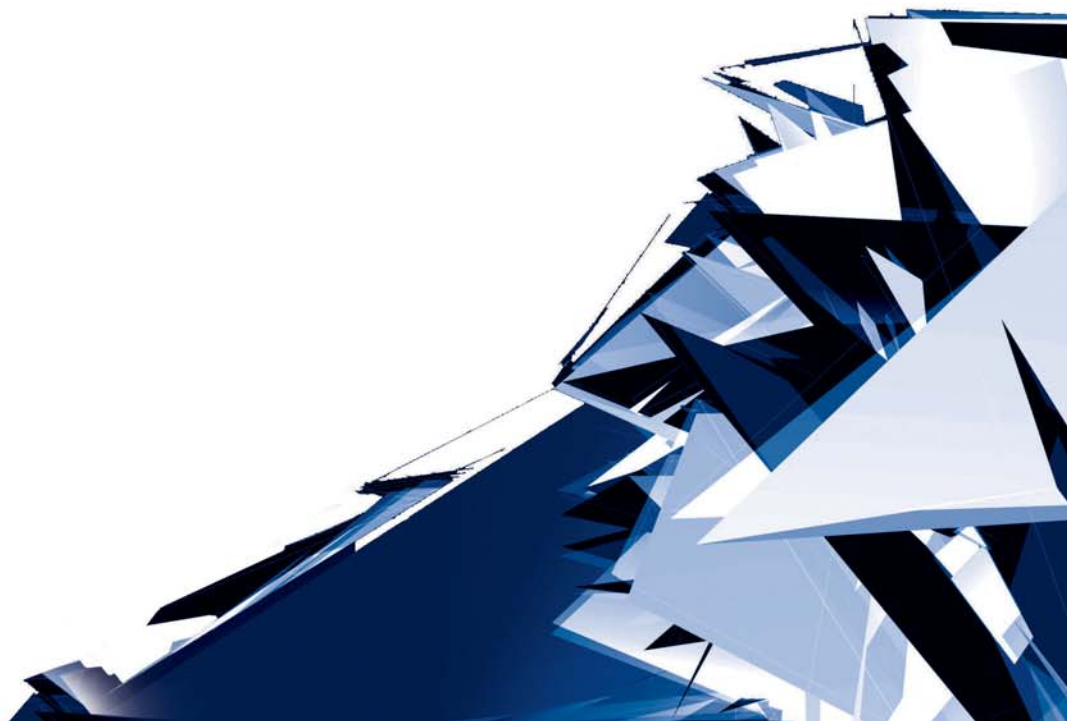


Technical Transactions

Czasopismo Techniczne

Issue 1

Volume 2019 (116)



Chairman of the Cracow University of Technology Press Editorial Board
Przewodniczący Kolegium Redakcyjnego Wydawnictwa Politechniki Krakowskiej

Tadeusz Tatara

Editor-in-chief
Redaktor naczelny

Józef Gawlik jgawlik@mech.pk.edu.pl

Scientific Council
Rada Naukowa

Jan Blachut – University of Liverpool (UK)
Wojciech Bonenberg – Poznan University of Technology (Poland)
Tadeusz Burczyński – Silesian University of Technology (Poland)
Massimo Corcione – Sapienza University of Rome (Italy)
Leszek Demkowicz – The University of Texas at Austin (USA)
Joseph El Hayek – University of Applied Sciences (Switzerland)
Ameen Farooq – Technical University of Atlanta (USA)
Zbigniew Florjańczyk – Warsaw University of Technology (Poland)
Marian Giżejowski – Warsaw University of Technology (Poland)
Sławomir Gzell – Warsaw University of Technology (Poland)
Allan N. Hayhurst – University of Cambridge (UK)
Maria Kušnierova – Slovak Academy of Sciences (Slovakia)
Krzysztof Magnucki – Poznan University of Technology (Poland)
Herbert Mang – Vienna University of Technology (Austria)
Arthur E. McGarity – Swarthmore College (USA)
Antonio Monestiroli – Polytechnic of Milan (Italy)
Marek Pabich – Lodz University of Technology (Poland)
Ivor Samuels – University of Birmingham (UK)
Mirosław J. Skibniewski – University of Maryland (USA)
Günter Wozny – Technical University in Berlin (Germany)
Roman Zarzycki – Lodz University of Technology (Poland)

Editorial Board

Kolegium redakcyjne

ARCHITECTURE AND URBAN PLANNING

Mateusz Gyurkovich mgyurkovich@pk.edu.pl

CHEMISTRY

Radomir Jasiński radomir@chemia.pk.edu.pl

CIVIL ENGINEERING

Marek Piekarczyk mpiekar@pk.edu.pl

ELECTRICAL ENGINEERING

Piotr Drozdowski pdrozdow@usk.pk.edu.pl

ENVIRONMENTAL ENGINEERING

Michał Zielina mziel@vistula.wis.pk.edu.pl

**PHYSICS, MATHEMATICS
AND COMPUTER SCIENCES**

Włodzimierz Wójcik puwojcik@cyf-kr.edu.pl

MECHANICS

Andrzej Sobczyk andrzej.sobczyk@mech.pk.edu.pl

Section Editor
Sekretarz Sekcji

Dorota Sapek
dsapek@wydawnictwo.pk.edu.pl

Editorial Compilation
Opracowanie redakcyjne

Aleksandra Urzędowska
aurzedowska@pk.edu.pl

Technical Proofreading
Korekta techniczna

Małgorzata Sikora

Native Speakers
Weryfikacja językowa

Mairead Coyle
Tim Churcher
Mike Timberlake

Typesetting
Skład i łamanie

Małgorzata
Murat-Drożyńska

Design
Projekt graficzny

Michał Graffstein

Online availability
Dostępność online

www.ejournals.eu/Czasopismo-Techniczne
www.biblos.suw.pk.edu.pl
www.czasopismotechniczne.pl

Contents

ARCHITECTURE AND URBAN PLANNING

Nicolai M. Demin, Olga O. Mykhailyk <i>Preservation methods and revitalisation of river ecosystems in coastal territories</i>	5
Katarzyna Hodor, Albert Fekete <i>The sacred in the landscape of the city</i>	15
Ewa Łużyniecka <i>Architecture of medieval breweries in Cistercian abbeys</i>	23
Agnieszka Ozimek <i>Landscape dominant element – an attempt to parameterize the concept</i>	35
Barbara Stec <i>Sunlight and atmosphere in the Ark of the Lord Church in Krakow</i>	63

CHEMISTRY

Bożena Tyliczszak, Sonia Kudłacik-Kramarczyk, Anna Drabczyk, Magdalena Głąb <i>Novel hydrogels modified with xanthan gum – synthesis and characterization</i>	79
--	----

CIVIL ENGINEERING

Andrzej Flaga, Renata Kłaput, Agnieszka Kocóń <i>Model tests of global stability of two types of lightning protection masts under wind action</i>	93
Agnieszka Makowska <i>Verification of the spline method and its application to curvilinear objects</i>	113

ENVIRONMENTAL ENGINEERING

Grzegorz Kacprzak, Seweryn Bodus <i>The modelling of excavation protection in a highly urbanised environment</i>	133
Bernard Twaróg <i>The analysis of the reactive work of the Alden turbine</i>	143

MECHANICS

Hubert Danielewski <i>Laser welding of pipe stubs made from super 304 steel. Numerical simulation and weld properties</i>	167
Sylwia Kosecka-Żurek <i>Application of it tools in optimization of logistics problems</i>	177
Anna Kufel, Stanisław Kuciel <i>Composites based on polypropylene modified with natural fillers to increase stiffness</i>	187

Marcin Noga, Zdzisław Juda	
<i>The application of NiMH batteries in a light-duty electric vehicle</i>	197
Norbert Radek, Piotr Kurp, Jacek Pietraszek	
<i>Laser forming of steel tubes</i>	223
Małgorzata Stojek	
<i>Engineering safety- and security-related quality requirements</i>	231

Nicolai M. Demin  orcid.org/0000-0002-3144-761x

deminmaster@gmail.com

KNUBA, Architecture, Kyiv

Olga O. Mykhailyk  orcid.org/0000-0003-3648-9410

mykhailykolga@gmail.com

State “Research and Development Design Institute of Urban Development”, Kyiv

PRESERVATION METHODS AND REVITALISATION OF RIVER ECOSYSTEMS IN COASTAL TERRITORIES

METODY KONSERWACJI I REWITALIZACJA EKOSYSTEMÓW RZEKI W TERYTORIACH PRZYBRZEŻNYCH

Abstract

This article examines the prevalent state of river ecosystems in the forest-steppe area of Ukraine with special focus on preservation methods and revitalisation of river ecosystems in the coastal territories.

Keywords: coastal territories, river ecosystem, natural factors, urban development, revitalisation measures

Streszczenie

W artykule przeanalizowano powszechny stan ekosystemów rzecznych w leśno-stepowej części Ukrainy, ze szczególnym uwzględnieniem metod konserwacji i rewitalizacji ekosystemów rzecznych na obszarach przybrzeżnych.

Słowa kluczowe: terytoria przybrzeżne, ekosystem rzeczny, czynniki naturalne, rozwój obszarów miejskich, działania rewitalizacyjne

1. Introduction

The river ecosystem in the coastal area of Ukraine is an integral complex. It comprises of flood meadows, ravines, gullies, fields and forests. As a result of paracentesis and paradigmatic bonds, the natural river-flood complex is extremely sensitive and vulnerable to human activity in the river basin. The distinctive feature of this river ecosystem is that each district in the coastal area is interdependent on the adjacent natural systems, particularly the districts through which the river flows. At the same time the river ecosystem also has an impact on the complexes which are below the river. In this article we have made a modest attempt to examine and understand the river ecosystem in the coastal belt of Ukraine.

2. The structure of the small river ecosystem

The river is the active component of the ecosystem, whereas the coastal area is the passive: it arises in the process of channel deformation and is formed under the influence of flow-forming mechanisms. The floods indirectly have an impact on the river: they determine its boundaries, its speed and the course of the flow during the flood, and cause an active interchange of substances and energy between the river and the floodplain. Coastal forests facilitate the balance of biocoenosis and the nutrient elements of the river ecosystem. It determines the hydrological regime of the rivers, and promotes the transfer of organic substances to other subsystems. Fields are a vehicle and carrier of organic and mineral fertilisers. Excessive cultivation requires watering and results in the diminishing of river water levels, soil erosion, and soil washing into the river floodplains. Row earth is a barrier between the river and other elements of the ecosystem. Luke is a battery and transformer of compounds of biogenic elements moving from the catchment area directly to the river.

In the 'vertical' structure of the river ecosystem, there are three main functionally distinct areas: upper, middle and lower. These natural, territorial complexes of the river basin are characterised by homogeneity of physico-geographical, hydrological and hydrobiological features. The upper plots, which are usually the tiniest, are the most vulnerable complexes with regard to anthropogenic impact due to the fact that the tributaries originate here and the main river runoff is formed; hydrobiocoenoses are characterised by their low self-cleaning potential. The middle and lower areas comparatively play a lesser role in the formation of river runoff, but they are more affected by the river. These areas are characterised by well-developed, large flood plains, with densely populated areas with a favourable hydrological regime and fertile soils, which are extremely conducive for agriculture [1].

Coastal territories belong to area of direct interaction of the lithosphere, hydrosphere, atmosphere and biosphere and is the ecotone of the littoral belt. Due to the similar climatic conditions, within the limits of coastal areas, the intensity of physical and geographical processes is much higher than in other landscapes. Any changes in the components of the river's ecological system lead to a violation of the ecological balance. The ecological equilibrium is dynamic due to constant cyclic or irreversible transformations of elements of

the river ecosystem and the interaction of its constituents by means of paradigmatic bonds. The ecosystem of the river is holistic, self-sufficient, interconnected, and dynamic due to the constantly operating links between its constituents. Thus, in the horizontal and vertical structure of the river ecosystem, there are certain features that need to be taken into account in the urban use of the coastal area.

3. Recent problems of coastal area usage

The modern practice of urban planning is unable to solve the problems of protecting the balanced, rational and harmonious use of smaller rivers in the urban areas of the coastal belt. Construction near the rivers is bereft of scientific planning; the aesthetic considerations of industrial and warehouse development in the vicinity of the river are significantly lacking. As a result the residential areas and community living is much below the desired standards i.e. the factors which constitute the panoramic core of any city.

Green plantations along the coastal protective strips are very scarce. Despite warning signs construction activity is on the increase. The coastal belt, although a narrow strip by and large consists of solid concrete cover, embankments with lanes along the highways, but lawns and woody vegetation is a rarity.

The lack of a felled shore, the existence of a built-up and ploughed floodplain deprives coastal areas of their natural water protection function. In such modern realities, the coastal area itself needs protection [Fig. 1 & 2].

Today, the river basins are virtually devoid of natural bio-filter. Their water intakes or ploughed almost to the bottom of the water, or destructively exploited by other means. This provides unobstructed access for the surface runoff with a variety of pollutants to the channel.



Fig. 1. Abandoned state of the coastal area of the river Stugna in the Borov village
(photo by Olga Mykhailyk, 2018)

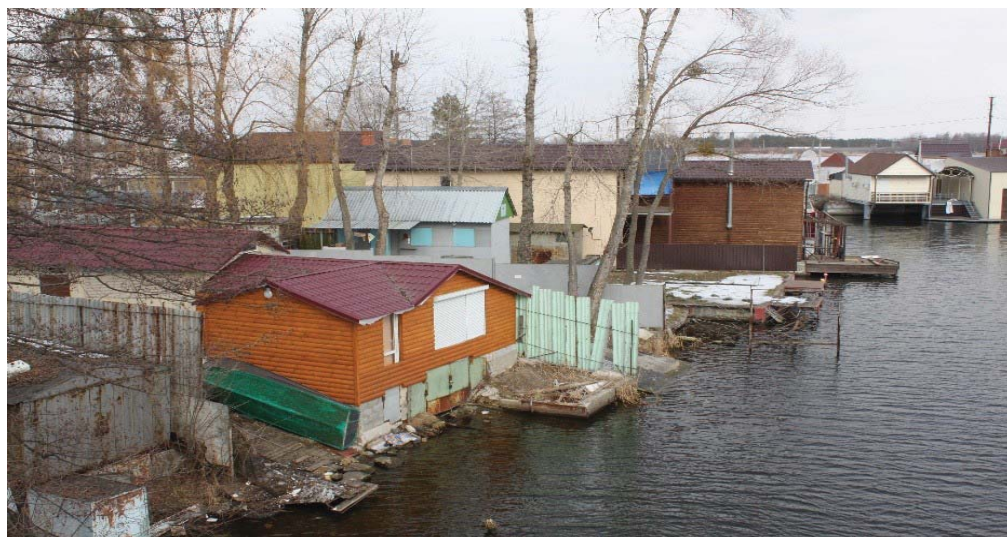


Fig. 2. Coastal area of the river Stugna in the Kozin village (photo by Olga Mykhailyk, 2018)

Many small rivers in settlement areas perform sewage function: the rivers are polluted with runoff domestic waters in settlements and livestock complexes, as well as runoff from roads and agricultural fields. Plots of land in the small rivers basins cover an area of almost 80%. The overgrown coastal areas of small rivers result in increased soil erosion and sedimentation.

Urbanisation of floodplain in the coastal areas has resulted in climatic changes. In built-up flood areas, humidity is lower than on an unfinished floodplain. To be precise 0.2–0.8 mb or 7% higher than in other parts of the city. Near the edge of water this difference increases to 3.2 mb, or up to 10–12%. In built-up areas, soil moisture is 4–8% higher than beyond its borders [2]. The construction substantially changes the soil moisture of the foundations and under conditions of deep groundwater contamination, which prevents the moisture exchange of the atmosphere with the soil. Due to the destruction of natural drainage (falling of ravines, beams, drainage of marshes, creation of artificial barriers for underground drainage) the groundwater level is raised and watering of forest species occurs, which leads to many negative phenomena. During construction work the artificially covered urban area increases. This reduces natural soil evaporation. The impact of Dnieper and Desna and their influx in the coastal territory is manifested in the permanent destruction of the floodplain and its wetlands. It also results in the accumulation of alluvium, especially during the spring flood. The construction work in the floodplains leads to an increase in water intakes. Consequent to which the natural regime of rivers is violated, thereby creating conditions for the formation of runoff change. Floods become more frequent and losses caused by them increase. Straightening the channel of small rivers is accompanied by frequent catastrophic floods which lead to the flushing and blurring of soils, flooding and water logging of a number of reclamation systems, and the destruction of the coastal belt. Due to the decreasing of channel's throughput, floodplains are flooded with gradual degradation of meadows and their replacement with low-value reindeer marsh. Such processes are most actively manifested in the forest-steppe Rivers, where the hilly relief is predominant.

Large-sized garbage sites are located in the coastal areas adjacent to urban roads, industrial enterprises, and rural areas, where garage-construction cooperatives, parking lots and territories are used for warehousing for construction and household. The sanitary norms, with regard to landscaping, in the coastal areas that border the residential and industrial buildings are in a precarious state.

Every year, recreational activity increases in suburban and urban areas. Due to allocation of Plots of land to country estates in the coastal areas, the pollution of communal and industrial sewage increases which results in the reduction of water purification levels. Many rivers (for example, the Lybid – Fig. 3) have undergone drastic changes because of construction work taking place in the river supply areas. The river bed is straightened, entangled in trays or into an underground tunnel. Existing coastal protective strips are erected to 1–2 rows of trees along the shores and often consist of such tree species that are not conducive to the coastal protection.

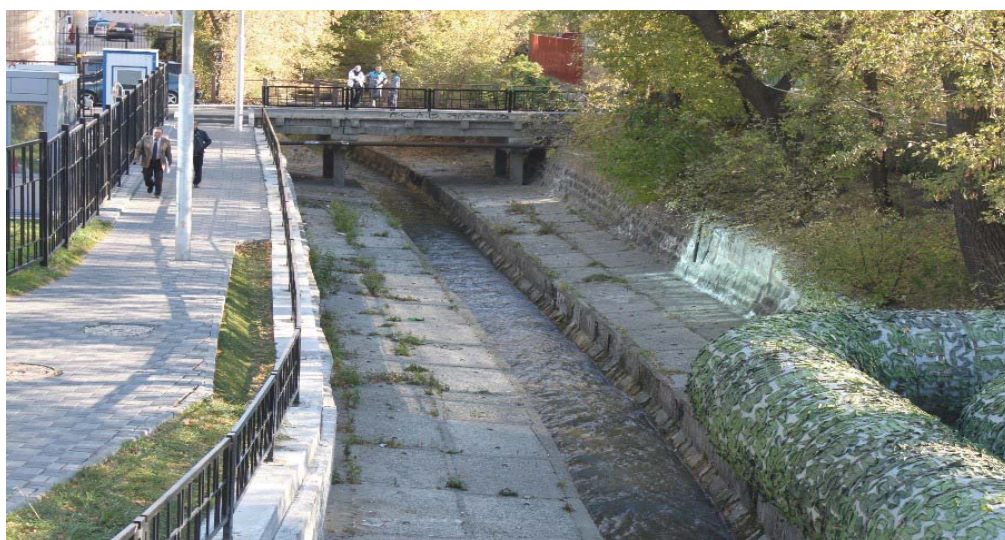


Fig. 3. The Lybid river, Kyiv (photo by Olga Mykhailiyk, 2018)

The construction of agricultural complexes in the coastal belt not only intensifies soil erosion, but also results in the clogging of natural phytocoenoses and the removal of organic and inorganic substances (from farms and from mineral fertiliser storage, respectively) along with the sewage. The placement of landfill sites, gas stations etc. in a river valley or in adjoining yards pollute rivers and their coastal areas. With the increase of cultivation in the coastal areas, the soil erosion also increases.

The drying up of small rivers mostly results in drainage reclamation, which involves rectifying the channel and removing water from the swamps located in the floodplains of the rivers. As a result of the construction of drainage and irrigation systems, the length and density of the network and its drainage role have increased due to the creation of channels that provide a rapid outflow of thaws and rainwater. Widespread reclamation in Polissya led to the disappearance of unique wetlands. Excessive cultivation of the territories almost

led to total destruction of forests in the forest-steppe. Oak forests of Polissya and the forest-steppe replaced low-productivity birch, hornbeam and maple forests. In general, the average forestry in Ukraine (14.3%) is the least in European countries [1]. The use of large-scale drainage reclamation had negative repercussions: rivers that were fed with groundwater disappeared, and rivers that feed on groundwater increased their water content. Reducing the area of mires, the deepening of reclamation canals lead to lower levels of groundwater and the drainage of mires. This directly impacted the reduction of the number of certain species of birds.

The self-cleaning ability of rivers due to chemical contamination has significantly decreased. Extensive overregulation of small rivers lethally effected water-purifying microorganisms. The construction of dam had repercussions on coastal microclimate (humidity increased and the peak of the rainy season shifted from autumn to summer), stability of the coastal areas (abrasion, appearance of landslides) was disturbed, the fish breaks up, the plant cover is destroyed. Rocks violate the flow and continuity from leakage to the mouth. This resulted in increased accumulation of sediments, deterioration of water quality, impacted the flood regime and prevented periodic discharge of water to the floodplain. While controlling the river, rocks inhibit the flow of sand, mud, and other bottom sediments, thereby impoverishing flood plains and swamps below the flow. This is a major factor in the devastation and deterioration of all processes of river life. Construction of hydroelectric power stations contributed to raising the level of groundwater. The rise of the Dnipro River level in Kiev increased from 91.9 m to 1.5 m. This in general is true for all rivers and streams. A significant number of existing treatment facilities is ineffective. There is deterioration in water quality. The minimum indicator of technogenic loading on water (up to 5 t/km²) is observed in the western regions of Ukraine, while in the eastern regions the maximum is (more than 20 t/km²). There are no clean rivers in the lower Dnieper River today. Underground water bodies are extremely limited and or unsuitable for water use.

Presently, in the case of smaller rivers, five parts of all sewage are discharged, and overregulation reaches almost three hectares per km of river. There is a negative trend to increase the excessive uncontrolled regulation of the rates of small rivers. This leads to the loss of the river's qualities and the acquisition of lake-pond qualities. To save rivers, it is necessary to eliminate unnecessary artificial stakes that are in poor condition [3]. Coastal areas – floodplain meadows, swamps, fields, and forests forming constitute an integral ecological system along the river. It requires active revitalisation measures. This entails multiple factors, such as organisational, architectural and planning, engineering and biotechnical works, taking into consideration the individual characteristics of each river ecosystem.

Destruction of the coastal areas results in the anthropogenic effect on land, pollution of water bodies which endanger human settlements, environment and cause irreparable harm to the regional economy. Strengthening anthropogenic impact leads to unification (simplification) and the destruction of coastal vegetation. Excessive ploughing of coastal areas and excessive cattle grazing caused the penetration of weeds into the vegetation group. This implies that the annual plants with weakly developed root system are not capable of forming turf and performing coastal and water protection functions.

4. Preservation methods and revitalisation of coastal areas of river ecosystems

The revival or revitalisation of rivers, particularly by linking small rivers, with medium-sized and large rivers, is very much on the agenda of ecologists, architects and urban planners. The riot crash is observed in almost all countries. All developed countries of the world pay special attention to coastal areas, by adopting through legislation, programs of rehabilitation and revitalisation of coastal areas. In Germany, for example, the federal law 'On water', brings all water objects under government control, and any activity on the banks of rivers and lakes is possible only by taking special permission from the concerned authorities. However, in practice all over the world, there is no single, generally accepted norm for the formation of special regimes with regard to the use of coastal areas of small rivers.



Fig. 4. Revitalisation of areas surrounding rivers

The concept of the European project REURIS (Revitalisation of Urban River Spaces) is to carry out measures on the revitalisation (reproduction) of pre-urban areas, their rational management and the preservation of cultural heritage. The goal of the RRC (River Restoration Centre) in UK is to create a centre for exchanging experiences on river rehabilitation and the spread of successful basin management practices. The REURIS and RRC programs are based on the basic premise of preserving natural environment and reducing anthropogenic effect on river basins [4].

Providing places for public life in the developed coastal area (the Ljubljana river in Slovenia), the landscaping and greening of the underdeveloped coastal belt (Prague suburb (Fig. 5), the central part of Krakow, Obolonskyi embankment in Kiev). The construction of walking 'fresh air' bridge on piles along the river bank in Lensing, Detroit (USA) (Fig. 6) contributes to the conservation of coastal biocoenosis and is an example of successfully developing river coastal areas. In USA during the last decade, 350 dams have been dismantled. Somewhat similar process has taken place in Ukraine at the end of the 20th century: hundreds of small hydroelectric plants were decommissioned so as to restore natural qualities of their highly regulated rivers and thereby revive them.

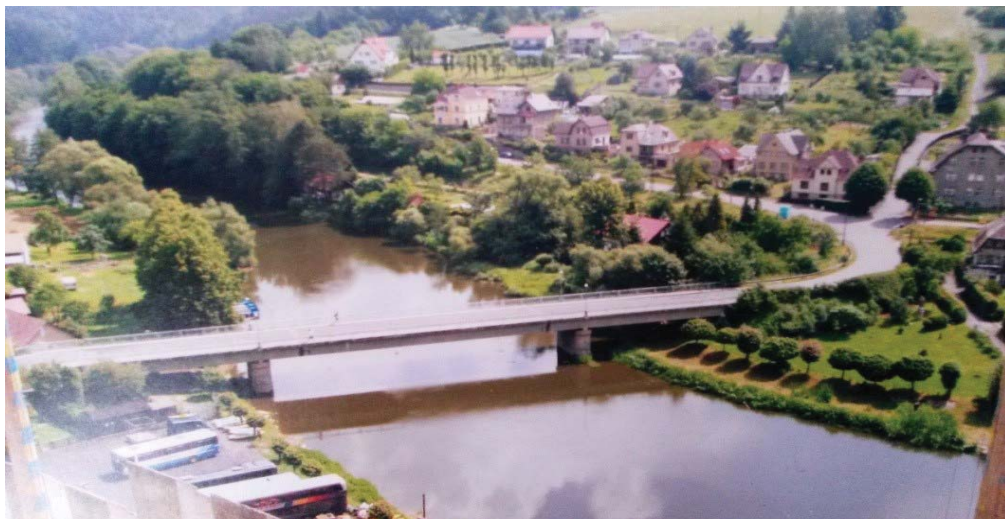


Fig. 5. Development of green belt along the coast line. Prague suburb
(photo by Olga Mykhailyk, 2018)



Fig. 6. Walking 'fresh air' bridge along the riverbank in Lensing, Detroit, USA
(photo by Olga Mykhailyk, 2016)

State Building Standards DBN B.2.2-12: 2018 'Planning and Building Territories' conceived the concept of a green line that ensures conservation of landscaped lands. This is a basic concept in urban planning documentation. On page 8 of DBN B.2.2-12: 2018, the concept is defined as follows: "Prohibition of disposing garbage and waste products in all green areas: recreational forests and forest parks (existing and reserved) and provision is made for funds for preserving nature, creating zones for protecting landscapes" [5]. Establishing a green line in the coastal areas will help to protect the natural conditions of the river ecosystem, maintain the livelihoods of the coastal and aquatic flora and fauna, ecotones, and improve

its self-cleaning and self-regulating ability. Protected zones, hedged by green line are water reserves and coastal biodiversity, protection of river with coastal areas from anthropogenic loading and from dangerous erosion processes.

Each ecosystem of the small river is a unique natural phenomenon, so the definition of the green line should be individual in nature. For each small river, it is necessary to carry out ecological and urban development investigation of the coastal area, taking into account individual natural features and the nature of anthropogenic loading.

5. Conclusion

The coastal area remains insufficiently defined as a holistic object of urban planning and exploration – this entails many unsolved problems for its urban development. Existing legislative and regulatory documents have a simplified way of defining protected areas for water bodies. They do not comprehensively take into account the natural features of small river ecosystem or the local factors of small river ecosystems, which leads to degradation and dying of small river ecosystems. Legislative documents need to be meticulously worked out in order to develop methods, structures and quantitative parameters that should form the basis for a comprehensive analysis and assessment of the coastal area for various types of functional use, taking into account the conservation and revitalisation of river ecosystems.

Translated by Yaroslav Boiko and Evgen Vasiliev

References

- [1] Yaczik A.V., *Ecology of the water economy*, in 4b., K: Geneza, 2003–2004, 306, 20.
- [2] Apollov B.A., *Learning about the rivers*, publishing house MSU, Moskow 1963, 166–177.
- [3] Zub L.M., Tomilczeva A.I., *Morden transformation of catchment basins in forest-steppe rivers*, Ecology protection and nature management, No. 3 (19), 2015.
- [4] Recommendation of the European Parliament and the Council dated 30th May, 2002 with regard to the implementation of Integrated Coastal, Zone Management in Europe, OJ L 148, 6.6.2002, 24–27.
- [5] DBN, Planning and building the territories, DBN B.2.2-12:2018, Kiev, Minregion 2018.



Katarzyna Hodor  orcid.org/0000-0002-4746-7535

khodor@pk.edu.pl

Institute of Landscape Architecture, Faculty of Architecture, Cracow University
of Technology

Albert Fekete

fekete.albert@tajk.szie.hu

Faculty of Landscape Architecture and Urbanism, Szent István University Budapest

THE SACRED IN THE LANDSCAPE OF THE CITY

SACRUM W KRAJOBRAZIE MIASTA

Abstract

In current times of progressing desacralisation, a retrospective view of the transformations that take place in building this phenomenon from the landscape perspective of the city appears essential. The work's main objective is the identification of the ongoing process on two scales: the micro and macro-scale and over time. The initial outline of the subject is meant to present the phenomenon within the structures of the city, the manner of its shaping and influence on the surroundings, orientation within space and strength of impact.

Keywords: sacrum, landscape of the city, landscape sacrum, identity of the place

Streszczenie

W obecnych czasach narastającej desakralizacji istotna wydaje się retrospekcja przemian zachodzących przy budowaniu tego zjawiska w ujęciu krajobrazowym miasta. Głównym celem będzie identyfikacja zachodzącego procesu w różnych skalach i w czasie. Wstępne zarysowanie problematyki ma na celu ukazanie zjawiska w strukturach miasta, sposobu jego kształtowania i wpływ na otoczenie, orientację w przestrzeni i siłę oddziaływania.

Słowa kluczowe: sacrum, krajobraz miasta, sacrum krajobrazu, tożsamość miejsca

1. Introduction – definitions of terms, the goal, state and scope of research

The introductory problem to the subject of the sacred (*sacrum*) in composed space that was taken up in the article covers a scope associated with this broadly understood phenomenon within the city. The outlook presented herein will focus on describing universal symbols associated with the establishment of settlements and cities, as well the consecration of their space based on the sacred. It will be an introduction to broader research leading to investigating these problems using semantic analysis and the assessment of current reception [10].

Often-used definitions of the terms *sacrum* and the city have been recalled here. The outlook upon them has depended on various conditions, both cultural, religious and social ones. The sacred is man's answer to his spiritual needs, it can be featured in complexes, but it can also be present in individual elements, as characteristic landscape and compositional forms belonging to *the field of garden design*. This phenomenon, built upon faith and memory of historical events, is often highlighted in the form of cultural sites [5, 6, 18].

The sacred is a multi-threaded symbolism, reading semantics and articulations, dependant on the time in which it is created. Associated with *such sciences as anthropology*, ethnography, sociology, psychology, religion and oriental studies. The manner of shaping the sacred is dependent on political, economic and social conditions [8, 12].

In order to attempt to define the city, we should use at least a number of terms. It is a *polis*, as a social city spanning between prehistory and the present; it is a system composed of two organically connected subsystems that cooperate based on the feedback loop principle and that are simultaneously autonomous – the urban and social one [21]. From an anthropological perspective, studies concerning the city involve identity as well as social and cultural systems. The city is also described as a dynamic entity, or as “a set of mental maps” by Lynch.

Studies on the perception of the sacred from a landscape perspective have been performed by numerous scholars. This problem group was investigated in terms of its philosophical aspects and those associated with religious (M. Eliade) and sociological studies (P. Kubicki.). K. Lynch and Ch. Delfante defined the basic principles of searching for the form of the city and relationships that take place within urban space. Beata Malinowska-Petelenz's publication, in turn, depicts the latest works of religious architecture from the turn of the twentieth and twenty-first centuries [16].

Norberg-Schulz wrote of semantics in architecture, discussing, among other things, the manner in which the *Christian church has been forming city skylines* since the beginning of the Middle Ages. This structure was becoming a new form and a sense of existence for many people [5].

2017 saw the organisation of the VI international edition of the XXIV scientific conference held as a part of the cycle on garden design and historical dendrology, on the subject “*Sacrum w przestrzeni komponowanej*” (The sacred in composed space in English) at the Cracow University of Technology¹. Multi-national teams presented problems that were various images

¹ Conference organiser: Division of Garden Design and Green Areas, Institute of Landscape Architecture of the T. Kościuszko Cracow University of Technology and the Section of Garden Design and Architecture of the Commission of Urban Planning and Architecture of the Krakow Branch of the Polish Academy of Science, Władysław Szafer Institute of Botany, Polish Academy of Sciences in Krakow.

of this broad research field, showing just how important this subject is in current conditions and how it is viewed from the point of view of different cultures.

The main goal of this article is to present changes that take place in reading the semantics of the sacred in the structures of the city on the example of Krakow (alleys, mounds, temples, monasteries, chapels, calvaries, stones, hills, small chapels, crosses, memorial sites, sites of tragedies, ritual sites) (Fig.1).



Fig. 1. Calvary near the church of the Reformed Franciscans, Reformacka Street, Krakow

The article is an introduction to research, whose continuation is the specific case of discussing the relationships and significance of monastic complexes of the Reformed Franciscans that were built in the seventeenth and eighteenth centuries within the structures of cities [10].

Taking up this subject was a result of the increasingly strong pressure of desacralisation of elements that are important to the composition of a city, changes in function and role that were defined in space where holy places still remain, becoming traces of history.

2. The consecration of the city

Prior to discussing problems associated with the consecration of the place linked with founding cities, elements that occurred in consecrated places often as forms of animate and inanimate nature of outstanding characteristics of the sacred that were used by various cultures in different time periods should be mentioned. These include stone, hills – mountains, a vertical element that takes on the form of a pillar, the tree and the garden as a substitute for nature [5].

Stone took on various meanings depending on a given culture, it was filled with the souls of ancestors, it was a sacrificial stone for the Aztecs, it highlighted Christian, but also Muslim holy places, like Hajjar – the black stone located in Mecca in Saudi Arabia [2, 5].

The stone vertical pillar-like form was thought of as an element that upheld the world, or as a point that marked a border. Known in various different cultural circles, in the case of the Vikings it featured in the form of runic stones. Similar use of these stones was made by the Celts, Germanic tribes, Romans and the pagan tribes of the Rus'. They marked the borders of

areas, they were used for burial – the bodies of the dead were placed on pillars, becoming an analogy for later column chapels [3, 5].

Natural hills were used for communication with the heavens, as an *universalis columna*, highlighting the symbolism of the centre. In various cultures these are special, elevated places to this day, such as Mount Garzim in Palestine, described in the Old Testament as the first site of the promised land given by God, with ruins of cities. Elevations – mounds could be places of burial and could also take on a symbolic significance – devoted to the memory of specific people, constituting observation points and dominants within city panoramas [4, 5, 10, 17].

Another symbol of the sacred is the repeatedly used tree motif – the tree of life, constituting the site of a holy space. In various cultures and times it conveyed multi-threaded symbolism: of nature's fertility, of immortality, the tree of Paradise. It is a topical archetype today and remains in use. The significance of this symbol depended on the tree species that it represented – an apple tree in European culture, while a fig and quince tree – in areas of Asia.

The garden as nature's sacrum became an exceptional, magical reference to the image of the world, combining such compositional elements within it like borders and gates.

It conceptually referred to the garden of Paradise, from the cloister garth gardens to English parks (*beautiful, picturesque, sublime*) in which tombs, temples and places of deep thought and contemplation were found [20].

Greenery accompanied residential complexes, castles, villas as well as monastic complexes, which started to appear in cities in the twelfth and thirteenth centuries. Cloister garths and orchards accompanying monasteries were based on the symbolism of the forms that were located there, as well as on vegetation. They were and are to this day places that are enclosed, fenced off from the world outside, recreating the landscape of the world on the microscale. Monasteries became *civitas dei* (*The City of God*), separated from the *profanum* of the world around them [2, 4, 5, 6].

3. Elements of the sacred in the landscape of the city

We can commonly find numerous elements of the sacred such as alleys, mounds and temples in the city, which are simultaneously places of ritual and remembrance.

We can also mention here various forms of monuments such as crosses, mausoleums, as well as examples of special areas. A holy river can be one such example, serving as a place of burial and purification – in India it is the Ganges.

In cities we can find both temples: the aforementioned monasteries and calvaries. Cemeteries that take on various forms depending on culture, religion and place. Established as communal, they took on the forms of park-like necropolises in the eighteenth and nineteenth centuries.

Problems associated with the influence of the sacred on a location are an essential aspect. Techniques of consecrating a site have been used since the beginning of cultures. They led to the orientating and construing of a holy area by recreating divine creation. The oldest uncovered map of the world is *imago mundi* from the sixth century, which has been presented here. Many cultures repeated the concept of the fourfold division. In ancient Rome, apart

from the site appointed by an augur, the settlement was surrounded with *mundus* – a circular ditch [3, 7]. The division of a square-shaped space into four elements was an archaic concept, repeated by successive cultures when building the foundations of human settlements.

In the structures of the city, the temple appeared as a dominant, becoming a universal *sacrum*, answering the needs of man in terms of searching for and experiencing archetypes, affecting the structure of space through emerging religious and symbolic axes based on the main axes of the mythical Jerusalem [7].

Some of the symbols that have been referred to here have survived, becoming universal. This outlook was the result of man's need to experience archetypes. And thus, when establishing cities and settlements, the process of consecration was based on repeating the model world, whose centre was the temple. Replicas of the cosmic mountain were built in various cultures, as were sanctuaries connecting the earth with the heavens. In Hebrew traditions, Jerusalem was built on the rock of *tehom* (the waters of chaos) – said rock being the “Stone of the Earth's Foundation” [5, 6].

Across the centuries, temples have always been ascribed to divine creation, their models, from Babylonian complexes whose appearance was revealed to king Gudea in a dream, through the Greek Acropolis, to the Roman forums or the model image of the monastery in Cluny, were a spiritual entity, indestructible and heavenly. It was a model in its geometric layout for subsequent temple complexes [17, 20].

The original founding of a city was based on cosmogony – on an image of the world produced by a given religion or philosophical system. This provided protection from impure forces. At its base was Plato's idea of the city-state, transformed into the Medieval axis mundi – a cosmic axis which was the implementation of the idea of Thomas Aquinas [18].

4. The case of Krakow

The case of Krakow can be an exemplification of these tendencies, analysed from the point of view of the transformations of a phenomenon of the significance of the sacred and various forms of content, read differently depending on specific time periods.

The discussion should be started from referring to the site associated with the seat of rulers – Wawel. It is a rocky hill that has fulfilled a special function since the beginnings of the settlement, attaining the well-established position of a national pantheon with a royal necropolis – the chapel of Zygmunt. Jacek Purchla stressed that after Mongol raids in the thirteenth century “the city was reborn anew, stronger, enriched by *ethnos* on the scale of an idea, a process” [19]. When analysing the structure of the sphere of the sacred in the city, an important role is ascribed to St. Stanislaus (canonised in Assisi in 1253) and another saint associated with the city, as the cult of saints has contributed to the building of this city as a place of pilgrimage for centuries. Of course this would not be possible without Krakow having an appropriate social, economic and political position within Europe.

Mounds, built over various periods, conveying different meanings and semantic values, were specific marks inscribed into the panorama of the city. The place of the legendary Krakus' Mound is associated with the tribal period, perhaps with Celtic roots. The mounds of



Kościuszko (1820) and Piłsudski (1935) were places built in order to highlight national identity and the fight for independence. These visual dominants have inscribed themselves into the city's panorama for good, becoming a sort of national sacrum within the landscape (Fig. 2).

Churches and monasteries build a specific atmosphere of the place, marking places of particular significance to history and religion. The number of monastic complexes in 1655 was 19, being limited after the transformations that decluttered the structure in the nineteenth century [11]. At the same time, Krakow's surface area was considerably expanded, incorporating existing temples and initiating the construction of new ones. They are structures that build the identity of the place to this day, being important both to the local community and tourists visiting the city. The sphere of the sacred is not confined to the area of historical Krakow. The Ark of the Lord in Nowa Huta and the Sanctuary of Divine Mercy in Łagiewniki have created new important points on the map of the contemporary city. Krakow's cemeteries include around 18 complexes belonging to a group of Catholic necropolises, with some playing the role of parish cemeteries [25]. Apart from this, we can also find a number of denominational and military cemeteries (Fig. 3).



Fig. 2. A showcase of selected elements of the sacred in Krakow on the axis of time: a view of the Wanda, Kościuszko and Krakus mounds, the Rakowice cemetery – a historical park-type necropolis established in 1803, a chapel near Mazowiecka Street (nineteenth century), monument to Kukliński near the Main Train Station (2018)

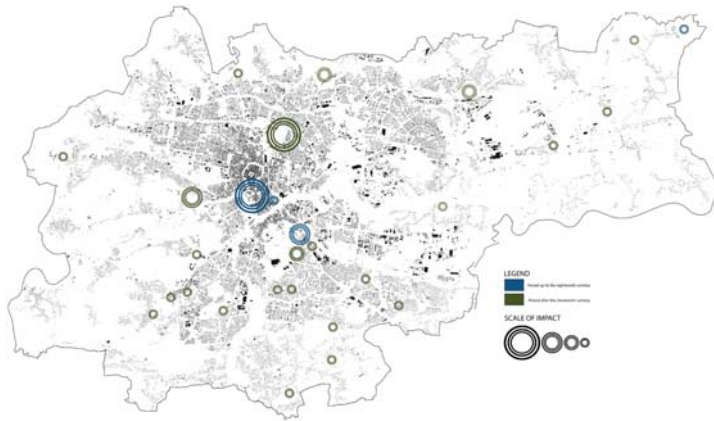


Fig. 3. Scale of impact of denominational and military cemeteries

Inscribed into the urban layout of the city are the many processions that are being organised to this day – including the one in May in commemoration of St. Stanislaus, the Corpus Christi procession and that of the Magi – permanently incorporated into the atmosphere and tradition of the place. They are a manifestation of the formation of the sacrum of the contemporary city.

5. Conclusion

It appears that in the culture of European cities, the sacred, by co-creating structures, has survived to this day, undergoing transformation. The impact of recent years has brought evident, increasing transformations of these spaces, building a new sanctity, while at the same time stripping Catholic temples of their original functions. It must be stated that a slow desacralisation of urban space has been taking place since the period of the industrial revolution, although a renewal of the sacred can take place at any time in accordance with the concept of hierophany – bringing a return to the exceptional sense of a given place [5, 6, 24]. However, identity and tradition still manifest themselves, being highlighted in various ways, referring to canons of the past and finding their place in the contemporary city in the form of spaces devoted to memory, rituals and traditions.

When analysing the original significance of the sacred of the landscapes of cities, it was determined to be based on a repetition of paradigmatic, model behaviours (the recreation of primal actions). It repeated the heavenly archetype, leading to the emergence of spatial structures and buildings associated with the symbolism of an “extraterrestrial centre”. It is still based on a repetition of lay rituals and gestures that have accompanied man since prehistory. In the ancient period it was the main factor affecting shape and location as an element that shaped settlements and cities – and within them, a safe world – in various cultures and religions, constituting a primal layer. At present, it highlights the identity and memory of a place.

References

- [1] Alexander Ch., Oshakawa S., Silverstein M., Jacobson M., Fiksdahl-King I., Angel S., *A Pattern Language*, New York, Oxword University Press 1977; polskie wydanie – *Język wzorów*, Gdańsk 2009, 133–136.
- [2] Bell S., *Landscape – Pattern, perception and process*, Spon., London, 1999.
- [3] Böhm A., *Planowanie przestrzenne dla architektów krajobrazu. O czynniku kompozycji*, PK Kraków 2006.
- [4] Derdowska J., *Praskie przemiany. Sacrum i desakralizacja przestrzeni miejskiej Pragi*, zakłady wydawnicze NOMOS, Kraków 2006.
- [5] Eliade M., *Sacrum, mit, historia. Wybór esejów*, Państwowy Instytut Wydawniczy, Warszawa 1970, 51–144.
- [6] Eliade M., *The Sacred and the Profane. A Harvest*. Book Harcourt, Brace & World, Inc. New York 1956.
- [7] Eysymontt R., *Kod genetyczny miasta, średniowieczne miasta lokacyjne Dolnego Śląska na tle urbanistyki europejskiej*, wyd. VIA NOVA, Wrocław 2009.
- [8] Fekete A., Van Den Toorn M., *Sacred eye-catchers*, Teka Komisji Urbanistyki i Architektury o. PAN w Krakowie Tom XLV, 2017.
- [9] Geghl J., *Życie między budynkami. Użytkowanie przestrzeni publicznych*, RAM, Kraków 2009.
- [10] Hodor K., *Reformaci Prowincji Małopolskiej od XVII do XVIII wieku i ich wpływ na kształtowanie krajobrazów kulturowych*, [manuscript].
- [11] Hodor K., *Ogrody klasztorne i ich rola w kształtowaniu tkanki urbanistycznej miasta Krakowa*, „Czasopismo Techniczne” 6-A/2012, 57–64.
- [12] Hodor K., Łakomy K., *Sacrum krajobrazowe, estetyzacja przestrzeni miejskiej*, „Przestrzeń i Forma”, 26/2016, 201–212.
- [13] Hodor K., *Założenia cmentarne w krajobrazach Krakowa*, „Czasopismo Techniczne” 7-A/2012, 279–286.
- [14] Kubicki P., *Miasto w sieci znaczeń. Kraków i jego tożsamość*, Księgarnia Akademicka, Kraków 2010.
- [15] Mandurowicz M., *Sfera sacrum w przestrzeni miejskiej Warszawy*, Wydaw. Akademickie Dialog, Warszawa 2002.
- [16] Malinowska-Petelez B., *Sacrum in civitas: wybrane zagadnienia*, wyd. PK, Kraków, 2018.
- [17] Norberg-Schulz Ch., *Znaczenie w architekturze Zachodu*, Murator, Warszawa, 1999.
- [18] Ostrowski W., *Wprowadzenie do historii budowy miast. Ludzie i środowisko*, PW, Warszawa, 2001.
- [19] Purchla J., *Kraków w Europie Środka*, Międzynarodowe Centrum Kultury, Kraków 2016.
- [20] Siewniak M., Mitkowska A., *Tezaurusz sztuki ogrodowej*, Warszawa, 1998.
- [21] Wallis, *Socjologia przestrzeni*, Niezależna Ofic. Wyd., Warszawa 1990.
- [22] Wierciński A., *Magia i religia. Szkice z antropologii religii*, Zakład Wydawniczy NOMOS, Kraków 2010.
- [23] <http://dictionary.cambridge.org/dictionary/english/sacred> (access: 20.07.2018).
- [24] <https://encyklopedia.pwn.pl/haslo/hierofania;3911617.html> cf. (access: 20.07.2018).
- [25] <https://www.zck-krakow.pl/> (access: 20.07.2018).

Ewa Łużyniecka  orcid.org/0000-0001-9664-0720
ewa.luzyniecka@pwr.edu.pl
Faculty of Architecture, Wrocław University of Technology

ARCHITECTURE OF MEDIEVAL BREWERIES IN CISTERCIAN ABBEYS

ARCHITEKTURA ŚREDNIOWIECZNYCH BROWARÓW W OPACTWACH CYSTERSKICH

Abstract

The paper presents some conclusions regarding the architecture of medieval breweries in selected Cistercian abbeys. The conclusions have been formulated on the basis of research of Cistercian monasteries in Poland, Germany, and the Czech Republic, as well as recently in France, which have been conducted for 30 years by the author. The main observation is that there are very few original structures like these which were built in the Middle Ages. Another conclusion regards the location of breweries within the area of the monasteries. The rule was to build them by watercourses either away from the centre of the abbeys or by the western wings of cloistral buildings. The examples presented in the paper also confirm the thesis known from previous publications, namely that the architecture of monastic breweries, on the one hand, reflected the economic situation of the abbey and, on the other, the time and style as well as the region where it was established.

Keywords: brewery, medieval, abbey, Cistercians

Streszczenie

W artykule przedstawiono kilka wniosków dotyczących architektury średniowiecznych browarów w wybranych opactwach cysterskich. Wnioski te zostały sformułowane na podstawie prowadzonych przez autorkę od 30 lat badań klasztorów cysterskich w Polsce, Niemczech i Czechach oraz ostatnio we Francji. Głównym spostrzeżeniem jest to, że przetrwało do dziś bardzo niewiele tego typu budowli z czasu średniowiecza. Następnym wnioskiem dotyczy lokalizacji browarów w obrębie murów klasztornych. Zasadą było budowanie ich przy ciekach w dwojaki sposób: w oddaleniu od centrum opactwa lub przy zachodnich skrzydłach budynków klauzur. Zaprezentowane w artykule przykłady potwierdziły także znaną z dotychczasowych opracowań tezę, że architektura browarów klasztornych była odzwierciedleniem z jednej strony pozycji ekonomicznej opactwa, z drugiej strony czasu i stylu oraz rejonu, w którym powstawał.

Słowa kluczowe: browar, średniowiecze, opactwo, cystersi

1. Introduction

The history of beer production goes back to ancient times and it probably began when people started to grow crops. The beer which was produced then greatly differed from the beer produced now – it had very little alcohol, it was less clear, and it was highly calorific and nutritious. It was the Babylonians who started to add hops to improve the taste of beer and to conserve it further. Beer was the main component of diet along with bread in ancient Egypt [1, p. 34].

The nutritious value of beer was equally significant in the Middle Ages. Its production was popular in monasteries, lord's and prince's courts, and in towns. Until the 12th century, the right to brew beer was reserved almost exclusively to monasteries. They brewed beer mainly for their own needs but they would also use beer or hops as a legal tender or trade it. Monks were famous for their continuous improvement of beer production technology and developing new recipes. Some abbeys were willingly investing; for instance, there are three breweries and several hop plantations on the plan of the Benedictine abbey of St. Gall (now Switzerland) from 820 [2, p. 117].

When the Cistercians built their first abbeys at the beginning of the 12th century, they also adopted the Benedictine tradition in the area of beer production. Their breweries were then built in every monastery; however, they were not always solid structures and few of them have survived until today. Usually, regarding their formal and technical condition, they could not match the monastic churches and cloistral buildings, and that is why they are not often subject to detailed analysis. The objective of this paper is then to draw more attention to these buildings. The author has been studying these structures for 30 years while doing research on Cistercian monasteries in Poland [3, 4], Germany[5] and the Czech Republic, as well as recently in France [6].

2. Functional parts

Just as in the case of monasteries, the layout of breweries in the Middle Ages was closely connected with the basic stage of beer production. These stages consist in processing wheat or barley grains in four basic functional zones: malthouse, millhouse, brewhouse and storage house.

The name malthouse derives from the word used to call sprouting grain. Before it was transported to the malthouse, it was cleaned with shovels in the open air or sieved through a mesh. Then malt was prepared. The grain was soaked in wooden cisterns or stone troughs to separate husks from starched seed. After draining water from the cisterns or troughs, the grain was spread out on large floors made of fired brick, stone or clay. Every now and then the grain was sprinkled until germination began that is when malt forms and a significant part of starch from the grain changes into sugar [7, p. 52].

Next, the malt is dried in a drying room with one or more kilns. The malt could be dried in different ways. The easiest way was to dry it in a heated room on a floor made of fired brick, clay or stone. The interior of the drying room had to be well heated and the malt was turned

over several times and sprinkled with water. The malt was sometimes dried directly on clay brick semispherical kilns dug into the ground. Another way of drying malt was on wooden shelves with drilled holes or on grates made of twigs. In the most primitive breweries there was a fireplace under the grates or there was a fireplace in more complex structures on the ground floor with a shaft for hot air going to upper levels and to the shelves with the malt. Sometimes bellows were used to dry and air the grain [7, p. 54].

The malt was then crushed in a millhouse. The milled malt or so called grits was stored or immediately transported to the brewhouse where mashing began. The malt was put into a wooden cistern and soaked with hot water, stirring the mix with special paddles. The mixture was heated up to about 70°C, pouring in boiling water or throwing in hot stones. The mash which was produced was then released to the trough, sieving it through a layer of straw or poured into a cistern with the use of a scoop. The liquid which was produced was poured into kettles or tuns and boiled again while adding hops. Some tuns or kettles were permanently fixed in basins with fireplaces underneath. Sometimes the kettle was placed on stone pillars with a huge chimney above it [8, p. 187].

After boiling, the malted liquid was poured using a wooden scoop or a gutter to a different vessel to cool off. After the liquid cooled it was poured into a keg or a barrel with the use of a funnel strainer, for instance. Yeast deposits from previous brewing were added to the liquid to induce fermentation – pure yeast was not yet known in the Middle Ages. The fermentation took place in the barrels – until the middle of the 19th century it was so-called high fermentation during which the yeast deposits form on the beer surface. The deposits were then removed to obtain a clearer liquid.

Next, the cleared beer was poured into barrels which were rolled to storage places. The main source of problems for beer was high temperature causing it to sour, and that is why the storage places were often dug in the ground and vaulted. In some cases the storage places had ice chambers to lower the temperature of the air.

3. Breweries located away from the church or cloistral buildings

The Cistercian abbeys are complexes of monastic buildings surrounded by walls or fences with different layouts, depending on topographical and hydrological conditions. Breweries were located in different places within the abbeys; however, a general principle can be seen in their location. Some of them were built away from the church or cloistral buildings – the most important buildings of the abbey.

This group includes the brewery in Fountains Abbey (foundation 1132) in England which after the dissolution in 1539 fell into ruin. We only know it from archeological finds [9, pp. 106–105, 10]. The brewery was located south-west of the church or cloistral buildings by a channel going from the south to the north into the monastery's mill stream [11].

According to archaeologists the oldest relic of the brewery was the north and south wall built in 1150–1160 (Fig. 1). The brewery could be entered through a great opening in the south. That opening was walled up in 1220–1247. At the same time, a new east wall was built



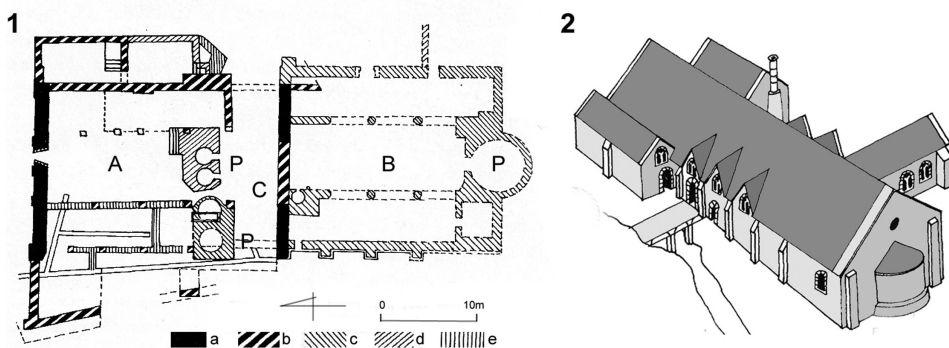


Fig. 1. Fountains, brewery and bakery. 1 – plan per [9, p. 106], 2 – reconstruction per [11, p. 11], A – brewery, B – bakery, C – entrance hall, P – kiln. Walls: a – ca.1150–60, b – ca.1220–1247, c – ca.1260–70, d – end of the 13th century, e – 15th century, developed by E. Łużyńska

and a three-bay interior was formed. The bays were most probably separated with arcades or columns. According to researchers' dating, a new west wall and north-east annex were built in 1260–1270. At the end of the 13th century, inside the brewery an elevated platform was built with openings for two kettles with chambers for brewing kilns underneath them. At the same time, a bakery with a huge round fireplace was built south of the brewery. According to researchers the brewery was extended again in 1320–1340. This is when another elevated platform with stairs was built. It had two round fireplace chambers with inlets from the south in its lower part. The brewery was last modernized in the 15th century and it included the construction of partition walls between older arcades or columns as well as the south-east annex.

The mediaeval brewery in Lubiąż Abbey in Silesia (foundation 1175) was most probably also located away from the church or cloistral buildings. Its location by a bakery was already known earlier. In about the middle of the 18th century, the Silesian painter Friedrich Bernhard Werner drew an aerial view of the abbey and he described one of the buildings with a Baroque form as *Das Back und Brauhaus* [12, p. 55] The neoclassical form of the building comes from the 19th century; at present the structure is not used (Fig. 2).

The author studied the brewery at Lubiąż Abbey twenty years ago in search of its mediaeval parts [3, pp. 312–313]. At present, the work's findings are being verified. Jan Kryštofa Lišk presented the mediaeval form of the brewery and the bakery seen from the north in his drawing from 1708 [12, p. 54]. The author drew two two-storied buildings with double-pitched roofs of different heights. This form of the buildings was in general confirmed by architectural research (Fig. 3).

It can be claimed on the basis of those drawings that the brewery in Lubiąż was most probably located in the west part of the present building. Brick walls of two rooms and small, almost semicircular windows were uncovered during research. Furthermore, it was found that the bakery was most probably located in the east part of the building. The most important part of the bakery was a square room with a hemispherical vault with pendentives connected with a chimney located above the fireplace. The relics of the vaults were found during the study. A pointed hip cap carved into the wall of the bakery was also discovered. It served

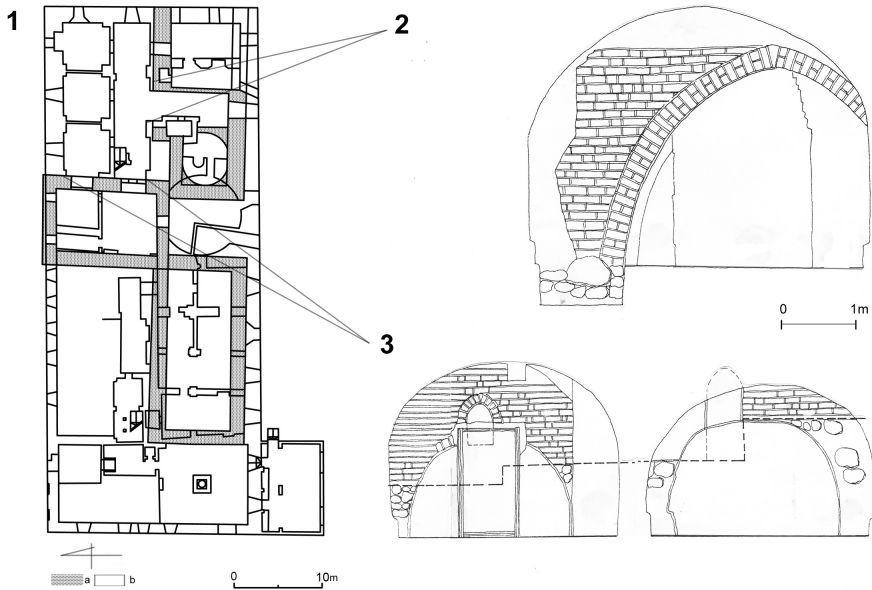


Fig. 2. Lubiąż, brewery and bakery. 1 – plan of basements, 2, 3 – building material survey. Walls: a – Middle Ages, b – 17th–18th century, c – 19th century, developed by E. Łużyniecka

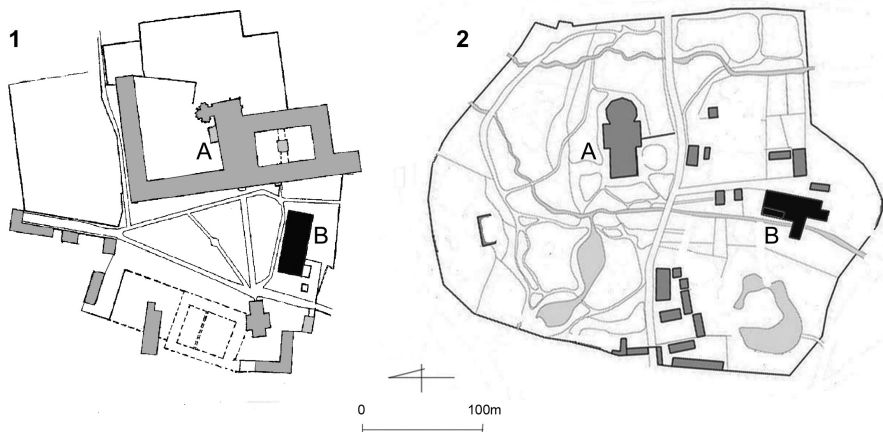


Fig. 3. Breweries located away from the church and the cloistral buildings: 1 – Doberan, 2 – Lubiąż, A – monastic church, B – brewery, developed by E. Łużyniecka

as a buttress for the cracking vault and as an entrance hall to the building. At present, it is difficult to determine the total length and number of buildings of the brewery and the bakery in the Middle Ages because the east buildings were demolished in the 18th century and a wide road was built there. The west buildings were transformed into one structure, changing the direction in which the walls were going.

Another monastic brewery located away from the church or cloistral buildings is Doberan Abbey in Mecklenburg (foundation 1177) founded in its present site in 1186. The brewery was located south-west of the cloister by a channel going from the south to the north to the monastery's millstream (Fig. 3.2). The building stands out against the other structures of this kind because of the good condition of its mediaeval fabric. Due to its significant dimensions, the building from the 13th and 14th centuries did not need any extension later on. In the 20th century, it burned down several times and at present it does not serve its original function. It has been renovated for many years and seasonal exhibitions are held in some of its interiors.

The author studied the monastery ten years ago [5, pp. 119–131, 458–482] and analysed the operations and the construction of the brewery (Fig. 4). Initially, it was a small building with a fragment of a brick wall being most probably its only original part; it is now inside a structure which has three sections (Fig. 5). The building was remodelled in the 14th century and it housed a malt house, a brewhouse and a millhouse.

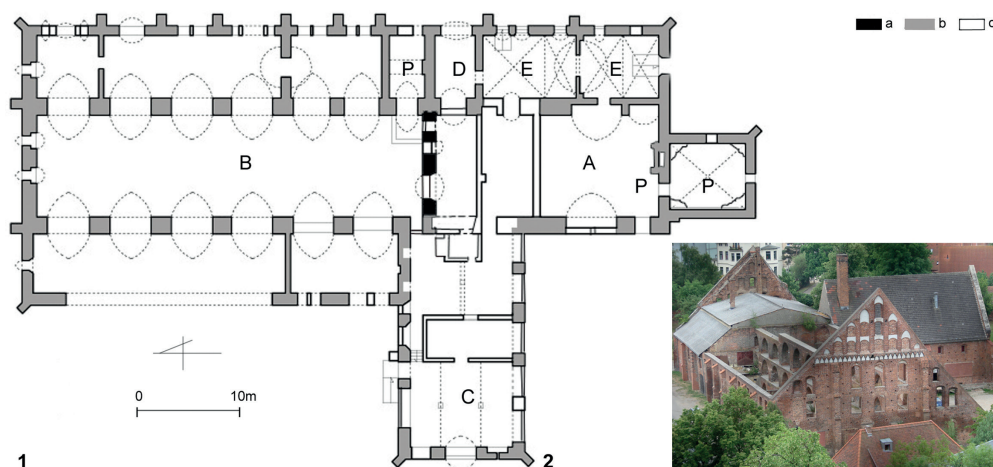


Fig. 4. Doberan, brewery. 1 – plan of basement, 2 – aerial view, 2009, A – malt house, B – brew house, C – millhouse, D – entrance hall, E – cooling room and beer storage, P – kiln, Walls: a – end of the 13th c., b – 14th century, c – 17th–20th centuries, developed by E. Łuzyniecka



Fig. 5. Brewery in Doberan, 1 – east facade, 2 – brew house interior, 2009, photo by E. Łuzyniecka

All of its load-bearing walls have arches. Depending on the number of stories, there was one, two or three levels of arches. Such a structure was very useful as it allowed for any division of the interior, both horizontal and vertical. The arches in the external walls were filled with thin brick walls so they could be visible only from inside. The flat surfaces of the wall on the outside were reinforced with buttresses.

The central element of the brewery was its entrance hall. One could get south from it to the brewhouse – the remains of the brewing equipment included the traces of fire and a relic of a chimney shaft. The malthouse was north-west of the entrance hall. In the malthouse on the ground floor there was a fireplace with a shaft for hot air provided to the upper stories.

One could also get from the entrance hall to the storage rooms in the south-east part of the building. They were dug into the ground and vaulted. One of them was an ice room called the ice cellar.

Along the axis of the entrance hall there was a millhouse with two milling machines until the 19th century – there were wheels with blades downstairs. At the height of the floor, there were millstones. Malt would be dried and ground on the same level. The excess of crushed malt was most probably stored on the 1st and 2nd floors in the east rooms.

The last example of a structure located away from the church or cloistral buildings is the 14th-century brick brewery in Lehnin Abbey in Brandenburg (foundation ca.1180). It was located north of the cloister; beer production stopped there in the 20th century. At present, its interiors are being converted to hold exhibitions and its external walls have been renovated recently [13, p. 62]. During the restauration of the gable walls of the brewery, wide openings with pointed arches were reconstructed at the bottom; narrow windows with pointed arches were reconstructed on two levels at the top. The side walls of the brewery still have their original structure with arches. The walls with narrow, rectangular windows are still visible inside the arches (Fig. 6).



1



2

Fig. 6. Brewery in Lehnin, 1 – view from the south-west, 2 – north wall, 2011, photo by E. Łuzyniecka

4. Breweries located by the cloistral buildings

The breweries in mediaeval Cistercian abbeys were also sometimes located by the cloistral buildings, close to the west wing called the wing of converts. Sometimes they were built also in front of the west facade of the monastic church.

The brewery of the Pomeranian Cistercian abbey in Oliwa had such a location (foundation 1178–1188) (Fig. 7.1). It no longer exists today but its height can be determined on the basis of the drawing by P. Willer from 1687 and a plan from 1847 [14, p. 39, 44]. At present, a trace of the brewery roof is displayed on the wall of the west towers of today's cathedral in Oliwa. It can be assumed on that basis that the brewery was an exquisite brick building, most probably two-storied. (Fig. 8.1).

The original brewery from the Pomeranian Pelplin Abbey (foundation 1276) no longer exists any more either. The location and the view of that brewery is known from a drawing from 1774 [5, p. 257]. Interestingly, its buildings most probably included a brewhouse and a malthouse located at some distance from it. The brewhouse was most probably located north-west of the cloistral buildings by the yard where beer was bottled and from where it was later taken to the cellars in the west wing of the cloistral buildings. The malthouse was located in the south-west part of the abbey, adjacent to the millhouse and it looked similar to the utility complex from Doberan. It is known from the descriptions from before the demolition in the 19th century that there was a granary with a room for grain storage in the basement. Directly above it there was a malthouse with a special floor to produce malt with high stairs leading to it. Hops and barley were also stored in those buildings.

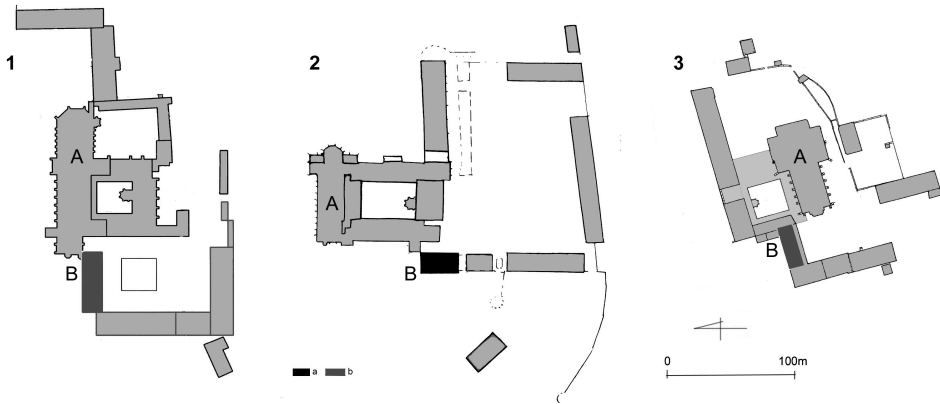


Fig. 7. Breweries by the cloistral buildings, 19th century: 1 – Oliwaper [14, p.44], 2 – Chorinper [15, p.29], 3 – Kamieniec Ząbkowicki acc. to [3, p. 501], A – monastic church, B – brewery, a – existent building, b – non-existent building, developed by E. Łużyńska

The malthouse of the Silesian Kamieniec Ząbkowicki Abbey (foundation 1247) was built right next to the west wing of the cloistral building (Fig. 7.2). Most probably the relics of those buildings are still in the walls of the present residential house. This is evident from the depiction of the malthouse from around the middle of the 18th century by F. B. Werner.

The author drew three buildings and described them as Maltzhaus, Beckenhs, bräühs [12, p. 80]. In the 19th century, all those buildings were converted and their function changed. The original, mediaeval cellarium in a good condition is still in the west wing of the cloistral building. It has two rooms, dug in the ground a little with a pointed, tunnel vault. They might have been used not only to store food products but also to store beer.

Unlike the buildings described above, which no longer exist, the next brewery is still in a relatively good condition. This is the brewery in Chorin Abbey in Brandenburg (foundation 1258) [15, pp. 44–45]. It is located by the west wing of the building and it adjoins the monastery gate. At present, it does not serve its original function; it is a place to hold exhibitions. It was built in two stages. Its only original, oldest part is the north facade with a tall stepped gable. The facade in the basement is decorated with pointed blanks (Fig. 8.2). The remaining walls of the brewery, built in the 14th century, have a different form. They are flat on the outside, with arches visible only from the inside. The north facade of the brewery differs

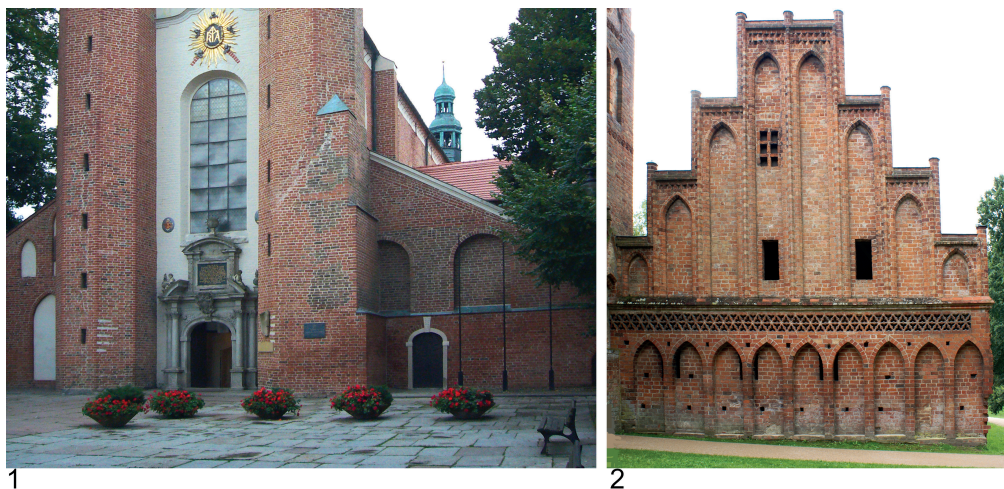


Fig. 8. Breweries by the cloistral buildings: 1 – relict in Oliwa, 2 – north wall of the building in Chorin, 2011, photo by E. Łużyniecka



Fig. 9. Brewery in Chorin: 1 – south wall, 2 – interior, 2009, photo by E. Łużyniecka

from the south facade described above. It has a tall triangular gable with tracery decoration. The inside of the brewery is a single room filled with timber structure. The basements are only under the south part of the brewery (Fig. 9).

5. Summary

Some conclusions regarding the breweries in Cistercian abbeys can be drawn on the basis of the presented analysis. The main observation is that there are very few original buildings of that type from the Middle Ages. If we assume that every abbey had at least one brewery, then their number should be at least close to a thousand. 343 monasteries were founded, mainly in France, from 1098, when the Cistercian order was founded, until 1153. In the following years, the Cistercians spread all over Europe and they reached Syria. Until the 14th century, the number of abbeys grew to about 750 [16, p. 13].

There are several reasons why there are so few original Cistercian breweries. They were destroyed in the 16th century when, as a result of the Reformation, some monasteries, especially German ones, were liquidated. On the other hand, in the times of the Counter-Reformation, in the 17th and 18th centuries, the complexes of monastic buildings in Austria, in Silesia, Bohemia, Hungary were extensively remodelled in the Baroque style. The breweries or even whole abbeys were also destroyed by the French Revolution – many abbeys were razed to the ground at the end of the 18th century in France. A lot of destruction was connected also with the secularization of monasteries at the end of the 18th and at the beginning of the 19th century.

Another reason why there are so few original breweries in abbeys is their function, which required the constant use of fireplaces so their exposure to the danger of fire was obvious especially in the Middle Ages when breweries, just like other outbuildings, were rarely built of fireproof materials. A partial protection against fire was provided by their brick or stone walls and roofs covered with slate or clay tiles and such buildings have survived until today. Unfortunately, as can be concluded on the basis of relicts and iconography, they were usually half-timbered with brick infills. Sometimes, against all logic, they were built exclusively of flammable materials, such as wood and were covered with straw, reed or laths [7, p. 54].

Another conclusion drawn on the basis of the presented analyses regards the location of breweries within the monastery walls. Principally, they were built by watercourses which provided the water needed for the production of beer and which moved the wheels in the malthouse. The water was supplied to the breweries from the rivers flowing near monasteries in narrow canals (Fontenay, Doberan, Pelplin, Oliwa, Kamieniec Ząbkowicki) or wider mill streams (Lubiąż, Chorin). Before pumps were invented the water inside the breweries was carried in buckets. It cannot be ruled out, however, that other methods known from other branches of industry could also have been used e.g. lifting water in buckets placed in a treadmill.

There were two kinds of location of breweries in relation to the church and the cloistral buildings. Some of them were built away from the centre of the abbey; they were usually bigger and they had beer storage rooms on lower levels (Fontenay, Lubiąż, Doberan). Other breweries were built by west wings of cloistral buildings and close to monastic churches

(Oliwa, Chorin, Kamieniec Ząbkowicki). In such cases the beer produced in the brewery was stored in the monastic cellars.

Furthermore, it can be concluded on the basis of the conducted analyses that it was uncommon to have a malthouse, a brewhouse and a millhouse in a single structure (Doberan). Most often the individual stages of beer production took place in separate buildings, standing close to each other (Oliwa, Kamieniec Ząbkowicki, Pelplin). Sometimes breweries were built together with bakeries (Fonteney, Lubiąż). Such a combination was useful as in both cases grain was processed with the use of water and kilns.

The presented examples also confirmed the thesis known from studies according to which the architecture of monastic breweries, on the one hand, reflected the economic situation of the abbey and, on the other hand, the time and style as well as the region where it was established. The best example of this is the brewery in Doberan Abbey. Its structure and architectural details are repeated in other original buildings of the abbey from the Middle Ages.

Currently, the mediaeval breweries in Cistercian abbeys have a different status and function. Most often they have been listed as historic structures and converted from industrial or utility buildings to centres of culture or museums where the history of the abbey is presented. Often they host meetings and concerts.

Translated by Tadeusz Szalamacha

References

- [1] Brzezowski W., Jagiełło M., *Ogrody na Śląsku*, Vol. 2., Barok, Oficyna Wydawnicza Politechniki Wrocławskiej, Wrocław 2017.
- [2] Coppack G., *The white monks. The Cistercians in Britain 1128–1540*, Tempus, Stroud 2000.
- [3] *Fountains Abbey. Studley Royal*, “The National Trust”, London 2000.
- [4] Gooss G., *Kloster Choerin. Gebrannte Geschichte-ein rundgang durch die Klosteranlage*, Kloster Chorin, Eberswalde (without the issue date).
- [5] Hebron S., *Fonteney Life in a Monastery*, PITKIN, (without the issue place) 2001.
- [6] Klonder A., *Napoje fermentacyjne w Prusach Królewskich w XVI–XVII wieku. Produkcja, import, konsumpcja*, Ossolineum, Wrocław 1989.
- [7] Klonder A., *Browarnictwo w Prusach Królewskich (2 połowa XVI–XVII w.)*, Ossolineum, Wrocław-Warszawa-Kraków-Gdańsk-Łódź 1983.
- [8] Laboa J.M., *Mnisi Zachodu i Wschodu. Historia monastycyzmu chrześcijańskiego*, Carta Blanca, Warszawa 2009.
- [9] Łuzyniecka E., *Architektura klasztorów cysterskich. Filie lubiąskie i inne cenobia śląskie*, Oficyna Wydawnicza Politechniki Wrocławskiej Wrocław 2002.
- [10] Łuzyniecka E., Świechowski Z., Kunkel R., *Architektura klasztorów cysterskich. Małopolskie filie opactwa Morimond*, Oficyna Wydawnicza Politechniki Wrocławskiej, Wrocław 2008.

- [11] Łużyniecka E., *Pelplin i Doberan. Architektura opactw cysterskich spokrewnionych filiacyjnie*, Oficyna Wydawnicza Politechniki Wrocławskiej, Wrocław 2014, 794–802.
- [12] Łużyniecka E., *Le plus grand monument cistercien de Pologne: l'ancienne de Lubiąż*, [in:] *Mélanges cisterciens 2012: offerts par l'ARCCIS au Père Placide Vernet, moine de Cîteaux, pour son 90e anniversaire*. Bégrolles-en-Mauges, Abbaye de Bellefontaine 2012, 277–297.
- [13] Łużyniecka E., *Badania architektury francuskich klasztorów cysterskich w Obazine i Grosbot – etap wstępny*, [in:] *Dzieje i kultura Cystersów w Polsce*, Vol. 1, M. Starzyński, D. Tabor (ed.), Wydawnictwo Towarzystwa Naukowego Societas Vistulana, Kraków 2016, 17–35.
- [14] Piwek A., *Architektura kościoła pocysterskiego w Oliwie od XII do XX wieku. Świątynia zakonna białych mnichów*, Bernardinum, Pelplin 2006.
- [15] Rutkowska-Płachcińska A., *Urządzenia młyńskie, przetwórstwo i wyrób artykułów spożywczych, organizacja sprzedaży*, [in:] *Historia kultury materialnej Polski w zarysie*, Vol. II, *Od XIII do XV wieku*, Ossolineum, Wrocław–Warszawa–Kraków–Gdańsk 1978, 180–204.
- [16] Warnatsch St., *Zisterzienser – Abtei Lehnin. Von der askanischen Familien-Grablege zur Einrichtung evangelischer Nächstenhilfe*, Verlag Langewiesche Nachf, Königstein 2008.
- [17] Wyrwa A.M., *Udział zakonu cysterskiego w kształtowaniu tożsamości kulturowej Europy (w świetle jego struktur organizacyjno-prawnych w średniowieczu)*, [in:] *Cistercium Mater Nostra. Tradycja – historia – kultura*, M. Starzyński (ed.), Opactwo Cystersów w Mogile, Kraków 2009, Vol. III, 11–24.

Agnieszka Ozimek  orcid.org/0000-0003-0115-3263
aozimek@pk.edu.pl
Faculty of Architecture, Cracow University of Technology

LANDSCAPE DOMINANT ELEMENT – AN ATTEMPT TO PARAMETERIZE THE CONCEPT

DOMINANTA KRAJOBRAZOWA – PRÓBA PARAMETRYZACJI POJĘCIA

Abstract

A “landscape dominant element” – an object with the greatest range of visual impact on the surrounding space, of a strong form that integrates the entirety of a composition, distinguished by its height, dimensions, colour, material, texture or the variety of its details. The attempts to define the concept presented herein, and which is intuitively perceived as obvious, illustrate its ambiguity. They bring to mind a visual contrast between this subject and others that surround it. This article attempts to analyse views using the author’s computer program. The objects in the photos are characterized by their interference in a panorama silhouette or skyline, size, colour, height, and shape. This helped to identify those that clearly stand out from the other forms, with which they come into visual interaction. The purpose of these considerations is to create tools that allow for a partial objectification of the landscape composition assessment.

Keywords: landscape dominant element, landscape assessment, view analysis, shape descriptors, colour, size, skyline

Streszczenie

Dominanta krajobrazowa – obiekt o największym zakresie wizualnego oddziaływania w otaczającej go przestrzeni, o formie silnej, integrującej kompozycję, wyróżniający się wysokością, gabarytami, barwą, materiałem, fakturą czy bogactwem detalu. Te próby definicji pojęcia, które intuicyjnie odbierane jest jako oczywiste, obrazują jego niejednoznaczność. Wpisany jest w nie także wizualny kontrast pomiędzy tym przedmiotem a innymi, które go otaczają. W artykule podjęto próbę oceny widoków z wykorzystaniem autorskiego programu komputerowego. Obiekty widoczne na zdjęciach scharakteryzowano pod względem stopnia ingerencji w sylwetę panoramy lub „linię nieba”, rozmiaru, barwy, wysokości i kształtu. To pomogło wskazać te z nich, które wyraźnie odróżniają się od innych form, z którymi wchodzi w wizualną interakcję. Celem tych rozważań jest stworzenie narzędzi umożliwiających częściową obiektywizację ocen krajobrazowej kompozycji.

Słowa kluczowe: dominanta krajobrazowa, analiza widoku, ocena krajobrazu, współczynniki kształtu, kolor, gabaryt

1. Introduction

When analysing a landscape composition, scholars utilise a range of terms that define its constituent parts. Polish scholars use the following hierarchy: dominant elements, sub-dominant elements and accents, which, respectively, fulfil an increasingly weaker role in the organisation and structuring of the whole [2, 3, 6, 25]. In English literature the term “landmark” has a similar meaning [28]. Despite the fact that we understand these terms intuitively, numerous examples of diverging opinions expressed by different scholars have confirmed the fact that the line between a dominant and a sub-dominant element or that between a sub-dominant and an accent has so far not been precisely defined [5, 20, 34].

When evaluating the function of each building within a structure we co-consciously use multi-criteria analysis, the basis of which is the scale of the impact of an object. It depends on the qualities of the object being observed and the spatial relations that connect it with others that are a part of a composition.

One advantage of multi-criteria analysis is the fact that it can be performed using machines and programs in a fully algorithmic and parameterised manner, which makes the assessment more objective. However, it is necessary to formulate parameters thanks to which our machine will be capable of identifying objects and assigning them to a given definition. These tools can work with data from various sources, even photographs that are shared by users on the Internet.

Studies of the landscape structure using digital techniques are usually made using maps and aerial photographs. Analyses of eye-level views are few. Attempts to characterize the landscape components of the composition were made at work [24], juxtaposing the map and view, and then determining the angle that the individual components cover. Another numeric indicator that determines the percentage of the object in the view is the average brightness of the image. Due to the possibility of different image framing, it is useful when comparing different variants of land development [23]. Alternative parameter that characterizes the structure of objects, their granulation and placement is the box fractal dimension [19]. In terms of the analysis of solids and architectural forms, the shapes of objects were characterized by the number of angles and vertices [29] and some shape coefficients, such as compactness, convexity, rectangularity or centricity [18].

The method proposed by the author can aid experts in finding landscape landmarks [17] and point to objects that are potentially important within the landscape. Developing such tools can also be particularly helpful in the event of the necessity of analysing large areas when identifying priority landscapes.

In the article the author made an attempt at analysing the semantics of the notion of the dominant element. Specifying the qualities that make us prone to assign this role to a given form served as a starting point for determining criteria on the basis of which it can be possible to perform a more objective assessment. The discussion that was engaged in was meant to develop numerical indicators that could make it possible to automatically classify dominant elements on landscape photographs. This approach requires verification over the course of a discussion with experts, particularly in relation to the selection of specific indicators and threshold values. The method of the classification of dominant elements developed by the author will be possible to use in order to parameterise other constituent elements of the landscape.



2. Term definitions

When starting our search from dictionary definitions, we can come across the following descriptions:

- „1. a principal, dominant quality or element of something;
2. in statistics, the value of a quality that occurs the most often in a group;
3. the fifth sound on the major or minor scale; also: a chord based on this sound;
4. in psalms: the longest lasting sound” [26].

The description provided above confirms that this term is used in many fields, including in statistics and musicology. In studies concerning visual aspects only the first part of the definition will be useful. We find here a reference to the most important part, which defines the character of a given object.

In the foreign loanword dictionary we will read that a dominant element is:

- „1. a main characteristics, fundamental to anything; an overruling element, one that stands out;
2. *in statistics*: a) the value of the characteristic which is present the most often in a given test group; b) the most probable value of a random variable;
3. *biol.* a species that dominates over other species in a group of living organisms in terms of number;
4. *phys.* the dominant wavelength of a colour, defining its shade;
5. *mus.* a) in psalmic tones it is the longest sound on which a text is recited; b) in a modal system, the fifth sound of the fundamental scale or the fourth of the derivative scale” [27].

Here we have another reference to biology and physics. Similarly as in the previous definition, only the first part refers to broadly understood composition. The content is similar, as the dominant element is treated as a quality or the part of the object that is the most essential as well.

If we narrow the term down to architecture, then an architectural dominant element can be defined as:

- ▶ the main architectural element that stands out in the foreground, formally constituting the most important accent of a work of architecture, to which other elements are subordinate [31];
- ▶ the main accent of an architectural or urban composition [33];
- ▶ a building or architectural and urban complex that stands out within a given area thanks to particular qualities [10];
- ▶ a work of architecture with the greatest scope of impact that dominates the entire space that surrounds it [14];
- ▶ a work of architecture with a strong form that stands out in terms of form and height, one that fulfils the role of a distinct mark that accentuates a space [4];
- ▶ a symbol of spiritual or secular power, clearly standing out within the panorama of a city due to its large scale and exposed appearance; the sign of an important place within urban tissue, that stands out within a space thanks to its formal exceptionality [11].



These definitions can, overall, be assigned to one of two groups. In the first group their author refer to the form, the external appearance of an element or of an entire structure that is considered the most important in terms of composition, one that stands out in some way. The second also refers to the function of a dominant element, as a structure that provides a certain character to a composition.

The scope of the concept of a landscape dominant element is broader, because it covers both natural objects, as well as man-made ones. In this case there is also a reference to an element that identifies a space [16, 17], however, we can also find definitions through enumerating characteristics thanks to which landscape dominant elements (natural or architectural objects or architectural and urban complexes) stand out from their surroundings. These can be: size, height, colour, an original form or details [6, 34].

Examples of natural dominant elements are old plant specimens, particularly of trees, terrain forms – objects that are extraordinary, that set the character of their surroundings, ones that impact the space around them. However, in our current time this does not equate with their natural origin, as many of them, particularly plants, appeared in a given area because of man. It is human activity that has given dominant elements their significance. Their genesis was usually accompanied by a goal for said object to highlight the entirety of a composition [6]. A large or exotic tree could fulfil an aesthetic function, being a true ornament to a garden, while at the same time signifying the prestige and wealth of its owner.

The matter was similar with architectural dominant elements. Religious, administrative and representative buildings were intentionally given forms that set them apart from their surroundings in visual terms. Such structures fulfilled the role of orientation points, in addition to establishing the identity of a locality [15], playing, apart from a pragmatic function, also that of a mark [6].

We can currently question the intentionality of creating dominant elements with a retail-related or technical function [8]. It appears that these efforts do not have a conscious character [5]. It is difficult to suspect the author to have a religious motivation, the need to highlight the prestige of a structure or that of its owner, the establishment of a point that makes orientation within a space possible or improving its aesthetic. It is often economic or pragmatic conditions that are responsible for a form (the need to make the maximum possible use of a space). Due to this, it is residential tower blocks, as well as industrial or storage buildings that become dominant elements [10].

3. Model of assessing an object as a dominant element

Every model is a sort of approximation of reality. In the community of landscape architects this term is understood as a physical element – a model or mock-up of an area, building or plant. The term has, however, a much broader meaning. We can, after all, model various types of processes and phenomena. A properly constructed model should take into consideration the most distinct qualities of an object (a static model) or, alternatively, the conditions that the course of a process or the occurrence of a phenomenon depend on (a functional model) [19].



To create a model of object evaluation as a dominant, a definition listing its characteristics that can be parameterized will be useful [21]. In table 1 the author presented a listing of the characteristics of objects and numerical indicators that can describe them. It should be highlighted that a dominant element always functions in the context of its surroundings, as the values that characterise it will always be read in the context of the parameters of neighbouring objects.

Table 1. A listing of the characteristics of an object and numerical indicators that can define them

Object characteristics	Numerical indicator
Considerable impact on the skyline	The highest point of the skyline
Considerable size	Surface area on a photograph
Significant height	Vertical dimension
Original form	Shape coefficients
Wealth of detail	Shape coefficients
Extraordinary colouration	Colour analysis

As the first of the factors that make it possible to define a form as a dominant element, the author took into consideration an object's impact on the skyline. This role can potentially be played by the tallest object, one that towers above the remaining ones. The author proposed an algorithm which searches for the highest-placed pixel of the highlighted objects.

The calculation of the next indicator is only seemingly without difficulty. Thanks to a raster image structure [13] we can highlight groups of pixels which correspond to individual objects visible on a digital photographic image. Their number will determine the size of a given element and will constitute a whole number. However, we should keep in mind the fact that due to perspective projection, objects located closer to the viewer appear larger, while those that are further away – appear smaller. This is why only comparisons between objects located on the same plane are conclusive [19, 22].

This also applies to the height of an object, which can be calculated as the maximum dimension on the vertical axis (y) and the result will also be a whole number.

Considerable complications appear during the stage of segmenting an image, which is based on highlighting the fragments that correspond with each object. The result is dependent on the resolution of the image, the chosen file format and the associated compression method and the tool used to select the image fragment.

The 3D form of an object is represented on a photograph by its shape, understood as a contour visible in a given projection. In order to characterise it, we can use shape coefficients that describe the size of a shape, its elongation, compactness, the irregularity of its contour and its complexity. We can thus assume that the dissimilarity of an object, as well as a greater wealth of its detail – in comparison to other objects – will be reflected in the differences of these parameters.

Eleven factors were considered in the study, of which the first two are defined as circularity coefficients (W_1 and W_2). They are calculated using the following formulae:



$$W_1 = \sqrt{\frac{4 \cdot A}{\pi}} \quad W_2 = \frac{P}{\pi} \quad (1) \quad (2)$$

for which:

A – is the surface area of an object, while P – is its perimeter.

W_1 is equal to the diameter of a disc with the same surface area as the object being analysed, while W_2 – the diameter of a disc with the same circumference as the aforementioned shape. They primarily illustrate the size of an object, but can also be used to calculate the next coefficient.

W_3 (the Malinowska coefficient) can be calculated based on the proportions of the previous two indices. For elongated shapes it will take on high values, while for those with a shape similar to a circle – low values.

The following equation was used in the calculations:

$$W_3 = \frac{P}{\sqrt{4 \cdot \pi \cdot A}} - 1 \quad (3)$$

The following W_4 coefficient (the Blair – Bliss coefficient) requires more complex calculations to be performed. In the formula:

$$W_4 = \frac{A}{\sqrt{2 \cdot \pi \cdot \sum_i r_i^2}} \quad (4)$$

r_i , is the distance between each pixel and a shape's centre of mass (a centroid, i – signifies a pixel's number). What is being calculated here is the proportion between the surface area of an object and the sum of all the distances of the pixels from the centre. This means that for objects with a shape that is close to a surface and with smooth edges W_4 will take on higher values. It is also defined as a measure of an object's hollowness, as forms with openings in them will have a higher surface area and the distances between pixels and the centre of a form can be relatively large, and, as a result – the value of the parameter will be low for them. In order to measure the regularity of an object, we can use W_5 (the Danielsson coefficient):

$$W_5 = \frac{A^3}{\left(\sum_i l_i\right)^2} \quad (5)$$

The formula makes it possible to calculate the sum of minimum distances between each of the pixels belonging to a shape and its edge, marked as l_i .

The next coefficient – W_6 (the Haralick coefficient) is calculated on the basis of the sum of the distances between a shape's centroid and the successive pixels that belong to its outline (d_i) using the formula:

$$W_6 = \sqrt{\frac{\left(\sum_i d_i\right)^2}{n \cdot \sum_i d_i^2 - 1}} \quad (6)$$

for which n is the number of border pixels. If the form is heavily fragmented, it will increase.

The W_7 coefficient is used to calculate the circularity of an object and is based on a very simple proportion:

$$W_7 = \frac{r_{\min}}{r_{\max}} \quad (7)$$

for which r_{\min} – is the minimum distance between the centre of mass of a given shape and its edge, while r_{\max} – is the maximum distance. Using it we can determine the elongation of an element, as well as the irregularity and fragmentation of a form, because with significant irregularities of the contour the value of the coefficient will be higher.

In order to determine irregularity we can use W_8 , which is calculated as:

$$W_8 = \frac{D_{\max}}{P} \quad (8)$$

which is the relation between D_{\max} – the maximum size of an object and its circumference. It would be good to highlight that this index will reach a low value for shapes with a frayed edge that is relatively long. If we want to verify whether a shape resembles a circle, then we can use W_9 (a modified Malinowska coefficient):

$$W_9 = \frac{\sqrt{4 \cdot \pi \cdot A}}{P} \quad (9)$$

signifies the circularity of an object and the closer it is to a circle, the closer its value is to that of 1. In this case it is the surface and circumference that are taken into account. The simplest in terms of calculation is the W_{10} coefficient, called the Feret diameter, which is the relation between a shape's highest horizontal (D_h) and vertical (D_v) dimension:

$$W_{10} = \frac{D_h}{D_v} \quad (10)$$

For horizontally elongated forms this will produce higher values, while for vertical ones – lower values.

The value of the last of the coefficients adopted by the author (W_{11}) signifies the compactness of a shape, defined as the degree of the form filling a rectangle circumscribed upon it. It will thus take on values ranging between 0 and 1, however, in the case of more fragmented forms it will take on lower values [18, 21, 32].

Table 2 presents the results of an analysis of the usefulness of shape coefficients in order to assess an architectural and landscape form. The values of each parameter were assigned the characteristics of a form whose value is directly dependent on them.

As it can be seen, some of the coefficients reflect a pronouncement of the same characteristic, e.g. coefficients W_1 and W_2 reflect size, while W_3 and W_9 – elongation. Others oppose each other – e.g. W_5 and W_7 .

During the stage of comparing values the author encountered another difficulty that resulted from the different scale of the data. For example, the value of coefficient W_{11} ranges between 0 and 1, while the values of W_1 and W_2 reach up to several thousand units.

Table 2. roportional dependence between the value of a coefficient and the characteristic of a figure

W_1 and W_2	size
W_3	elongation
W_4	lack of openings, hollow spaces
W_5	regularity
W_6	fragmentation
W_7	irregularity, fragmentation
W_8	smoothness of the outline
W_9	circularity
W_{10}	horizontal elongation
W_{11}	compactness

A standard formula, presented below, was used during standardisation:

$$n'_i = \frac{n_i - n_{i\min}}{n_{i\max} - n_{i\min}} \quad (11)$$

for which:

n'_i – is the standardised value,

$n_{i\max}$, $n_{i\min}$ – are the highest and lowest values within a group of results, respectively [7].

This made it possible to bring all of the values to a range of between 0 and 1. Because we are interested in the distinctness of an object that fulfils the role of the dominant element within its surroundings, an average value for all objects (a median) was calculated for each coefficient. This was followed by an analysis of the differences between the values obtained for individual objects and this median. This made it possible to produce charts which clearly illustrated how much a given object differs from the others.

The colour of every pixel of an image is recorded using the RGB system, which means that it utilises the basic constituent colours – red, green and blue, however, the higher the value of one of these constituents, the greater the saturation of a pixel with a given colour. Bright colours are usually characterised by higher values [9, 13]. An averaged colour was calculated for each object highlighted on a photograph, as an arithmetical mean of the value of the colour of all pixels belonging to said object. Afterwards, the average colour (a median) was calculated for all objects, with the deviation from the mean colour of the entire object or its part, e.g. in the case of a building – its walls or roof, while in the case o a tree – the crown and the trunk. However, we should be aware of various factors that affect the perception of colour, such as lighting, depending on the time of day and atmospheric conditions, or the transparency of air. Typically objects located on planes located further from the viewer lose their contrast and colour intensity. Due to this fact, the best course of action when performing colour analysis, similarly as in analysing the size of the objects, is to compare those that are located at a similar distance away from the observer [12, 20].

4. Materials

Assuming that the perception of the landscape is typically performed from the perspective of a standing person and photographs constitute an equivalent of visual experiences, four views of the Vistula River Boulevards in Krakow were subjected to an analysis. The author used digital photographs with a 3264 x 2448 pixel resolution obtained using a focal length of 35 mm, which were later combined into panoramas. With the presented settings we can record a view covering a horizontal angle of 54.43° and a vertical angle of 37.85°. A single pixel of the image thus corresponds to the vision of approximately one angular minute. This reflects the resolution of human sight, which means that a single pixel on a photograph reflects the smallest object that a human can see [1].

In order to perform an assessment of the shape, height and surface area of objects, the author used appropriately prepared images on which the analysed objects had been coloured white, and the background had been coloured black. Segmentation, which is a process based on highlighting objects (buildings, fragments of greenery) [9, 13] was performed by hand, attempting to outline the contours of each element with the greatest possible amount of fidelity. This precision can affect the results that are obtained, both in terms of surface area, maximum height, as well as shape [21, 22]. In three of the analysed cases these were works of architecture, while in one – a natural object. The individual buildings, plants and surfaces covered with greenery (lawns), were separated by lines with a width of 1 pixel, so that they could be treated as separate objects. When doing so, the contour of an object needs to be verified, as separated pixels and even ones that touch at the vertices could become identified as separate objects.

Colour analyses required that colours be applied to the objects, which was performed through multiplying the original photograph and a black and white image discussed above. As a result of this operation, the objects that were coloured white preserve their original colour (like when we multiply a value by 1) and the background, which we multiply by 0 (the colour black) becomes black [13].

5. Software interface

Due to a lack of free software that could perform all of the planned analyses, the author developed a program using the MATLAB environment with the use of the Image Processing Toolbox, an additional library of functions, the use of which simplifies coding. The graphical user interface of the program is very simple. It makes it possible to load an image from a selected folder and place tags on individual objects, which provides orientation in future results. The tagged image can be saved, thanks to which it is easier to interpret the calculation results. As characteristic parameters of objects, their size, height, shape coefficients and averaged colour (calculated as the arithmetic mean of the colours of all pixels) are calculated. In addition, the program also highlights the point located at the highest elevation, drawing a red, downward facing arrow above it. The possibility of saving an image with this marking has been introduced,





load an image

label areas

save the image with labels

calculate objects' areas

calculate objects' heights

calculate shape factors

calculate mean colours

save the image with the mean colour

indicate the highest point

save the image with the highest point

save the results and exit

Fig. 1. Program interface

as well as of the image with objects coloured using the averaged colour. The individual functions are initiated using buttons, which makes it possible to select any set of indicators (e.g. surfaces and shapes only). The results are exported into an Excel file in the form of a table, which enables their future processing and the generation of charts presenting the results in graphical form. The user can specify the location and name of the file with the results.

The functions of calculating the shape coefficients are highly complex and their calculation time is very long, which is why a progress bar was introduced, which shows the user that the program runs appropriately, as well as the level of progress of the calculation.

6. Research results

6.1. Case 1 – Hotel Forum

The first case is a view of Hotel Forum from Bulwar Inflancki. It is intuitively seen as a dominant element. The building has not been in use for many years and its owner draws profit from making its facade available as an immense advertisement surface. The colour of the building can be considered temporary, dependent on the graphic currently displayed on it. The image recorded in 2015 shows the building as a strong colour dissonance within its surroundings.



Fig. 2. View of Hotel Forum from Bulwar Inflancki

Fig. 3 shows that the highest point of the skyline (marked with a red arrow) is located at the top of the building. The surface of the white shape (tagged with the number 9) that corresponds to the hotel is larger than that of the neighbouring objects by over a dozen times, and its height – is almost twice as that of the highest object in its vicinity, which can be seen in the graphs shown on Fig. 4. The numeration of the horizontal axis corresponds to the successive objects, starting from left, while the values on the vertical axis correspond to the number of pixels.

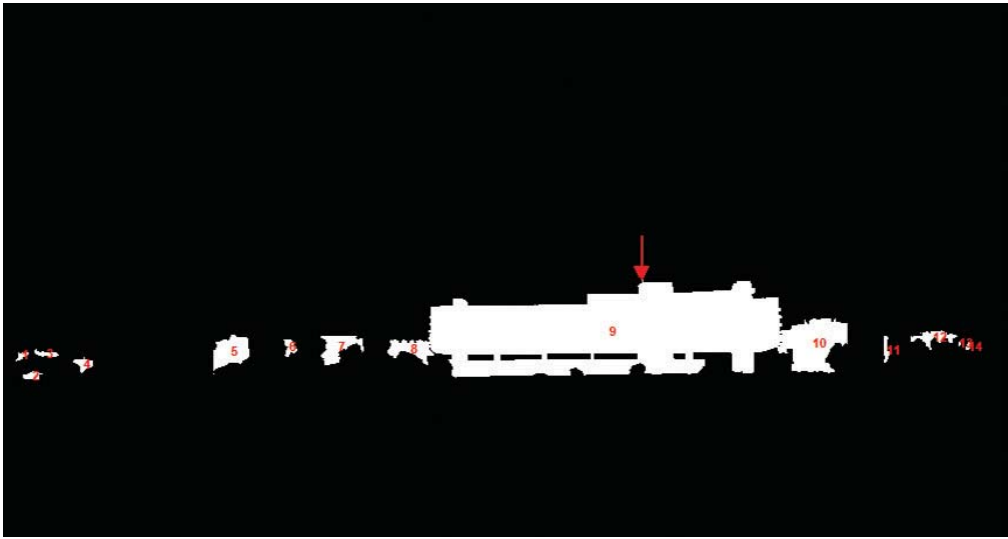


Fig. 3. View of Hotel Forum with a highlight of the visible fragments of buildings, tags for visible fragments of buildings and an indication of the highest point

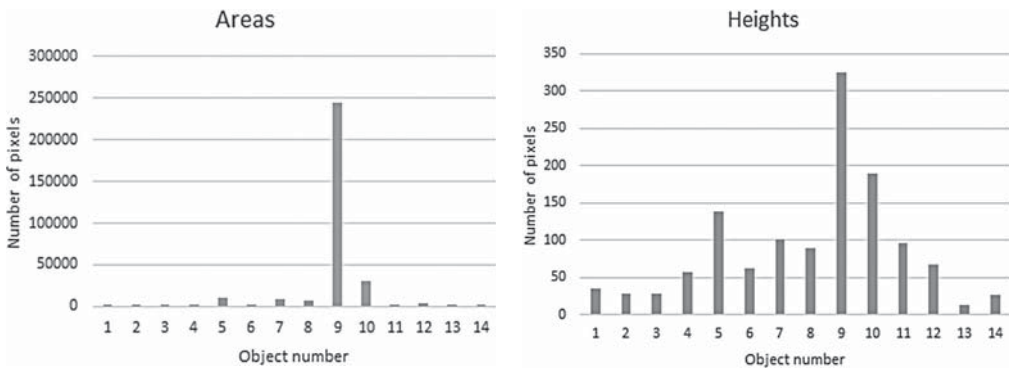


Fig. 4. Surface area and maximum height of the objects (in pixels)

Fig. 5 shows the differences between the values of shape coefficients (W_1-W_{11}) calculated for the individual objects (numbered 1–14 according to Fig. 3) and the median value of the coefficient for all visible objects. The massing of the hotel differs from other objects in the analysed view primarily by its size, which is shown by high values for coefficients W_1 and W_2 . It is also horizontally elongated, which can be concluded from a high value of coefficient W_{10} . A low value for W_4 and W_5 indicate that the form features openings and is irregular. Coefficient W_6 , in turn, is close to the median of the surroundings, as the outline of the objects is rather orthogonal and does not feature too much detail that would cause the contour to become fragmented. In this case, due to significant cover by plants, only the visible parts of the objects were analysed. It should be noted that apart from the obvious lowering of their surface area, this also causes their shape to become falsified. The massing of the building located to the

left of the hotel was divided into 4 separate fragments. A different approach, which has been presented in the following example, is possible as well.

Fig. 6 depicts the buildings with their colours applied to them. Their analysis was based on calculating an averaged colour for every object (Fig. 7) and comparing their RGB constituents with the median values calculated for all fragments of buildings visible on the photograph.

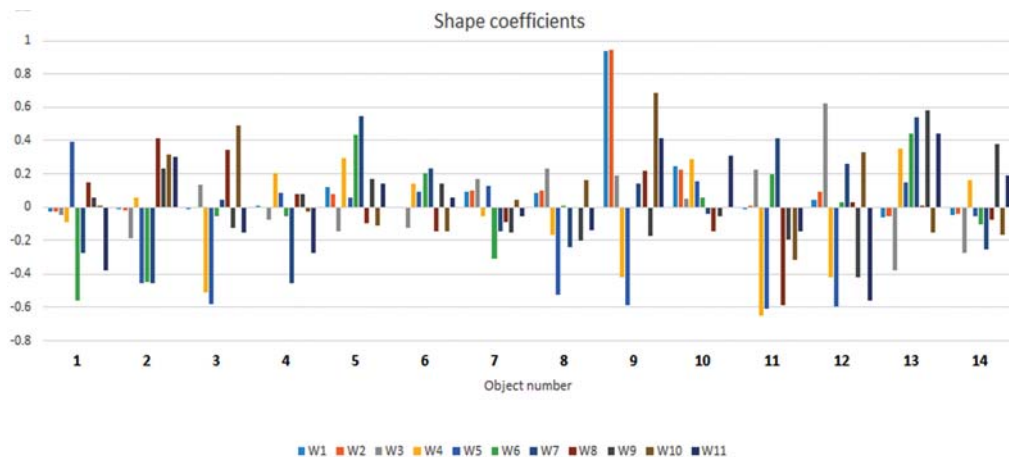


Fig. 5. The difference between values for shape coefficients for each object and the median values for all objects ($y = 0$ is the median value for each coefficient)



Fig. 6. Buildings with their original colours (to the left – the entire building of the hotel, to the right – the advertisement surface)



Fig. 7. The median colours of the objects: to the left – taking into account the entire building of the hotel, to the right – taking into account the facade covered by the advertisement

In the case of subjecting the entire massing of the hotel to the analysis, it turned out that it is slightly less saturated with the colours blue and green. Bright residential blocks with a dominance of blue and green constituent colours located in the right part of the photograph (objects 10–14, according to Fig. 3) were proved to stand out. The fragments of the blocks to the left of the hotel were much darker (4–8). Most of the buildings sported significantly less of the red constituent. The exception was the object tagged with the number 3, which corresponded to a fragment of a roof visible amidst greenery. Despite the fact that the majority of the surface the object of the hotel (object 9) was its facade (around 59%), its median colour was also influenced by the lower storeys that remained in the shadow, as well as the pylons and the infrastructure located on the roof. Should we analyse solely the facade used as the advertisement surface, then the results will be much clearer. The colour red was clearly dominant within the area (object 9) (Fig. 8).

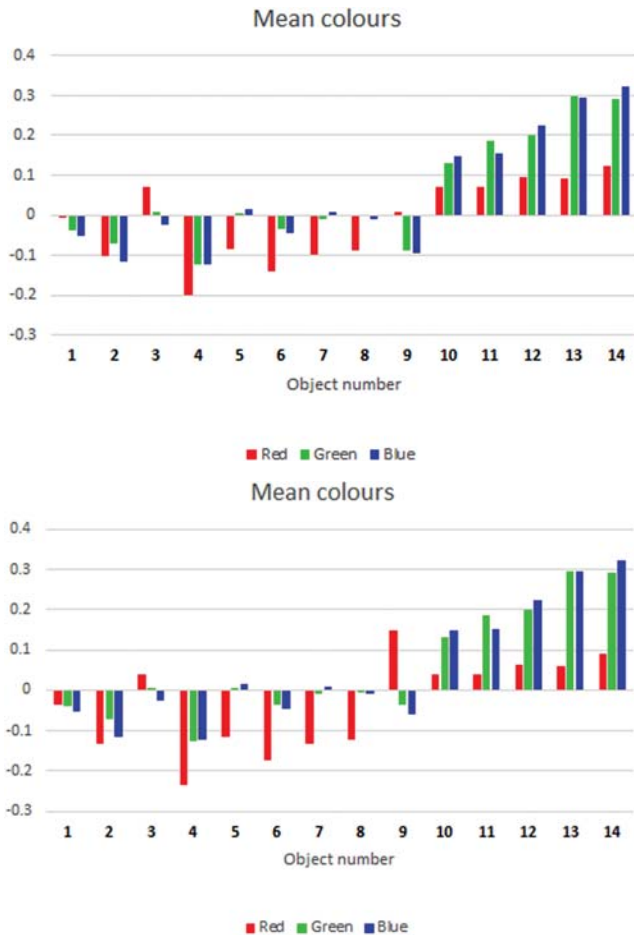


Fig. 8. The difference between the median colour of an object and the median for all objects: to the left – for the entire hotel building, to the right – for the facade covered by an advertisement (y = 0 is the median value for each colour channel)

6.2. Case 2 – the church and monastery of the Pauline Fathers at Skalka

The next case to be analysed by the author was a view of the Monastery of the Pauline Fathers at Skalka, observed from Bulwar Kurlandzki. The view is framed by groups of tall greenery which segment this fragment of the panorama. We can intuitively tell that the Monastery is the view's dominant element (Fig. 9).



Fig. 9. View of the Monastery of the Pauline Fathers from Bulwar Kurlandzki

This belief was confirmed by the results of the author's calculations. The highest point of the skyline was found at the top of the church bell tower (the object tagged with the number 9) (Fig. 10).

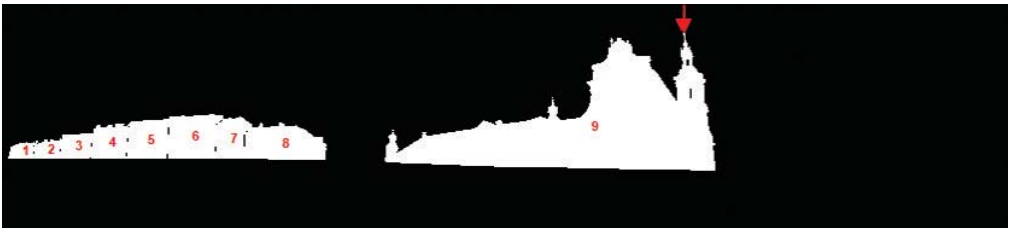


Fig. 10. View of the Monastery of the Pauline Fathers with the highlighted buildings, their tags and the highlight of the tallest point

The surface area of the shape that represents the outline of the monastery complex (9) exceeds the surface area of the neighbouring townhouses by around a dozen times, while the height of this shape – is almost three times as large (Fig. 11). In this example it was decided that, despite the see-through greenery blocking the buildings, in the picture with the original resolution we can identify their surface areas and highlight entire structures without making significant errors.

In this case the object had a shape that was clearly different than its surroundings, which was confirmed by shape coefficient values. Some of them reached high values, including W_1 and W_2 – which signified its above average size, while W_3 and W_{10} – its horizontal elongation. The values for W_4 , which were below average, were caused by the presence of openings, while W_5 and W_{10} – the irregularity of the form and its lower compactness, respectively (Fig. 12).

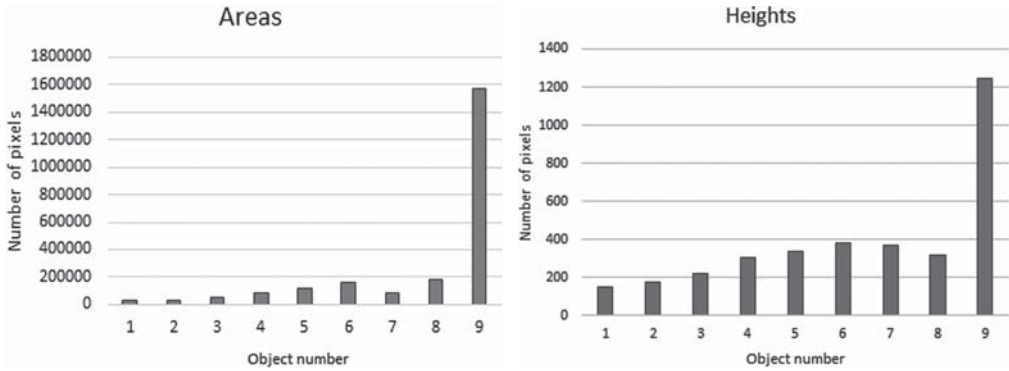


Fig. 11. The surface and maximum height of the objects (in pixels)

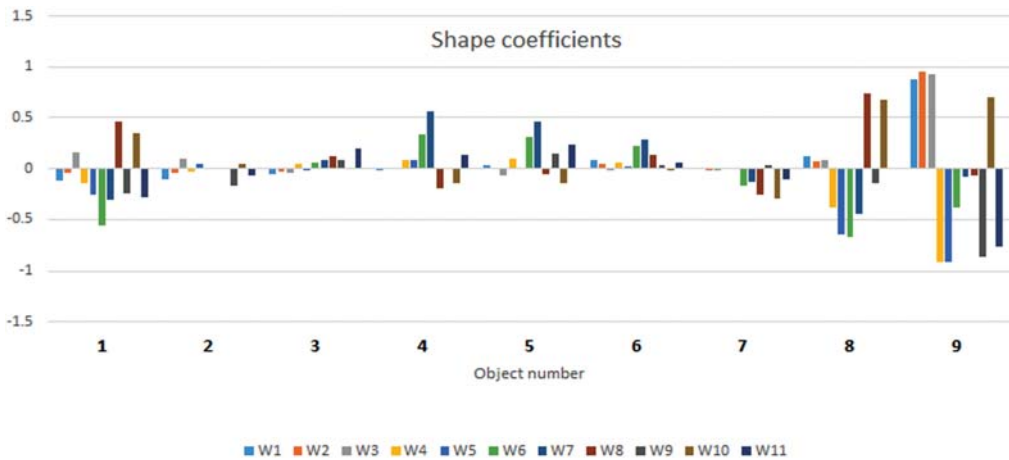


Fig. 12. The difference between the values of shape coefficients for each object and the median values for all objects ($y = 0$ is the median value for each coefficient)

Highlighting the entire outlines of buildings causes green to constitute an admixture in the averaged colour of an object (Fig. 13 numbered according to Fig. 10). An approach was presented which appears to be justified in the situation when greenery can be seen through to some degree (e.g. in seasons when there are no leaves on trees). As a result of this approach,



Fig. 13. Buildings with their colours applied

however, the averaged colour of some townhouses (particularly those tagged with the numbers 1, 4–8) became relatively dark (Fig. 14).

The monastic complex was the brightest, but its colour was comparable to the pastel colour of the facade of a townhouse (Fig. 15).

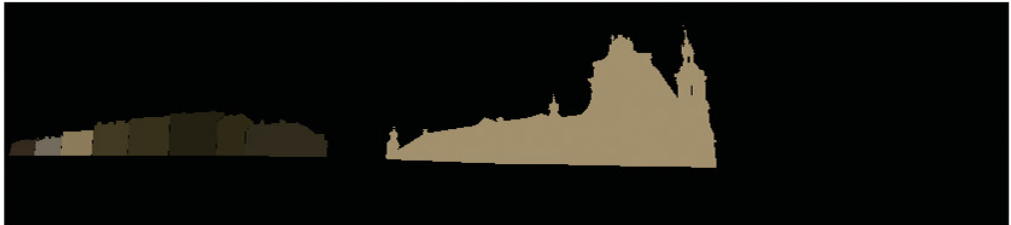


Fig. 14. Averaged object colours

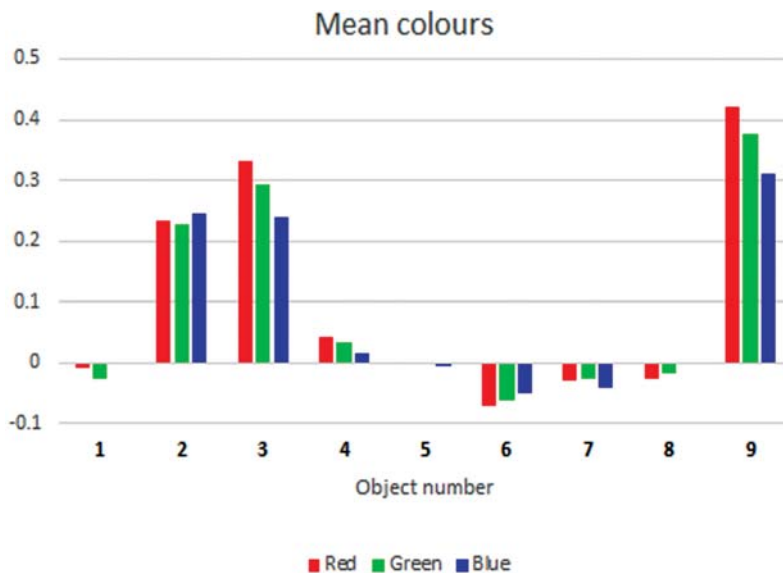


Fig. 15. The difference between the averaged colour of an object and the median for all objects ($y = 0$ is the median value for each colour channel)

6.3. Case 3 – the Krakow Heat and Power Generation Plant (PGE)

The following analysis was performed for the case of a view in which the natural material is dominant (tall, medium-sized and low-lying greenery), however, we perceive the tall smokestack of the heat and power generation plant in Łęg as the dominant element.

Anthropogenic elements within the view belong to technical infrastructure and are relatively small (Fig. 16).

An analysis of the image indicated that the highest point had been located at the top of the heat and power plant's smokestack, marked with tag number 10 (Fig. 17).



Fig. 16. View of the Krakow Heat and Power Generation Plant from the Bouelwards in Dąbie

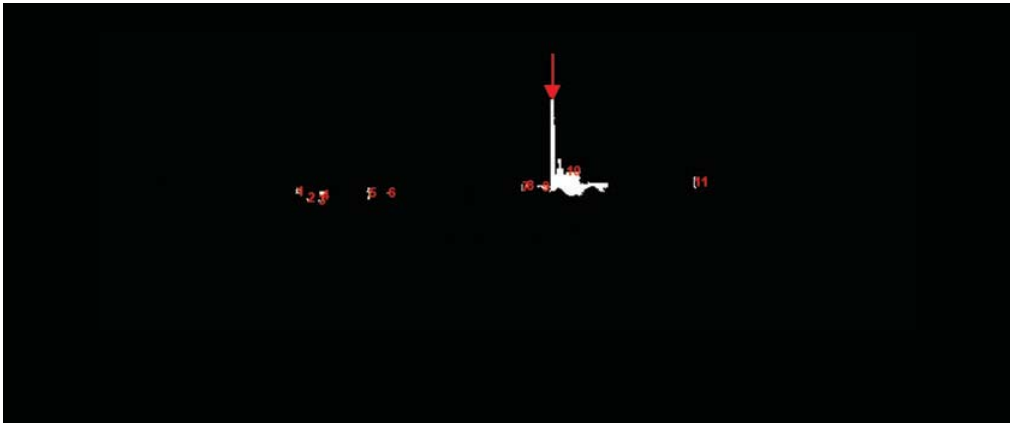


Fig. 17. The same view with a highlight of infrastructure objects, their tags and the highlight of the highest point

The surface area of this objects was nearly thirty times the size of the largest of the remaining visible fragments of buildings and its height – was almost eight times greater (Fig. 18).

The distinctness of the form of the heat and power generation plant from its surroundings was confirmed by high values for coefficients W_1 and W_2 , which were a result of its dominant size. The shape was elongated (vertically), which was shown by the W_3 value, it was also irregular and fragmented to a greater degree than those of other objects (W_6 and W_7). The W_4 , W_9 and W_{11} coefficients confirmed, in turn, that it did not feature openings or hollow spaces, while its shape was characterised by neither circularity nor compactness (Fig. 19).

Colour analysis did not indicate the heat and power generation plant, with its white and red smokestack and its overall massing featuring grey colour tones, to be significantly different in terms of colour from the other objects (Fig. 20 and 21). The most distinct in these terms was the yellow fragment of a silo marked with number 3 (numbered according to Fig. 17), which, unfortunately, was difficult to see on the scale used for printing (Fig. 22).

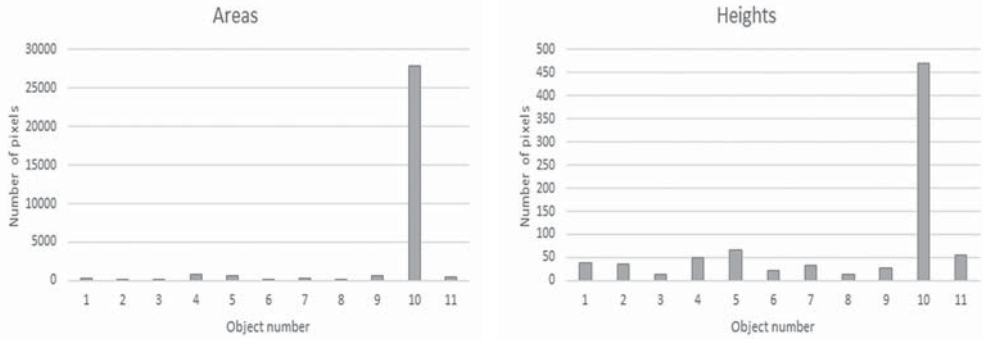


Fig. 18. Object surface area and maximum height (in pixels)

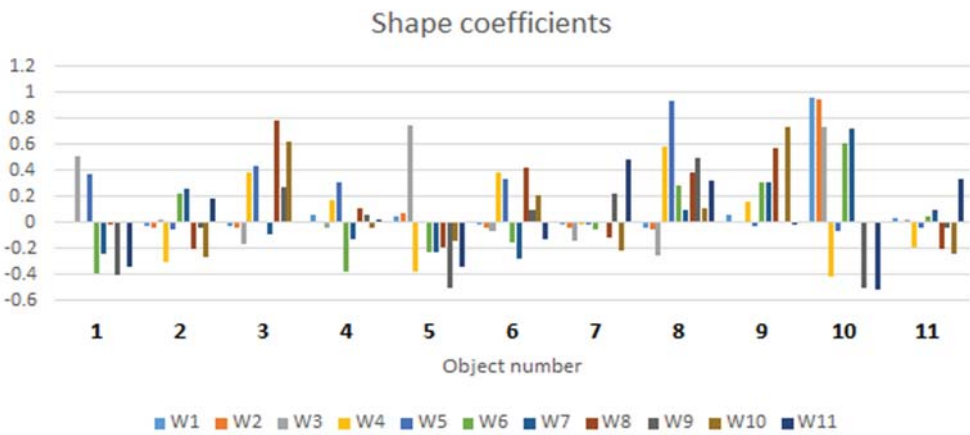


Fig. 19. The difference between the shape coefficients for visible fragments of objects and median values ($y = 0$ is the median value for each coefficient)



Fig. 20. Coloured objects



Fig. 21. Averaged object colours

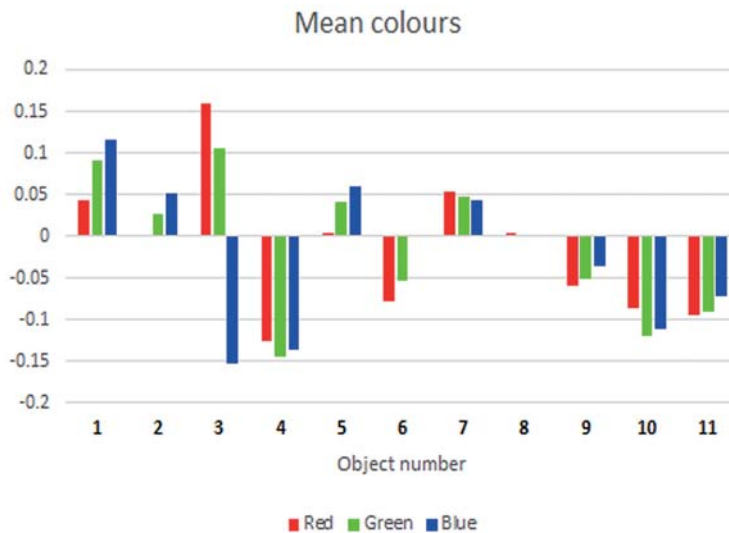


Fig. 22. The difference between the averaged colour of the object and the median for all objects ($y = 0$ is the median value for each colour channel)

6.4. Case 4 – A fragment of Bulwar Wołyński

The final case proves that program can be used to analyse both buildings and natural objects. In order to do so, a fragment of Bulwar Wołyński was selected, in which the crown of a tree is intuitively perceived as a dominant element (Fig. 23). At its top (object with tag number 23) was the highest point of the skyline (Fig. 24).

The tree was also the largest object in the view, especially when it was observed that the object with tag 7 corresponded to a lawn. It was around 10 times larger than the tree tagged with the number 27.



Fig. 23. View of a fragment of Bulwar Wolyński

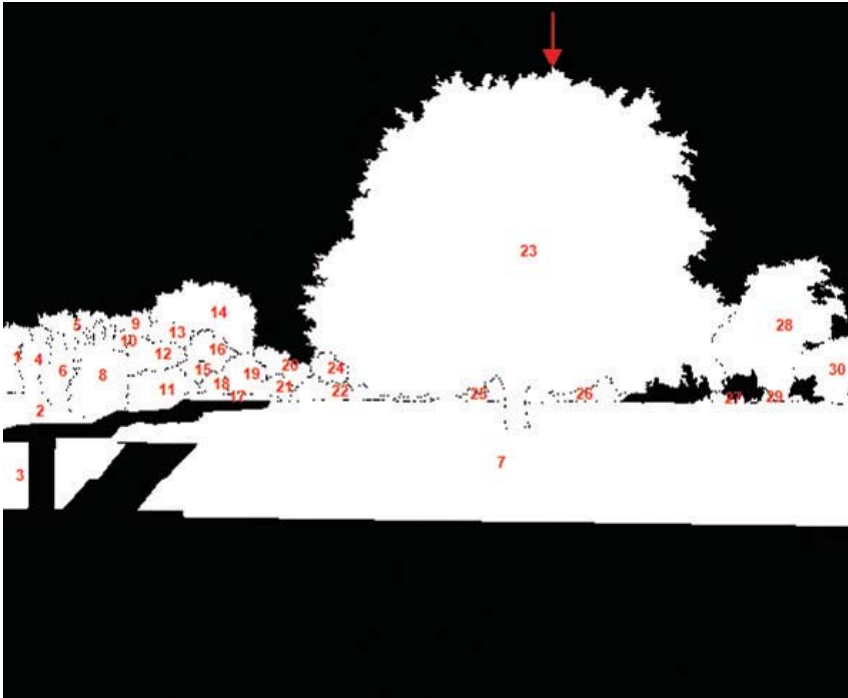


Fig. 24. The same view with a highlight of natural objects their tags and the arrowhead showing the highest point

Its maximum height was also two and a half times greater than that of the remaining objects (Fig. 26).

The chart showing the deviation of coefficient values from the mean was not legible on this scale due to the considerable number of objects (30) highlighted on the image (Fig. 27).

This is why the author decided to include an additional illustration (Fig. 28) showing that an object intuitively perceived as a dominant element stood out primarily through its size (W_1 and W_2), which significantly differed from the median. The W_{10} coefficient reached a very low value, which signified a lack of elongation. A low value of W_8 was the result of fragmentation, the lack of smoothness of the contour, which had been caused by a greater precision when seeing an object on the first plane and the fact that its crown was viewed against the background of the sky, which made it possible to discern its outline with greater precision. W_9 corresponded to a lower degree of the tree's circularity, which was understandable, because we could see its entire trunk, and in the case of the remaining trees and bushes – only the crowns.

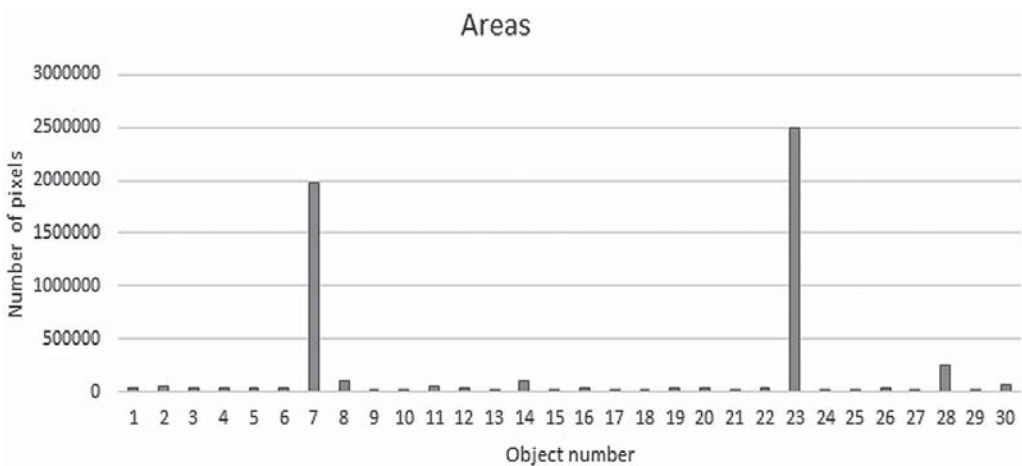


Fig. 25. Object surface area (in pixels)

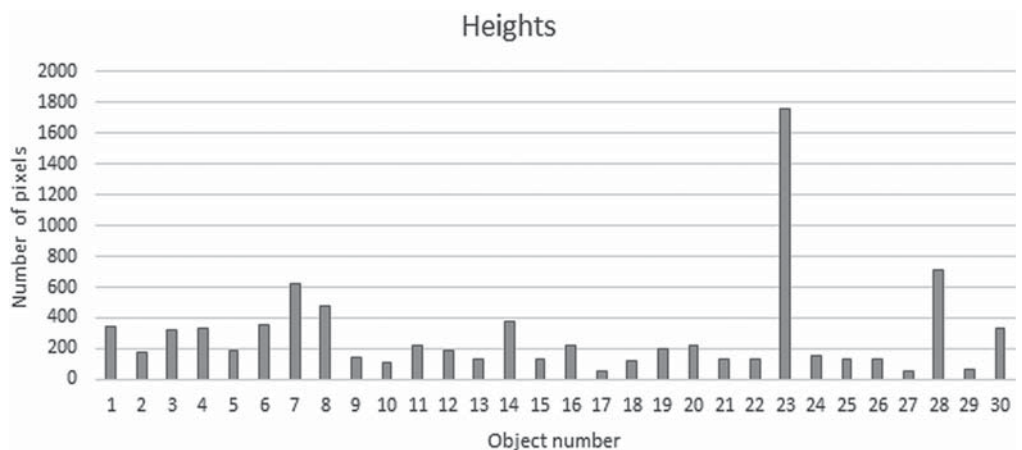


Fig. 26. Maximum object height (in pixels)

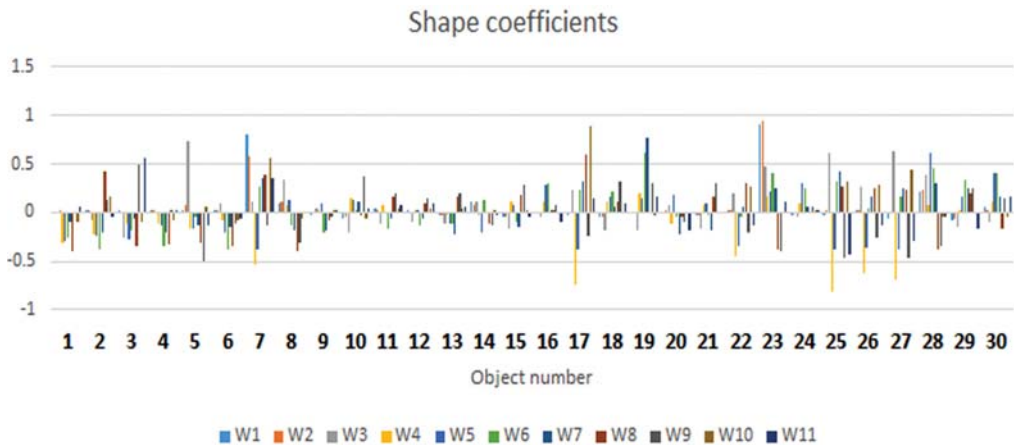


Fig. 27. The difference between the shape coefficients for objects and median values ($y = 0$ is the median value for each coefficient)

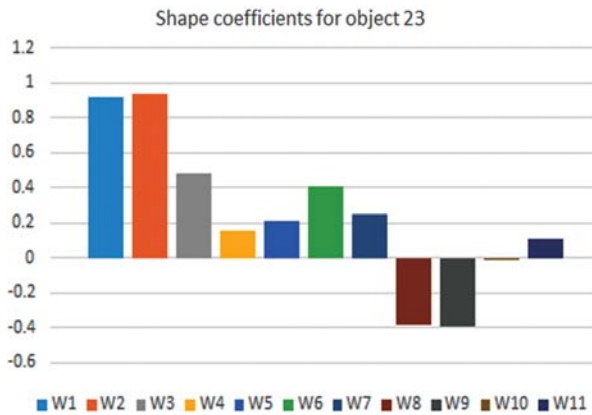


Fig. 28. The distinctness of the shape of the largest tree from the surrounding natural objects



Fig. 29. Plants with colour enabled



Fig. 30. Averaged colours of the objects

The colour analysis also produced predictable results. The dominant object did not stand out from its surroundings in terms of colour (Fig. 29–31). Both the illustration showing the averaged colours of the objects and the chart presenting the results of the calculations indicated that the object tagged with the number 12 stood out the most from the background. This was the result of the fact that a white billboard was located within the outline of the crown of this small tree.

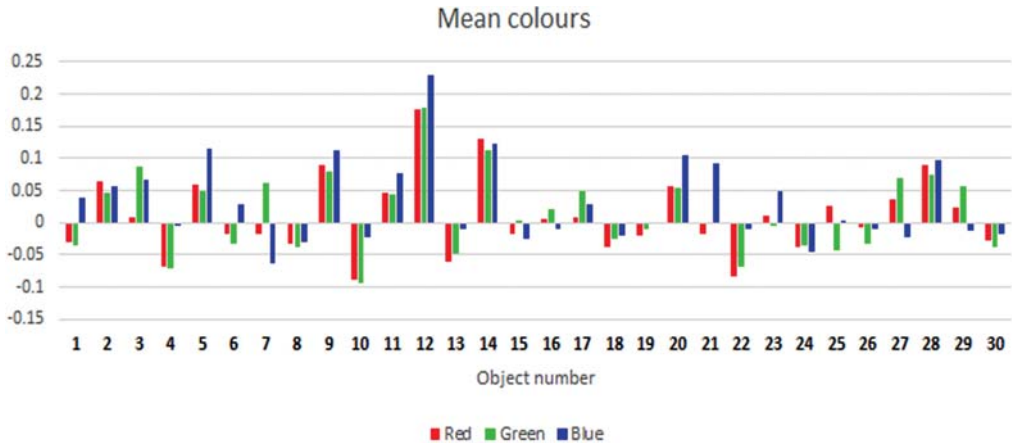


Fig. 31. The difference between the averaged colour of an object and the median colour of the surroundings ($y = 0$ is the median value for each colour channel)

7. Conclusion and summary

The research method developed by the author was meant to parameterise the concept of the dominant element of the landscape. Characteristic qualities of dominant elements of the landscape were listed, such as: a distinct size and height, alteration of the panorama of the city or the skyline, a shape and colour that are different from the surroundings. The results of the calculations performed with the use of an original computer program and presented in Table 3 have shown that objects intuitively assessed to be dominant elements do indeed possess either some or all of these qualities.

It appears that the size and height of an object and its impact on the outline of a panorama or a skyline play a deciding role in our judgement. In the case of architectural forms, their form was also parameterized by means of 11 coefficients. Their values clearly differed from the average and showed the original form of the dominant. The historical object was also characterized by a rich detail, which was indicated by the high values of W5 and W10 coefficients. In the last example, the tree in the foreground was evaluated similarly. This resulted from the greater detail of its contour, which in turn depends on the distance from the observer. The analysed objects, however, did not stand out from other colours, except for the facade of Forum Hotel, which was obscured by a blatant advertising in red.

Table 3. Characteristics of objects signifying that an object fulfils the role of a dominant element

Object characteristics	Case 1 Hotel Forum	Case 2 Monastery of the Pauline Fathers at Skalka	Case 3 Krakow Heat and Power Generation Plant (PGE)	Case 4 A Tree
Significant impact on the skyline	+	+	+	+
Significant size	+	+	+	+
Significant height	+	+	+	+
An original form	+	+	+	-
A wealth of detail	-	+	-	+
Extraordinary colour	+	-	-	-

The research, however, was performed on only four cases, which does not make it possible to prepare full statistical documentation. Due to the complexity of the problem and the variety of spatial situations it should be expanded to include a greater number of different cases.

The results presented by the author show that the method has a universal character and can be applied both in the case of buildings and natural elements. The results that were obtained were similar to intuition. The analysis of the objects in terms of their size, shape, height or colour can constitute an objective tool which can help to precisely determine their role in a composition. Numerical indicators can be helpful in the assessment of existing landscapes, as well as in the monitoring of changes that take place in views or in the making of design decisions.

Due to there being a lack of software on the market that could precisely meet the requirements that were specified, while software with comparable functionality that does exist is expensive, the author decided to develop an original application. Image segmentation, based on highlighting objects of interest, was performed manually using the freeware GIMP program, which is an image editor, and is very labour-intensive and can cause imprecise selection that can produce small errors in the results. Previous attempts at automatic view and panorama segmentation, however, had not produced the desired results [19, 22]. The author encountered numerous dilemmas when performing colour analysis. Some wall fragments of buildings were covered by trees. Two approaches to the solving of this problem were presented. In the first, the greenery was compact – only the visible fragments of buildings were selected, which entailed a change in their surface area, height and shape. In the second, where greenery had the appearance of being see-through – entire objects were highlighted, and thus their geometric parameters were not being changed, but the admixture of the colour of the trees distorted their averaged colours. The method allows for a significant degree of freedom in this regard. We can subject maximally large fragments of the walls of individual buildings that are not covered by trees, to a colour analysis. The next decision concerning the decision as to whether the colours would be analysed for walls along with window openings

and other details or would they be ignored, or would only the colours of roofs be analysed. Another problem appears when a building features the use of materials of a different colour in different parts of it.

The decisions presented above were not free of subjectivity, however, it is most essential to adhere to a consistent approach throughout the analysis of a specific image in relation to all of the objects that are visible in it.

The method is far from fully automatic and from being a machine classification of dominant elements. It constitutes a tool that must be supervised by an expert, but thanks to precise indicators it equips them with objective premises for decision-making, both during the stage of surveying the landscape, as well as during the design process.

Carrying out research involving the calculation of numerical indicators characterizing the objects was possible thanks to the program created in MATLAB by Piotr Łabędź. I would like to thank him for cooperation.

References

- [1] Bishop I.D., *Testing perceived landscape colour difference using the Internet*, „Landscape and Urban Planning”, No. 37, 1997, 187–196.
- [2] Bogdanowski J., *Kompozycja i planowanie w architekturze krajobrazu*, Ossolineum, PAN, Wrocław 1976.
- [3] Böhm A., *Architektura krajobrazu*, Wydawnictwo Politechniki Krakowskiej, Kraków 1994.
- [4] Czarnecki W., *Planowanie miast i osiedli*, PWN, Warszawa 1960.
- [5] Czyńska K., Rubinowicz P., Zwoliński A., *Analizy zabudowy wysokiej w krajobrazie miasta/Analyses of tall buildings in the cityscape*, „Teka Komisji Urbanistyki i Architektury o. PAN w Krakowie”, Tom XLV, 2017, 319–341.
- [6] Dąbrowska-Budziło K., *Wśród panoram Krakowa. O przemianach widoków i o tym, jak je ocalić*, Wydawnictwo Literackie, Kraków 1990.
- [7] Funkcje normalizacji, http://sztuczna-inteligencja.eprace.edu.pl/1001,Funkcje_normalizacji.html (access: 19.07.2018).
- [8] Gadomska W., Marks E., *Contemporary structures dominant due to height in the landscape of the great masurian lake district/Współczesne dominanty wysokościowe w krajobrazie krainy wielkich jezior mazurskich*, „Space&Form = Przestrzeń i Forma”, Nr 33, 2018, 207–224.
- [9] Gonzales R.C., Woods R.E., *Digital Image Processing*, Prentice Hall, New Jersey 2002.
- [10] Graczyk R., *Identyfikacyjna funkcja dominanty architektonicznej w strukturze małego miasta*, Politechnika Poznańska, Poznań 2005.
- [11] Gyurkovich J., *Znaczenie form charakterystycznych dla kształtowania i percepcji przestrzeni*, Monografia PK, No. 258. Architektura, Wydawnictwo Politechniki Krakowskiej, Kraków 1999.

- [12] Łabędź P., Ozimek A., *Detecting greenery in near infrared images of ground-level scenes*, [In:] *Peer reviewed proceedings of Digital Landscape Architecture 2012 at Anhalt University of Applied Sciences*, eds. E. Buhmann, M. Pietsch, M. Heins, Wichmann, Berlin 2012.
- [13] Malina W., Smiatacz M., *Metody cyfrowego przetwarzania obrazów /Methods of Digital Image Processing*, EXIT, Warszawa 2002.
- [14] Małachowicz E., *Ochrona środowiska kulturowego*, PWN, Warszawa 1988
- [15] Myczkowski Z., *Krajobraz wyrazem tożsamości w wybranych obszarach chronionych w Polsce*, Wydawnictwo Politechniki Krakowskiej, Kraków 2003.
- [16] Niedźwiecka-Filipiak I., Borc Z., *Dominants of a Farmer and Modern Village in South-West Poland/Dominanty dawnej i współczesnej wsi południowo-zachodniej Polski*, „Architektura Krajobrazu”, No. 1–2, 2006, Vol. 12.
- [17] Niedźwiecka-Filipiak I., *Wyróżniki krajobrazu i architektury wsi Polski południowo-zachodniej*, Wydawnictwo Uniwersytetu Przyrodniczego we Wrocławiu, Wrocław 2009.
- [18] Niezabitowski A., *O strukturze przestrzennej obiektów architektonicznych. Podstawy ogólnej morfologii przestrzeni architektonicznej*, Wydawnictwo „Śląsk”, Katowice 2017.
- [19] Ozimek P., Böhm A., Ozimek A., Wańkowicz W., *Planowanie przestrzeni o wysokich walorach krajobrazowych przy użyciu cyfrowych analiz terenu wraz z oceną ekonomiczną/ Planning spaces with high scenic values by means of digital terrain analyses and economic evaluation*, Wydawnictwo Politechniki Krakowskiej, Kraków 2013.
- [20] Ozimek A., *Cyfrowa analiza dopasowania kolorystycznego nowych obiektów do istniejącego otoczenia = Digital analysis of new objects colour matching to the existing environment*, „Space & Form = Przestrzeń i Forma”, Nr 26, 2016, 271–283.
- [21] Ozimek A., Łabędź P., *Quantitative and qualitative analyses of landscape views*, [In:] *Peer reviewed proceedings of Digital Landscape Architecture 2013 at Anhalt University of Applied Sciences*, eds. Buhmann, E., Ervin, S. M., Pietsch, M., Wichmann, Berlin 2013, 93–100.
- [22] Ozimek A., Ozimek P., *Algorytmy przetwarzania obrazu w wyróżnianiu tworzywa kulturowego i przyrodniczego na fotografiach krajobrazowych/Image processing algorithms in cultural and natural substance distinction in landscape photographs*, Nauka Przyroda Technologie 2009, T. 3, z. 1, 12, Poznań 2009.
- [23] Ozimek P., *Zastosowanie algorytmów światła lokalnego w wyznaczaniu wykresów widoczności* (PhD Thesis, promotor: Böhm, A) Politechnika Krakowska, Kraków 2003 .
- [24] Pardo-García S., Mérida-Rodríguez M., *Measurement of visual parameters of landscape using projections of photographs in GIS*, *Computers, Environment and Urban Systems* 61, 2017, 56–65.
- [25] Siewniak M., Mitkowska A., *Tezaurusz sztuki ogrodowej*, Wydawnictwo „Rytm”, Warszawa 1998.
- [26] *Słownik języka polskiego PWN*, <https://sjp.pwn.pl> (access: 19.07.2018).
- [27] *Słownik wyrazów obcych*, PWN, Warszawa 1995.
- [28] Swardon R., Palmer J., Felleman J., *Foundations for Visual Project Analysis*, A Wiley Interscience Publications, New York 1986.
- [29] Stamps III A.E., *Psychology and the aesthetics of the built environment*, Springer, Boston 2000.

- [30] Steinitz C., *Toward a Sustainable Landscape with High Visual Preference and High Ecological Integrity: the Loop Road in Acadia National Park, U.S.A.*, „Landscape and Urban Planning”, 54(2001), Elsevier.
- [31] Szolginia W., *Architektura*, Sigma NOT, Warszawa 1992.
- [32] Tadeusiewicz R., Korohoda P., *Komputerowa analiza i przetwarzanie obrazów/Computer image analysis and processing*, Wydawnictwo Fundacji Postępu Telekomunikacji, Kraków 1997.
- [33] *Terminy architektoniczne i urbanistyczne*, http://www.dolana.pl/sloownik_wyrazow_architektonicznych.php (access: 19.07.2018).
- [34] Vogt B., Nassery F., *Geometryczne przesłanki zaistnienia dominandy w przestrzeni współczesnego miasta/Geometrical premises of becoming the architectural landmarks in the space of the contemporary city*, „Czasopismo Techniczne”, 6-A/2008, 561–573.

Barbara Stec  orcid.org/0000-0002-8366-0367

bstec@afm.edu.pl

Faculty of Architecture and Fine Arts, Andrzej Frycz Modrzewski Krakow University

SUNLIGHT AND ATMOSPHERE IN THE ARK OF THE LORD CHURCH IN KRAKOW

ŚWIATŁO SŁONECZNE I ATMOSFERA W KOŚCIELE ARKA PANA W KRAKOWIE-BIEŃCZYCACH

Abstract

The article presents the relationship between sunlight and the atmosphere of the architecture of the Ark of the Lord Church in Krakow and outlines the history of this church. The research method was based on analysis of the design in the personal perceptual experience of the article's author. The article defines the 'atmosphere of architecture' concept that is adopted in the study. The relationship between sunlight and architecture was examined in terms of the exposure of the physical properties of architecture and the astrophysical nature of sunlight. The analysis confirmed the strict dependence between light and atmosphere in the Ark of the Lord Church: sunlight is a form-creating factor in architecture that is related not only to the use of translucent materials, but also to the shape and spatial structure of the massing of the church. This light is an effective means of building a sacred atmosphere.

Keywords: sunlight, architecture, interior, atmosphere of architecture, orchestration of sunlight, choreography of sunlight

Streszczenie

Tematem artykułu jest zależność między światłem słonecznym a atmosferą architektury w kościele Arka Pana Krakowie-Bieńczykach. Zauważono, że projekt kościoła oparty jest na idei światła słonecznego: starannie obmyślonych sposobach jego wprowadzania do konkretnych części wnętrza. Podstawą metody badania była analiza wnętrza w osobistym doświadczeniu percepcyjnym autorki. Określono przyjęte w badaniu znaczenie atmosfery architektury. Relacja światła słonecznego z architekturą została zbadana w aspekcie ekspozycji właściwości fizycznych architektury i astrofizycznej natury światła słonecznego. Analiza potwierdziła ścisły związek światła i atmosfery w Arce Pana: światło jest formotwórczym czynnikiem architektury, wynikającym nie tylko z zastosowania materiałów przepuszczających światło, ale także z kształtu i struktury przestrzennej bryły kościoła. Światło to jest skutecznym środkiem budowania atmosfery sacrum.

Słowa kluczowe: światło słoneczne, architektura, wnętrze, atmosfera architektury, orkiestracja światła słonecznego, choreografia światła słonecznego

1. Experience

The reflection on the dependency between sunlight¹ and the atmosphere of the architecture within the Ark of the Lord Church in Krakow was borne out of the author's perceptual experiences during her visits to the church. At different times of day, sunlight tempered the darkness of the interior sufficiently enough for liturgy to take place. The atmosphere inside was conducive to prayer but was also refreshing and enlivening. A deeper analysis of the architecture of the interior made it possible to conclude that sunlight was an essential component of the atmosphere experienced within it – sunlight that was appropriately modified in relation to the architecture of the building.

The author assumed that the atmosphere of architecture is a physical property of an interior² that is essential to eliciting specific sensory experiences and states of mind within people [7]. In other words, it constitutes an interior's physical capacity to affect people and is the result of numerous components³, among which light or a lack thereof plays an important role. In this way, architects 'treat' the atmosphere: objectivizing the atmosphere and treating it as a physical property of the interior facilitates its design so the end result is that it is subjectively perceived by users in the way the architect expected. Contemporary aesthetic reflection, undertaken by Gernot Böhme [1, 2]⁴ in particular, also supports treating the atmosphere of architecture in the category of the almost objective properties of architecture.

When looking at the problem from the perspective of the observable and experience able sunlight that operates within an interior, we can ask what kind of atmosphere and to what degree does it build the atmosphere within a given interior. Keeping in mind the impact of an interior on the individuals within it, the mutual exposure of the physical properties of architecture inside an interior (in front of an individual) and the astrophysical nature of sunlight [7] were assumed to be the criterion of assessing the relation between light and architecture in the aspect of atmosphere.

2. Outline of the history of the Ark of the Lord Church

The Church of the Mother of God, Queen of Poland, called the Ark of the Lord Church, was built in 1967–1977 in Bieńczyce, very close to Nowa Huta, on the initiative of Father

¹ According to the author, sunlight is a light whose source is the sun and that operates on Earth: during the day it is the light of the sun's rays, both directed and reflected from the sky, while at night the light of the sun is reflected off of the moon [7].

² According to the author, an interior is an architectural, urban and even landscape interior; it is thus a term that is close to concepts such as "man's surroundings" or "man's environment" [7].

³ Apart from light it also includes the sonority of interiors and materials, temperature, the hardness and softness of materials, the smells of materials and the air in an interior. These components were written about by Peter Zumthor [8].

⁴ The concept of *quasi-objective atmospheres*, formulated by Gernot Böhme, was commented upon by Krystyna Wilkoszewska [10, pp. 20–23].

Józef Gorzelany. The architectural design was developed in 1965 by Wojciech Pietrzyk, while the structural design was by Jan Grabarski. Political restrictions caused the construction, which began two years after the completion of the design, to be carried out in stages over nine years. Difficulties caused by the authorities of the time were the result of not only general opposition to the construction of Catholic churches in a communist state, but also the fact that Nowa Huta was planned near Krakow as a model “city without God” – a manifestation of the triumph of communist ideology. The intervention of the Krakow metropolitan bishop Karol Wojtyła, who would later go on to become Pope, and the great involvement of Father Gorzelany along with the support of many foreign backers, were of great significance in obtaining a construction permit. In the political context of the time, the massing of the church was legible to the faithful, as it was meant to be a reference to Noah’s Ark, protecting people from the deluge of atheism [12]. The association with a ship that ran aground (a tall plateau) went much further than simple ornamentation and became the basis for the original structural system of the massing and the idea of introducing light into the interior.

In architectural terms, the Ark of the Lord Church constitutes an example of late modernism in Poland and is a reference to the chapel in Ronchamp by Le Corbusier, although it is larger (it has a floor area of 1300 m²) and is laid out on three levels [11]. The main nave is entered from the level of the plateau which surrounds the church, and which can be accessed by two extensive stairways from the southern and western sides (accessible from Obrońców Krzyża Street), as well as by a narrow circulation route from the north. Entrances to the Reconciliation Chapel and the Chapel of the Mother of God of Fatima, both of which are located at a lower level, are accessible directly from the level of Obrońców Krzyża Street.

The oval walls of the massing of the church, slightly slanted towards its centre, were built out of poured concrete and clad in round river stones (brought from mountain rivers by the residents involved in the construction). They were meant to be a reference to full sails blown by the wind. Irregularly shaped openings were left between the walls/sails. These walls support the roof, which extends beyond their outline, bent like a shell and covered in shingles.

The church does not feature a traditional bell tower; however, it does have an almost twenty-metre-tall concrete mast which fulfils a structural role within the building and is topped with a cross in a golden crown.

There is a total of seven entrances leading into the church from various sides. The entrance from the plateau on the northern side of the church, but from the direction of the western shift in the wall, is of particular significance. This entrance leads the visitor beneath a stained-glass window-like tower which symbolises the biblical Pillar of Fire, which led the Chosen People through the desert. The main altar extends towards the centre of the eastern part of the nave. It is from this side that a broad matroneum and choir gallery starts, providing the church with a third level and protruding outwards from the base of the buildings as if on a cantilever. The entrance to the choir gallery is located on the western side of the church, opposite the altar. Beneath the nave is the Chapel of the Mother of God of Fatima. Its space partially joins the space of the nave thanks to numerous openings: from the north it is the opening of the circulation route that connects both levels, in the area of the altar there are openings beneath the seven steps of the openwork stairs; from the south, a significant opening makes it possible to look into the nave from the lower chapel.





Fig. 1–3. The Ark of the Lord Church visible from the south (source: author's own archives)



Fig. 4. The Ark of the Lord Church visible from the northwest (Source: author's own archives)

3. The idea of light in the Ark of the Lord Church

Light, which has a particularly strong symbolism in Christian churches, became the basis for the idea behind the design of the Ark of the Lord Church and its orientation, the many different planned openings, its shape, structure and, finally, its materials. The massing of the church has a floor plan shaped like an elongated oval, resembling the outline of a ship with its prow facing the east. This orientation is continued in the interior of the nave and the chapels: the front of the altar and the spheres of the sacrum of the chapels are situated on the eastern side. The nave is illuminated by sunlight from practically all sides. The openings, however, were planned in such a manner that the cardinal directions do not always correspond to the direction of sunlight: 1) from the southern side, the nave is illuminated most intensely by light from the south, which enters through a high opening that has the shape of an arch and is located underneath the roof, and then by light from a small window in the southern wall near an opening in a structural beam that protrudes outside, as well as light from the east, which enters through an opening between two walls/sails; 2) eastern light enters the interior from the eastern side of the nave thanks to a glazed wall; 3) from the northern side, northern light



Fig. 5. Nave of the Ark of the Lord Church in the direction of the main altar
(Source: author's own archives)

enters through a glazed wall at the level of the matroneum and the second glazing underneath it, and western light is captured by the tower of the Pillar of Fire in a shift in the massing that opens towards the west; 4) delicate western light enters the interior from the northern side of the nave thanks to an opening in the bottom which spans between the strongly bent arch of the wall/sail and the gentle arch of the base.

4. Methods of operating with sunlight within the interior the church

In the church we can see three basic types of operating with sunlight in an interior: light introduced directly from outside, reflected light and filtered light. Within each of these types we can find detailed methods of operating with light: carving⁵, mirror reflecting, scattering – bending⁶, scattering–slipping⁷, as well as absorption [7].

During the day the interior of the nave is dominated by the form of a luminous arch between the wall and the ceiling on the southern and south-eastern side. This arch is created out of side light that is carved by the opening between a massive concrete wall and the roof; the light introduced in this manner easily slips across the bottom curvature of the roof and the translucent glass panes produce mirror-like reflections.

⁵ According to the author, carving means limited by the dimensions of an opening; rays enter directly from the outside, which can be seen through the opening [7].

⁶ According to the author, scattering–bending means a sequence of scattering that breaks up the rays on a rough concave or convex surface [7].

⁷ According to the author, scattering–slipping means a sequence of scattering that breaks up the rays on a rough surface perpendicular or almost perpendicular to the opening [7].

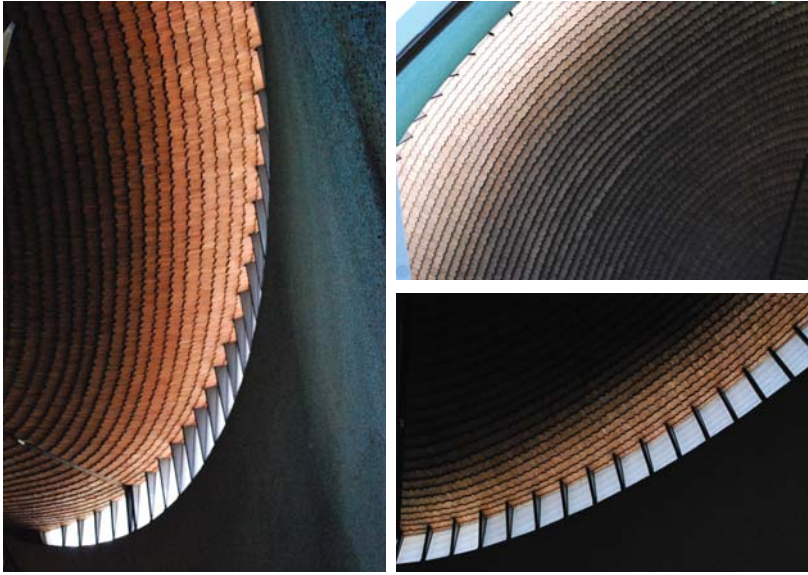


Fig. 6. Fragment of the southern side of the nave: a visible arch at the top of the wall, the carving, bending and slipping of sunlight (Source: author's own archives)

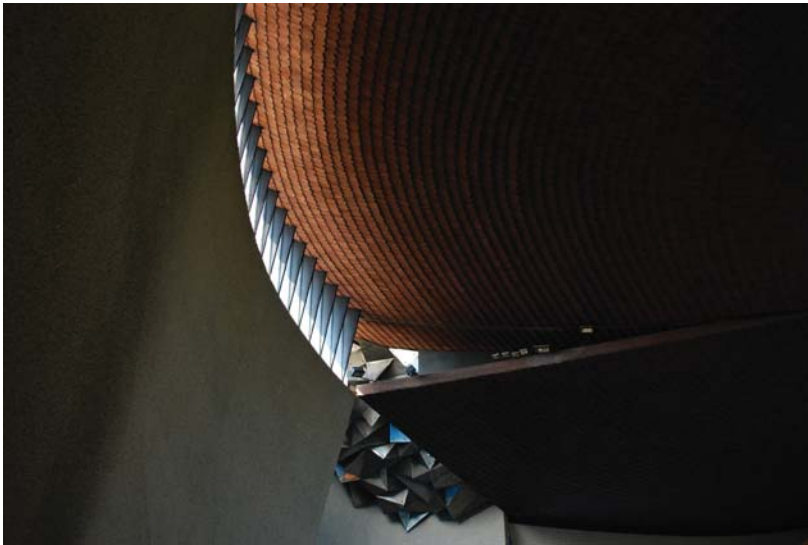


Fig. 7. Fragment of the southern side of the nave: a visible arch at the top of the wall, the carving, bending and slipping of sunlight (Source: author's own archives)

On the southern side of the nave the eastern vertical opening carves out an expressive slender triangle of dynamic light which slips across the curved wall and bends on its concave surface. This slipping light perfectly exposes the coarse texture of the concrete. The triangular lower part of the opening is equipped with a blue stained-glass window. This light thus tints the naturally grey concrete wall, in addition to casting blue reflections on other materials within

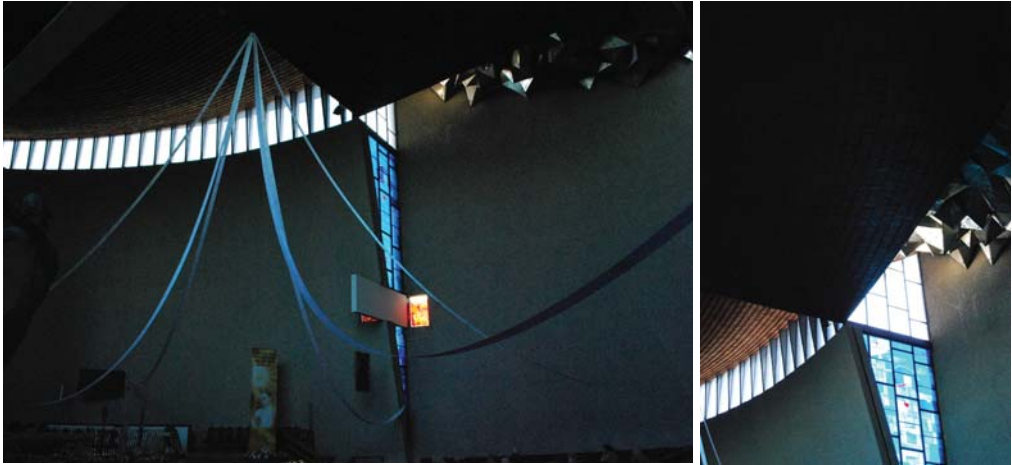


Fig. 8. Fragment of the southern side of the nave: a visible arch at the top of the wall, a slit in the ceiling, and the metal ceiling decoration (Source: author's own archives)

the nave. The upper part of the nave does not have stained-glass window and introduces more intense eastern light into the interior which slips across the expressive sculptural texture of the ceiling – a decoration of pyramidal shapes of polished metal. This light reflects numerous times on the irregular sharp surfaces, intensifying the illumination of the nave from the top with a flickering glow. A similar ceiling decoration is in the northern side of the nave, where it reflects the light of the Pillar of Fire and of the stained-glass windows from the east.

The casting of side light on the concave walls of the four concrete sails and its scattering through slipping and bending is used several times in the nave.

From the east, on the left side behind the altar, there is a wall that is completely filled with a stained-glass window, with a sharp angle at its top that is similar in form to a vertical triangle with an acute top angle. Stained-glass windows always cause walls to become filters which, by absorbing specific colours of the light spectrum, significantly reduce the intensity of light and give it a specific colour. In this case it is dynamic and changing eastern light from the side which, thanks to the stained-glass window, gains warm colour shades with a dominance of yellow greens, oranges, and ochre.

The largest openings are located on the northern side of the nave; this is justified as northern light enters through here and is dispersed in the blue sphere. However, on this side of the nave the interior is also illuminated with western light, filtered several times through the spatial stained-glass window of the tower of the Pillar of Fire, whose lower part (which features the entrance to the church) is built out of glass masonry units that are green in colour, while the upper part consists of shaped glass in the colours of fire: red, orange and yellow. The fiery colours of the stained-glass window are intensified by warm western light, which falls onto this structure without interference because of the shift in the massing that is open towards the west.

From this side of the nave there is a passage to the lower level of the Chapel of the Mother of God of Fatima, from which one can exit to a small square below the plateau. This exit is located in the completely glazed northern wall, which provides additional light to the chapel and the space of the stairs. This spatial structure of the massing causes the main nave to be

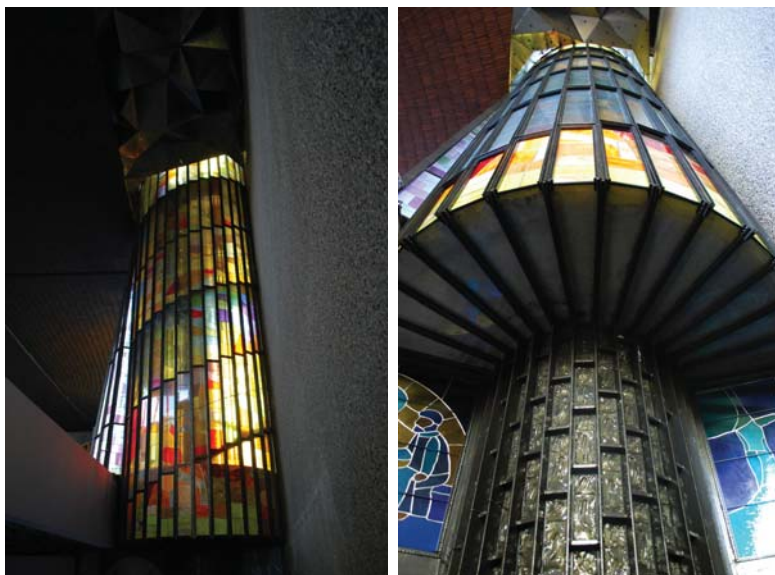


Fig. 9., 10. The stained-glass window-like tower which symbolises the biblical Pillar of Fire
(Source: author's own archives)



Fig. 11. The open vertical space between the upper and lower level of the church, which makes it possible for the interior of the main nave to be entered by *lume di lume* from the lower chapel of the Mother of God of Fatima (Source: author's own archives)

penetrated by delicate sunlight from this bottom side, from the space of the chapel; this is *lume di lume*, secondary light, which comes from a neighbouring interior [6, 9]. In this case light comes from the lower chapel, which it enters through the northern wall (dispersed, static and permanent light) and through the southern wall (intense, dynamic and changing light), where the second entrance to the chapel is located. *Lume di lume* enters the nave, including from between the steps of the stairs which lead to the altar in the main nave, as well as from the southern opening that connects two of the church's levels.

Of particular note is the light that enters the interior from the back of the nave from the west. This is side light which enters the interior thanks to a glazed slit that winds along the arch between the western, strongly concave wall/sail and the gently curved base, upon which the stairs to the choir gallery are anchored. This delicate and warm light is never direct but enters the interior in a form that is scattered in numerous reflections.

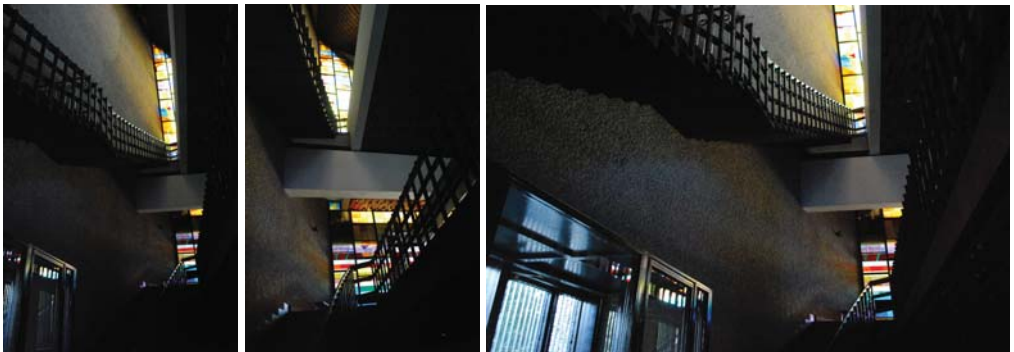


Fig. 12., 13. The side western light from below which enters the interior thanks to a glazed slit that winds along the arch between the western, strongly concave wall/sail and the gently curved base, upon which the stairs to the choir gallery are anchored (Source: author's own archives)

skylight are semi-translucent, which causes them to absorb some of the light. The light that does enter the interior and which is also reflected from the surface of the stone floor slips from the bottom towards the top along the coarse concrete surface of the curved wall, illuminating the space of the stairs to the choir gallery. This space is simultaneously illuminated and coloured in shades of blue thanks to the northern stained-glass window near the matroneum.

These methods of working with light in the interior of the Ark of the Lord Church are accompanied by others; for instance, the reflection of light off the smooth marble, glass,



Fig. 14. The reflection of light on the marble floor (Source: author's own archives)



Fig. 15. The floor of the matroneum with small panes of glass placed between small boards (Source: author's own archives)

and metal materials, fittings and decorations. We can also mention the original concept of providing additional illumination to the space beneath the matroneum, both inside the church and outside of it, where the matroneum extends. The floor of the matroneum has small panes of glass that are placed between small boards; they create the illusion of a ship's deck with regularly spaced wooden boards, between which light shimmers as if reflected off water.

5. Exposing architecture with light

Thanks to its unique operation, Light in the Ark of the Lord Church expressively exposes the materiality of the interior, the structure of its surfaces, its massing and space, as well as the visual character of the shape of the interior and the atmospheric and projection capacity of its architecture⁸.

The light quite strongly exposes the materiality of the architecture here: the Carrara marble of the main altar appears as a soft, milky white stone; the shingles on the ceiling become a relief in a red colour; the concrete walls/sails reveal their coarse texture, and the glass masonry is the massiveness and redness of the glass of the Pillar of Fire. Thanks to mirror-like reflections, the smoothness of the marbles and various metals – for instance the bowls of holy water – is exposed, while scattered reflections on the walls expose the coarseness of the concrete. Light also highlights the smoothness of the steel rings around the tabernacle and the coarseness of the tabernacle itself, which is made out of unpolished brass in the form of a sphere. In specific conditions sunlight can fall onto the “moonstone” in the wall of the tabernacle, causing it to sparkle [3, 5]⁹.

Thanks to sunlight, the interior gains visually in terms of the articulation of the concaveness of its walls/sails. In terms of highlighting the visual character of this interior, the most effective technique is the slipping of light across the various surfaces and curves of the massing, which attractively highlights the complex shape of the nave. This provides the effect of the interior's constraints being sprinkled with small parts of luminous matter (an illusion of the materialisation of light). The shape and convexity of the roof and the texture of the shingles are most strongly highlighted by the intense, dynamic and changing southern light from the side, which falls through the glazed arch underneath the roof. Exposure of the concavity of the walls/sails is obtained particularly thanks to the slipping of side light, which enters through the vertical slits between these walls. The gradation of light causes the interior to feature places which are covered in shadows that are only slightly tempered.

The slits are narrow enough to limit the visibility of the interior of the church. This effect is strengthened by the stained-glass windows in the glazed walls, as well as in the vertical openings.

⁸ Projection capacity is the ability of an interior to form projections (illusions and associations) in the human mind [7].

⁹ According to macroscopic analysis, “Moonstone” is an aggregate of pyrite crystals glued to a fine crystalline concretion composed of the same material [5].

The light inside the church exposes the various structures of the filters, particularly the stained-glass windows that glow in the Pillar of Fire and are cooler from the north, with yellow colours from the east.

An individual who spends longer in the Ark of the Lord Church and carefully observes the interior is taken on a tour of its architecture by sunlight.

6. Architecture as an instrument of sunlight

The exposure of the interior as an instrument of light is equally rich. In this case, the astrophysical qualities of sunlight can be perceived thanks to the architecture. The architectural apparatus that is used to introduce light into the church simultaneously provides exposure of the sunlight's properties, primarily exposing the transcendental nature of this light as its source is always located outside of the interior. Sunlight, as if imprisoned in the architectural apparatus, clearly directs the attention of people inside the interior to outside of its bounds – towards the sun and its shining heavenly sphere. Simultaneously, thanks to the shape of the interior of the Ark of the Lord Church, the architecture exposes the local, geographic conditions of sunlight in a specific place (Bieńczyce), with its constant, uncontrolled changes that depend on the time of year, day, and the weather. Exposing it in human perception unites the interior with its place on Earth and the cosmos itself.

The Ark of the Lord Church, treated as an instrument of light, exposes the orchestration and choreography of light [7]. This orchestration is, in the author's view, the result of different forms of working with light in a single interior at the same time. As a result, the architecture primarily exposes the spatial character of sunlight scattered in the celestial sphere. The orchestration creates a new, coherent effect of a whole (the spatial character of light in the celestial sphere) out of a multitude of individual methods of introducing and modifying light – one that goes beyond the sum of its parts (similarly to the combination of sounds in an orchestra).

The choreography, in the author's opinion, is the result of working with light within an interior over time. It primarily exposes the slow change and movement of light in accordance with how the sun travels along its ecliptic. The direction of penetration and the intensity and colour of the light all change.

In the Lord's Ark Church, we can experience a full orchestration of light. From dawn until dusk, all of the tools that introduce light from every side of the interior and from the bottom are active, yet they have varying intensity at different moments. On a May morning the light enters from behind the altar with direct and warm rays, while the upper southern slit is still quite dim. In the noon hours the orchestration changes completely: an intense illumination of the arch beneath the roof takes place. The range of the light of the luminous arch increases during the autumn months and reaches its apogee in winter, while in the summer it is the weakest, when the noon rays produce an intense streak of sunlight. A different orchestration plays out at sunset, when the main instruments are quieter and the warm light of the Pillar of Fire from the left side of the altar and the reflected light of the west near the stairs to the gallery play out their solos.

In particular, choreography of light is made possible in this interior thanks to the opening beneath the roof as it has a relatively large outline from the south-east to the south. This outline makes it possible to expose the changes in the location of the sun throughout the day, as well as of the flow of time. The vertical openings from the east and the south create a specific choreography.

7. Atmosphere as the result of the mutual exposition of light and architecture

The combination of the expositions discussed above – of architecture and light – is essential to the perceptual experience. It is from this mutuality that the unique atmosphere of the Ark of the Lord Church originates. The exposition of the architecture and the nature of light that changes with time and the weather can easily elicit many different yet similar sensory experiences, feelings, and thoughts associated with the symbolic significance of light or the church–ship associations in individuals.

In the main nave there is an atmosphere of intimacy and clarity – of a spatial depth, a luminosity and isolation of the interior. Openings towards all the cardinal directions and the bending of light along the curvatures produces a dynamic and a tension that is stabilised in harmonious balance. However, the gradation of bent light on the curvatures reinforces an atmosphere of peace, quiet[4], and softness, easing the sharpness of the luminous openings and the sharp forms of the decoration of the ceiling. Thanks to this the atmosphere of this interior is soothing, refreshing, stimulating.

The atmosphere in the area around the altar achieves a particular dynamic harmony that extends along the directions: of direct rays of sunlight from the top right, scattered cool rays from the Bronisław Chromy’s “From life to life” sculpture, warm rays from the east, from behind the altar, subtle rays from below – from the west. This atmosphere of a tense balance increases intimacy and focus. This tense focus can also be seen between the mystery and symbolism achieved by the luminous arch, the stream of light that falls onto the altar, and the clarity achieved by the visual articulation of the shape of the church.

The carving of light through the slits between the walls/sails has a telling symbolism. It brings to mind associations with cracks, of the cracking of a shell with light. The reflections on the marble also have their own symbolism: the white marble of the altar, the green marble of the floor, whose white veins suggest a tangled deep. The curved opening that introduces light underneath the roof provides the effect of a raised cover and the beam of light that falls from this opening onto the altar produces the effect of the connection between the Eucharist and Divine Light. Of note is the fact that in relation to the chapel in Ronchamp, where Le Corbusier also designed a narrow slit between the roof and the massive wall from the south, the similar slit in the Ark of the Lord Church is broader and illuminates the interior more intensely, causing a stronger effect of the roof being raised above the interior – of carving a luminous arch and a beam that falls onto the altar. From the symbolic significance created by light, the luminous arch underneath the roof affects the atmosphere of the interior the most. It has its own universal theological symbolism which connects with its perception in

the perspective of viewers inside the interior, within which it always has two of its endpoints raised upwards (it “smiles”).

The scattered *lume di lume* has its own expressive symbolism within the interior, providing exposition of the structure and shape of the church. This light connects the three levels of the building, reinforcing the clarity and cohesion of the entire massing, in addition to providing a high projection capacity to the interior. The impression of the suspension of the zone of the altar in space and the associations that it brings add a lightness and spatiality to the atmosphere of the interior, in addition to eliciting feelings of the extraordinary, mysteriousness and dynamism. The expressiveness of the three levels of the church, articulated through light, also resembles the decks of a ship – the biblical Ark.

Limiting visibility of the interior of the church reinforces an atmosphere of the fencing off of the space of the sacred from its surroundings, and of a focus on prayer. As a result of the reflections and the filtering, the light brightens and slightly tempers the dark, thus increasing the intimacy and co-creating the theological purpose of the church. Sunlight in the interior of the Ark of the Lord Church co-creates an atmosphere of the sacred; it is conducive to awe associated with luminous illusions and the symbolism of light. The impressive, emotional and intellectual reception of the interior together form a single, coherent perceptual experience.

8. Conclusion

The author’s analysis confirms the close relationship between sunlight and the atmosphere inside the Ark of the Lord Church in Krakow. This light, which is introduced into the church and modified inside thanks to a sort of architectural apparatus, creates a unique atmosphere in the interior. It is a form-creating element of architecture, associated not only with the materials that let either white or coloured light through, but also with the massing and structure of the three-level church, the shape of the space, and the constraints of the interior. Thanks to sunlight, the architecture of the interior is exposed in front of visitors in a specific manner. On the other hand, we can look at this architecture as an instrument of light which exposes the astrophysical nature of sunlight to man: its ceaseless, uncontrolled change and travel, as well as its scattering in the celestial sphere. The exposing of the transcendental nature of the cosmos and the identity of the specific site on which the Ark of the Lord Church stands is extraordinarily valuable to the atmosphere of the sacred. Thanks to light, the balance between the centripetal and centrifugal exposition of the interior becomes stabilised within the nave of the Ark of the Lord Church in the dynamics of time and weather. The openings towards the cardinal directions, the exposition of the visual character of the church, particularly thanks to the slipping of light across its curved surfaces, and at the same time the expression of the luminous arch produces a dynamic and tension that stabilises in the harmonic balance between clarity, intimacy and unreality. The significant constraining of the visibility of the surroundings, despite the illumination of the church, is conducive to focus on prayer. The analysis led to the conclusion that familiarity with the laws of physics that govern sunlight, as well as identifying the ways in which it operates in an interior through the use of architecture, increases the chance of obtaining a desired atmosphere.

References

- [1] Böhme G., *Architektur und Atmosphäre*, Wilhelm Fink Verlag, München 2006.
- [2] Böhme G., *Atmospheric Architectures. The Aesthetics of Felt Spaces*, Bloomsbury Academic, Bloomsbury 2017.
- [3] Kordaszewski M., „Arka Pana”. *Przewodnik. Historia i symbolika*, Wydawnictwo Benedyktynów, Kraków 1995.
- [4] Plummer H., *The Architecture of Natural Light*, Thames & Hudson, London 2009.
- [5] Rajchel J., *Kamienny Kraków*, UWND AGH, Kraków 2005.
- [6] Scamozzi V., *L'Idée dell'Architettura Universale*, Venezia 1615.
- [7] Stec B., *O Świetle we wnętrzu. Relacja między światłem słonecznym a architekturą w aspekcie atmosfery architektury*, Wydawnictwo Krakowskiej Akademii im. Andrzeja Frycza Modrzewskiego, Kraków 2017.
- [8] Zumthor P., *Atmospheres. Architectural Environments. Surrounding Objects*, Birkhäuser, Basel-Boston-Berlin 2006.
- [9] Borys A.M., *Lume di Lume. A Theory of Light and Its Effects*, „Journal of Architectural Education”, 2004 Vol. 57, No 4.
- [10] Wilkoszewska K., *Uwagi na marginesie książki Gernota Böhme „Filozofia i estetyka przyrody”*, „Sztuka i filozofia” 2004, 24, 20–23.
- [11] Smaga A. <http://szlakmodernizmu.pl/szlak/baza-obiektow/arka-pana> (access: August 2018).
- [12] <http://www.arkapana.pl> (access: August 2018).



Bożena Tylińczak  orcid.org/0000-0002-2761-6185

Sonia Kudłacik-Kramarczyk  orcid.org/0000-0003-2049-6536

(skudlacik@chemia.pk.edu.pl)

Anna Drabczyk  orcid.org/0000-0002-4629-2059

Magdalena Głąb

Faculty of Chemical Engineering and Technology, Cracow University of Technology

NOVEL HYDROGELS MODIFIED WITH XANTHAN GUM – SYNTHESIS AND CHARACTERIZATION

INNOWACYJNE MATERIAŁY HYDROŻELOWE MODYFIKOWANE GUMĄ KSANTANOWĄ – SYNTEZA I CHARAKTERYSTYKA

Abstract

Due to their interesting features, hydrogels are attracting growing interest in the polymer materials market. Therefore, many studies are currently conducted to characterize these materials and to modify them in order to increase the range of their potential use. In the presented article, hydrogels based on acrylic acid and chitosan and modified with xanthan gum were obtained by photopolymerization. Their swelling ability and behaviour in solutions that simulate fluids in the human body were determined. The effect of incubation in various fluids on the chemical structure of the synthesized materials was characterized using spectroscopic analysis. Furthermore, the surface morphology of the attained materials was characterized with scanning electron microscopy (SEM).

Keywords: hydrogels, xanthan gum, acrylic acid, chitosan, surface morphology of hydrogels

Streszczenie

Hydrożele z uwagi na swoje interesujące właściwości należą do grupy związków cieszącej się dużym zainteresowaniem na rynku materiałów polimerowych. Dlatego też prowadzone są badania mające na celu charakterystykę tych materiałów oraz ich modyfikację w celu zwiększenia możliwości ich potencjalnego zastosowania. W artykule przedstawiono syntezę hydrożeli na bazie kwasu akrylowego i chitozanu modyfikowanych gumą ksantanową. W toku badań określono zdolności pęcznienia hydrożeli oraz ich zachowanie w symulowanych płynach ustrojowych. Ponadto określono wpływ inkubacji otrzymanych materiałów w wybranych płynach na ich strukturę chemiczną z wykorzystaniem analizy spektroskopowej. Dodatkowo scharakteryzowano morfologię powierzchni hydrożeli za pomocą skaningowego mikroskopu elektronowego (SEM).

Słowa kluczowe: hydrożele, guma ksantanowa, kwas akrylowy, chitozan, morfologia powierzchni hydrożeli

1. Introduction

In recent times a big rise in the popularity of polymers has been observed. The materials which are attracting the greatest interest are undoubtedly hydrogels (also known as superabsorbent polymers, SAPs). They consist of a three-dimensional network of polymer chains. This structure contains hydrophilic groups and, due to their presence, these materials are characterized by a strong ability to absorb liquids. This property depends on features of the hydrogels (such as crosslinking degree or type of additives introduced into the polymer matrix). However, the properties of the liquid that is absorbed (pH, type of ions in the solution) can also have an impact on the sorption capacity of the tested material [1–4].

What is more, hydrogels are also characterized by their biocompatibility, biostability and non-toxicity. Moreover, these materials are flexible and at the same strong. The hydrogel matrix can be enriched with different substances of natural origin, thus giving the hydrogel material additional properties. All these characteristics make hydrogels suitable for use in many fields such as medicine or pharmacy. Superabsorbent polymers are used in controlled drug release systems [5–6]. Hydrogels are also the raw material for the preparation of modern dressings that provide a favourable environment that is conducive to the wound healing process [7]. Another field in which these materials are applied is tissue engineering, where hydrogels find application not only in the preparation of artificial organs or implants, but also as three-dimensional scaffolds for cell growth and proliferation [8].

Xanthan gum, which acts as a modifying agent of the polymer matrix, is a well-known polysaccharide. It is characterized by unusual rheological properties that make it applicable in many fields such as the food industry [9–13], agriculture, textiles or even in pharmacy or tissue engineering [14]. Furthermore, xanthan gum plays an important role in controlled drug delivery systems [15–16]. In many previous studies, xanthan gum was used as a substance constituting a hydrogel matrix. Tao et al. [17] described the synthesis and physicochemical properties of hydrogels based on this polysaccharide. Such materials have been proposed as polymers for the controlled release of various substances in the food industry and tissue engineering. A three-dimensional network of polymer chains of xanthan gum was obtained by the application of sodium trimetaphosphate as the crosslinking agent. Various compounds can be used as crosslinkers in the preparation of hydrogels based on this polysaccharide, and the obtained polymers are characterized by a variety of properties [18–19]. An interesting solution is the application of hydrogels based on both xanthan gum and magnetic nanoparticles for adsorption of different dyes from aqueous solutions [20–21]. It is also worth noting that hydrogels based on the described polysaccharide and methylcellulose [22] or starch [23] represent an excellent material for drug delivery. Xanthan gum is also an interesting component of nanofibers [24] or hydrogel films [25].

In the framework of the research, novel hydrogels based on acrylic acid and modified with xanthan gum and chitosan are proposed. The materials used as additives in the polymer matrix are of natural origin and therefore are designed in order to provide the attained polymers with characteristics such as biodegradability or biocompatibility. What is more, such properties are desirable in materials destined for biomedical applications.

2. Materials

The chitosan (low molecular weight), acrylic acid (anhydrous, colourless liquid, 99%, $d = 1.051$ g/ml), poly(ethylene glycol) diacrylate ($M_n = 256$ g/mol), $d = 1.12$ g/ml), phenylbis(2,4,6-trimethylbenzoyl)phosphine oxide (colourless liquid, powder, $M = 418.46$ g/mol) and xanthan gum used for preparation of the hydrogels were supplied by Sigma Aldrich; potassium hydroxide was received from Avantor Performance Materials Poland (formerly POCH SA). All compounds were characterized by analytical purity and applied without further treatment.

3. Experimental Part

The preparation of hydrogels containing xanthan gum involves several steps. In the first of them, 45 ml of acrylic acid was neutralized by the addition of 50 ml of KOH (40% solution). This reaction is exothermic, therefore the mixture had to be cooled to room temperature. The next step was to prepare the chitosan solution by dissolving 10 g of it in 200 ml of 2% acrylic acid solution. 5 ml of the prepared solution was added to the mixture of acrylic acid and KOH. Then, an appropriate amount of xanthan gum, 1 ml of initiator solution (made up by adding 2 g of phenylbis(2,4,6-trimethylbenzoyl)phosphine oxide to 10 ml of acrylic acid) and 1 ml of crosslinker (poly(ethylene glycol) diacrylate ($M_n = 256$ g/mol)) were introduced into the previously prepared mixture, which was poured onto a Petri dish and subjected to UV radiation for 1 min. An Emita VP-60 quartz lamp (120 W power, applied wavelength $\lambda = 320$ nm) was used for the process of photopolymerization. In this manner, a series of hydrogels containing different amounts of xanthan gum was obtained. The following quantities of xanthan gum were added (based on the amount of acrylic acid):

- a) 0 wt%
- b) 1 wt% (0.075 g)
- c) 3 wt% (0.224 g)
- d) 5 wt% (0.373 g)
- e) 7 wt% (0.522g).

4. Methods

4.1. Swelling measurements

A 1.0 g hydrogel sample was immersed in 100 ml of liquid (distilled water, solution of salts 0.9% NaCl, 0.9% $MgCl_2$; Ringer's liquid and artificial saliva solution) for 1 h. After this time the hydrogel was taken out of the solution and weighed. The swelling ratio (Q , g/g) was calculated from the following formula (1):

$$Q = \frac{w - w_0}{w_0} \quad (1)$$

where:

- w – weight of swollen sample,
- w_0 – weight of hydrogel before swelling.

4.2. Incubation studies

In order to determine the behaviour of the obtained materials in selected fluids, samples of hydrogels were introduced into 100 ml of a suitable liquid (i.e. distilled water, Ringer's liquid and a solution of artificial saliva). The incubation time in distilled water and Ringer's liquid was 63 days; in the solution of artificial saliva the hydrogels were immersed for 21 days. The pH of the solutions was measured once a week.

4.3. Fourier Transform Infrared spectroscopy (FT-IR)

FT-IR spectroscopy was used in order to analyse the chemical structure of the obtained hydrogel polymers. The test was performed using an FT-IR spectrometer with ATR diamond/ZnSe (Perkin Elmer Spectrum 65). In order to determine the impact of immersion in suitable liquids on the chemical structure of the tested hydrogels, materials were investigated before and after the incubation period.

4.4. Scanning electron microscopy (SEM)

Surface morphology of the tested samples was determined by means of an FE-SEM Zeiss Supra 55VP scanning electron microscope. This method was used in order to characterize the surfaces of the hydrogels and to define the impact of the presence of the additive on the morphology of the materials.

5. Results and discussion

5.1. Swelling measurements

The calculated values of the swelling ratios of hydrogels containing different amounts of xanthan gum are presented in Figure 1 and Figure 2.

The attained hydrogels containing xanthan gum were characterized by a relatively low swelling capacity. The highest swelling ratios were found for the samples placed in distilled water. Under the influence of water, the hydrophilic functional groups present in the polymer chains dissociate and ions are then formed. As a result, electrostatic interactions between these ions occur. Ions with the same charge repel each other, which consequently increases the distance between the polymer chains. As a result, there is more free space for water, therefore hydrogel is able to absorb large quantities of liquid. In the case of 0.9% NaCl, lower values of Q were observed due to the presence of ions in the solution that is absorbed. An

ion interaction between the polymer matrix and the sodium cations takes place that reduces the hydrophilic nature of the carboxyl group (Na^+ joins the aforementioned group) and, as a result, the interactions between the COO^- ions that were previously observed are limited. The presence of divalent ions in 0.9% MgCl_2 contributes to the increase of the crosslinking degree of the tested hydrogel. As a result, a reduction of swelling ability is observed.

Significantly, the tested hydrogels are able to absorb salts. Thus, these materials can be used as alternative dressings which can absorb wound exudates and impurities, thereby contributing to disinfection.

Relatively high swelling ratios for the samples immersed in the solution of artificial saliva were observed. The swelling ability of the samples tested in artificial saliva was lower than those tested in distilled water but higher in comparison to the swelling ability determined in the other tested liquids. The solution of artificial saliva contains carbonate and orthophosphate ions that provide its buffering properties but do not reduce its sorption capacity. Lower values of Q were observed for samples tested in Ringer's solution. There are a lot of monovalent and divalent ions in this mixture, which reduces its absorption properties.

Based on the results of swelling in both the tested solutions, it can be also said that the presence of xanthan gum in the polymer matrix has an impact on the swelling properties of the tested materials. It is not easy to find any dependency between the amount of the introduced additive and the sorption capacity of the modified samples. However, in most cases the modified hydrogels were characterized by higher swelling capacity. This could be the result of the presence in xanthan gum of compounds that contain hydrophilic functional groups in their structure. Such groups can form additional hydrogen bonds with the molecules of the solvent and therefore the sorption capacity of samples modified with this additive can be higher. In other cases, a certain amount of this additive can cause a kind of system disorder or even accumulate between the polymer chains in a way that reduces swelling ability. Moreover, the synthesized hydrogels have a low sorption capacity that is important from the point of view of the potential applications of these materials.

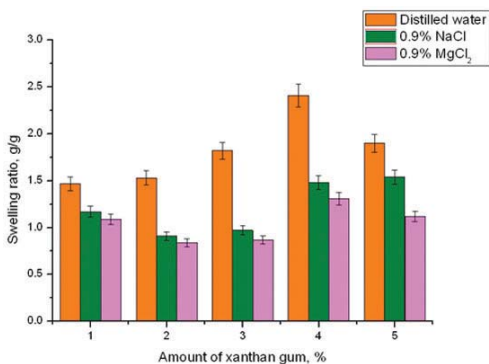


Fig. 1. Results of swelling in distilled water, 0.9% NaCl and 0.9% MgCl_2 (number of repetitions $n = 3$)

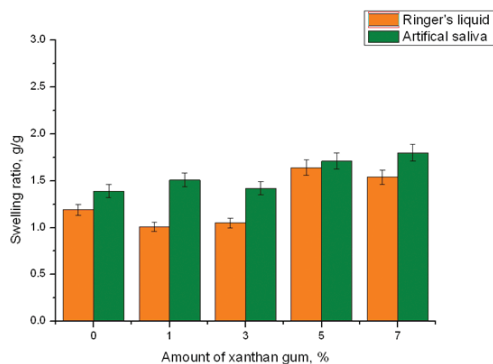


Fig. 2. Results of swelling in Ringer's liquid and in artificial saliva solution (number of repetitions $n = 3$)

5.2. Incubation studies

The pH values of the solutions determined once a week during the 63 days of incubation are shown below in Figures 3–5.

Sudden changes in pH values were not observed during the incubation; this indicates the compatibility of the tested material with a given environment. Therefore, these hydrogel matrices can be considered as materials that are useful in medicine. The pH value fluctuates around neutral, which promotes the process of wound healing. Importantly, the form and shape of the hydrogel did not change during incubation in distilled water, i.e. absorption of water did not cause the disintegration of the material.

The highest values of pH were observed in the case of the liquid containing hydrogel without xanthan gum. When immersed in Ringer's liquid, the pH of the hydrogels modified with this polysaccharide show a slight tendency to change. This could attest not only to their in vitro stability, but also to the compatibility of these materials with bodily fluids (Ringer's liquid is isotonic with human blood). These features allow the use of these hydrogels as biomedical materials.

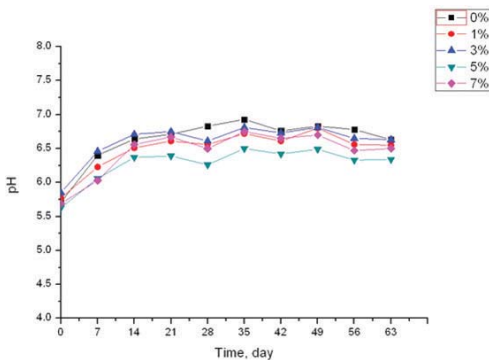


Fig. 3. Changes in pH of distilled water containing hydrogels

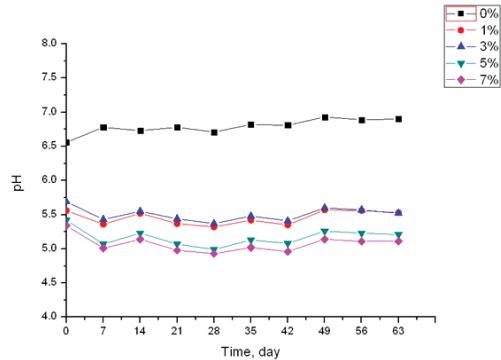


Fig. 4. Changes in pH of Ringer's liquid containing hydrogels

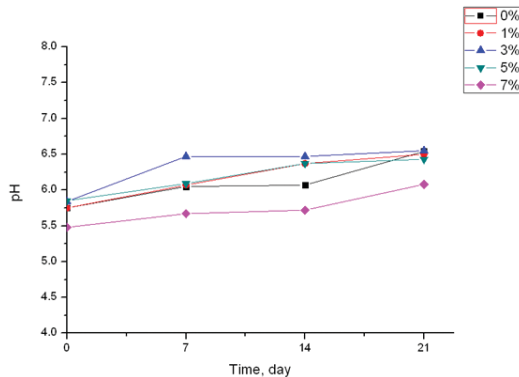


Fig. 5. Changes in the pH of the solution of artificial saliva containing hydrogels

The results do not show any relationship between the pH of the liquid in which the sample is immersed and the amount of the xanthan gum in the hydrogel matrix. The lowest pH values were observed for a sample containing the biggest amount of the aforementioned polysaccharide. Additionally, in each case a gradual increase in pH during incubation was observed that is a result of the ion exchange that takes place between the polymer matrix and the ions in the Ringer's liquid. It should also be mentioned that the carbonate and orthophosphate anions in the saliva which are responsible for its buffering properties cause the whole system to tend to reach a pH of approx. 6.8–7.

5.3. Results of FT-IR spectroscopy

The IR spectra of attained hydrogels before and after immersion in particular fluids are presented in Figures 6–9. This study makes it possible to determine the effect of incubation on the chemical structure of polymer samples.

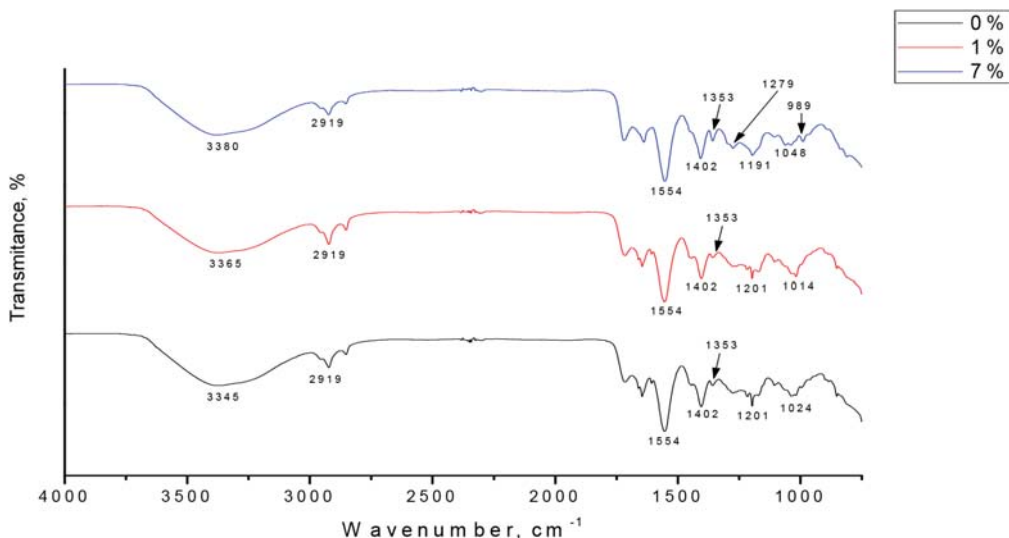


Fig. 6. IR spectra of samples modified with xanthan gum before immersion

The IR spectra of the hydrogel samples prior to the incubation show considerable similarity. Table 1 shows a compilation of the vibrations occurring in the studied materials.

On the basis of the attained IR spectra, it can be stated that long-term immersion of the obtained materials in simulated body fluids has an impact on their chemical structure. According to the results of the spectroscopy, a decrease or total disappearance of the peaks characteristic of particular bonds is observed (e.g. the peaks at 1548 cm⁻¹ or 1406 cm⁻¹).

Incubation in Ringer's liquid and in distilled water lasted 63 days; immersion of samples in a solution of artificial saliva lasted 21 days. Nevertheless, the greatest change was observed in case of incubation in the artificial saliva.

Table 1. Compilation of characteristic vibrations occurring in the tested samples

Region of vibration [cm^{-1}]	Assigned to
3300–3500	N-H
2850–2970	C-H
1550–1650	N-H
600–1500	C-C
1180–1360	C-N
1050–1300	C-O
675–995	C-H

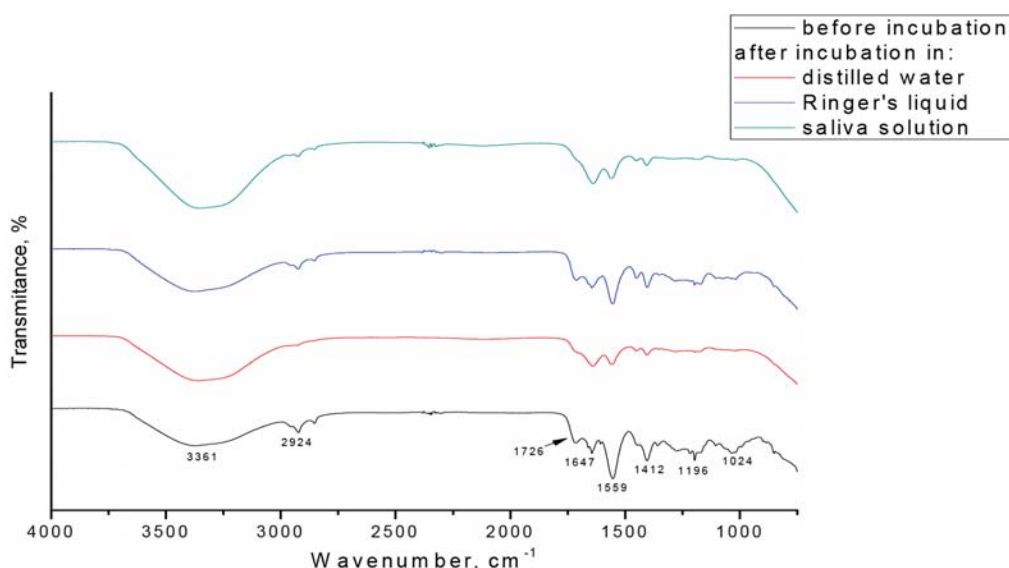


Fig. 7. IR spectra of samples without xanthan gum (0 wt%)

In Figure 6, the impact of the introduction of xanthan gum into the hydrogel matrix on the structure of the tested material can be observed. A lower intensity of the peak at a wavelength of approx. 1720 cm^{-1} derived from carboxylic acid can be seen that is due to the fact that with the increasing amount of the additive the total amount of the acid in relation to the amount of the rest of the reagents becomes lower. Furthermore, the disappearance of the band at 989 cm^{-1} (observed in the case of samples with 1%wt. and 7%wt. of xanthan gum) that is derived from the C-H group can be seen. This group becomes less visible as a result of the increasing amount of the additive.

Based on the obtained spectra, it was found that incubation in Ringer's liquid caused only a slight change in the structure of the material. Regardless of the incubation, vibrations characteristic of structures such as N-H ($3300\text{--}3500\text{ cm}^{-1}$), N-H ($1550\text{--}1650\text{ cm}^{-1}$), C-C ($600\text{--}1500\text{ cm}^{-1}$) or the band corresponding to the carboxylate ion ($1554\text{--}1552\text{ cm}^{-1}$) were observed. Also, the band characteristic of the -CH_2 group ($2925\text{--}2923\text{ cm}^{-1}$) can be seen on

all obtained spectra of samples incubated in Ringer's liquid. Thus, it can be concluded that during incubation in Ringer's liquid, unreacted reactants were not completely eluted from the inside of the tested hydrogel. This may have been caused by the presence of divalent calcium ions in the Ringer's liquid, which contributes to the increase of the crosslinking density of the material hindering the elution of unreacted substances.

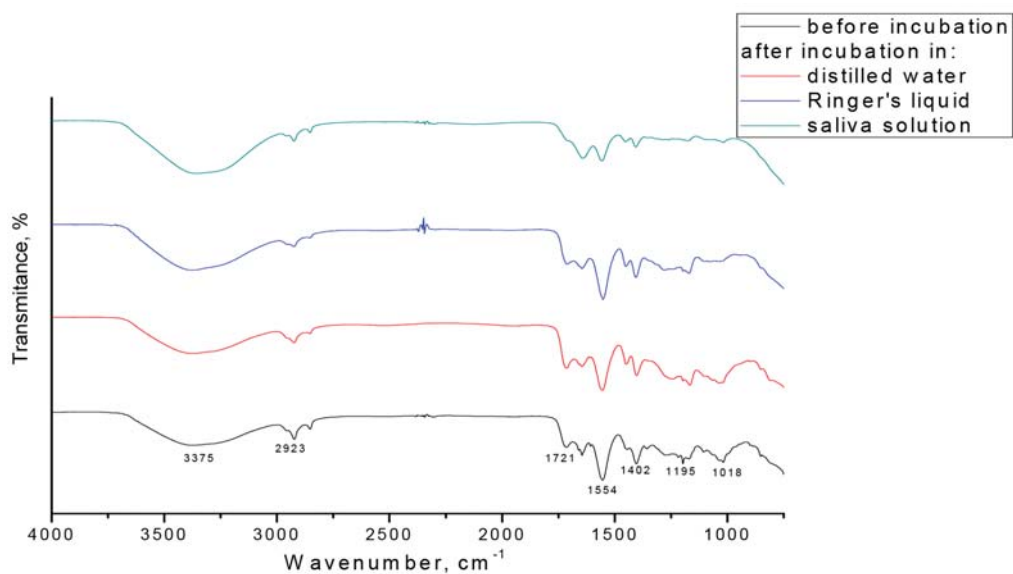


Fig. 8. IR spectra of samples with 1%wt. of xanthan gum

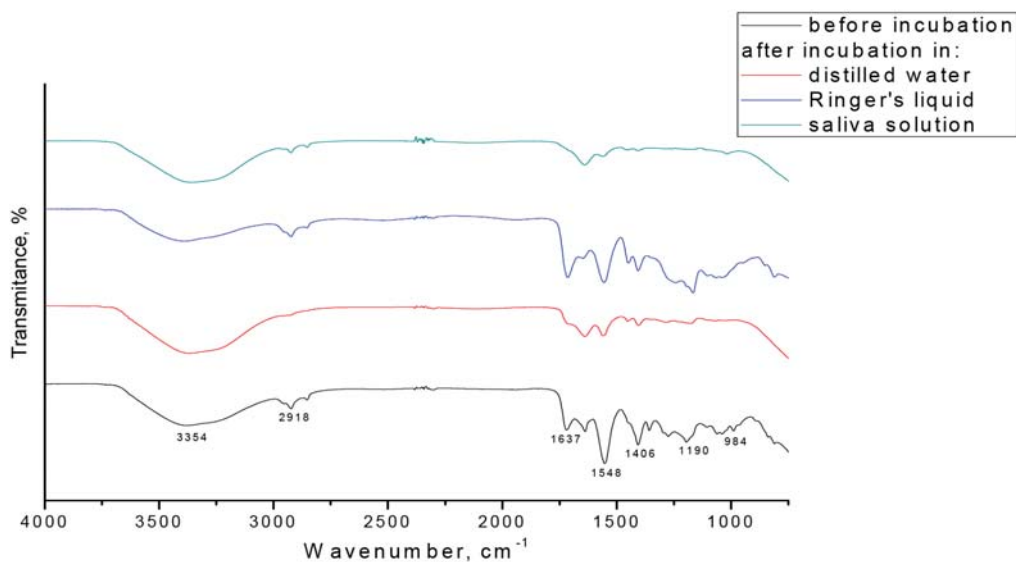


Fig. 9. IR spectra of samples with 7%wt. of xanthan gum

In the case of the spectra of the hydrogels after incubation in both distilled water and the solution of artificial saliva, there were no bands characteristic of the vibration of groups C-C and C-O. Vibrations of these bands were observed in the structure of hydrogels before incubation. Samples that were incubated in distilled water and in the solution of artificial saliva degraded to a greater extent. This applies both to the sample without additive, and of that containing 7%wt. xanthan gum in its matrix.

The sample containing 1%wt. of xanthan gum degraded the least. This is probably because this system is crosslinked most intensively, i.e. a suitable amount of xanthan gum improves the crosslinking of the tested structure, but this does not disrupt the system, as might happen in the case of 7%wt. of this additive.

5.4. Scanning electron microscopy (SEM)

In Figure 10, the surface of the synthesized hydrogels modified with xanthan gum is shown.

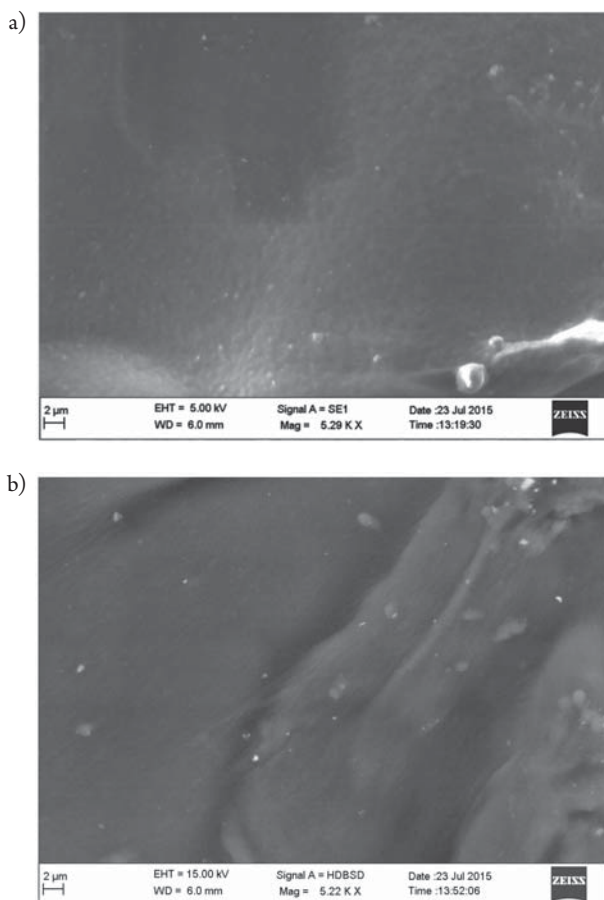


Fig. 10. SEM microphotographs of hydrogel: unmodified (a) and containing xanthan gum (b)

On the basis of the presented microphotographs, it can be seen that the surface of the unmodified hydrogel material is smooth and homogeneous. The surface morphology of the sample containing xanthan gum is similar to the surface morphology of the sample without xanthan gum. However, on the surface of the hydrogels modified with xanthan gum, some irregularities can be observed. The sample with the additive in its matrix is characterized by a slight porosity that could be the cause of the higher swelling ability of the modified hydrogels. These irregularities could cause a specific surface area of the tested materials and therefore this material has higher sorption capacity.

6. Conclusion

A series of hydrogels based on acrylic acid and chitosan and containing different amounts of xanthan gum in the polymer matrix was synthesized using UV radiation. The obtained materials were characterized by a very low swelling ability. Many factors have an impact on this property, including the composition of the absorbed liquid as well as the structure of the tested material. The highest swelling ratios were calculated in the case of distilled water due to the absence of ions, which cause the crosslinking density to increase and thereby reduce the swelling capacity. Also, it can be noticed that in some cases the presence of xanthan gum in the polymer matrix resulted in higher sorption capacity of the modified hydrogels. This could be the result of the slightly more heterogeneous and porous structure of the hydrogels containing xanthan gum, as can be observed in the SEM microphotographs. This causes a specific surface area and therefore the sample has higher sorption capacity.

The samples of the tested hydrogels did not cause any sudden pH changes of the selected fluid solutions in which they were submerged. This indicates the in vitro stability and biocompatibility of the synthesized hydrogels with body fluids. Also, on the basis of FT-IR spectroscopy, it was found that immersion of the hydrogel samples in distilled water and in artificial saliva solution causes the disappearance of bands specific to certain functional groups. Moreover, it was observed that the samples incubated in these solutions degraded to a greater extent.

To sum up, the features of the synthesized hydrogels modified with xanthan gum allow them to be considered for biomedical purposes. Therefore, in the near future more advanced research including further modifications or studies on cell lines are planned.

References

- [1] Tylińczak B., Pieliński K., *Charakterystyka matryc hydrożelowych zastosowania biomedyczne superabsorbentów polimerowych*, „Czasopismo Techniczne”, 1, 2007, 59–167.
- [2] Ahmed E.M., *Hydrogel: Preparation, characterization, and applications: A review*, “Journal of Advances Resarch”, 6, 2015, 105–121.

- [3] Hoffman A.S., *Hydrogels for biomedical applications*, "Advances Drug Delivery", 54, 2002, 3–12.
- [4] Rosiak J.M., Ulański P., Pajewski L.A., Yoshii F., Makuuchi K., *Radiation Formation of Hydrogels for Biomedical Purposes*, "Radiation Physics and Chemistry", 46, 1995, 161–168.
- [5] Gimpel K., Luliński P., Maciejewska D., *Wybrane technologie optymalizujące dostarczenie substancji czynnych w nowoczesnych postaciach leku*, "Wydawnictwo Farmaceutyczne", 3, 2009, 19–23.
- [6] Pluta J., Karolewicz B., *Hydrożele: właściwości i zastosowanie w technologii postaci leku. I. Charakterystyka hydrożeli*, "Polymer in Medicine", 34, 2004, 1–12.
- [7] Jones A., Vaughan D., *Hydrogel dressings in the management of a variety of wound types: A review*, "Journal Ortopedic Nursong", 9, 2005, 1–11.
- [8] Drury J.L., Mooney D.J., *Hydrogels for tissue engineering: scaffold design variables and applications. Review*, "Biomaterials", 24, 2003, 4337–4351.
- [9] Habibi H., Khosravi-Darani K., *Effective variables on production and structure of xanthan gum and its food applications: A review*, "Biocatalysis and Agricultural Biotechnology", 10, 2017, 130–140.
- [10] Ozdai M., Kurbanoglu E.B., *Valorisation of chicken feathers for xanthan gum production using Xanthomonas campestris MO-03*, "Journal of Genetic Engineering and Biotechnology", 2018, In Press, DOI: <https://doi.org/10.1016/j.jgeb.2018.07.005>. (access)
- [11] Jafari M., Koocheki A., Milani E., *Functional effects of xanthan gum on quality attributes and microstructure of extruded sorghum-wheat composite dough and bread*, "LWT", 89, 2018, 551–558.
- [12] Zhang R., Tao Y., Xu W., Xiao S., Du S., Zhou Y., Hasan A., *Rheological and controlled release properties of hydrogel based on mushroom hyperbranched polysaccharide and xanthan gum*, "International Journal of Biological Macromolecules", 2018, In Press, <https://doi.org/10.1016/j.ijbiomac.2018.09.008>. (access)
- [13] Xu J., He Z., Zeng M., Li B., Qin F., Wang L., Wu S., Chen J., *Effect of xanthan gum on the release of strawberry flavour in formulated soy beverage*, "Food Chemistry", 228, 2017, 595–601.
- [14] Kumar A., Rao K.M., Han S.S., *Application of xanthan gum as polysaccharide in tissue engineering*, "Carbohydrate Polymers", 180, 2018, 128–144.
- [15] Katzbauer B., *Properties and applications of xanthan gum*, "Polymer Degradation and Stability", 59, 1998, 81–84.
- [16] Garcia-Ochoa F., Santos V.E., Casas J.A., Gomze E., *Xanthan gum: production, recovery, and properties*, "Biotechnology Advances", 18, 2000, 549–579.
- [17] Tao Y., Zhang R., Xu W., Bai Z., Zhou Y., Zhao S., Xu Y., Yu D., *Rheological behavior and microstructure of release-controlled hydrogels based on xanthan gum crosslinked with sodium trimetaphosphate*, "Food Hydrocolloids", 52, 2016, 923–933.
- [18] Bueno V.B., Bentini R., Catalani L.H., Petri D.F.S., *Synthesis and swelling behavior of xanthan-based hydrogels*, "Carbohydrate Polymers", 92, 2013, 1091–1099.

- [19] Gils P.S., Ray D., Sahoo P.K., *Characteristics of xanthan gum-based biodegradable superporous hydrogel*, "International Journal of Biology Macromolecules", 45, 2009, 364–371.
- [20] Mittal H., Parashar V., Mishra S.B., Mishra A.K., *Fe₃O₄ MNPs and gum xanthan based hydrogels nanocomposites for the efficient capture of malachite green from aqueous solution*, "Chemical Engineering Journal", 255, 2014, 471–482.
- [21] Mittal H., Kumar V., Saruchi R.S.S., *Adsorption of methyl violet from aqueous solution using gum xanthan/Fe₃O₄ based nanocomposite hydrogel*, "International Journal Biology Macromolecules", 89, 2016, 1–11.
- [22] Liu Z., Yao P., *Injectable thermo-responsive hydrogel composed of xanthan gum and methylcellulose double networks with shear-thinning property*, "Carbohydrate Polymers", 132, 2015, 490–498.
- [23] Shalviri A., Liu Q., Abdekhodaie M.J., Wu X.Y., *Novel modified starch-xanthan gum hydrogels for controlled drug delivery: Synthesis and characterization*, "Carbohydrate Polymers", 79, 2010, 898–907.
- [24] Shekarforoush E., Ajallouueian F., Zeng G., Mendes A.C., Chronakis I.S., *Electrospun xanthan gum – chitosan nanofibers as delivery carrier of hydrophobic bioactives*, "Materials Letters", 228, 2018, 322–326.
- [25] Balasubramanian R., Kim S.S., Lee J., *Novel synergistic transparent κ- Carrageenan/ Xanthan gum/Gellan gum hydrogel film: Mechanical, thermal and water barrier properties*, "International Journal of Biological Macromolecules", 118(A), 2018, 561–568.

Andrzej Flaga  orcid.org/0000-0002-9143-2014

liwpk@windlab.pl

Renata Kłaput  orcid.org/0000-0002-2691-1937

Agnieszka Kocoń

Department of Civil Engineering, Institute of Structural Mechanics, Wind Engineering Laboratory, Cracow University of Technology

MODEL TESTS OF GLOBAL STABILITY OF TWO TYPES OF LIGHTNING PROTECTION MASTS UNDER WIND ACTION

MODELOWE TESTY GLOBALNEJ STATECZNOŚCI MASZTÓW

PRZY SILNYM WIETRZE

Abstract

The paper presents results of wind tunnel experiments of wind action on two free-standing lighting protection masts: cantilevered and tripod. Own similarity criteria concerning phenomenon of global stability loss were used in these tests. It was determined whether masts fulfill the requirements of overturning and shift global stability in range of base wind velocities adequate for Poland and different categories of terrain roughness according to the Eurocode [13]. Two possible forms of the loss of the global stability of lighting protection masts in strong wind were considered: overturning a mast and shifting of mast as a whole structures. The measurements were conducted for eight directions of wind attack, five positions of masts on the roof, two settings of the mast for tripod mast and one for cantilevered mast, two categories of terrain roughness. Conducted tests allowed to determine whether it is safe to locate tripod mast in all wind zones in Poland. Cantilevered mast can be located safely in I and II wind zone in Poland.

Keywords: wind tunnel test, masts, similarity criteria, global stability

Streszczenie

W artykule przedstawione zostały wyniki badań oddziaływania wiatru na dwa wolnostojące maszty odgromowe: pojedynczy i na trójnogu. W badaniach tych zastosowano własne kryteria podobieństwa dotyczące zjawiska globalnej utraty stateczności. Określono, czy maszty spełniają warunki stateczności globalnej na obrót i przesuw w zakresie prędkości bazowych wiatru adekwatnych dla Polski i różnych kategorii chropowatości terenu według Eurokodu [13]. Rozpatrywano dwie możliwe formy utraty globalnej stateczności masztów przy silnym wietrze: wywrócenie masztu (jako całości) i przesunięcie masztu (jako całości). Pomiar przeprowadzono dla ośmiu kierunków natarcia wiatru, pięciu położenia masztu na dachu, dwóch ustawień masztu na trójnogu i jednego ustawienia masztu pojedynczego, dwóch kategorii chropowatości terenu. Przeprowadzone badania pozwoliły na stwierdzenie, czy bezpiecznie jest ustawić maszt na trójnogu we wszystkich strefach wiatrowych w Polsce. Wykazano, że maszt pojedynczy może być ustawiony w I i II strefie wiatrowej w Polsce.

Słowa kluczowe: badania modelowe, maszty, kryteria podobieństwa, globalna stateczność

1. Introduction

Lightning protection plays an important role in protection against direct lightning strikes in buildings. The lightning protection mast is an ideal and low-cost solution to protect all types of objects from the destructive influence of atmospheric discharges. The free standing lightning protection mast is intended for lightning protection of devices on the roofs of buildings. It can find particular application on large surfaces – where we cannot afford on anchoring the structure to the roof. The self-supporting structure of the mast allows to avoid the perforation of the roofing material, so these masts can be used on flat roofs. In wind zones, it is necessary to predict increased load of the construction and apply appropriate measures to ensure its stability.

Wind action is one of the most important action in designing of free-standing lightning protection masts. Two types of lightning protection masts, i.e. cantilevered and tripod masts, were considered in this paper. Two possible forms of global stability loss of lightning protection masts in strong winds were tested and analysed: overturning and shifting of the masts as a whole structure. Investigations were conducted on models of the masts, so it had mainly practical aspect.

Problems of aerodynamics of such type of structures were considered in many publications e.g. [1–7] in the case of free-standing towers; and [8–12] in the case of guyed masts. Completely different aerodynamic and stability problems take place in the case of light small free-standing lightning protection towers placed on the building roofs, together with additional supporting ballast [13]. Taking it into account it is necessary to analyse this type of construction in the aspect of wind zones.

2. Considered research arrangements

Wind tunnel tests of the cantilevered and tripod free-standing masts of 4.0 m and 6.0m height (comp. Fig. 1) were carried out in a boundary layer wind tunnel of the Wind Engineering Laboratory at the Cracow University of Technology.

The basic dimensions of the wind tunnel working section are: 2.20 m (width), 1.40 m (height), 10.00m (length). Formation of the mean wind velocity profile and atmospheric turbulence takes place in the first part of the working section at the length of 6 m by use of respective turbulence elements: barriers, spires and blocks of respective geometry and mechanically controlled height. In the working section of the tunnel, there is a round rotational table of 2 m diameter which enables the change of a wind inflow direction on the examined model.

The masts models used in wind tunnel tests were made in a scale of 1:6.

The measurements were realized at the following measuring conditions and situations:

- ▶ Two terrain roughness category: suburban (III) and city (IV) according to Eurocode [13];
- ▶ Kind of roof: flat, covered with asphalt, rectangular (2:1), 15 meters height;

- ▶ Placement of masts on the roof according to Fig. 2.2; a distance between the building edge and mast vertical axis is 0.25 m in model scale (i.e. 1.5 meter in natural scale);
 - ▶ Different arrangement of tripod mast on the roof with respect to wind direction as in Fig. 2.3(b);
 - ▶ Eight directions of wind attack: N, NE, E, SE, S, SW, W, WN;
 - ▶ Range of wind velocities: 22–36.2 m/s (I–III wind zones according to Eurocode [13]).
- It gives 160 measuring cases for tripod mast and 80 for cantilevered mast.

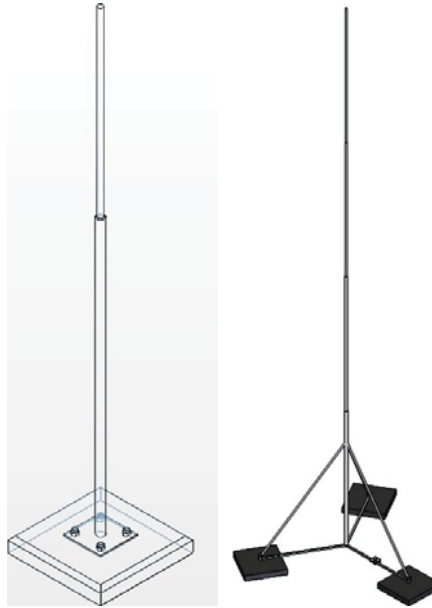


Fig. 1. View of cantilevered mast MA4-4m (a) and tripod mast MAT6-6m (b)

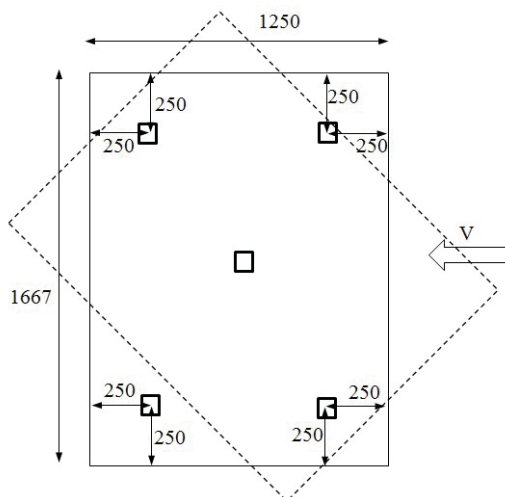


Fig. 2. Placement of masts on the roof in the model scale (dimensions in mm)

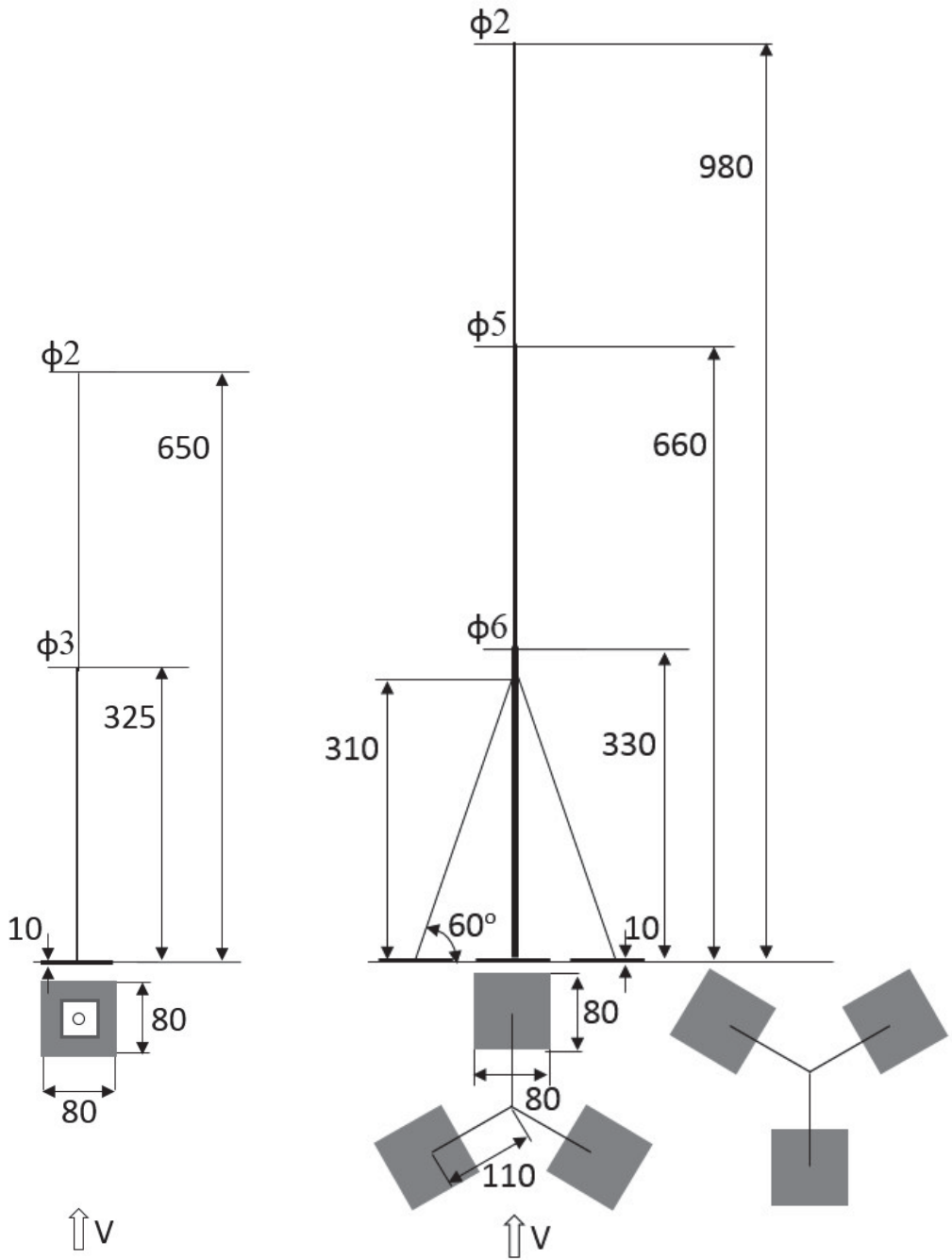


Fig. 3. Schematic drawing of masts settings of cantilevered MA4-4m (a) and tripod MAT6-6m (b) analyzed in the paper (dimensions in mm)

A view of the tested models in the wind tunnel working section is presented in Fig. 4.



Fig. 4. Models of the masts: cantilevered (a) and tripod (b) in the wind tunnel working section

3. Simulation of boundary layer

During the investigations the wind profile was formed with use of barrier, spires and blocks. Thermo-anemometers were used to measure mean as well as fluctuation part of wind velocity in 6 points located in the working section of the wind tunnel on the height from 10 cm to 100 cm above the floor level in front of the model. Using power-law form of wind profile and data obtained from measurements, the following wind profile parameters were obtained:

$$V(z) = V_{ref} \left(\frac{z}{z_{ref}} \right)^\alpha \quad (1)$$

$$z_{ref} = 1\text{m}, V_{ref} = 11.9 \frac{\text{m}}{\text{s}}, \alpha = 0.20$$

$$z_{ref} = 1\text{m}, V_{ref} = 12.3 \frac{\text{m}}{\text{s}}, \alpha = 0.24$$

where:

z_{ref} – reference height [m], α – exponent depend on terrain roughness, V_{ref} reference wind velocity.

Turbulence intensities were calculated according to the formula:

$$I_v(z) = \frac{\sigma(z)}{V(z)} \quad (2)$$

Obtained wind profile and turbulence intensity profile are shown in Fig. 5 (a) and (b). Red points mark values from wind tunnel tests and black line marks function determined by least-square regression. The turbulence intensity I_v on the reference level ($z_{ref} = 1\text{m}$) was 13% for III and 29% for IV category of terrain roughness.

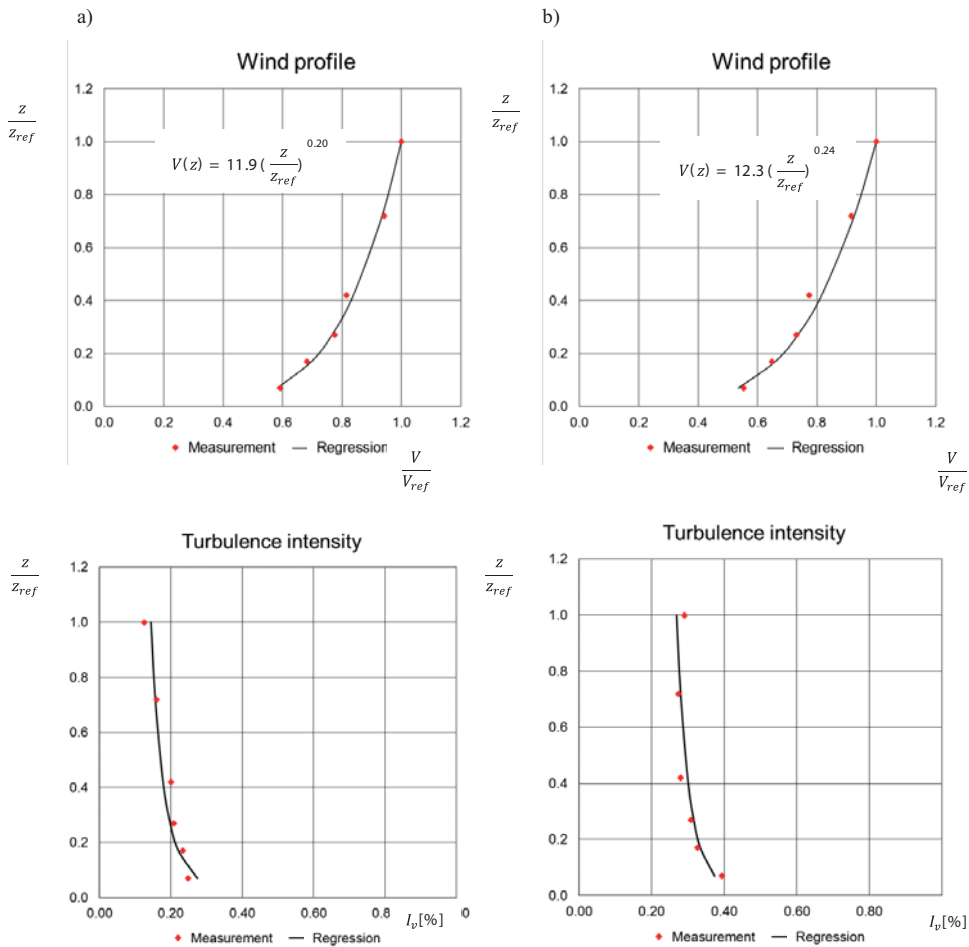


Fig. 5. Measurements results of wind characteristics: wind velocity profiles and turbulence intensity profiles for two categories of terrain roughness III (a) and IV (b)

4. Similarity criteria of global stability loss of lighting protection masts in strong wind

4.1. The definition of global stability loss

There are considered two possible forms of global stability loss of lighting protection masts in strong wind:

- ▶ Overturning a mast (as a whole structure);
- ▶ Shifting a mast (as a whole structure).

Critical velocities of wind when these phenomena occur will be designated respectively as: V^{roll} and V^{shift} .

4.2. Variable quantities and parameters affecting for the loss of global stability of lighting protection masts

- Parameters characterizing the incoming air

$$\{W\} = \{\rho, \nu, V_{ref}, V_H, V_b, \Theta, I_v\} \quad (3)$$

where:

- ρ – air mass density.
- ν – kinematic viscosity of atmospheric air,
- V_{ref} – reference wind velocity,
- V_H – wind velocity at the top of the model,
- V_b – basic wind velocity for the given localization according to Eurocode [13],
- Θ – angle of wind attack,
- I_v – turbulence intensity (fluctuation) of wind velocity.

Geometrical quantities characterizing the particular structural element of the mast and the spatial relationships between them

$$\{G\} = \{\{x_e, y_e, z_e; \alpha_e, \beta_e, \gamma_e; c_e; D_e, L_e\}; \{x, y, z; X, Y, Z\}; \{d_e, h_e\}, H, A\} \quad (4)$$

where:

- x_e, y_e, z_e – local Cartesian coordinates of the structural element,
- $\alpha_e, \beta_e, \gamma_e$ – angles defining spatial relationships between local system x_e, y_e, z_e and global system X, Y, Z ,
- c_e – curved contour coordinate of the cross-sectional element,
- D_e, L_e – characteristic transverse dimension and length of the structural element,
- x, y, z – coordinates of wind system which specifies the characteristics of air flow velocities,
- d_e, h_e – diameter and height of the mast foundation,
- H – height of the mast,
- A – projection area of the mast in the vertical plane.

- Mechanical quantities characterizing the mast

$$\{O\} = \{\rho_{me}, f, g, E\} \quad (5)$$

where:

- ρ_{me} – material density of the structural element.
- f – friction coefficient between the base of mast foundation and the upper surface of the roof.
- g – gravity acceleration.
- E – structure modulus of elasticity.

- Parameters characterizing wind effects on the mast system:

$$\{F\} = \{M_A, M_S, F_A, F_S\} \quad (6)$$

where:

M_A – aerodynamic rolling moment,

M_S – stabilizing moment due to mast weight,

F_A – aerodynamic sliding force,

F_S – aerodynamic stabilizing force due to friction.

4.3. The basic functional dependencies of the analyzed issue

Taking into account above sets of parameters, there can be determined functional relationships of the analyzed problem. Parameters of investigations depend on the following quantities sets:

$$M_A = f_{MA}(\{W\}, \{G\}) \quad (7)$$

$$M_S = f_{FA}(\{G\}, \{O\}) \quad (8)$$

$$F_A = f_{FA}(\{W\}, \{G\}) \quad (9)$$

$$F_S = f_{FR}(\{G\}, \{O\}) \quad (10)$$

In critical situation, which is the subject of these measurements, the global stability loss can appear in two cases:

- (1) Aerodynamic rolling moment is equal to stabilizing moment, hence the starting point of the mast overturning:

$$V^{roll} = V_H |_{M_A = M_S; V_{ref} \leq V_b}; \quad V^{roll} = f_{V^{roll}}(\{W\}, \{G\}, \{O\}) \quad (11)$$

- (2) Aerodynamic sliding force equals drag force, so the starting point of the mast shifting:

$$V^{shift} = V_H |_{F_A = F_S; V_{ref} \leq V_b}; \quad V^{shift} = f_{V^{shift}}(\{W\}, \{G\}, \{O\}) \quad (12)$$

4.4. Dimensional base of the issue and dimensionless quantities

Next step in dimensional analysis is to assume a dimensional base of the issue:

$$\{B\} = \{\rho, V_{ref}, H\} \quad (13)$$

Using above base and $\Pi\omega$ theorem (Buckingham's), the following dimensionless parameters can be obtained:

Dimensionless critical roll-over/ shift wind velocity	$\check{V}^{roll} = \frac{V^{roll}}{V_{ref}}, \check{V}^{shift} = \frac{V^{shift}}{V_{ref}}$
Reynolds number	$Re = \frac{V_{ref} H}{\nu}$
Dimensionless wind velocities	$\check{V}_b = \frac{V_b}{V_{ref}}, \check{V}_H = \frac{V_H}{V_{ref}}$
Dimensionless geometrical quantities	$\{\check{G}\} = \left\{ \frac{x_e}{H}, \frac{y_e}{H}, \frac{z_e}{H}, \frac{c_e}{H}, \frac{D_e}{H}, \frac{L_e}{H} \right\}; \left\{ \frac{x}{H}, \frac{y}{H}, \frac{z}{H}, \frac{X}{H}, \frac{Y}{H}, \frac{Z}{H} \right\};$ $\left\{ \frac{b_e}{H}, \frac{h_e}{H} \right\}; \left\{ \frac{A}{H^2} \right\}$
Dimensionless mass density	$\check{\rho}_{me} = \frac{\rho_{me}}{\rho}$
The Froude number (dimensionless acceleration):	$Fr = \frac{V_{ref}^2}{gH}$
The Cauchy number	$Ca = \frac{\rho V_{ref}^2}{E}$

4.5. The Π theorem of dimensional analysis and similarity criteria

The following dimensionless relationships can be presented on the base of theorem of dimensional analysis:

$$\check{V}^{roll} = \check{f}_{V^{roll}} \left(Re, \check{V}_b, \check{V}_H, \Theta, I_v, (\check{G}), \check{\rho}_{me}, Fr, Ca \right) \quad (14)$$

$$\check{V}^{shift} = \check{f}_{V^{shift}} \left(Re, \check{V}_b, \check{V}_H, \Theta, I_v, (\check{G}), \check{\rho}_{me}, f, Fr, Ca \right) \quad (15)$$

All dimensionless quantities appearing in these functional relationships are the similarity criteria of the analyzed issue.

4.6. Similarity scales in the model tests

The following denotations were adopted in further analysis: superscripts M and P relates to model and prototype (object in natural scale), respectively.

The assumptions assumed in model tests are as follows:

- (3) It is assumed one geometric scale k_H for all geometric quantities;
- (4) A model will be made of the same materials as the prototype, hence a scale of material similarity will be fulfilled ($k_{\rho_m} = 1.0$);
- (5) It is assumed one velocity scale k_v for all velocities;
- (6) Directions of the wind attack and turbulence intensity will be the same in model tests and in the nature;
- (7) The friction coefficient f in model tests will be similar with the coefficient in nature ;
- (8) Gravity acceleration in model tests and in nature is the same i.e. $k_H = 1.0$;
- (9) The fulfilment of similarity criteria for Froude number can be written as:

$$Fr^M = Fr^P; \left(\frac{V_{ref}^2}{H} \right)^M = \left(\frac{V_{ref}^2}{H} \right)^P \quad (16)$$

On the base of above, it can be defined wind velocity scale:

$$k_v = \sqrt{k_H} \quad (17)$$

The fulfilment of similarity criterion for Reynolds number can be presented as:

$$Re^M = Re^P; \left(\frac{V_{ref} H}{\nu} \right)^M = \left(\frac{V_{ref} H}{\nu} \right)^P \quad (18)$$

hence:

$$k_v = k_D \quad (19)$$

This criterion is inconsistent with the criterion of Froude number, but the range of wind velocity for both models and prototypes will be at a subcritical range of Re number. Hence, unfulfillment of Reynolds criterion does not result in essential mistakes in outcomes of tests in model and natural scales.

Fulfilment of Cauchy number similarity criterion leads to the relationships:

$$Ca^M = Ca^P; \left(\frac{\rho V_{ref}^2}{E} \right)^M = \left(\frac{\rho V_{ref}^2}{E} \right)^P \quad (20)$$

hence:

$$k_v = 1 \quad (21)$$

This criterion would be fulfilled only if $k_D = 1$ (with respect to Eq. (15)). In model tests a geometrical scale was assumed as $k_H = \frac{1}{6} = 0.17$. So, assuming Froude number as a basic similarity criterion, the velocity scale is: $k_v = 0.41$. It is impossible to fulfill criteria of Froude and Cauchy numbers simultaneously with adopted assumptions.

In problem of stability loss of such type of structures the most meaningful are structure gravity forces, so fulfilment of Froude number is essential. Vibrations of mast have secondary role in stability loss, hence unfulfillment of Cauchy number is not significant negligence in practical assessment of investigated phenomena.

Hence, respective basic velocities in model scale for I-st and III-rd wind zones can be determined:

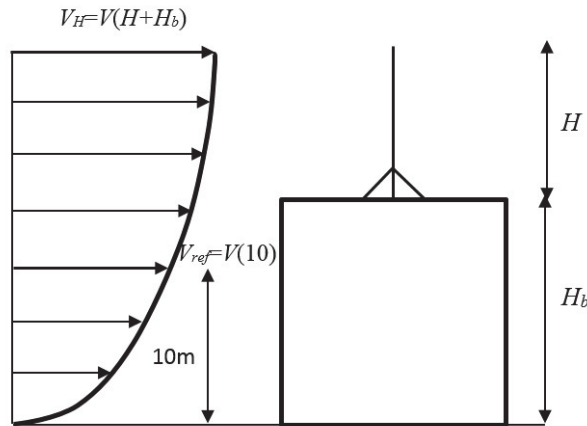
$$V_I^P = 22.0 \text{ m/s} \quad V_I^M = 8.98 \text{ m/s} \quad (22)$$

$$V_{III}^P = 36.2 \text{ m/s} \quad V_{III}^M = 14.78 \text{ m/s} \quad (23)$$

5. Quantities characterizing wind velocity field

5.1. Initial information

Relations for 10-minutes mean wind velocities are shown in Fig. 6.



$H_b=15\text{m}$ (height of the building), $H=4\text{m}/6\text{m}$ (height of cantilevered mast/tripod mast)

Fig. 6. Relations for mean 10-minutes mean wind velocities

According to Eurocode [13] vertical profile of mean wind velocity is described by:

$$V(z) = c_r(z) \cdot c_o(z) \cdot V_b \quad (24)$$

where:

$c_r(z)$ – terrain roughness coefficient dependent on terrain category roughness,

$c_o(z)$ – orography coefficient (assumed as 1.0),

V_b – base wind velocity dependent on the wind zone.

For two categories of terrain roughness (III, IV) the coefficient $c_r(z)$ can be given by:

Terrain category	$c_r(z)$
III	$0.81 \cdot \left(\frac{z}{10}\right)^{0.19}$; for $z=10\text{m}$ $c_r=0.81$
IV	$0.62 \cdot \left(\frac{z}{10}\right)^{0.24}$; for $z=10\text{m}$ $c_r=0.62$

Reference wind velocity is defined as follows:

Terrain category	$V_{ref} = V(z = 10\text{m})$
III	$0.81V_b$
IV	$0.62V_b$

Base velocities for I–III wind zones are assumed as:

$$V_{b,I} = 22.0\text{m/s}; V_{b,III} = 36.1\text{m/s} (30\text{m/s})$$

Therefore, in the natural scale there will be following velocities for respective masts:

Terrain category	$V(15+4) = V(19) - \text{cantilevered mast}$
III	20.13 m/s
IV	15.91 m/s

Terrain category	$V(15+6) = V(21) - \text{tripod mast}$
III	33.67 m/s
IV	26.74 m/s

5.2. Relations for stream velocity in model scale

Reference wind velocity in model scale can be written as follows:

Terrain category	$V_{ref}^M = V^M (z \cdot k_H = 1.67\text{m})$
III	$0.81V_b^M$
IV	$0.62V_b^M$

Taking into consideration the velocity scale, one may obtain model base velocity:

$$V_b^M = k_v \cdot V_b = 0.408V_b = \begin{cases} 8.98 \frac{\text{m}}{\text{s}} & \text{– I wind zone} \\ 14.73 \frac{\text{m}}{\text{s}} & \text{– III wind zone} \end{cases} \quad (25)$$

Velocities in model scale for both masts and different terrain categories are summarized below:

Terrain category	I wind zone	
	$H = 4m$	$H = 6m$
III	8.21 m/s	8.37 m/s
IV	6.49 m/s	6.65 m/s

Terrain category	III wind zone	
	$H = 4m$	$H = 6m$
III	13.48 m/s	13.74 m/s
IV	10.65 m/s	10.91 m/s

6. Results of experiments

A set of arrangements for cantilevered and tripod masts for different angles of wind attack is given in Tab. 1. In further analysis, the respective masts arrangements are identified by the prescribed numbers given in Fig. 7–12. These figures show wind velocity at which masts started losing its stability because of foundation one-side-lifting. It can be interpreted as V^{roll} . There are also marked dash lines of basic wind velocity for I and III wind zones. All presented velocities are in model scale.

Table 1. Set of arrangements for cantilevered and tripod masts

Angle of wind attack	Cantilevered mast			Tripod mast		
	1	2	3	1 (a/b)	2 (a/b)	3 (a/b)
N (0°)						
NW (45°)						
W (90°)						

SW (135°)						
S(180°)						
SE(225°)						
E(270°)						
NE(315°)						

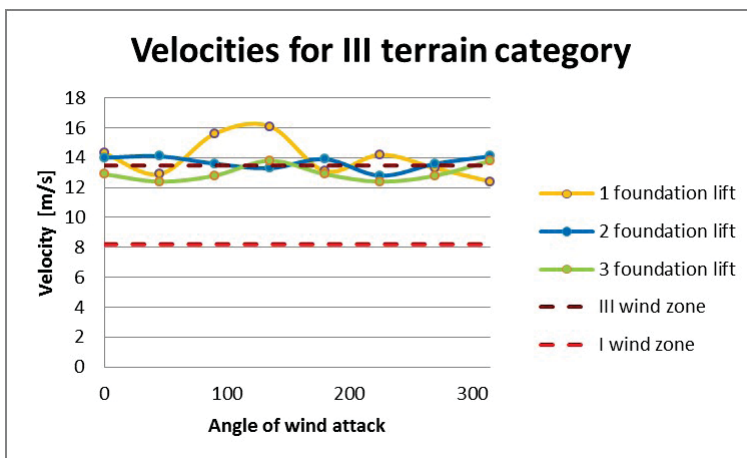


Fig. 7. The velocities of the windward foundations lift for cantilevered mast and III terrain category

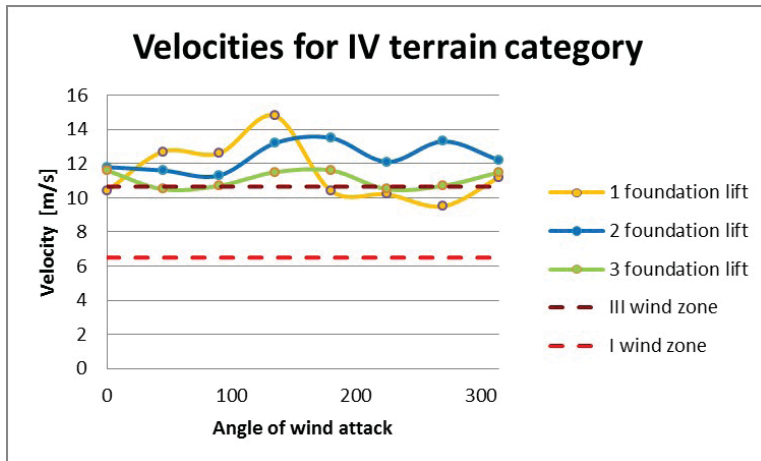


Fig. 8. The velocities of the windward foundations lift for cantilevered mast and IV terrain category

Two states of masts arrangements were distinguished from results of measurements: favourable and unfavourable. As favourable for cantilevered mast are considered these cases when wind velocity which caused one-side foundation lift was high, say generally greater than basic wind velocity in III wind zone. The opposition to them were unfavourable arrangements when stability loss appeared at wind velocities lower than basic wind velocity in III wind zone.

On the base of results given in Fig. 7, 8, the following conclusions concerning cantilevered mast can be drawn:

- ▶ The most unfavorable angles of wind attack for both terrain categories appear in the situations when mast is localized in the middle of the building roof;
- ▶ The most favorable angles of wind attack for both terrain categories appear in the situations when mast is localized on the leeward side of the building;
- ▶ The most unfavorable mast arrangement:
 - ▷ Terrain III: 3rd;
 - ▷ Terrain IV: 3rd (but for the angles of wind attack above 180 1st arrangements is the most unfavorable);
- ▶ The most favorable mast arrangement:
 - ▷ Terrain III: 1st;
 - ▷ Terrain IV: 1st (only for the angles of wind attack below 180), 2nd (whole range of the angles of wind attack);
- ▶ Windward foundations lift: for IV terrain category it appears much faster ($10 - 14 \frac{m}{s}$) than for III ($12 - 16 \frac{m}{s}$). In most cases foundation lift for III terrain category starts at the wind velocity below the velocity for III-rd wind zone. Regarding to IV terrain category, foundation lift starts generally at the velocity above the velocity for III-rd wind zone.

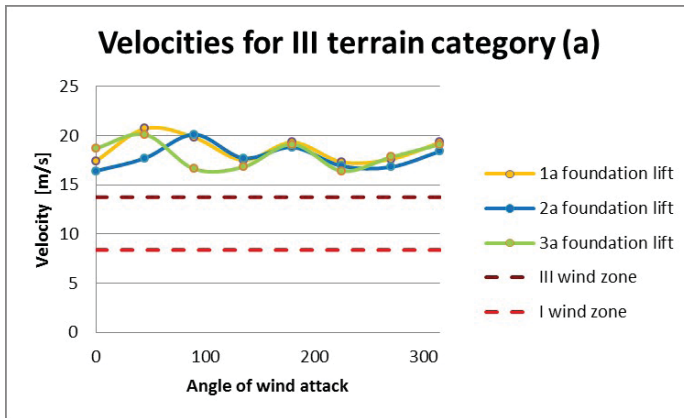


Fig. 9. The velocities of the windward foundations lift for tripod mast and III terrain category for arrangements 1a–3a

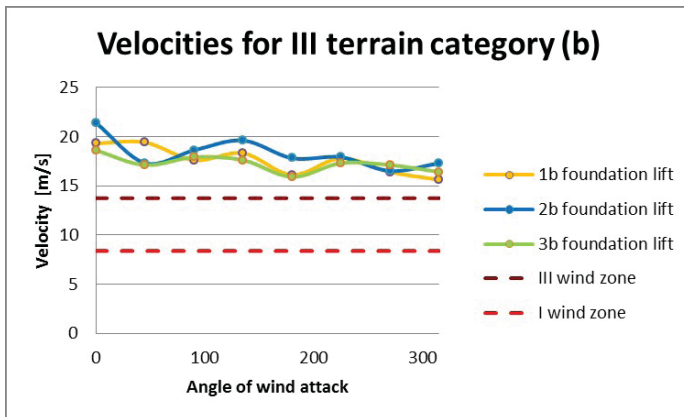


Fig. 10. The velocities of the windward foundations lift for tripod mast and IV terrain category for arrangements 1a–3a

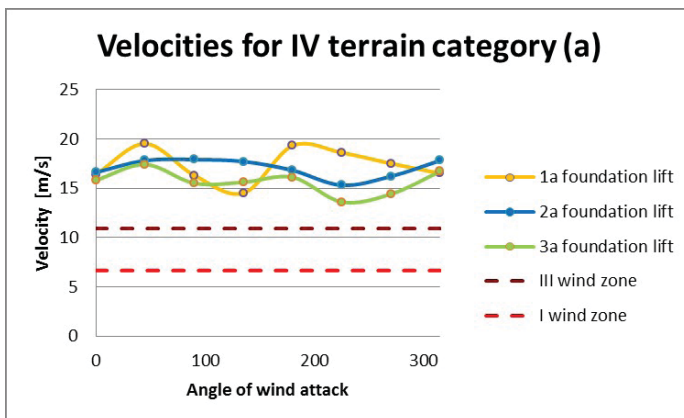


Fig. 11. The velocities of the windward foundations lift for tripod mast and III terrain category for arrangements 1b–3b

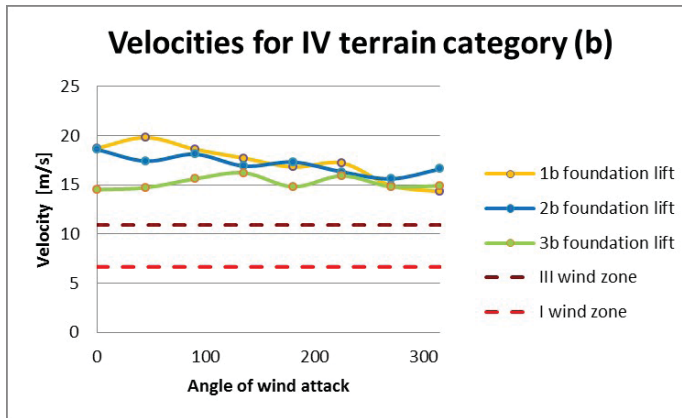


Fig. 12. The velocities of the windward foundations lift for tripod mast and IV terrain category for arrangements 1b–3b

As favourable for tripod mast are considered these cases when wind velocity which caused one-side foundation lift was greater than 1.22 basic wind velocity in III wind zone (16.7 m/s). The opposition to them were unfavourable arrangements when stability loss appeared at lower wind velocities. It was decided to use coefficient of 1.22 because the mass of tripod mast is higher, so consequences of its overturning would be greater than in the case of cantilevered mast.

On the base of results given in Fig. 9–12, the following conclusions concerning tripod mast can be formulated:

- ▶ The most unfavorable angles of wind attack for both terrain categories appear in the situations when one mast leg is on the windward side and two legs are on the leeward side of the mast; the most favorable are the opposite situations;
- ▶ The most unfavorable mast arrangement:
 - ▷ Terrain III: 3rd (a and b) ;
 - ▷ Terrain IV: 3rd (a and b);
- ▶ The most favorable mast arrangement:
 - ▷ Terrain III: 1st (a), 2nd (b);
 - ▷ Terrain IV: 1st (a) (beside the range of the angles of wind attack between 45–180° (a)), 2nd (a) in the range of the angles of wind attack 45–180°;
- ▶ Windward foundations lift: for IV terrain category it appears a little earlier (14–20 $\frac{m}{s}$) than for III (16–21 $\frac{m}{s}$). Phenomenon occurs above wind velocity for I-st and III-rd wind zone for both terrain categories. It starts at the wind velocity greater than the velocity for III-rd wind zone of for III terrain category and of 3 $\frac{m}{s}$ for IV terrain category.

The results of particular wind velocities obtained in these investigations are summarized in Tab. 2.

Table 2. Particular wind velocities obtained in wind tunnel tests for different mast arrangements and terrain categories for both types of masts

Type of mast	Terrain category	Masts arrangement	Velocity of windward foundations lift Vroll[m/s]	Velocity for I-st wind zone [m/s]	Velocity for III-rd wind zone [m/s]	
Cantilevered mast	B	1	12–16	8.2	13.5	
		2	13–14			
		3	12–14			
	C	1	9.5–15	6.5	10.7	
		2	11–14			
		3	10–12			
Tripod mast	B	1	a	17–20.5	8.4	13.7
			b	15–20		
		2	a	16–20		
			b	17–21		
		3	a	16–20		
			b	16–19		
	C	1	a	14.5–20	6.7	10.9
			b	14.5–20		
		2	a	15–18		
			b	15.5–19		
		3	a	13.5–17		
			b	15–16		

7. Final conclusions and remarks

7.1. General conclusions

Basing upon results of obtained velocities which cause windward foundations lift, the following two general conclusions can be drawn:

1. The cantilevered mast is safe with respect to global stability loss in the range of the base wind velocities up to 30 m/s.
2. The tripod mast is safe with respect to global stability loss in the range of the base wind velocities up to 36.2 m/s.

These conclusions concern nature scale. On the base of them one can state that it is safe to locate tripod mast in all wind zones in Poland. Cantilevered mast can be located safely in I and II wind zone in Poland. It should be pointed out that even if free-standing mast are located in appropriate wind zone, there will be still need to check local features of their localization place. One must take care of any circumstances which could increase wind action on masts and, in such cases, examine this instance separately.

7.2. Factor of safety for lightning protection masts design

During design of lightning protection masts there should be taken into consideration uncertainty of input data, mainly as: wind velocity field, location of the mast on the roof, geometry of the building or the roof, computational model of global stability loss of roll-over or shift type, possible measuring errors during wind tunnel tests, etc.

On the base of included in Eurocodes procedures and taking into account the fact that wind action on buildings depends, with enough assessment, on wind velocity square, it is recommended in this study to introduce safety factor for lightning protection masts design, defined as follows:

$$\gamma_m = \left(\frac{V_{H, \min}^{\text{model, roll}}}{V_{H, b}^{\text{model}}} \right)^2 \geq 1.5 \quad (26)$$

so:

$$\frac{V_{H, \min}^{\text{model, roll}}}{V_{H, b}^{\text{model}}} \geq 1.22$$

where:

$V_{H, \min}^{\text{model, roll}}$ – the smallest velocity of lightning mast roll-over in model tests measured at the top height of the mast;

$V_{H, b}^{\text{model}}$ – base wind velocity in model tests measured at the top height of the mast.

This work was sponsored by ZERPOL, Witkowo.

References

- [1] Schafer B.L., Banks R.W., Holmes J.D., *Wind-induced oscillations of a free-standing tower*, Proceedings of the 8th Conference on the 'In situ Behaviour of Structures', Bacu, Romania, 20–22 September 1990.
- [2] Holmes J.D., Glass T., Cook B.W., Schafer B.L., Banks R.W., *The dynamic characteristics and response to wind of tall free-standing lattice towers*, Proceedings of the 2nd National Structural Engineering Conference, Adelaide, Australia, 3–5 October 1990.
- [3] Holmes J.D., Schafer B.L., Banks R.W., *Wind-induced vibration of a large broadcasting tower*, Journal of Wind Engineering and Industrial Aerodynamics, 43/1-3, 1992, 2101–2109.
- [4] Haritos N., Stevens L.K., *The assessment of response of tall free-standing towers to along-wind loading*, Journal of Wind Engineering and Industrial Aerodynamics, 14, 1983, 331–344.
- [5] Ahmad M.B., Pande P.K., Krishna P., *Self-supporting towers under wind loads*, ASCE, J. Struct. Eng, 110, 1984, 370–384.
- [6] Mackey S., Ko P.K.L., Lam L.C.H., *Response of a 180-ft latticed tower to high winds*, Proceedings of the 2nd USA-Japan Research Seminar on Wind Effects on Structures, Kyoto, Japan, September 1974, University Press of Hawaii, 1976.

- [7] Célio F., Carril J., Nicholas I., Reyolando M.L.R.F., *Experimental study of the wind forces on rectangular latticed communication towers with antennas*, Journal of Wind Engineering and Industrial Aerodynamics, 91/8, 2003, 100F–1022.
- [8] Gioffrè M., Gusella V., Materazzi A.L., Venanzi I., *Removable guyed mast for mobile phone networks, wind load modeling and structural response*, Journal of Wind Engineering and Industrial Aerodynamics, May 2004, Vol. 92, Issue 6, 463–475.
- [9] Peil U., Nölle H., *Guyed masts under wind load*, Journal of Wind Engineering and Industrial Aerodynamics, 1992, Vol. 43, Issues 1–3, 2129–2140.
- [10] Holmes J.D., Banks R.W., Roberts G., *Drag and aerodynamic interference on microwave dish antennas and their supporting towers*, Journal of Wind Engineering and Industrial Aerodynamics, December 1993, Vol. 50, 263–269.
- [11] Gioffrè M., Gusella V., Materazzi A.L., Venanzi I., *Removable guyed mast for mobile phone networks, wind load modeling and structural response*, Journal of Wind Engineering and Industrial Aerodynamics, May 2004, Vol. 92, Issue 6, 463–475.
- [12] Jiang W.Q., Wang Z.Q., McClure G., Wang G.I., Geng J.D., *Accurate modelling of joint effects in lattice transmission towers*, Engineering Structures 33(2011) 1818–1827.
- [13] PN-EN 1991-1-4 Eurocode 1: Actions on structures. Part 1–4: General actions. Wind actions; PKN, November, 2008.

Agnieszka Makowska  orcid.org/0000-0003-1067-7130

amakow@pk.edu.pl

Faculty of Civil Engineering, Cracow University of Technology

VERIFICATION OF THE SPLINE METHOD AND ITS APPLICATION TO CURVILINEAR OBJECTS

WERYFIKACJA METODY SPLAJN I JEJ ZASTOSOWANIE DO OBIEKTÓW KRZYWOLINIOWYCH

Abstract

Two methods of interpolation are presented in this article: interpolation with the help of orthogonal polynomials and interpolation on a cubic spline path (with the help of glued-together functions). Two procedures have been written by the author: *WielOrt* and *Splajn*. A comparative analysis of these procedures was conducted by four verification methods that have been created by the author. The examples of verification were chosen so as to make it possible to compare the created by author interpolating function $f(x)$ and the known function $g(x)$. Graphics, numerical procedures and examples were prepared in the *Mathematica* program.

Keywords: interpolating, spline, orthogonal polynomial

Streszczenie

W artykule omówione zostały dwie metody interpolacji: interpolacja za pomocą wielomianów ortogonalnych oraz interpolacja za pomocą sześciennych funkcji sklepanych (splajnów). Napisane zostały przez autora dwie procedury *WielOrt* and *Splajn*. Przeprowadzono wnikliwą analizę porównawczą tych procedur, przykłady zostały dobrane tak, aby możliwe było porównanie utworzonej przez autora funkcji interpolacyjnej $f(x)$ ze znaną funkcją interpolowaną $g(x)$. Weryfikację przeprowadzono czterema opracowanymi przez autora metodami. Grafika, procedury numeryczne i przykłady zostały przygotowane w programie: *Mathematica*.

Słowa kluczowe: krzywoliniowość, interpolacja, splajn, wielomian ortogonalny

1. INTRODUCTION

The aim of this scientific description is to prove the correctness *The Spline Method* created by author, by verifying the basic *Splajn* procedure of this method, using four verification methods in addition created by the author, and demonstrating the universal *Splajn* procedure application for curved objects without classification in the fields of science. The procedures apply to creating objects with a free, irregular soft form. The package of computational procedures called *The Spline Method* contains the following procedures: *Splajn*, *Splajn1*, *SplajnDluku*, *SplajnObjPow*, *SplajnDzialkaSciana*, *SplajnRurociag*, *Splajn 4G* combine components graphic and mathematical.

The *Splajn* procedure is the basic procedure of this method. It is necessary to perform a thorough verification of the method. Four verification methods were created for thoroughly checking the calculation results of the *Splajn* procedure.

The basis calculating is the exact calculation of the length, the surface area and the volume. The exact calculation of the surface and the volume of rectilinear forms is easy; however, in the case of curvilinear objects, it is harder.

An attempt to describe curvilinear objects made with the application of cubic spline interpolation is presented in this paper.

2. SOME METHODS OF INTERPOLATION

Based on literature [5], the basic concepts of the spline theory are presented in this section.

2.1. Elementary theory of cubic spline

We have got $n+1$ points in the interval $\langle a, b \rangle : a = x_0, x_1, \dots, x_n = b$, we call nodes and value function $y = f(x)$ in the points: $f(x_0) = y_0, f(x_1), \dots, f(x_n)$. Pair (x_k, y_k) we call nodal points. We seek estimate values of function $f(x)$ class C^2 between nodes using third degree polynomial for $x \in \langle x_{i-1}, x_i \rangle$.

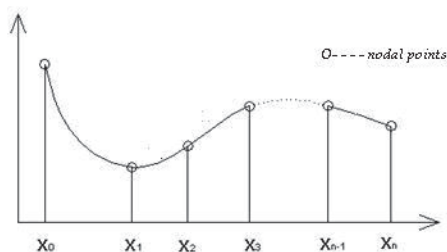


Fig. 1. Illustrative figure (prepared by author)

Let us mark M_i as second derivative in point x_i :

$$M_i = f''(x_i) \quad \text{for } i=0,1,2,\dots,n \quad (1)$$

from definition of function $f(x)$, it is known that $f''(x)$ is the continuous function in interval $\langle a, b \rangle$ and linear for $x \in \langle x_{i-1}, x_i \rangle$, so:

$$f''(x_i) = M_{i-1} \frac{x_i - x}{h_i} + M_i \frac{x - x_{i-1}}{h_i} \quad (2)$$

where: $x \in (x_{i-1}, x)$, $h = x_i - x_{i-1}$.

Integrating twice (2) and evaluating the constants of integration:

$$f'(x) = -M_{i-1} \frac{(x_i - x)^2}{2h_i} + M_i \frac{(x - x_{i-1})^2}{2h_i} + A_i \quad (3)$$

$$f(x) = M_{i-1} \frac{(x_i - x)^3}{6h_i} + M_i \frac{(x - x_{i-1})^3}{6h_i} + A_i (x - x_{i-1}) + B_i \quad (4)$$

where:

$$B_i = y_{i-1} - M_{i-1} \frac{h_i^2}{6}; \quad A_i = \frac{y_i - y_{i-1}}{h_i} - \frac{h_i}{6} (M_i - M_{i-1}) \quad (5)$$

Using the condition of continuity of function and the first derivative by algebraic conversion we obtain linear system of equations:

$$\mu_i M_{i-1} + 2M_i + \lambda_i M_{i+1} = d_i \quad \text{for } i=1, 2, \dots, n-1 \quad (6)$$

where:

$$\lambda_i = \frac{h_{i+1}}{h_i + h_{i+1}}, \quad \mu_i = 1 - \lambda_i$$

$$d_i = \frac{6}{h_i + h_{i+1}} \left(\frac{y_{i+1} - y_i}{h_{i+1}} - \frac{y_i - y_{i-1}}{h_i} \right) \quad \text{for } i=1, 2, \dots, n-1$$

System (6) has $n-1$ equations and $n+1$ unknown coefficients: M_0, M_1, \dots, M_n .

We often accept two additional conditions:

$M_0 = 0, M_n = 0$ ($f''(x_0) = 0, f''(x_n) = 0$: Natural cubic Spline), system (6) can be written in matrix form as:

$$\begin{bmatrix} 2 & \lambda_1 & 0 & \dots & 0 \\ \mu_2 & 2 & \lambda_2 & \dots & 0 \\ \dots & \dots & \dots & \dots & \dots \\ 0 & \dots & \mu_{n-2} & 2 & \lambda_{n-2} \\ 0 & \dots & \dots & \mu_{n-1} & 2 \end{bmatrix} \begin{bmatrix} M_1 \\ M_2 \\ \dots \\ M_{n-2} \\ M_{n-1} \end{bmatrix} = \begin{bmatrix} d_1 \\ d_2 \\ \dots \\ d_{n-2} \\ d_{n-1} \end{bmatrix} \quad (7)$$

This is a special three-diagonal linear system;

on this Fortuna Z. [5] finished the description of the method, the author continues to solve the system of equations and describes the function $f(x)$

The elementary method of solving system (6):

System (6) in the explicit form is:

$$\begin{aligned} \mu_1 M_0 + 2M_1 + \lambda_1 M_2 &= d_1 \\ \mu_2 M_1 + 2M_2 + \lambda_2 M_3 &= d_2 \\ \mu_3 M_2 + 2M_3 + \lambda_3 M_4 &= d_3 \\ &\dots\dots\dots \\ \mu_{n-1} M_{n-2} + 2M_{n-1} + \lambda_{n-1} M_n &= d_{n-1} \end{aligned} \tag{8}$$

where:

$$\begin{aligned} \lambda_i &= \frac{h_{i+1}}{h_i + h_{i+1}}, \mu_i = 1 - \lambda_i \quad i = 1, 2, \dots, n-1 \\ h_i &= x_i - x_{i-1}, \quad i = 1, 2, \dots, n. \end{aligned}$$

Let us mark u_i and z_i as:

$$u_i = 2 - \frac{\mu_i}{u_{i-1}} \lambda_{i-1} \quad \text{for } i = 2, 3, \dots, n-1 \tag{9}$$

$$z_i = d_i - \frac{\mu_i}{u_{i-1}} z_{i-1} \quad \text{for } i = 2, 3, \dots, n-1 \tag{10}$$

and for symmetrical expression:

$$u_1 = 2, z_1 = d_1 \tag{11}$$

From the first equation of system (8), we obtain:

$$2M_1 + \lambda_1 M_2 = d_1$$

from (9), (10), (11) :

$$M_1 = \frac{z_1 - \lambda_1 M_2}{u_1}$$

we calculate the next coefficients:

$$M_2 = \frac{z_2 - \lambda_2 M_3}{u_2}; \quad M_3 = \frac{z_3 - \lambda_3 M_4}{u_3}$$

by recurrence and algebraic conversion, we obtain:

$$M_k = \frac{z_k - \lambda_k M_{k+1}}{u_k} \quad \text{for } k = 1, \dots, n-2 \tag{12}$$

Using principle of mathematical induction easily proof the truth of this expression (12)

From the last equation of system (8), by algebraic conversion we obtain:

$$M_{n-1} = \frac{z_{n-1}}{u_{n-1}}$$

after calculation coefficients M_k , we construct function $f(x)$:

$$f(x) = \begin{cases} f_0 & \text{dla } \langle x_0, x_1 \rangle \\ f_1 & \text{dla } \langle x_1, x_2 \rangle \\ \dots & \dots \\ f_{n-1} & \text{dla } \langle x_{n-1}, x_n \rangle \end{cases}$$

where f_i is the right side of expression (4).

We define Heaviside's function [11]:

$$H(x-a) = \begin{cases} 0 & \text{dla } x < a \\ 1 & \text{dla } x \geq a, \end{cases}$$

and then function $f(x)$ is expressed as one formula:

$$f(x) = \sum_{i=1}^{n-1} f_i \cdot [H(x-x_{i-1}) - H(x-x_i)] + f_n \cdot H(x-x_{n-1}) \quad (13)$$

Now we can write in any programming language the basic procedure called *Splajn*, in which the input parameters are data points: (x_0, y_0) , (x_1, y_1) , ..., (x_n, y_n) and at the output of that procedure, we will get function $f(x)$.

```
Splajn[lista_] :=
Module[{ }, Clear[n, m, u, z, d, X, Y, h, a, b, λ, μ, f];
n = Length[lista] - 1; m[0] = 0; m[n] = 0; u[1] = 2;
z[1] = d[1]; For[i = 0, i ≤ n, i++, X[i] = lista[[i + 1, 1]];
Y[i] = lista[[i + 1, 2]]];
For[i = 1, i ≤ n, i++, h[i] = X[i] - X[i - 1];
b[i] = Y[i - 1] - m[i - 1] * h[i]^2 / 6;
a[i] = (Y[i] - Y[i - 1]) / h[i] - h[i] * (m[i] - m[i - 1]) / 6;
f[x_, i_] := m[i - 1] * (X[i] - x)^3 / (6 * h[i]) +
m[i] * (x - X[i - 1])^3 / (6 * h[i]) + a[i] * (x - X[i - 1]) +
b[i]]; For[i = 1, i ≤ n - 1, i++,
λ[i] = h[i + 1] / (h[i] + h[i + 1]); μ[i] = 1 - λ[i];
d[i] = 6 / (h[i] + h[i + 1]) *
((Y[i + 1] - Y[i]) / h[i + 1] - (Y[i] - Y[i - 1]) / h[i])];
For[i = 2, i ≤ n - 1, i++, u[i] = 2 - μ[i] / u[i - 1] * λ[i - 1];
z[i] = d[i] - μ[i] / u[i - 1] * z[i - 1]];
m[n - 1] = z[n - 1] / u[n - 1];
For[i = n - 2, i ≥ 1, i--,
m[i] = (z[i] - λ[i] * m[i + 1]) / u[i]]; H[x_] := 0 /; x < 0;
H[x_] := 1 /; x ≥ 0;
f[x_] := Sum[f[x, i] * (H[x - X[i - 1]] - H[x - X[i]]) +
f[x, n] * H[x - X[n - 1]], {i, 1, n - 1}];
```

Fig. 2. The *Splajn* procedure written in the *Mathematica* program (prepared by author)

Mathematica notebooks ensure a sophisticated environment for creating technical documents, particularly if we want to merge your work with existing material in *TeX*.

We export the notebook from the *Mathematica* program to *Microsoft Word* as a *Metafile* or *Bitmap*.

2.2. Natural Spline

The *NaturalSpline* procedure written by John H. Mathews, Ph.D. Emeritus Prof. of Mathematics, California State University, Fullerton has an open source code on the internet site [13].

The *NaturalSpline* procedure solves (7) based on the tridiagonal linear system theory.

```

In[1]:= NaturalSpline1[XY0_] := Module[{XY = XY0},
  Differences := Module[{k}, n = Length[XY] - 1; X = Transpose[XY][[1]];
  Y = Transpose[XY][[2]];
  h = d = Table[0, {n}]; m = Table[0, {n + 1}]; a = b = c = v = Table[0, {n - 1}];
  s = Table[0, {n}, {4}]; h[[1]] = X[[2]] - X[[1]];
  d[[1]] = (Y[[2]] - Y[[1]]) / h[[1]]; For[k = 2, k <= n, k++, h[[k]] = X[[k+1]] - X[[k]];
  d[[k]] = (Y[[k+1]] - Y[[k]]) / h[[k]]; a[[k-1]] = h[[k]]; b[[k-1]] = 2 (h[[k-1]] + h[[k]]); c[[k-1]] = h[[k]];
  v[[k-1]] = 6 (d[[k]] - d[[k-1]])];];
  TriDiagonal := Module[{k, t}, m[[1]] = 0; m[[n+1]] = 0;
  For[k = 2, k <= n - 1, k++, t = (a[[k-1]]) / b[[k-1]]; b[[k]] = b[[k-1]] - t c[[k-1]];
  v[[k]] = v[[k-1]] - t v[[k-1]];]; m[[n]] = (v[[n-1]] - c[[n-1]] m[[n-1]]) / b[[n-1]];];
  ComputeCoeff := Module[{k}, For[k = 1, k <= n, k++, s[[k, 1]] = Y[[k]];
  s[[k, 2]] = d[[k]] - (1/6) h[[k]] (2 m[[k]] + m[[k+1]]); s[[k, 3]] = (m[[k]]) / 2; s[[k, 4]] = (m[[k+1]] - m[[k]]) / (6 h[[k]])];];
  CS[t_] := Module[{j}, For[j = 1, j <= n, j++, If[X[[j]] <= t && t < X[[j+1]], k = j];];
  If[t < X[[1]], k = 1]; If[X[[n+1]] <= t, k = n]; w = t - X[[k]];
  Return[({s[[k, 4]] w + s[[k, 3]} w + s[[k, 2]} w + s[[k, 1]})];];
  Differences; TriDiagonal; ComputeCoeff];

```

Fig. 3. The *NaturalSpline* procedure written in the *Mathematica* program (source: Internet [13])

2.3. Basic concept of orthogonal polynomials

We will now discuss interpolation using orthogonal polynomials [5]

Def. Sequence of function $\varphi_0(x), \varphi_1(x), \dots, \varphi_n(x)$ is called the orthogonal on the set of points x_0, \dots, x_n if:

$$\sum_{i=0}^n \varphi_j(x_i) \varphi_k(x_i) = 0 \text{ dla } j \neq k$$

The following relations can be proven [5]:

$$\varphi_{j+1}(x) = (x - \alpha_{j+1}) \varphi_j(x) - \beta_j \varphi_{j-1}(x) \quad \text{dla } j = 0, 1, \dots, n$$

$$\varphi_0(x) = 1, \quad \varphi_{-1}(x) = 0,$$

where the constants α_{j+1} i β_j are defined by the formulas:

$$\beta_j = \frac{\sum_{i=0}^n \varphi_j^2(x_i)}{\sum_{i=0}^n \varphi_{j-1}^2(x_i)}, \quad \alpha_{j+1} = \frac{\sum_{i=0}^n x_i \varphi_j^2(x_i)}{\sum_{i=0}^n \varphi_j^2(x_i)}$$

finally the function $f(x)$ has the form:

$$f(x) = \sum_{k=0}^n b_k \varphi_k(x)$$

where:

$$b_k = \frac{C_k}{S_k}, \quad C_k = \sum_{i=1}^n y_i \phi_k(x_i), \quad S_k = \sum_{i=0}^n \phi_k^2(x_i)$$

We can now write the procedure called *WielOrt1* where the input parameters are data points: $(x_0, y_0), (x_1, y_1), \dots, (x_n, y_n)$ and at the output of that procedure, we obtain the function $f(x)$ and its graph. The basic procedures we extend by adding the graphical and numerical instructions.

```
ln[1]= << WielOrt1
ln[2]= daneW = {{1, 3}, {2, 4}, {4, 6}, {5, 8}, {6, 4}};
ln[3]= WielOrt1[daneW]
```

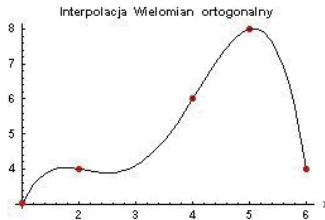


Fig. 4. The execution procedure *WielOrt1* [*daneW*] (prepared by author)

3. VERIFICATION AND SELECTION OF THE INTERPOLATION METHODS

We will verify three procedures: *WielOrt1*, *Splajn1* and *NaturalSpline1* and the corresponding them errors we call as: *errW*, *errS* and *errNS*. A comparative analysis of these procedures was conducted by four author-prepared methods. The examples of verification were chosen in such a manner that it was possible to compare the identified interpolating function $f(x)$ created by author with the known function $g(x)$.

As a measure of the method error, the following expression was applied.

$$err = \frac{1}{b-a} \int_a^b [f(x) - g(x)]^2 dx$$

3.1. FTV – Function Table Verification Method

In the first method verification of procedure the nodal points were introduced as the coordinates from the formula of the function.

Example: The *LosujDane* procedure generating random input data was written for the verification of all procedures.

```

LosujDane[a_, b_, ld_] :=
Module[{}, dane = Table[Random[Real, {a, b}], {ld}];
<<SortujListe; dane1 = SortujListe[dane];
dane2 = Table[{dane1[[i]], g[dane1[[i]]]}, {i, 1, ld}];
Print["dane2=", dane2];
Print["dane2 wygenerowane losowo dla funkcji g[x]= ",
g[x], " z przedziału < ", a, ", ", b, ">"]

g[x_] = e^-x^2; LosujDane[-2, 2, 10]

dane2={{-1.73421, 0.0494152}, {-0.918374, 0.430241},
{-0.905201, 0.440701}, {-0.649464, 0.655863},
{-0.496048, 0.781873}, {0.444826, 0.820476},
{0.494177, 0.783323}, {0.573378, 0.719814},
{0.953878, 0.402571}, {1.87649, 0.0295634}}

dane2 wygenerowane losowo dla funkcji g[x]=
e^-x^2 z przedziału <-2,2>

```

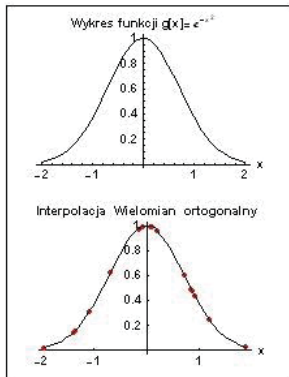
Fig. 5. Random values of the function $g(x)$ (prepared by author)

The comparison graphs of procedures for [dane2] with function $g[x]$

```

In[6]:= Show[GraphicsArray[{{(wykres), (wielort)}}, Frame -> True];

```



```

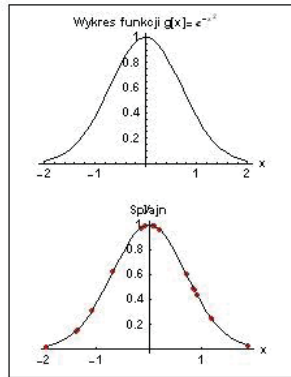
In[7]:= Print["errW=",  $\frac{1}{X[n] - X[0]}$  -> NIntegrate[(f[x] - g[x])^2, {x, X[0], X[n]}]]
errW=2.4299 x 10^-7

```

Fig. 6. The graphs and $errW$ for the *WielOrt1* procedure [dane2] (prepared by author)

For the *Splajn1* procedure we have:

```
In[10]= Show[GraphicsArray[{{wykres}, {splajn}}, Frame -> True];
```

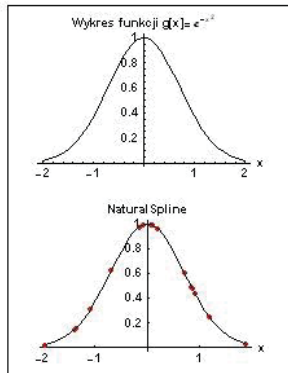


```
In[11]= Print["errS=",  $\frac{1}{X[n] - X[0]}$  * NIntegrate[(f[x] - g[x])^2, {x, X[0], X[n]}]]
errS=8.0908 * 10^{-6}
```

Fig. 7. The graphs and *errS* for the *Splajn[dane2]* procedure (prepared by author)

and for the *NaturalSpline1* procedure, we obtained:

```
In[14]= Show[GraphicsArray[{{wykres}, {NS}}, Frame -> True];
```



```
In[15]= Print["errNS=",  $\frac{1}{X[[n+1]] - X[[1]]}$  * NIntegrate[(CS[x] - g[x])^2, {x, X[[1]], X[[n+1]]}]]
errNS=8.0908 * 10^{-6}
```

Fig. 8. Comparison of graphs and *errNS* for the *NaturalSpline1[dane2]* procedure (prepared by author)

Other functions have been tested (the data determined) and the results are shown in Table 1:

Table 1. Statement of errors for the FTV method

Function; Interval	Splajn	NaturalSpline	WielOrt
e^{-x^2} ; <-2,2> random	$8.0908 \cdot 10^{-6}$	$8.0908 \cdot 10^{-6}$	$2.4299 \cdot 10^{-7}$
$(1-x^2)^{1/2}$; <0,1>	0.000454465	0.000454465	0.000117545
$\text{Sin}(x)$; <0,1.5>	$3.79068 \cdot 10^{-6}$	$3.79068 \cdot 10^{-6}$	$2.74535 \cdot 10^{-15}$
x^2 for $x < 1$ $2 - x$ for $x \geq 1$; <0,2>	0.00027388	0.00027388	0.0915378

The *WielOrt* procedure proved to be a better approximation than the *Splajn* and *Natural Splajn* procedures. In the last row, where the function is defined by two formulae, the *WielOrt* procedure gives an error that is approximately 300 times larger.

3.2. CCM – Coordinate Conversion Verification Method

For the second verification method, the *ZmienWsp* procedure was written; this transforms the graphic coordinates drawn to real coordinates. After delivering real coordinates to suitable procedures, we can formulate an analytical description of the curve and perform a verification.

Example:

In publications or websites we can often see a graph of function, but we do not know the value of this function. We will show in three steps, how we can find a formula of function.

Step. 1: We import a scanned graph of function to the *Mathematica* program

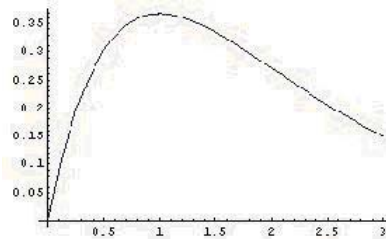


Fig. 9. Graph of unknown function $g[x]$ (prepared by author)

Step. 2: We read and write coordinates of the screen with Fig. 9:

```
In[3]:= WspEkran = {{26.2174, 17.6913}, {39.9499, 73.6776}, {66.3586, 142.34},
{105.443, 171.918}, {147.697, 161.354}, {183.613, 138.115},
{236.43, 104.312}, {278.684, 81.072}};
```

Fig. 10. Coordinates of screen function $g[x]$

We read the coordinates: (xB, yB) of the beginning at the graph and coordinates: (xE, yE) of the end at the graph and corresponding them coordinates of screen are: (xBs, yBs) and (xEs, yEs) . Now we create a procedure that uses linear interpolation and will transform all screen coordinates into real coordinates.

```

In[4]:= ZmienWsp[lista_] := Module[{xB = 0, yB = 0, xE = 3, yE = 0.15}, nz = Length[lista];
xB = 26.2174; yB = 17.6913; xES = 278.684; yES = 81.072;
fz[t_, u_] :=  $\frac{u[u] - u[t]}{u[t] - u[t]}$  - (t - u) + u;
ux = {xB, xB, xES, xE}; uy = {yB, yB, yES, yE};
WspReal := Table[{fz[WspEkran[[i, 1]], ux], fz[WspEkran[[i, 2]], uy]}, {i, nz}];
Print["WspReal=", WspReal]

```

Fig. 11. The *ZmienWsp* procedure (prepared by author)

After executing this procedure with *WspEkran* parameters, we obtain real coordinates:

```

In[5]:= ZmienWsp[WspEkran]
WspReal = {{0., 0.}, {0.16318, 0.1325},
{0.476988, 0.295}, {0.941419, 0.365001}, {1.44351, 0.339999},
{1.87029, 0.285001}, {2.49791, 0.205001}, {3., 0.15}}

```

Fig. 12. Real coordinates

Step. 3: We execute procedure *WielOrt1*[*WspReal*] and we obtain function $f[x]$ and its graph:

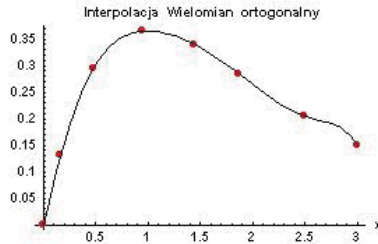


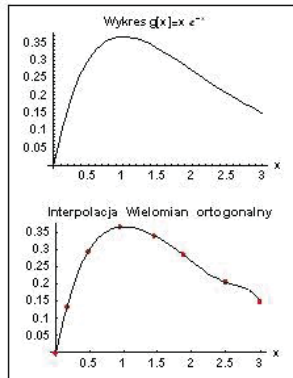
Fig. 13. Graph interpolation function (prepared by author)

Comparing Figs 13&9, we see that they are similar, author knows function: $g[x] = x e^{-x}$; therefore, we can find the estimated error using this method:

```

In[21]:= Show[GraphicsArray[{{funkcja}, {wielort}}, Frame -> True]:

```



```

In[22]:= Print["errW =",  $\frac{1}{3} * NIntegrate[(f[x] - g[x])^2, \{x, 0, 3\}]$ ]

```

```

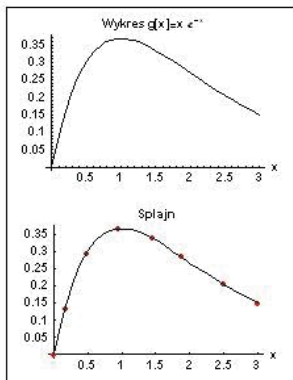
errW = 0.0000356719

```

Fig. 14. Comparison graph function $g[x]$ with *WielOrt1* and the *errW* (prepared by author)

Following analogical steps we have for *Splajn1* and *NaturalSpline1*.

```
In[25]:= Show[GraphicsArray[{{funkcja}, {splajn}}], Frame -> True];
```



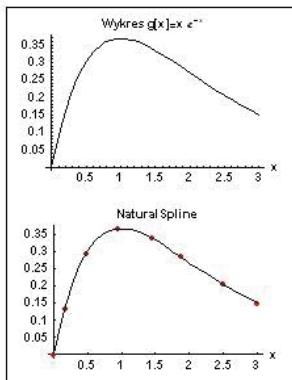
```
Print["errS =",  $\frac{1}{3} * NIntegrate[(f[x] - g[x])^2, \{x, 0, 3\}]$ ]
```

```
errS = 5.71099 × 10-6
```

Fig. 15. Comparison graph function with *Splajn1* and the *errS* (prepared by author)

The compatibility is near perfect.

```
In[17]:= Show[GraphicsArray[{{funkcja}, {NS}}], Frame -> True];
```



```
In[18]:= Print["errNS =",  $\frac{1}{3} * NIntegrate[(CS[x] - g[x])^2, \{x, 0, 3\}]$ ]
```

```
errNS = 5.71099 × 10-6
```

Fig. 16. Comparison graph function with *NaturalSpline1* and *errNS* (prepared by author)

In the same way, other functions have been tested and the results are presented in Table 2.

Table 2. Statement of errors for the CCM method

Function; Interval	Splajn1	NaturalSpline1	WielOrt1
$x e^{-x}; <0,3>$	$5.71099 \cdot 10^{-6}$	$5.71099 \cdot 10^{-6}$	$35.6798 \cdot 10^{-6}$
$\text{Cos}(x); <0,1>$	0.000323145	0.000323145	0.00046454
$x \text{Log}(x); <0.01,1.2>$	0.0940895	0.0940895	0.0941283

The *NaturalSpline* and *Splajn* procedures give identical errors. Based on Tables 1&2, the *WielOrt1* procedure is rejected.

3.3. ALC – The Arc Length of the Curve -Verification Method

The first derivative is necessary for example to calculate the arc length of curve, the surface area, and to evaluate the line integral $\int_C \phi$, where C is the given curve.

Adding formulas (2) and (3) to the *Spline1* procedure, we obtain the new procedure: *SplajnPoch2*.

We now create the *SplajnPoch2* procedure. After executing *SplajnPoch2[dane]*, we obtain: $\text{dane} = \{\{-3, 9\}, \{-1, 1\}\{0, 0.7\}, \{1, 1\}, \{2, 4\}, \{3, 3\}\}$.

Example:

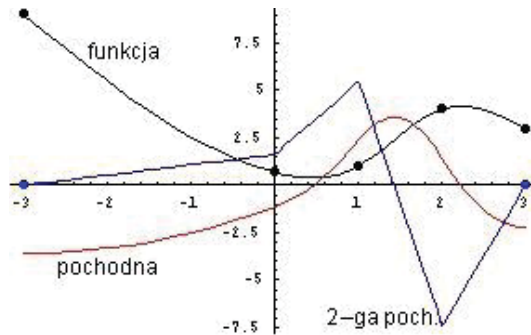


Fig. 17. Graph of the function, first and second derivatives (prepared by author)

The *NaturalSpline* procedure does not exactly calculate the first derivative, it requires a large modification to the inside of the procedure; however, this is not the purpose of this paper.

Now we can execute the *SplajnDluku* procedure and compare the result with the length calculated from the formula. Nodal points we get randomly.

```

In[1]:= << LosujDane
In[2]:= g[x_] = a^-x^2; LosujDane[-2, 2, 10]
dane2 = {{-1.78761, 0.0409445}, {-1.57445, 0.0838358},
{-1.16189, 0.25924}, {-0.0579191, 0.996651},
{0.0575693, 0.996691}, {0.411726, 0.844071}, {0.761755, 0.559747},
{0.820024, 0.510462}, {1.64186, 0.067495}, {1.87224, 0.0300384}}
dane2 wygenerowane losowo dla funkcji g[x] = e^-x^2 z przedziału <-2,2>
In[3]:= << SplajnDluku
In[4]:= SplajnDluku[dane2]

```

```

długość łuku=4.21745
In[5]:= Print["dł.ze wzoru=", NIntegrate[√(1 + g'[x]^2), {x, X[0], X[n]}]]
dł.ze wzoru=4.2191
In[6]:= {X[0], X[n]}
Out[6]:= {-1.78761, 1.87224}

```

Fig. 18. Comparison of arc length the curve (prepared by author)

Table 3. Comparison of the method results ALC

Function;Interval	SplajnDluku	Formuła
e^{-x^2} ; <-1.78761;1.87224> Random	4.21745	4.2191
$x e^{-x}$; <0,3>	3.10959	3.10978
$\text{Sin}[x]$; <0,6>	7.24261	7.24256

The compatibility is near perfect.

3.4. RO – Real Object Verification Method

The next method of verification was based on a real object for example, element of the bell, the heart of Zygmunt's Bell. The calculated weight of the heart was compared with its known weight.

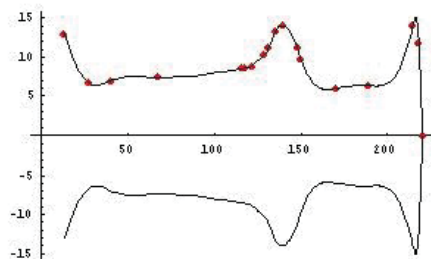
Example:

In the *SplajnObjPow* procedure, the input parameters are data points, the output parameters is graphs and volume of the solid formed by the revolution of the curve $y = f[x]$ around x -axis.

```

In[1]:= << Graphics`SurfaceOfRevolution`
In[2]:= << SplajnObjPow
In[3]:= DaneSerce = {{13.26, 12.94}, {27.37, 6.72}, {40, 6.98},
  {66.98, 7.41}, {115.51, 8.54}, {117, 8.58},
  {121.7, 8.9}, {128.4, 10.29}, {131.1, 11.18},
  {135, 13.25}, {139.11, 14}, {147.98, 11.18},
  {150, 9.82}, {170.37, 6}, {188.85, 6.36}, {214.54, 14},
  {218, 11.86}, {220, 0}};
In[4]:= SplajnObjPow[DaneSerce]

```



Pole pow. bryły obrotowej =11704.6[cm²]

Objętość bryły obrotowej =47371.7[cm³]

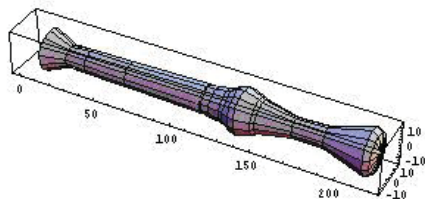


Fig. 19. Result of the *SplajnObjPow[DaneSerce]* procedure (prepared by author)

These calculations were made without taking into account the handle of the bell heart. The mass of the handle was estimated to be 20 kg. The density of the heart is unknown; there are some admixtures: phosphorus, sulphur, etc. According to the accessible data, the heart mass is about 350 kg. The specific mass of the heart is estimated as 7.7 g/cm³.

Calculated mass of the bell: $\text{mass} = 47371.7[\text{cm}^3] \cdot 7.7[\text{g}/\text{cm}^3] / 1000 + 20[\text{kg}] = 384.762[\text{kg}]$, error of calculations = $(384.762 - 350) / 350 \cdot 100\% = 9.9\%$

Inference:

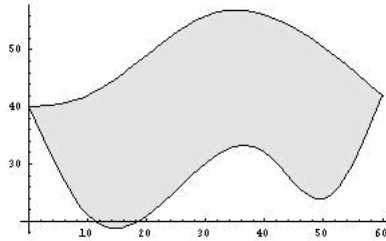
The verification of three procedures was performed: *Spline* Fig. 2., *NaturalSpline* Fig. 3. and *WielOrt* (Table 1&2). Procedure *Wielort1* (large calculated error), procedure *NaturalSpline* (it is not calculate the derivative) were rejected.

4. APPLICATIONS OF SPLINE METHOD

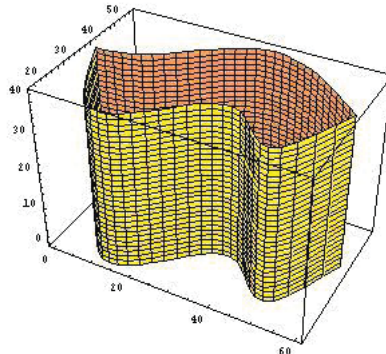
Example:

```
ln[3]:= dane1 = {{0, 40}, {10, 42}, {30, 56}, {60, 42}};
       dane2 = {{0, 40}, {10, 21}, {40, 32}, {50, 24}, {60, 42}};

ln[4]:= SplajnDzialkaSciana[dane1, dane2, 40, 0.2]
```



pole działki=1305.3 [m²]
 obwód działki=161.347 [m]



pole powierzchni ściany = 6453.87 m²
 objętość ściany = 1290.77 m³

Fig. 20. Result of the *SplajnDzialkaSciana*[dane1, dane2, 40, 0.2] procedure (prepared by author)

Example:

Let us consider a more general case in which the contour C of area D is described by the union of four curves: $C = C_1 \cup C_2 \cup C_3 \cup C_4$. We calculate the area field as a line integral:

$$\frac{1}{2} \oint_C x dy - y dx$$

where the direction of circulation of contour C is chosen as anticlockwise.

We create a new procedure: *Splajn4G*. After execution of this procedure with parameters $[daneXd]$, $[daneXg]$, $[daneYl]$, $[daneYp]$, we obtain:

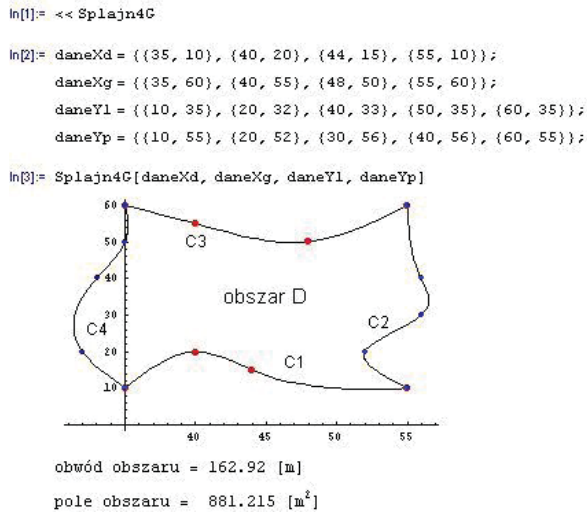


Fig. 21. Perimeter and area of the region D (prepared by author)

Example:

We construct the circle with centre on a curve. The circle moves after curve in normal plane to curve. In the *SplajnRurociag* procedure, the input parameter are: the data points and the radius of the pipeline; the output parameters are: the graph and the surface area of the pipeline.

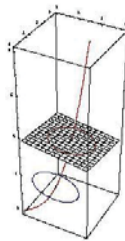


Fig. 22. Illustrative figure (prepared by author)

```

In[1]:= dane = {{0, 6}, {1, 2}, {3, 5}, {7, 9}, {8, 6}, {15, 8}, {17, 5}};

In[2]:= SplajnRurociag[lista_, promien_] :=
Module[{}, << SplajnPR; SplajnPR[lista, promien]; << PowRurkowa;
Show[PowRurkowa[{x, f[x], 0}, {x, X[0], X[n], 40}, 9, 0.7]]];

In[3]:= SplajnRurociag[dane, 0.7]

Pole powierzchni rurkowej=148.399

```

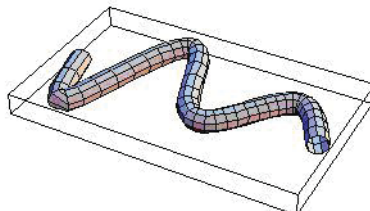


Fig. 23. Surface area of the pipeline (prepared by author)

5. APPLICATION IN MECHANICS

Example:

Moment of inertia relative to the x axis of the heart

Changing to cylindrical coordinates, we have:

$$B_x = \mu \int_0^{2\pi} d\varphi \int_{x[0]}^{x[n]} dx \int_0^{f[x]} \rho^3 d\rho$$

and finally:

$$B_x = \frac{1}{2} \pi \mu \int_{x[0]}^{x[n]} f^4[x] dx$$

```
In[4]:= Print["B_x=",  $\frac{1}{2} \pi \mu$  NIntegrate[f[x]^4, {x, X[0], X[n]}], " [g*cm^2]"]
```

```
B_x=2.3285 x 10^6  $\mu$  [g*cm^2]
```

Fig. 24. Moment of inertia relative to the x axis of the heart (prepared by author)

6. CONCLUSION

On the basis of studies of the available literature, the author has developed their own method for calculating parameters curvilinear objects: *The Spline Method*.

The four verification methods presented in this study show the correctness of the calculations. With the support of the prepared procedures, can be calculate the needed parameters in the *Mathematica* program. *The Spline Method* enables the precise definition of the necessary object parameters and their optimisation. This creates the possibility of modelling objects and enables quick parameter changes in the design process. This can be implemented in various fields of science, also beyond the framework of engineering. In summary, the state of knowledge and research presented in this article, supplemented with the results of our own research, still needs to be developed through further research that will enable the systematic development of *The Spline Method* and the calculation of the parameters of curvilinear objects.

References

- [1] Ahlberg J.H., Nilson E.N., Walsh J.L., *The Theory of Splines and Their Applications*, Academic press New York–London 1967.
- [2] Drwal G., Grzymkowski R., Kapusta A., Słota D., *Mathematica 4*, Wydawnictwo Pracowni Komputerowej J. Skalmierskiego, Gliwice 2000.
- [3] Drwal G., Grzymkowski R., Kapusta A., Słota D., *Mathematica programowanie i zastosowania*, Wydawnictwo Pracowni Komputerowej J. Skalmierskiego, Gliwice 1995.
- [4] Dryja M., Jankowscy J. i M., *Przegląd metod i algorytmów numerycznych Część 2*, WNT, Warszawa 1998.
- [5] Fortuna Z., Macukow D., Wasowski J., *Metody numeryczne*, WNT, Warszawa, 2005.
- [6] Grzymkowski R., Kapusta A., Słota D., *Mathematica narzędzie inżyniera*, Wydawnictwo Pracowni Komputerowej J. Skalmierskiego, Gliwice 1994.
- [7] Jankowscy J. i M., *Przegląd metod i algorytmów numerycznych Część 1*, WNT, Warszawa 1998.
- [8] Knott Gary D., *Interpolating Cubic Splines*, Birkhauser, Boston Basel, Berlin 2000.
- [9] Leja F., *Rachunek różniczkowy i całkowy ze wstępem do równań różniczkowych*, WNT, Warszawa 2008.
- [10] Makowska A., *Metoda kalkulacji kosztów krzywoliniowych obiektów budowlanych z zastosowaniem współczynnika trudności*, praca doktorska, Kraków 2009.
- [11] Trajdos-Wróbel T., *Matematyka dla Inżynierów*, WNT, Warszawa 1974.
- [12] Wolfram S., *The Mathematica book*, Cambridge University Press, 1999.
- [13] <http://mathfaculty.fullerton.edu/mathews/n2003/CubicSplinesMod.html> (access: 15.04.2018).

Grzegorz Kacprzak  orcid.org/0000-0003-0731-5761

g.kacprzak@il.pw.edu.pl

Seweryn Bodus  orcid.org/0000-0002-7813-1073

seweryn.bodus@warbud.pl

Warsaw University of Technology, WARBUD S.A, Poland

THE MODELLING OF EXCAVATION PROTECTION IN A HIGHLY URBANISED ENVIRONMENT

MODELOWANIE ZABEZPIECZENIA WYKOPU W ŚRODOWISKU MOCNO ZURBANIZOWANYM

Abstract

This paper presents the problem of excavation protection in an 'infill' construction environment surrounded by neighbouring buildings. It presents a method of protecting deep excavation within a palisade of CFA reinforced piles in casing pipes. The 3D model was built using the ZSoil program, in which the neighbouring buildings were taken into account in modelling. The HSs model of the ground base was adopted. Based on the ITB instruction [1], an analysis was performed on the impact of building expansion on neighbouring buildings; this analysis provides guidelines for the first two phases, i.e. the phase of shoring construction and the phase of actual excavation. The study also takes into account the phase of building serviceability. After including the results of numerical analysis in the estimation of the displacements of neighbouring structures, the results were compared with indicative displacement limit values of displacement building structures.

Keywords: deep excavation, neighbourhood building, palisade, cased CFA piles, HSs model

Streszczenie

W pracy przedstawiono problem zabezpieczenia wykopu realizowanego w środowisku „plombowym”, w otoczeniu sąsiedniej zabudowy. Opisano metodologię zabezpieczenia głębokiego wykopu w technologii palisady z pali zbrojonych CFA w rurach osłonowych. Zbudowany został model 3D w programie geotechnicznym ZSoil, w którym uwzględniono sąsiednią zabudowę. Przyjęto ośrodek gruntowy modelu HSs. Na podstawie instrukcji ITB [1] przeprowadzono analizę wpływu rozbudowy obiektu na sąsiednią zabudowę, która podaje wytyczne dla pierwszych dwóch faz, tj. fazy wykonania obudowy i wykonania wykopu. W opracowaniu uwzględniono dodatkowo fazę eksploatacji obiektu. Włączając uzyskane rezultaty analizy numerycznej do oszacowania przemieszczeń na sąsiednie obiekty, wyniki porównano z orientacyjnymi wartościami granicznymi przemieszczeń konstrukcji budynków.

Słowa kluczowe: głęboki wykop, sąsiednia zabudowa, palisada, rurowane pale CFA, model HSs

1. INTRODUCTION

Nowadays, one can colloquially say that ‘we build wherever we can’, meaning that it is becoming more and more difficult to find a space to erect buildings in an attractive location and at a good price. We use every possible piece of land, especially in city centres, which costs more and more, and often use neighbouring areas.

With reference to the investment that is the subject of this paper carried out in reality, this paper describes the spatial 3D model of the designed building with the protection of a deep excavation for palisade technology with CFA reinforcement piles in casing pipes. Based on the ITB instruction [1], an analysis was performed of the impact of building extension on neighbouring buildings. To estimate the vertical displacements of neighbouring buildings, numerical results from the second and the third phase were taken into account; this is from the phase at the stage of excavation protection and the phase at the building serviceability stage.

2. SOIL AND WATER CONDITIONS

The area under consideration is located within the Polish Uplands in the sub-province of the Śląsko-Krakowska Upland. In terms of morphology, the research area lies on the Katowice Plateau. The plot under investigation is located in the depression of the Rawa river whose regulated bed is located approximately 300 m north of the area in question. The investment area is surrounded by high-density development located in the city centre. The location of the structure is shown in Fig. 1.



Fig. 1. Location of the building

In the ground of the investigated area there are both, man-made soils and native soils with diverse lithology and consistency. Therefore, based on the available soil engineering report, the most unfavourable layer layout was chosen for modelling; this is shown in the V-V' cross section in Fig. 2. The red line marks the bottom of the foundation slab of the designed building, which is 4.5 m below the ground surface. The groundwater level is situated at a depth of approx. 6.2 m below the ground surface.

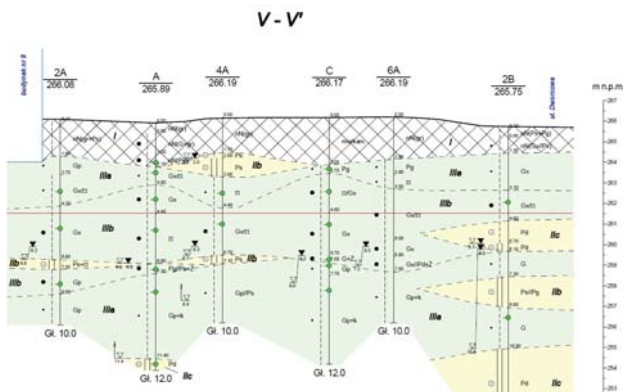


Fig. 2. Geological engineering cross section V-V'

Below the existing layer of man-made soil with a thickness of around 2.0 m, there are clays interbedded with sandy lenses. The clays may be generally characterised as being stiff and firm. The thicknesses of the medium and fine sand lenses range between 0.5 and 1.5 m. The values of geotechnical parameters of individual soil layers are presented in Table 1.

Table 1. Values of the geotechnical parameters of the soil models

Parameters of Coulomb-Mohr model													
Layer I													
E	ν	Φ	Ψ	c	K_0								
[M Pa]	[-]	[°]	[°]	[-]	[M Pa]								
27.8	0.25	20	0	10	0.66								
Layer III _b													
46.7	0.25	15	0	18	0.74								
Parameters of HSs model													
Layer II _b													
E_{ur}^{ref}	σ_{ref}	ν_{ur}	m	σ_L	E_0^{ref}	$\gamma_{0.7}$	E_{50}^{ref}	Φ	Ψ	c'	E_{ocd}	σ_{ocd}^{ref}	K_0^{NC}
[M Pa]	[k Pa]	[-]	[-]	[k Pa]	[M Pa]	[-]	[M Pa]	[°]	[°]	[-]	[M Pa]	[k Pa]	[-]
180	100	0.25	0.4	10	440	$4 \cdot 10^{-5}$	60	31.5	6	0	60	200	0.48
Layer II _c													
180	100	0.25	0.4	10	540	$1 \cdot 10^{-4}$	60	31.5	6	0	60	200	0.48
Layer III _a													
49.5	100	0.25	0.65	10	440	$2 \cdot 10^{-5}$	16.5	35	4.5	0	16.5	232.56	0.43

3. 3D NUMERICAL MODEL IN ZSOIL

This part of the paper presents an example of the modelling of the designed building and the excavation protection for the project which encompasses the addition of floors to the existing building and the addition of a 7-level building (with one underground floor) in the place of a demolished house. The buildings will be independently and structurally connected with each other. The designed building will be based on a piled-raft foundation (CPRF [2]) utilising the CFA reinforced pile palisade technology. In the foundation slab are local thickenings at the column locations. There are also, two pits in the left area of the slab. Figure 3 shows the geometry of a piled-raft system with the locations of columns, the shafts of the building and a system of columns for the palisade protecting the excavation.

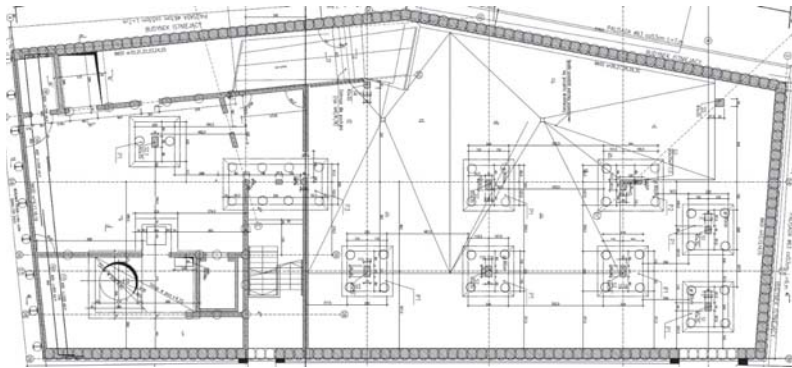


Fig. 3. Sheet of the foundation slab of the designed building

The foundation slab is 50 cm thick. The two pits have a depth of about 2.0 m. The slab is thickened at column locations to a total thickness of 80 cm.

In order to create a three-dimensional numerical model using the ZSoil program (2016_16.04), the following assumptions were made for the structural elements:

- ▶ The foundation slab is modelled as a 50 cm thick discrete 3D continuum element.
- ▶ The palisade is modelled around the circumference as discrete beam elements – piles with a cross section of Φ 50 cm, spaced at 45 cm and with a length of 7.0 m from the bottom of the foundation slab. Above the bottom of the slab, 3D continuum elements were used. The total height of the palisade is 11.75 m from ground level.
- ▶ Piles/columns under the slab were modelled using discrete beam elements – piles with cross sections of Φ 50 cm and with a length of 7.0 m from the bottom of the foundation slab.
- ▶ In pit locations, vertical elements with a length of approx. 2.50 m were built with the use of discrete 3D continuum elements. Under these elements, beam-like elements were placed as piles with a cross section of Φ 50 cm and 3.0 m long. The total height of the vertical wall elements in the pits measured from the bottom of the slab is 5.50 m.

This solution allowed the authors to go with the base of the modelled palisade and the piles tip into the load-capacity layer of the II_c sands

- ▶ Floor slabs and structural shafts were modelled using discretised elastic isotropic shells with thicknesses from 0.2 m to 0.35 m

Adjacent buildings were taken into account by modelling the foundations of individual buildings at an appropriate depth. Discrete 3D continuum elements were used with material parameters corresponding to the concrete class C30/37. The estimated system of forces was collected from the whole structures and applying to the foundations.

The ground base was created in the model in which the underground part of the building was created and then the entire building. An elastic-plastic model with Coulomb-Mohr yield conditions was used to define the subsurface soil layers, while the hard plastic clay deposits ($I_L = 0.17$), i.e. layer III_a and sand layers II_b and II_c , were parameterised using the HSs model.

A view of the 3D model with the adopted layout of layers in ZSoil is shown in Fig. 4.

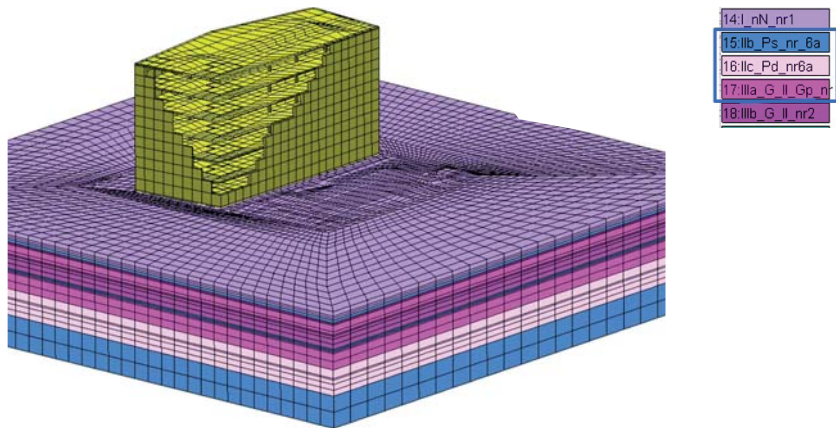


Fig. 4. 3D view of the ZSoil model; the designed building with the adopted layout of layers

4. NUMERICAL ANALYSIS AND RESULTS

The conducted analysis concerns the impact of the extension of the designed structure on the neighbouring buildings. There are three phases each of which generates an impact on the environment. The calculations are divided into three suitable stages.

To specify the maximum displacements in direct contact with the excavation shoring $max v_o$, we should determine the sum of the maximum displacements caused by excavation shoring v_i and horizontal displacement of the wall v_u :

$$max v_o = v_i + v_u$$

Figure 5 shows a simplified distribution of soil displacements in the vicinity of a deep excavation [1].

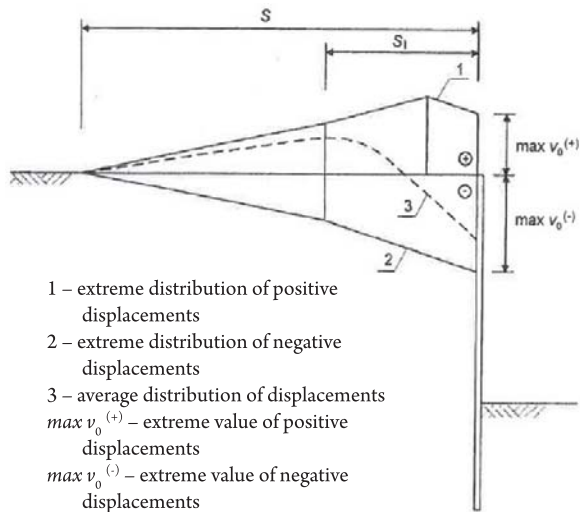


Fig. 5. Simplified distributions of soil displacements in the vicinity of a deep excavation [1]

FIRST PHASE OF EXCAVATION SHORING

The excavation shoring will be made from level of the work platform, situated at 1.3 m below the ground level. Cased CFA piles combine the quality of classic CFA piles with piles made in casing pipes. This technology of piles is known as CFP (Cased Flight Auger Piles) or VDW (Vor der Wand – in front of the wall) [3]. The piling machine is equipped with a double rotary head that rotates the auger and the casing pipe independently and in opposite directions. In the process of drilling with the auger, the hole drilling is simultaneously by inserting a casing pipe which ensures hole stability during drilling. When an assumed depth is reached, the auger is pulled out together with the pipe, while at the same time, a well-formulated concrete mix is pumped through the auger core pipe. Reinforcing cages or steel sections are inserted by pressing and vibrating.

Maximum vertical displacement caused by construction of the excavation shoring v_i is determined using formula (1) suggested by instruction [1].

$$v_i = \alpha (H_w)^{\frac{1}{2}} \quad (1)$$

By inserting the following values into formula (1)

$H_w = 7.3$ m – excavation depth,

$\alpha = 1.3$ – empirical coefficient

we get the value $v_i = 3.51$ mm

SECOND PHASE OF EXCAVATION

The excavation stage has been included in the model. The protection of the palisade includes one level of strutting with steel pipes. The excavation phases are schematically presented in Fig. 6. Horizontal displacements of the retaining wall were read from the map of

horizontal strain of the palisade for the different excavation phases. The maximum horizontal displacement of the excavation shoring is shown in Figure 7.

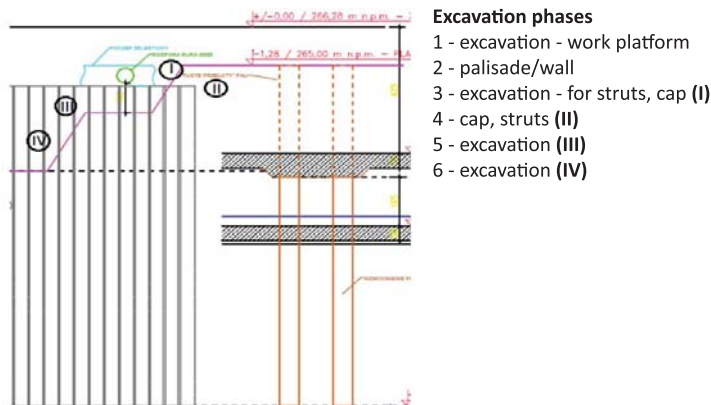


Fig. 6. Excavation phases

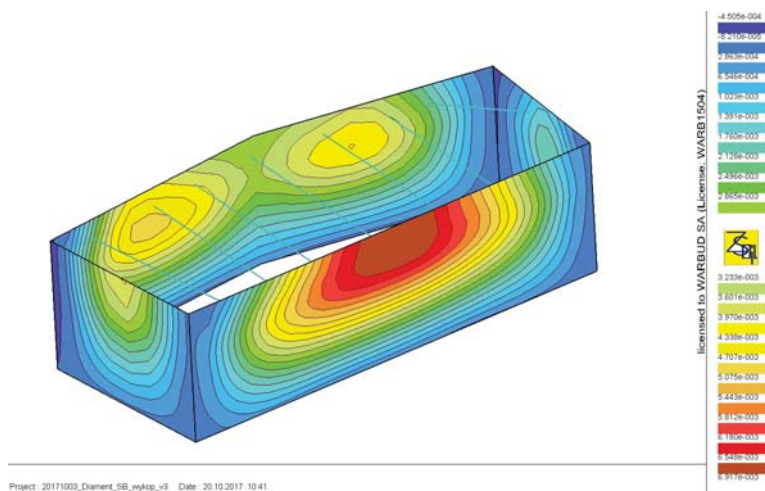


Fig. 7. Horizontal displacement map of excavation shoring

Vertical displacements v_u caused by deformation of the excavation shoring wall are calculated from formula (2).

$$v_u = 0.75(\max u_k) \quad (2)$$

When entering the obtained value of maximum horizontal displacement of the excavation shoring $\max u_k = 6.92$ mm into formula (2), we get the value $v_u = 5.19$ mm.

Vertical displacements of the neighbouring terrain caused by the excavation can also be obtained directly from the results of numerical calculations by reading the value of displacements from the vertical displacement map shown in Fig. 8.

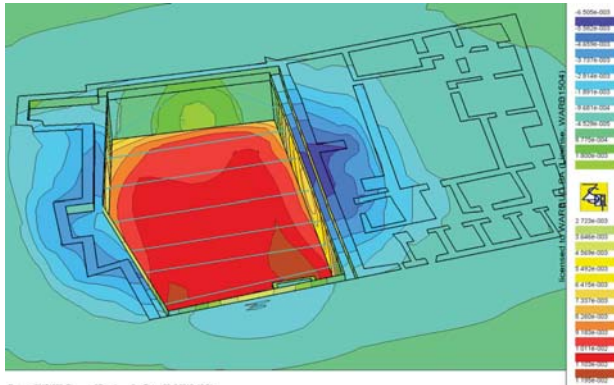


Fig. 8. 3D map of vertical displacements from the ZSoil model after phase II – excavation

The maximum value of the vertical displacement of the adjacent area in the immediate vicinity of the excavation shoring, read from the map in Fig. 8 is $\nu_u = 6.5$ mm.

PHASE III BUILDING SERVICEABILITY

The results from the building serviceability phase were obtained directly from the calculations made in the 3D model using the FEM algorithm.

Modelling phases:

- ▶ existing buildings in the form of strip footings and foundations were assumed
- ▶ estimated load values were applied to the strip foundations of the neighbouring buildings
- ▶ execution of a wide excavation in order to take into account the influence of soil relaxation on the neighbouring buildings – excavation phase in accordance with Fig. 6
- ▶ construction of the target structure
- ▶ applying a configuration of forces to the structure

Figure 9 shows a settlement map for the foundation slab and the neighbouring buildings.



Fig. 9. Map of settlement of the foundation slab and neighbouring buildings in the building serviceability phase

The obtained value of settlement of the neighbouring foundations in the phase of serviceability of the designed building is 9.1 mm.

RESULTS

The maximum vertical displacements behind the excavation shoring amount to:

$$\max v_0 = 3.51 + 5.19 = 8.70 \text{ mm (phases I + II)}$$

The area displacements at distance $d_{min} = 0.25 \text{ m}$ – the minimum distance between the adjacent foundations and the excavation shoring – estimated on the basis of linear interpolation is:

$$v_0 = 8.5 \text{ mm}$$

The obtained value is contained within the range of approximate characteristic limit values of building structure displacement according to Table 2.

Rodzaj konstrukcji	$[s_k]_u, \text{ mm}$	$[s_k]_n, \text{ mm}$
Budynki murowane bez wieńców, ze stropami drewnianymi lub ceramicznymi typu Kleina	5–7	15–18
Budynki murowane ze stropami gęstożebrowymi lub żelbetowymi, albo budynki prefabrykowane	7–9	20–25
Budynki o konstrukcji monolitycznej	9–11	25–35

Table 2. Limit values for building structure displacements [1]

Taking into account the results obtained in the third phase – the serviceability of the structure – we get:

$$\max v_0 = 3.51 + 5.19 + 9.1 = 17.6 \text{ mm (phases I+II+III)}$$

The obtained value is not contained within the range of approximate characteristic limit values of building structure displacements, see Table 2. It can be said that we are even at the limit of design/ultimate values of structure displacements which may result in the loss of load capacity and lead to structural failure.

5. CONCLUSIONS

There was conducted the spatial analysis the impact of the extension of the designed building on the neighbouring buildings. The phase regarding the deep excavation work estimated with the use of empirical formulas and numerical tools gives convergent results.

Taking into account the results obtained at the building serviceability stage, it is suggested not to limit the analysis of the impact on the neighbouring environment to only the first two phases.



The application of numerical tools which take into account all the discussed elements may prove to be a solution for conducting a comprehensive analysis of a spatial geotechnical-design problem.

References

- [1] Kotlicki W., Wysokiński L., *Ochrona zabudowy w sąsiedztwie głębokich wykopów*, Instytut Techniki Budowlanej, no. 376, Warszawa 2002.
- [2] Kacprzak G., *Comparison analysis of raft-pile system – theory and practice*, Technical transactions, 3-Ś/2011, 59–72.
- [3] Gwizdała K., *Fundamenty Palowe. Technologie i obliczenia*, PWN, Warszawa 2010.
- [4] Kacprzak G., Bodus S., *Numerical analysis of the load distribution under the piled raft foundation of the high-rise building*, Ann Warsaw Univ. Life Sci. – SGGW, Land Reclam. 50(2), 2018, 129–138.
- [5] Katzenbach R., Leppla S., *Realistic Modelling of Soil-Structure Interaction for High-Rise Buildings*, Technische Universität Darmstadt, Institute and Laboratory of Geotechnics, Germany 2015.
- [6] Kutera B., Kacprzak G., *The pile stiffness in a piled-raft foundation*, Technical transactions, 2-B/2013, 59–69.
- [7] Truty A., *Small strain stiffness of soil. Numerical modeling aspects*, Technical transactions, 3-Ś/2008, 107–126.
- [8] Truty A., Podleś K., *Application of Hardening Soil – Small model for analysis of soil-structure interaction problems*, Technical transactions, Environmental Engineering, 1-Ś/2010, 117–134.
- [9] Obrzud R., Truty A., *The Hardening Soil Model – A Practical Guidebook*, Technical Report ZSoil, Zace Services LTD, 2016.
- [10] PN-EN 1997, Eurokod 7. Projektowanie geotechniczne.

Bernard Twaróg  orcid.org/0000-0003-3150-1409

btwarog@pk.edu.pl

Faculty of Environmental Engineering, Cracow University of Technology

THE ANALYSIS OF THE REACTIVE WORK OF THE ALDEN TURBINE

ANALIZA PRACY REAKCYJNEJ TURBINY ALDENA

Abstract

In the analysis of the reactive work of the Alden turbine, two systems of energy recovery were utilized: conical, a straight suction pipe, and a curved diffuser – the so-called bend. The simulations executed on both the systems allowed the operation and selected installation components to be described. Full distribution curves for pressures, velocities were presented, and spectral analyses of pressure fluctuations for the selected points over and under the turbine rotor were also performed. For some structural parts, by means of the FSI – Fluid System Interaction model – the distributions of main stresses and strains according to von Mises theory were illustrated. Additionally, the shapes of deformed installations parts caused by unsymmetrical loads generated mainly by a turbulent water flow were presented.

Keywords: hydropower, Alden turbine, hydrodynamic cavitation, hydrodynamic loads, vortex core, suction pipe

Streszczenie

W prezentowanej analizie pracy reakcyjnej turbiny Aldena wykorzystano dwa systemy odzyskiwania energii: rurę ssącą w postaci stożkowej oraz krzywaka. Symulacje wykonane w obu systemach pozwoliły na prezentację wyników oraz szczegółowy opis pracy wybranych komponentów instalacji. Przedstawiono krzywe zmian ciśnień oraz prędkości, a także przeprowadzono analizę spektralną pulsacji ciśnienia dla wybranych punktów nad i pod wirnikiem turbiny. W przypadku wybranych elementów konstrukcyjnych z zastosowaniem teorii FSI zilustrowano rozkłady naprężeń według teorii von Misesa. Ponadto przedstawiono kształty zdeformowanych części instalacji spowodowane przez niesymetryczne obciążenia generowane głównie przez turbulentny przepływ wody.

Słowa kluczowe: turbina Aldena, hydrodynamiczna kawitacja, siły hydrodynamiczne, rdzeń wiru, rura ssąca

1. Introduction

The idea of an eco-friendly Alden turbine (Fig. 1) was born in 1993 [1]. Two main assumptions, viz. an improvement in efficiency and a reduction of environmental impact determined the trends for developing a new turbine structure. A concentration of work resulted in a radically new construction for the turbine rotor. The number of blades was limited, both pressure and velocity gradients were reduced, the clearance between the rotor and the guide vane was minimized, and eventually, the size of flow spaces was maximized.

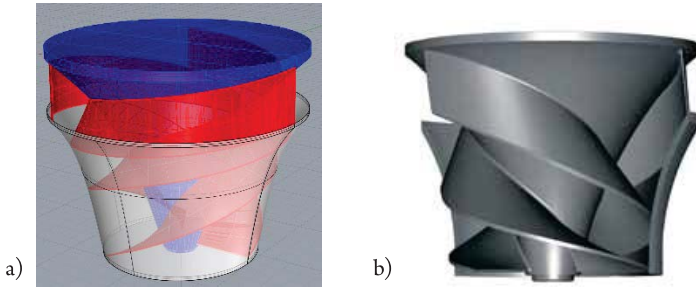


Fig. 1. Alden turbine rotor used in the modelling: a) model, b) template [1]

The selection of Alden turbines takes place according to 2 parameters: head and flow [3]. In particular, a hydraulic head for the Alden turbine is assumed ranging from 7.6 to 43 [m] and a minimum flow rate from 14 [m³/s] onwards [3]. Typical parameters are the values of the head, rotational speeds and power. Rational diameter values for the Alden turbine range from 2.4 to 4.5 [m] [3]. For diameters under 2.4 [m], the spacing of turbine parts (vanes and spaces among them) will diminish unfavourably, which reduces the fish survival rate. Instead, large diameters will mean inefficiency in the system. An appropriate rotational speed of the Alden turbine amounts to 90–140 [rpm] [3].

2. Principals of CFD modelling

The model for the installation under analysis was developed in the **Flow-3D** software. the viscous and turbulent flow was assumed, without taking into consideration the limited compressibility of water. The spinning parts have been described by means of the General Moving Objects, made available in the **Flow-3D** interface. For the description of water, a time-averaged form of the Navier-Stokes (N-S) equations, known also as the Reynolds equation, was applied:

$$\rho \left(\frac{\partial \bar{U}_i}{\partial t} + \bar{U}_j \frac{\partial \bar{U}_i}{\partial x_j} \right) = \frac{\partial}{\partial x_j} (\sigma_{ij}) + \bar{F}_i \quad (2-1)$$

where U , p , ρ , F stand, respectively, for velocity, pressure, fluid density and body force.

The expression $(\sigma_T)_{ij}$ which does not appear in the N-S equations, represents the Reynolds stress tensor:

$$\sigma_{ij} = -\bar{p}\delta_{ij} + \nu\rho \left(\frac{\partial \bar{U}_i}{\partial x_j} + \bar{U}_j \frac{\partial \bar{U}_i}{\partial x_i} \right) - (\sigma_T)_{ij} \quad (2-2)$$

$$(\sigma_T)_{ij} = \rho \overline{u_i u_j} \quad (2-3)$$

An extra term, viz. $(\sigma_T)_{ij}$ is a symmetric Reynolds stress tensor whose elements constitute components of unitary, turbulent momentum flux.

For an extra term which appears in N-S equations, this will entail a closing hypothesis. It is the domain of turbulence models. Historically, the first hypothesis was a proposal for closing the system of N-S equations formulated by Prandtl (1925), nowadays referred to as the concept of 'mixing length model'. Yet, the most numerous group is composed of models based upon the Boussinesq model, which assumes the occurrence of the so-called eddy viscosity which corresponds to the coefficient of fluid molecular viscosity. Prandtl's hypothesis belongs to the first group of 'viscous' models, commonly referred to as the class of zero-equation models which do not need extra differential equations in order to close the N-S system of equations. Another group of viscous models for closing the N-S equations utilizes the equation of transport of turbulence kinetic energy (TKE) " κ ". The first model of this class was also proposed by Prandtl (1945). These models represent the class of one-equation models which, due to the introduction of the TKE equation, will concern the specific nature of the process of energy transmission in a cascade of turbulent vortexes. A veritable breakthrough in this branch was, however, the publication of the proposal of Harlow and Nakayama (1968) nowadays known as the model *Standard* " $\kappa - \varepsilon$ ". In this concept, the system of (N-S) equations was closed with two additional differential equations of transport, but to the " κ " equation of transport, already known, one added the equation of dissipation rate of turbulence kinetic energy (TKE) " ε ", and this value could be assessed by means of the Kolmogorov hypothesis:

$$\varepsilon = \frac{\kappa^{3/2}}{l} \quad (2-4)$$

in which the macroscopic flow length (expressed by the linear scale of flow " l ") is linked to dissipation, which describes the smallest eddy scales. Soon after, other two-equation models were developed, of which most popular became the hypotheses " $\kappa - \kappa l$ " and " $\kappa - \omega$ " of Rodi and Spalding (1970).

The applied turbulence model *RNG* $\kappa - \varepsilon$ [4] constitutes an expansion of the model *Standard* $\kappa - \varepsilon$. It satisfies the assumptions of physics of turbulent flows and selected mathematical assumptions for Reynolds stresses, which eventually will increase the efficiency of this model. The model is suitable for complex flows with fast variations of fluid parameters, moderate turbulences and local disturbances. It can guarantee high efficiency in the case of both flows around a body and straight flows, taking into consideration the boundary layer,

rotations, stream detaching and recirculation. The constants in $\kappa - \varepsilon$ equations are obtained by means of the theory of renormalization groups. This model is more efficient than the model *Standard* $\kappa - \varepsilon$ in the case of complex flows with densely arranged stream lines, vortexes and cases where the stream is detached.

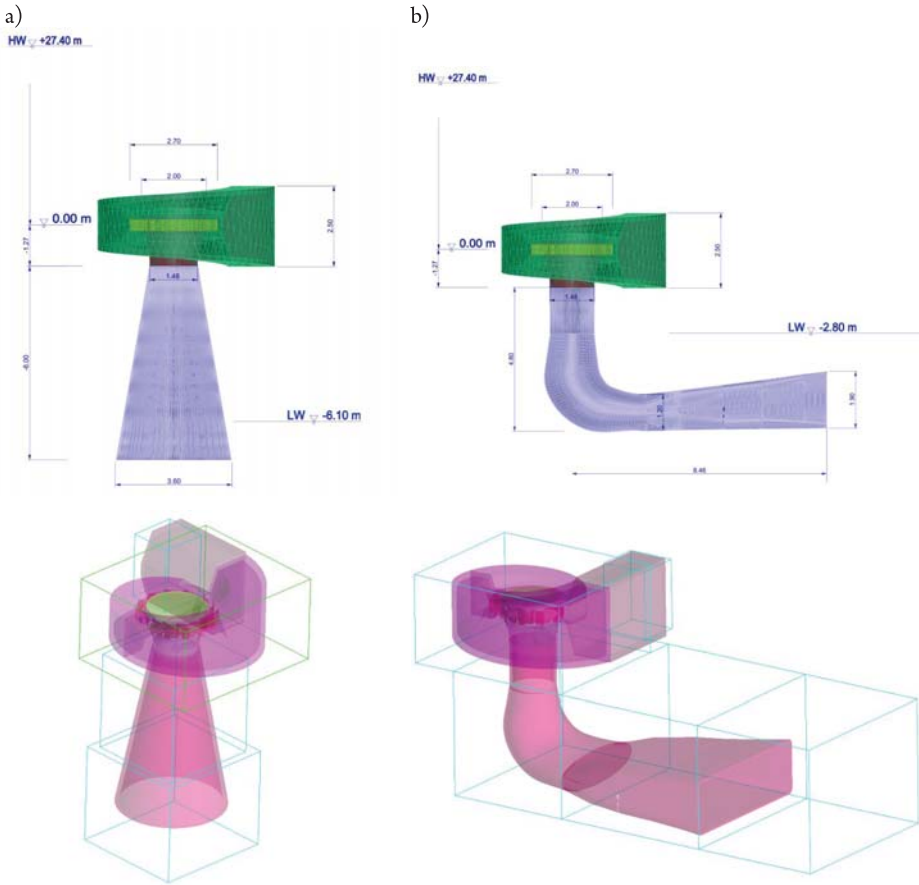


Fig. 2. The part of Alden installation under modelling: a) conical suction pipe, b) pipe bend

3. Description of the installations under analysis

The installation to be tested was adapted to the maximum hydraulic head in the Dobczyce power plant [5]. A model turbine diameter equal to 2.0 [m] was assumed. The system feeding water to the turbine rotor was made of a trapezoid cross section spiral and a guide vane with 14 flow channels (Fig. 3–5).

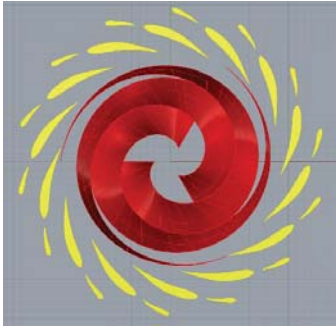


Fig. 3. View of runner of the Alden turbine with guide vane

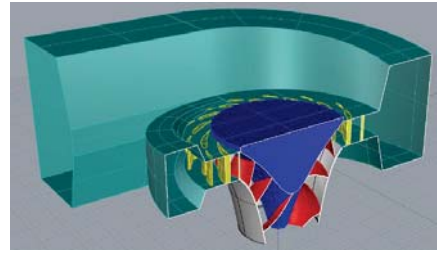


Fig. 4. Crosssection of the installation of the Alden turbine

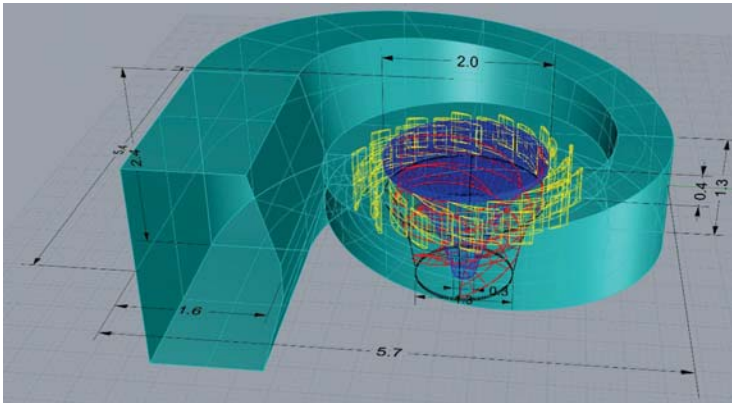


Fig. 5. Dimensions of the Alden turbine system [m]

The calculations were made for the following parameters:

- ▶ turbine rotational speed 140 [min^{-1}],
- ▶ upper water surface elevation: +30.00 [m asl]
- ▶ lower water surface elevation: -0.20 [m asl], in the case of a pipe bend
- ▶ lower water surface elevation -3.50 [m asl], in the case of a conical suction pipe
- ▶ guide vane elevation +2.60 [m asl]
- ▶ external pressure assumed: 101325 [Pa] (normal pressure),
- ▶ water temperature 5 [$^{\circ}\text{C}$],
- ▶ water steam pressure 900 [Pa],
- ▶ water density 999.9 [kg/m^3]
- ▶ water dynamic viscosity 0.001515 [Pa s]

The analysis of the simulation results for the turbine operation was performed with the professional **Flow-3D – FlowSight** post-processing software. The area in which a solution was searched for resulted from a diversification of the grid mesh. The inlet spiral was covered with a 0.02 [m] mesh cubic grid. Other elements within the areas were covered with a 0.05 [m] grid. The spinning parts were described by means of the General Moving Objects made available in the **Flow-3D** interface. All simulations were performed on an HP Z800 Workstation.

4. Hydrodynamic cavitation in hydroelectric power installations

The effect of hydrodynamic cavitation will occur in a fluid under a pressure field subject to variations in time and space. Such variations are related to fluid expansion up to the critical level at which spaces filled with saturated steam as well as with dissolved gases will appear. While being transported in a running stream towards the zone of increased pressure, they are subject to violent compression at which implosions will occur in the areas filled with steam and gases. For a very low water compressibility, pressure values can reach even 150 MPa, which means destruction and erosion of materials. While decreasing pressure isothermally to the level of saturation pressure, the fluid will pass into steam, but this effect is not discontinuous within the fluid space; instead, the steam is released as spherical bubbles from all over the volume. It is assumed that the critical pressure causing a phase transformation is almost equal to the pressure of saturated steam of a fluid in the determined conditions. A fluid pressure variation

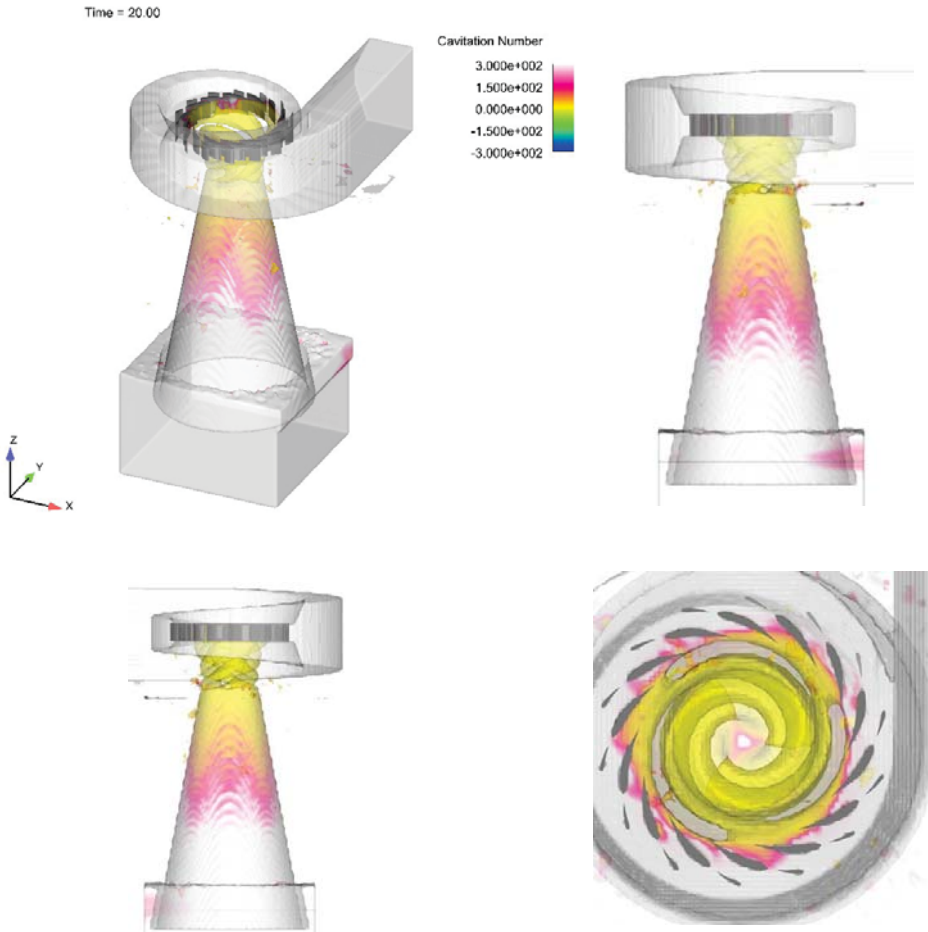


Fig. 6. Cavitation number, conical suction pipe (temperature 5[°C], external pressure: 101325 [Pa], water steam pressure 900 [Pa])

leads thus to a transformation of the liquid phase into gaseous. The agents influencing the occurrence of cavitation are therefore temperature, pressure and fluid flow rate. Other factors which favour the occurrence of cavitation are also the shape of the surface contacted by the fluid, pollutions in the fluid, and gases dissolved, if any. Cavitation often occurs in the throats of the channels and where flows become curved as well as due to the motion of solids in fluids. It is also caused by a local narrowing of stream lines of the passing fluid or stream detached from the streamlined surfaces of bodies. The effect is influenced by diffusion, degassing, evaporation, condensation, fluid inertia, surface tension, adhesion and fluid viscosity.

While analysing the phenomenon of cavitation, one can determine the parameter or dimensionless number which permits one to perform a quantitative evaluation of flows in two aspects:

- ▶ The parameter which assumes an identical value for any and dynamically similar conditions of cavitation;
- ▶ The parameter determining the conditions of cavitation-free flow and the conditions for the occurrence, disappearance or development of the respective cavitation phases.

Although in this analysis the effect of cavitation is not modelled, an identification of places where cavitation is likely to occur could be postulated (Fig. 6, 7); a reliable indicator is, which describes the propensity for cavitation in the areas concerned:

$$c_a = \frac{(p - p_n)}{\frac{\rho u^2}{2}} \quad (4-1)$$

where: c_a – cavitation number, p – pressure value at a point of flow [Pa], p_n – steam pressure [Pa], ρ – fluid density [kg/m^3], u – fluid velocity [m/s]

Investigations into the effect of cavitation in hydroelectric power installations suggest that both a diminished lower water surface level and a gross increase in the hydraulic head will negatively affect the cavitation conditions in the turbine. As the pressure value in the suction area goes down, pressure fluctuations and vibrations of the turbine shaft will intensify, and therefore, symptoms will appear which may be caused by cavitation and may also contribute to this phenomenon. Such relationships are taken into consideration while designing water power plants; it is checked whether the obtained value of cavitation index exceeds the critical value:

$$\sigma = H_B - \frac{H_s}{H} > \sigma_c \quad (4-2)$$

where H_B barometric pressure in [m] of water column is, H_s is suction pressure in [m] on the turbine outlet or the rotor height above the lower water surface level, H is the hydraulic head of the power plant turbine in [m]. The value of σ_c may be found by applying appropriate empirical formulae [9].



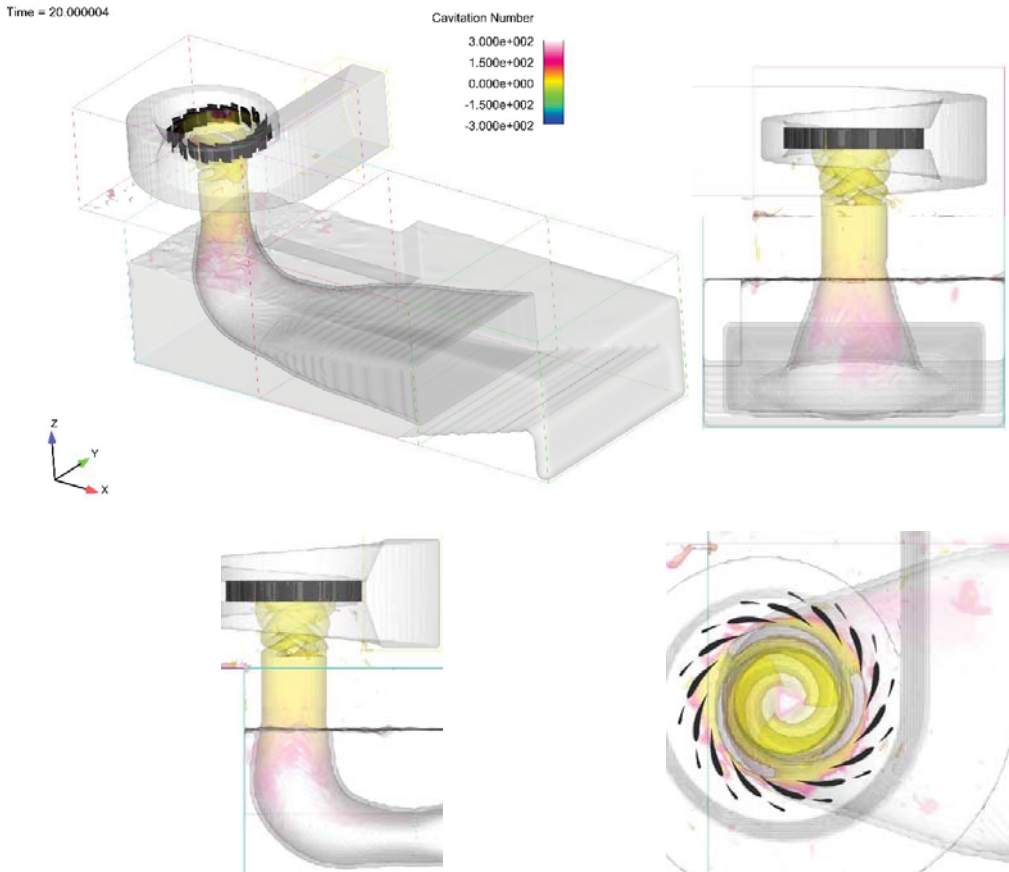


Fig. 7. Cavitation number, pipe bend (temperature 5[°C], external pressure: 101325 [Pa], water steam pressure 900 [Pa])

5. Determination of the vortex core

While describing flows of real fluids, two forms of flow are considered: laminar (ordered) and turbulent (violent, chaotic). The principal criterion for separating these two forms from each other is the Reynolds number. The loss of stability of the laminar flow and its transition into a turbulent flow results from an excessive increase in the inertial forces vs. the forces of internal friction which act upon moving water particles. In the turbulent flow there will appear spatial vortexes of various length scales (small, medium and large), which means the occurrence of small, non-stationary departures of velocity fields and pressure from average values, and eventually, the turbulent flow will become spatial and chaotic. Numerous vortexes which enter into interactions may be curved or twisted, which brings about a rotation in several different planes of each single vortex, which, in turn, will impede the identification and visualization of this effect.

The scales of turbulent vortexes cover the range from 10^{-6} [m] (scale of dissipative processes constituting one of the essential features of turbulence) to an order of metres (technical applications) or even hundreds and thousands of miles (geophysical turbulence) continuously [10]. An infinite number of relationships existing among the respective scales of the effect, and in each of them, the processes of turbulent transport of mass, momentum or scalar energy (energy, heat) will cause interactions in the form of an infinite cascade of vortexes performing transport processes in a manner typical of turbulent flow. This means that the intensity of mass, momentum and energy transport is a few orders of magnitude higher than for laminar flow.

Vortexes will occur because of free and forced dissemination in the zone of turbulent flow. The occurrence of a vortex is of consequence for pressure fluctuations, which affects the initiation of the effect of cavitation, since the pressure value at the centre of a vortex may be considerably lower than the average pressure within the flow area. After the discovery of vortex structures in the turbulence, interest was immediately aroused in doing research into the vortex, which resulted in a series of methods used for identifying vortexes. One makes use of several classifications (Yuning Zhang [7]); in general, one may enumerate so-called objective and subjective methods; in the former case, the methodology of vortex identification will not affect its shape. Instead, the objective methods rely mainly upon invariants of vortex structures viz. Galileo, Lagrange or rotations.

One of the objective methods based upon the tensor of velocity gradient for the identification of vortex areas is the *Q-criterion*.

The velocity gradient tensor \overline{D} may be given as:

$$D_{ij} = \frac{\partial u_i}{\partial x_j} \quad (5-1)$$

Second rank tensors are subject to well-known mathematical operations typical of the vector space. However, unlike conventional vectors in the Euclidean space, extra operations, like transposition, superposition or inverse may be defined for them. In addition, each second rank tensor may be separated additively into its symmetric and antisymmetric parts.

$$D_{ij} = S_{ij} + \Omega_{ij} \quad (5-2)$$

where:

$$S_{ij} = \frac{1}{2} \left(\frac{\partial u_i}{\partial x_j} + \frac{\partial u_j}{\partial x_i} \right) \quad (5-3)$$

$$\Omega_{ij} = \frac{1}{2} \left(\frac{\partial u_i}{\partial x_j} - \frac{\partial u_j}{\partial x_i} \right) \quad (5-4)$$

where:

S_{ij} – symmetric tensor

Ω_{ij} – tensor called tensor.

The characteristic equation for may be given as follows:

$$\lambda^3 + P\lambda^2 + Q\lambda + R = 0 \quad (5-5)$$

P , Q i R are three invariants of the velocity gradient tensor. With a separation into the symmetric and antisymmetric tensor parts, the invariants may be expressed as follows

$$P = -tr(\bar{D}) \quad (5-6)$$

$$Q = \frac{1}{2}(tr(\bar{D})^2 - tr(\bar{D}^2)) = \frac{1}{2}\|\bar{\Omega}\|^2 - \|\bar{S}\|^2 \quad (5-7)$$

$$R = -det(\bar{D}) \quad (5-8)$$

In this analysis, the motion vorticity was assessed using the Q - criterion (Hunt, Wray& Moin, 1988, [11]), which corresponds to the second invariant of the velocity gradient tensor. The criterion complies with the identification of big scale vortexes in a turbulent flow of incompressible fluids. It identifies the areas of flows in which the forces generating the rotation exceed the forces of internal frictions (Fig. 8, 11).

This criterion identifies the vorticity as an area with a positive second invariant of tensor ∇u , $Q > 0$.

In this criterion a second condition for pressure, which should be lower than the pressure value in the vortex neighbourhood, is also added. Looking at the definition, the second invariant expresses the local equilibrium between the strain rate at shearing and the vortex size. Its positive value indicates that the vorticity value is higher than the strain rate.

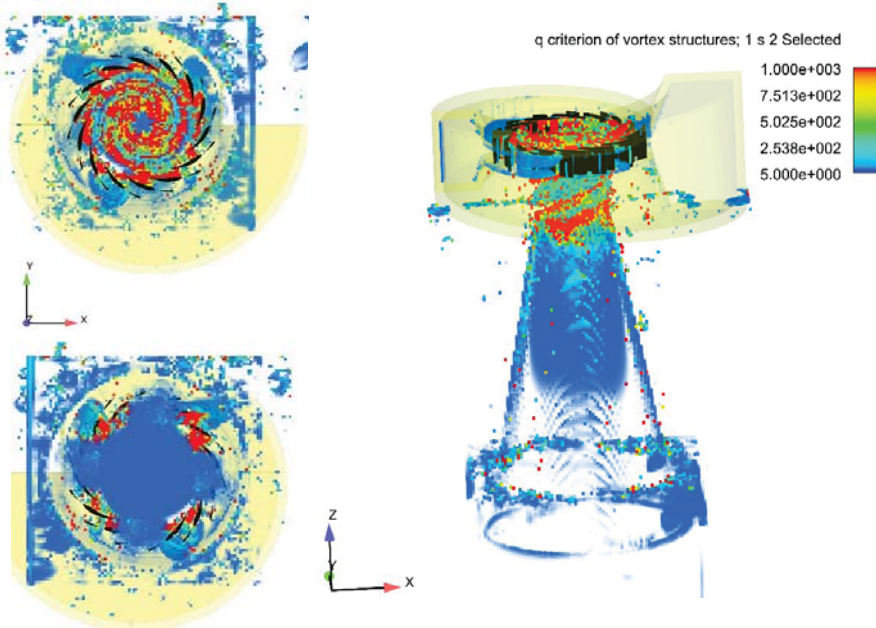


Fig. 8. Vorticity in the Alden installation with a conical pipe according to the Q -criterion

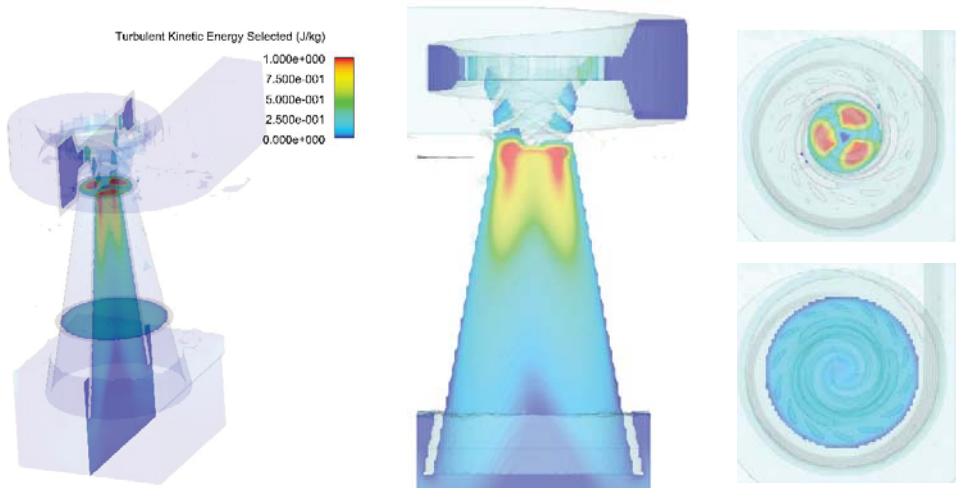


Fig. 9. Turbulent kinetic energy in the Alden installation with a conical pipe

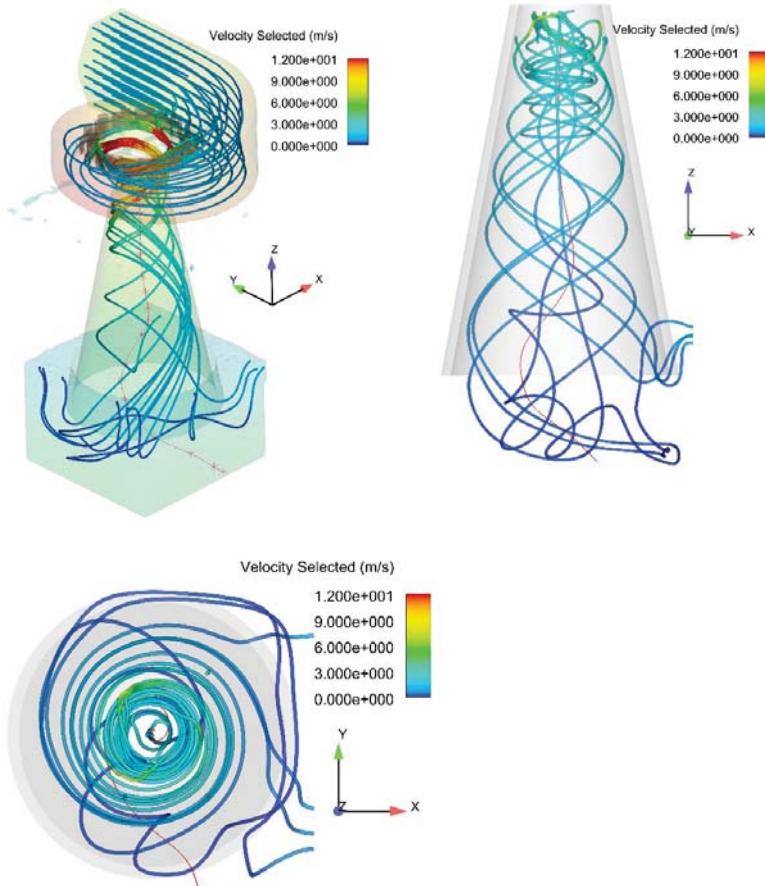


Fig. 10. Vortex core in the conical suction pipe against the stream line

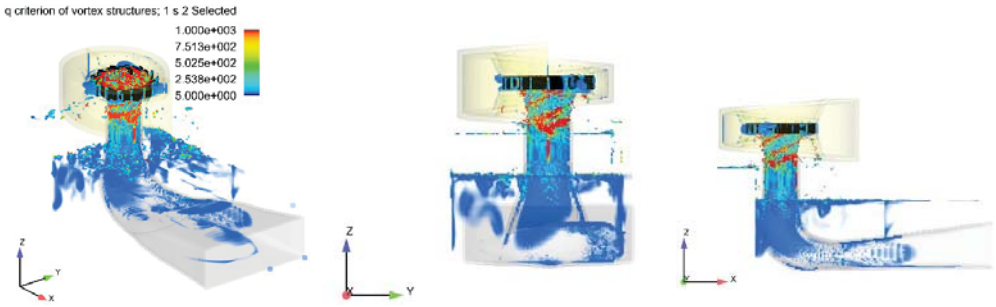


Fig. 11. Vorticity in the Alden installation with a pipe bend according to the Q -criterion

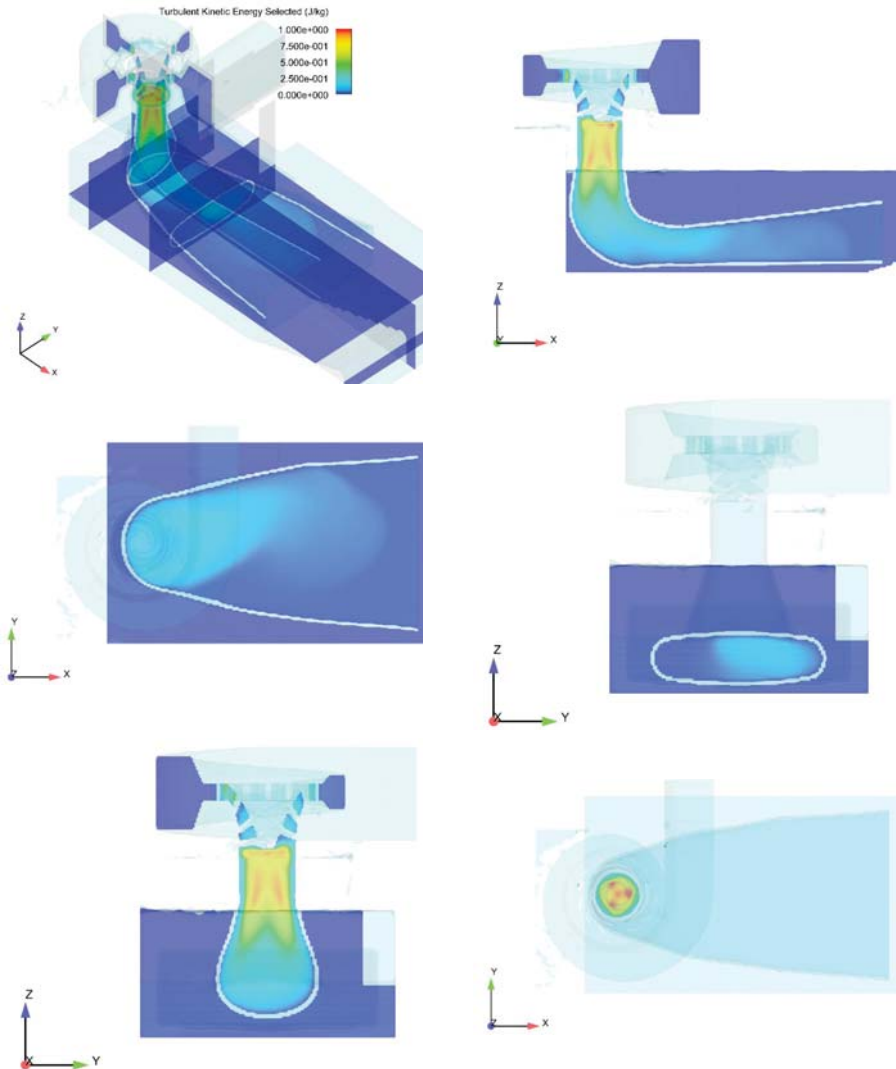


Fig. 12. Turbulent kinetic energy in the Alden installation with a pipe bend

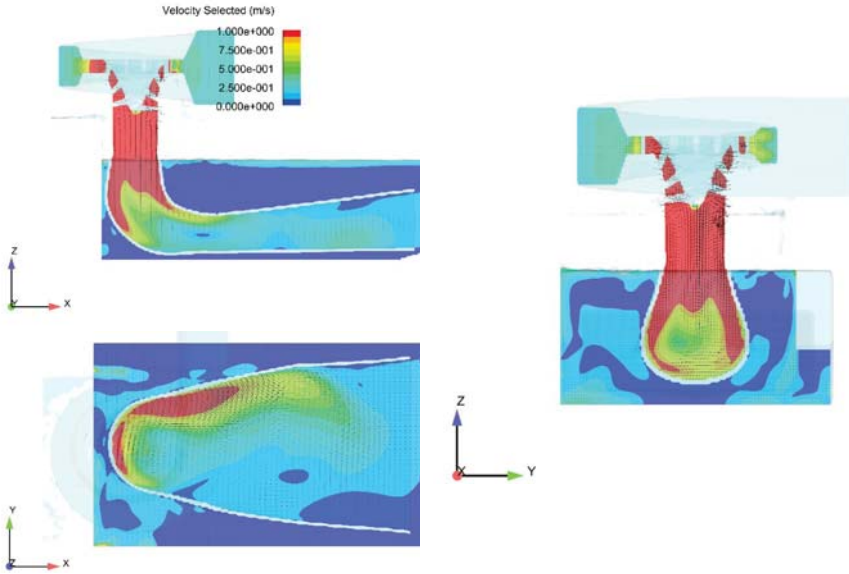


Fig. 13. Vectors of velocity field in selected cross sections the Alden installation with a pipe bend (under 1 [m/s])

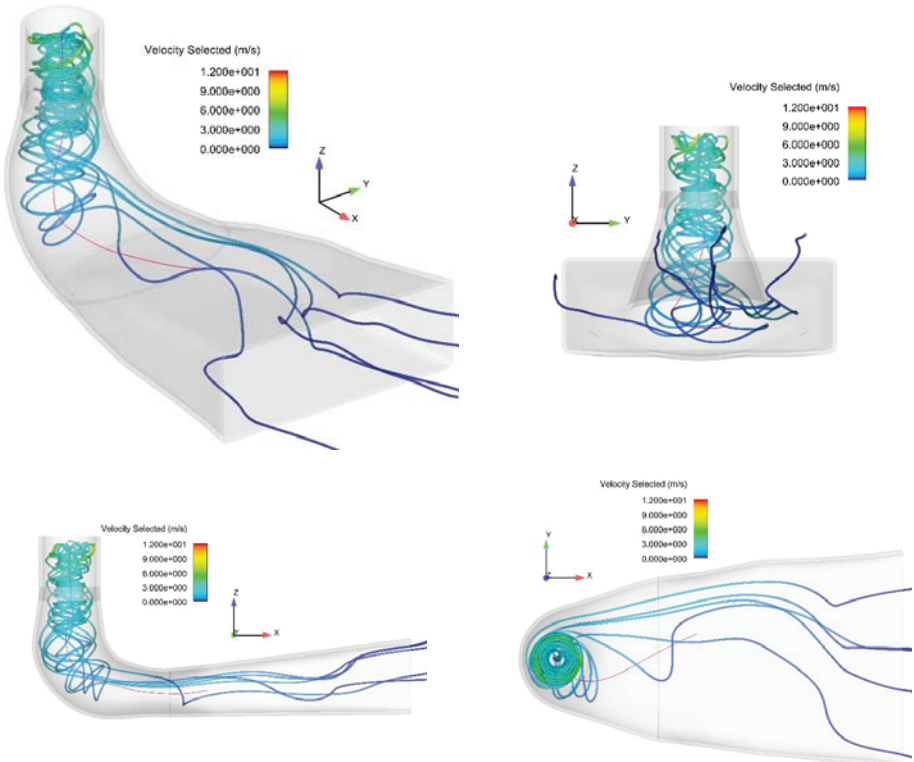


Fig. 14. Vortex core in a pipe bend against the stream line

The vortex core line was set out with an algorithm for determining eigenvalues (Robert Haines and David Kenwright [6]). In short, the applied algorithm divides the search area into elementary subareas. For each of them a unique form of the velocity gradient tensor is determined. While using the algorithm for the analysis of eigenvalues the reduced velocity values at nodal points are determined which, in turn, allow one to identify the areas of elementary subareas pierced by the vortex core. The set of those lines enables the determination of the shape and course of the vortex core (Fig. 10, 14).

6. Hydrodynamic loads in the suction pipe

The water flow through the turbine set is characterized by large pressure fluctuations. The amplitude of oscillations increases towards the rotor and then decreases towards the suction pipe outlet. Statistical curves of fluctuations are variable and depend on the location of the analysis point (Tab. 1, 2). Figures 18 and 21 show the course of fluctuation in time for the pressure obtained for the model at the points situated:

- ▶ under the rotor at the suction pipe jacket (Point no. 1) (Fig. 15, 18),
- ▶ under the turbine rotor in its axis (Point no. 2) (Fig. 15, 18),
- ▶ in the rotor axis immediately above the lower water surface (Point no. 3) (Fig. 15, 18),
- ▶ in the turbine inlet behind the guide vanes (Point no. 4) (Fig. 15, 18).

Table 1. A list of statistics of pressure fluctuations for selected points; suction conical pipe

Statistics	Unit	Point no. 1	Point no. 2	Point no. 3	Point no. 4
Mean	[Pa]	57154.67	51479.60	100095.50	381890.75
Standard deviation	[Pa]	18847.41	12787.10	5224.37	64915.96
Coefficient of variation	[]	0.33	0.25	0.05	0.17

Table 2. A list of statistics of pressure fluctuations for selected points; suction pipe in the form of a bend

Statistics	Unit	Point no. 1	Point no. 2	Point no. 3	Point no. 4
Mean	[Pa]	91853.87	80086.01	97274.15	374043.40
Standard deviation	[Pa]	28563.55	23675.69	20665.33	42839.28
Coefficient of variation	[]	0.31	0.30	0.21	0.11

The rotor structure, revolutions per minute and the number of guide apparatus channels indicate that the highest level of harmonic components will appear at frequencies of approx. 2.33, 7.00, 32.67, 98.00 [Hz]. The spectral analysis performed confirms the dominating frequencies of pressure fluctuations (Fig. 17, 20). Those frequencies are strictly related to the rotor rotational speed, the number of flow channels and the number of rotor vanes. In the

case under analysis, we have 3 rotor blades, 14 guide apparatus flow channels mating with the rotor moving at a rotational speed of $140 \text{ [min}^{-1}\text{]}$. The main source of oscillations will be flow fluctuations caused by the rotor and guide apparatus vanes. Actually, the values of those fluctuations are also influenced by cavitation effects at the fluid discharge from the rotor.

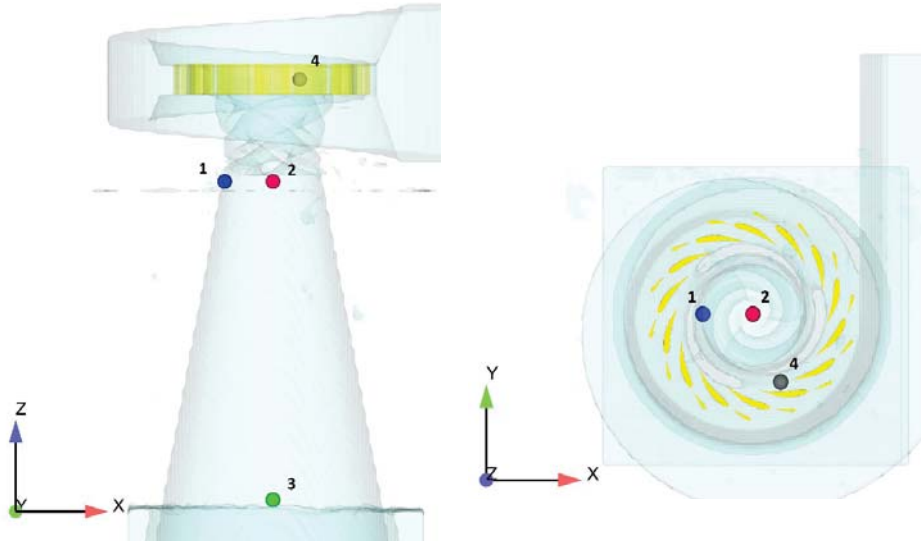


Fig. 15. Arrangement of measurement points – conical pipe

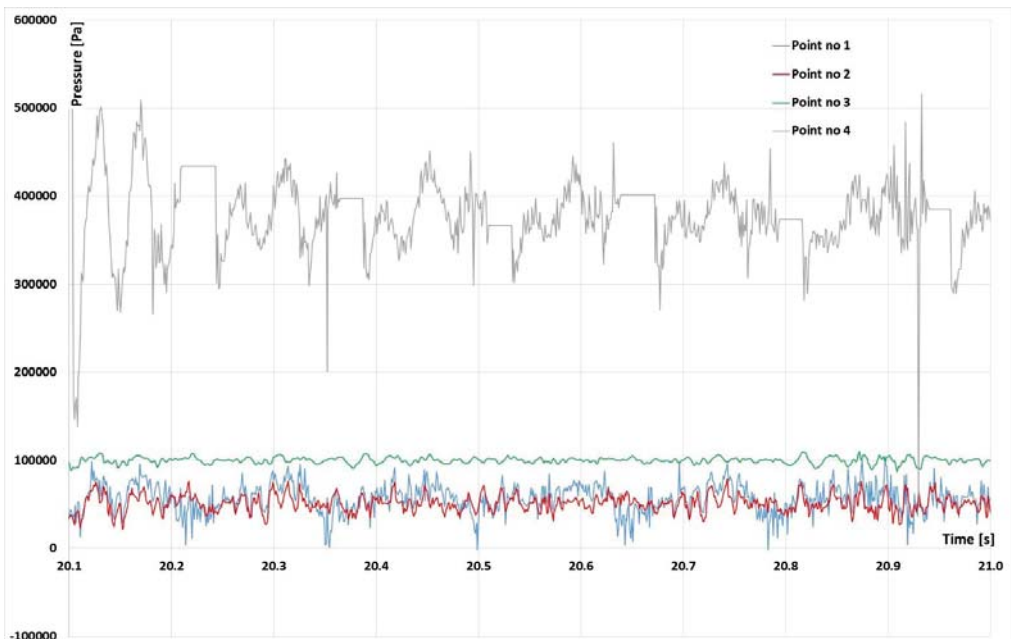


Fig. 16. Pressure fluctuations in the installation with a conical suction pipe

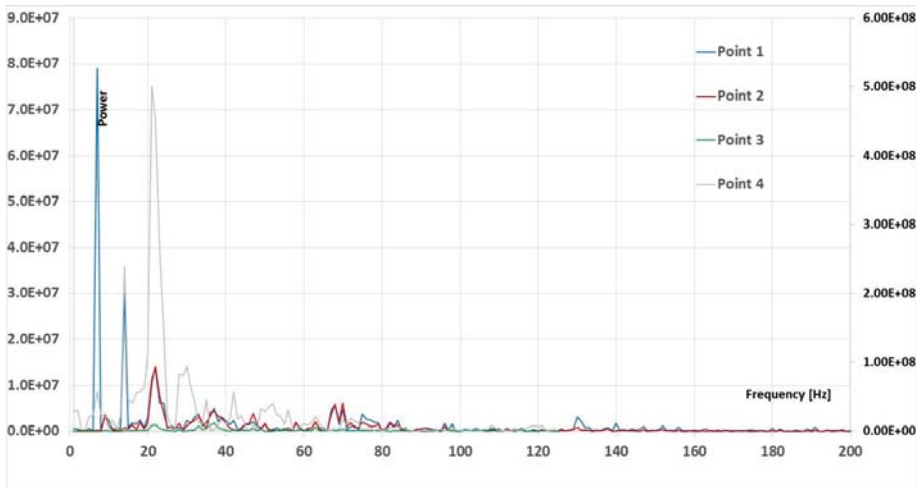


Fig. 17. Spectral analysis of pressure fluctuations in the installation with a conical suction pipe

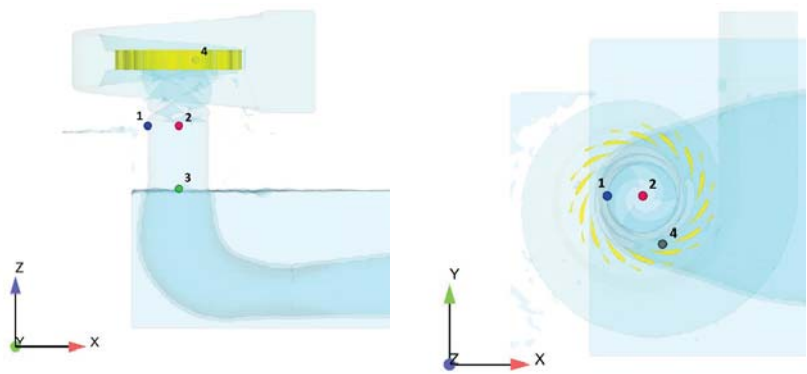


Fig. 18. Arrangement of measurement points – pipe bend

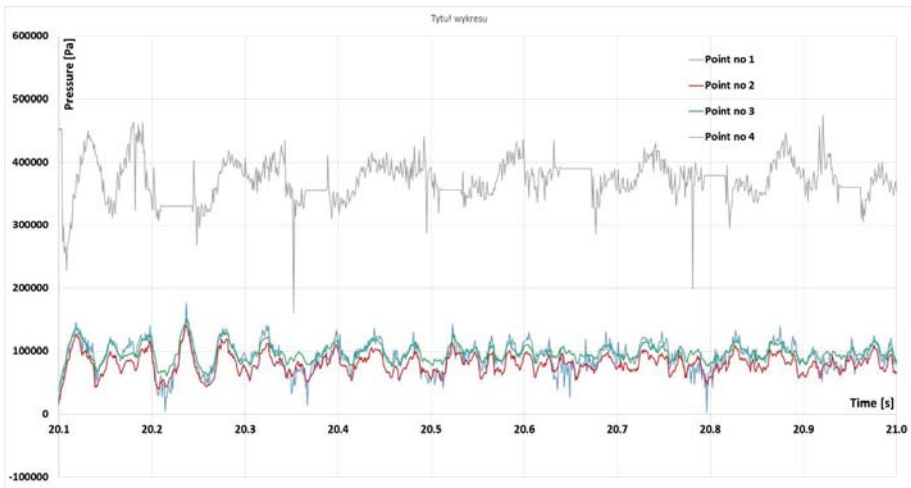


Fig. 19. Pressure fluctuations in the installation with a pipe bend

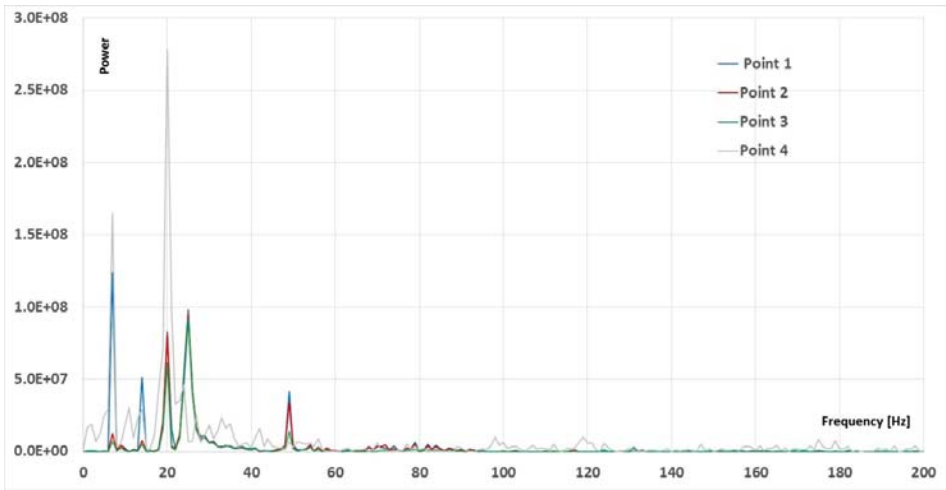


Fig. 20. Spectral analysis of pressure fluctuations in the installation with a pipe bend

7. Stresses and strains in selected parts of the hydroelectric power installations

In order to determine stresses and displacements of selected parts of the installation, the FSI model was selected. The suction pipes and the inlet spiral of the installation were analysed. For each part a stress distribution is presented according to the effort theory of von Mises.

The criterion for the maximum reduced stress by von Mises is based upon the theory of von Mises-Hencky, also referred to as Distortion-Energy Theory or the Maximum Distortion Energy Criterion. According to the theory, yielding of a ductile material begins when the reduced stress according to Mises becomes equal to the limiting stress. In most cases, the limiting stress is used as the yield point; however, *Flow-3D* software allows the user to use a subjective limiting stress (Fig. 21–23).

$$\sigma_{VM} = \sqrt{\frac{3}{2} \sigma_{ij} \sigma_{ij} - \frac{1}{2} (\sigma_{kk})^2} \quad (7-1)$$

where:

σ_{ij} – elements of Cauchy stress tensor

The discrete grids in the area have been arranged in such a way that constraints for the elements under investigation are guaranteed. A simulation model has been defined for a linear operating range of those elements – within the area described by Hooke's law [12].

D'Alembert's principle is the basic equation describing the solid body motion, used to solve FSI problems [12]

$$\rho \frac{d^2 x}{dt^2} = \nabla \sigma + \rho b \quad (7-2)$$

where:

ρ – solid body density,

t – time,

x – coordinates of the points

σ – Cauchy stress tensor

\mathbf{b} – mass forces

In the approach slight, gradual deformations calculated from the formula were applied:

$$E' = \frac{1}{2} \left\{ \left[\nabla(\delta x) \right]^T + \nabla(\delta x) \right\} = \frac{1}{2} \left[\frac{\partial(\delta x)_i}{\partial x_j^n} + \frac{\partial(\delta x)_j}{\partial x_i^n} \right] e_i e_j \quad (7-3)$$

where:

E' – increase in strain

i, j – indices to describe the Cartesian coordinates in directions

e_i – unit vector in the system

δx – describes the displacement vector

$$\delta x = x^{n+1} - x^n \quad (7-4)$$

where:

x^n – is the position of the preceding point in the solid body at moment n

x^{n+1} – is the position of the point in the solid body j at moment $n+1$

The Cauchy stress tensor for the moment $n+1$, σ^{n+1} is obtained from the linear Hooke's model:

$$\sigma^{n+1} = \sigma^n + \left(K - \frac{2}{3}G \right) tr(E') + 2GE' \quad (7-5)$$

where:

$n, n+1$ – are time indices

K – volumetric modulus of elasticity

G – modulus of non-dilatational strain,

$tr(E')$ is a trace of the strain tensor, viz. a sum of its elements on the main diagonal.

In the algorithm, relationships between material constants are used:

$$K = \frac{E}{3(1-2\nu)}, \quad G = \frac{E}{2(1+\nu)} \quad (7-6)$$

The conditions of the acceleration (127) are solved according to the location of the points at various times:

$$\rho \frac{d^2 x}{dt^2} = \rho \left(\frac{x^{n+1} - 2x^n + x^{n-1}}{\Delta t^{n+1} \Delta t^n} \right) \quad (7-7)$$

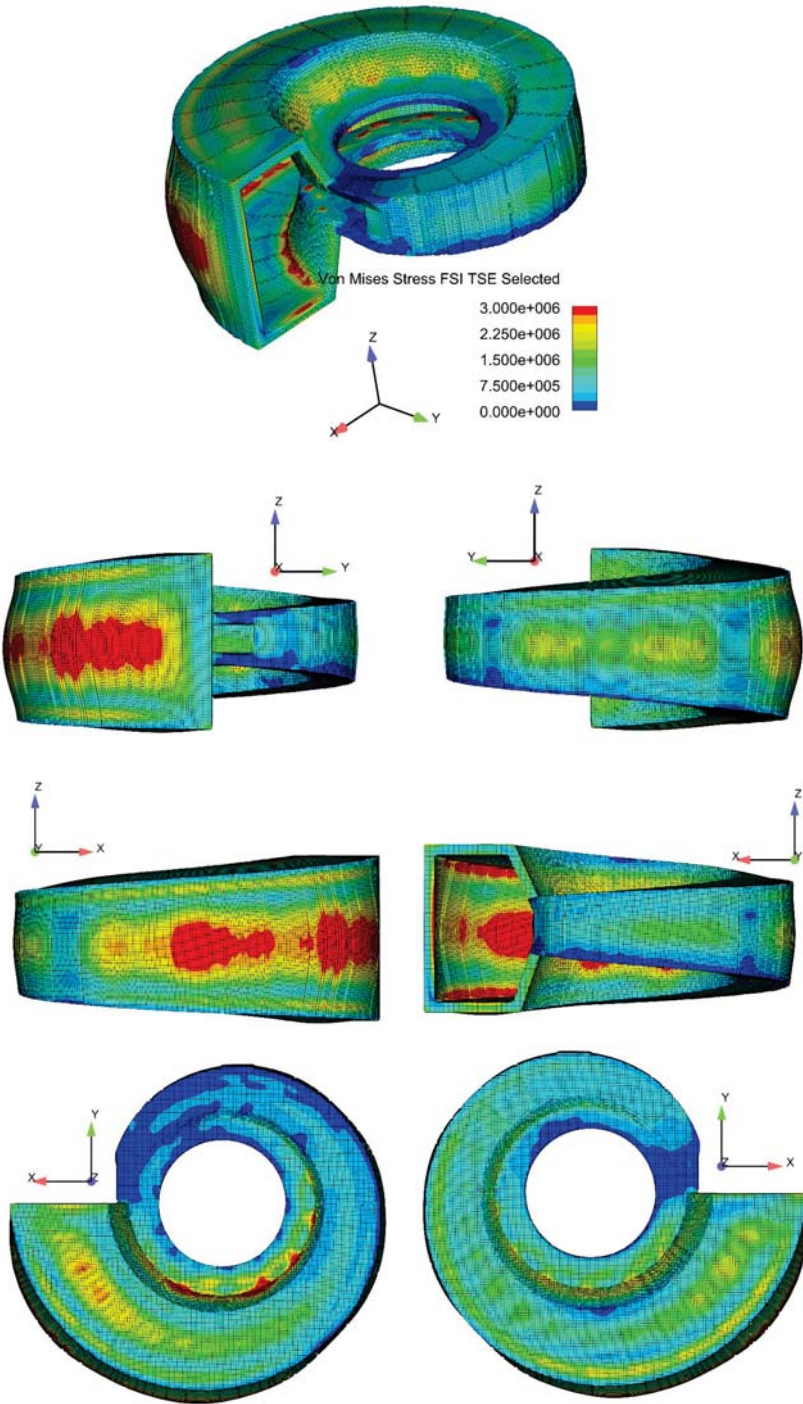


Fig. 21. Stresses according to Mises theory [Pa] against deformed elements in non-uniform scale – inlet spiral

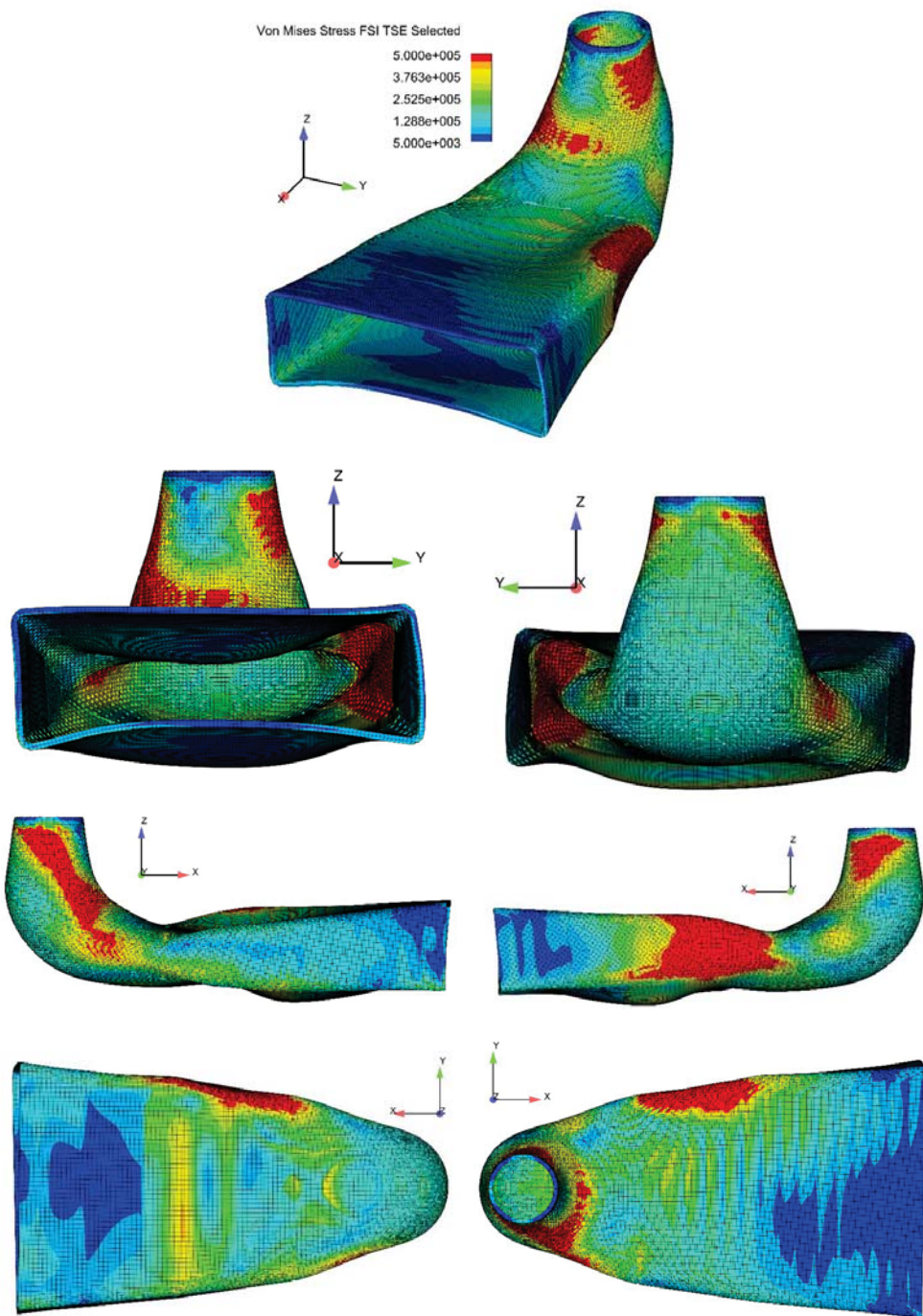


Fig. 22. Stresses according to Mises theory [Pa] against deformed elements in non-uniform scale, pipe bend

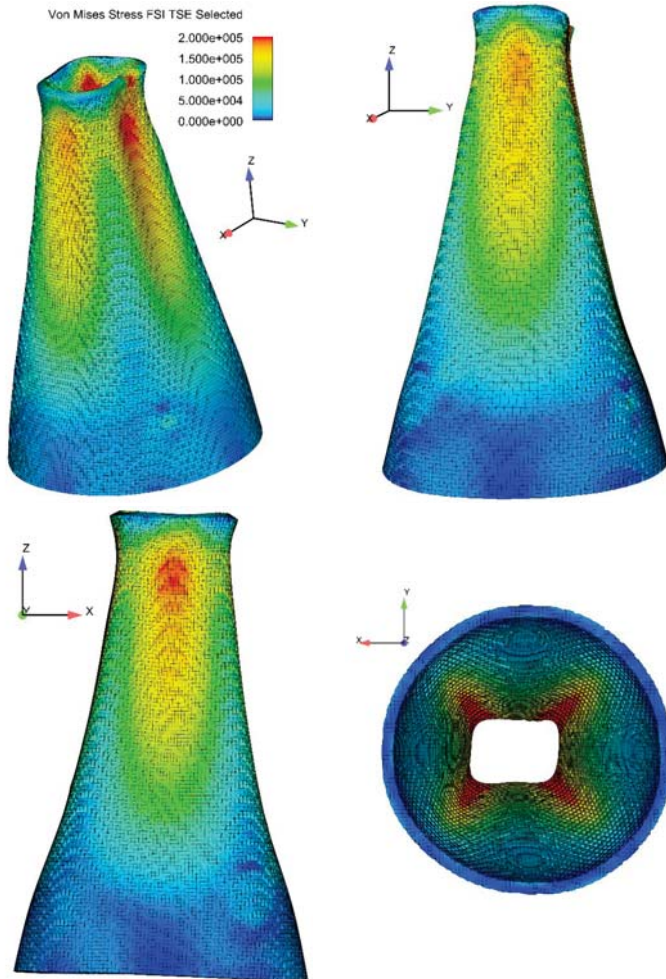


Fig. 23. Stresses according to Mises theory [Pa] against deformed elements in non-uniform scale, conical suction pipe

The interaction of the fluid and the solid area as well as the evolution of the stress tensor will determine the boundary conditions on the solid surface. If the solid surface contacts the fluid, then the local pressure determines the force of interaction $n\sigma^{n+1}$. Therefore:

$$n\sigma^{n+1} = -np_{fluid} \quad (7-8)$$

For all parts of hydroelectric power installation subject to FSI analysis the following parameters of materials were assumed:

- ▶ material – steel
- ▶ density 7700 [kg/m³]
- ▶ Young's modulus 2.15 e+11 [Pa]
- ▶ Poisson's rate 0.3

8. Ecological criteria for the operation of the installations under analysis

The consideration of the environmental criteria and standards aimed at minimizing the negative environmental impact of turbines is becoming one of the fundamental principles applied in the choice of hydroelectric power installations. Most serious harm is done to the fish population. The variability of pressure, velocity, strains and sudden changes of shapes and geometry of the channels in which a fish can move will decrease its survival rate.

The trajectory to be covered by a fish moving from the upper to the lower station contains a series of factors affecting its strength. Zones occur with sudden pressure increases and decreases, cavitation areas where a fish is exposed to abrasion, hitting, crushing and turbulences. The Alden turbine is one among few where at the design stage it was tried to regard the environmental criteria established by [2]. The criteria are shown below:

- ▶ peripheral velocities of the rotor should not exceed 12 [m/s],
- ▶ the minimum pressure in the rotor should not be under 69 [kPa],
- ▶ the rate of pressure variation in the rotor should be under 550 [kPa/s],
- ▶ the rate of velocity variation in the shearing zone should not exceed 4.5 [m/s] per 2.54 [mm],
- ▶ the rate of shearing stress variations should be not higher than 180 [m/s/m],
- ▶ the spacing between the rotary and stationary parts should be shorter than 2 [mm],
- ▶ the flow channel in the rotor should be as large as possible,
- ▶ the number and length of rotor blade edges should be minimized.

At the location points at the guide apparatus inlet provided as a mobile measuring point moving as water flowed by. The measured values of pressure and velocity are shown below

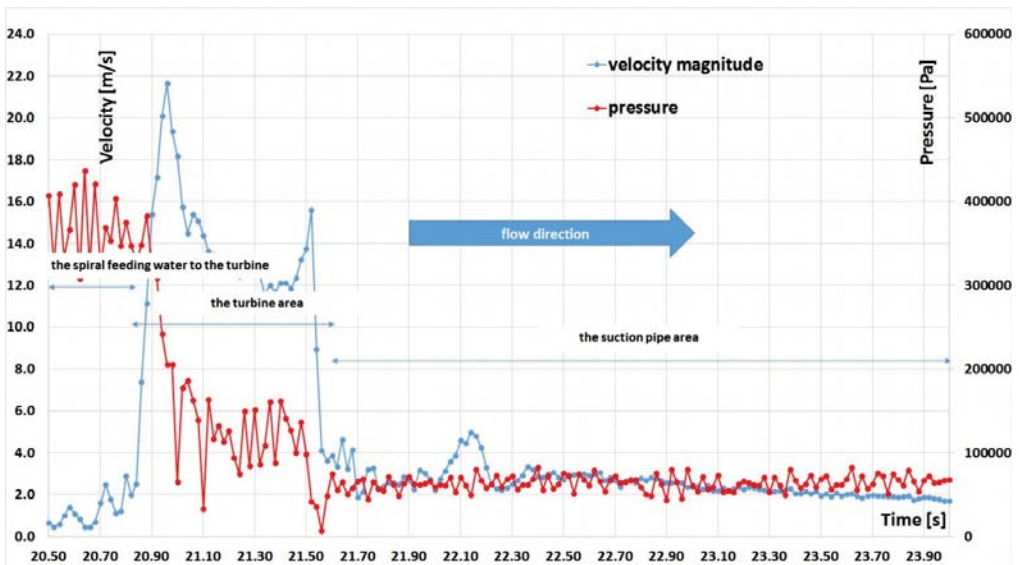


Fig. 24. Record of pressure and velocity values at the mobile measuring point

(Figure 24). In the figure, three areas are marked: the area of the spiral feeding water to the turbine, the turbine area and the suction pipe area. Each of those areas was described with the pressure and velocity values recorded at the mobile measuring point moving as water flows by.

9. Summary

The results presented in conjunction with the analyses have been entirely obtained from CFD modelling. Not all analyses are directly feasible in the proposed post-processing interfaces of *Flow-3D* or *FlowSight*. Some analyses required resorting to advanced *FlowSight* techniques through enquiries, definition of variables or by using programming.

Attention was focused not only on the development of models, simulations and analyses of results, but attempts were also made at contemporary analytical methods for solving CFD problems. The application of the Navier-Stokes equation also referred to as the Reynolds equation was described in brief. For the specific nature of the problem under investigation, a modification resulting from the necessity of regarding the turbulent momentum flux in the Reynolds tensor was described. The most onerous problems occurring in the operation of hydroelectric power installations are described: cavitation, vorticity and hydrodynamic loads. Some results for mechanical and biomechanical analyses are presented. For the selected parts of the system – viz. the inlet spiral and the suction pipe – their stress distributions according to the effort theory of von Mises are displayed, as well as a picture of the parts deformed.

References

- [1] Alto P., *“Fish Friendly” Hydropower Turbine Development and Deployment: Alden Turbine Preliminary Engineering and Model Testing [M]*, Washington D.C.: 2011.1019890, USA, E Electric Power Research Institute, 3420 Hillview Avenue, Palo Alto, California 94304-1338, 2011.
- [2] Cook T.C., Hecker G.E., Amaral S.V., Stacy P.S., Lin F., Taft E.P., *Final report – pilot scale tests Alden/Concepts NREC Turbine [M]*, Holden MA, USA, Prepared for U.S. Department of Energy, Washington, DC., USA, Contract No. DE-AC07-99ID13733, 2003.
- [3] Fay C., Hecker G., Hogan T., Perkins N., *Alden Turbine Market Analysis for New York State, Final Report, Report Number 13-19 [M]*, Albany, New York, New York State Energy Research and Development Authority, Alden Research Laboratory, Inc., 2012.
- [4] Orszag S.A., Yakhot V., Flannery W. S., Boysan F., Choudhury D., Maruzewski J., Patel B., *Renormalization Group Modeling and Turbulence Simulations [C]*, International Conference on Near-Wall Turbulent Flows, Tempe, Arizona, 1993.
- [5] Twaróg B., *An analysis of the application of the Alden turbine - a case study of the Dobczyce hydroelectric power plant [J]*, Technical Transactions, 1-Ś/2015, 147–156.

- [6] Haimes R., Kenwright D., *On the velocity gradient tensor and fluid feature extraction [C]*, 14th Computational Fluid Dynamics Conference, Fluid Dynamics and Co-located Conferences, Norfolk,VA,U.S.A., <https://doi.org/10.2514/6.1999-3288>, 1999, (access).
- [7] Zhang Y., Liu K., Xian H., Du X., *A review of methods for vortex identification in hydroturbines [J]*, Renewable and Sustainable Energy Reviews, 81, 2018, 1269–1285.
- [8] Kumar P., Saini R.P., *Study of cavitation in hydro turbines-A review [J]*, Renewable and Sustainable Energy Reviews 14, 2010, 374–383.
- [9] Bogusławski A., Drobniak S., Tyliczszak A., *Turbulencja – od losowości do determinizmu, Modelowanie Inżynierskie [M]*, Gliwice, Instytut Maszyn Ciepłych, Politechnika Częstochowska, 2008, 41–48.
- [10] Haller G., *An objective definition of a vortex [J]*, Journal of Fluid Mechanics, 525, 2005, 1–26.
- [11] Hou G., Wang J., Layton A., *Numerical Methods for Fluid-Structure Interaction A Review [J]*, Communications in Computational Physics, 12, 2, 2012, 337–377.

Hubert Danielewski  orcid.org/0000-0003-4675-6236

hubert_danielewski@o2.pl

Faculty of Mechatronics and Mechanical Engineering, Kielce University of Technology

LASER WELDING OF PIPE STUBS MADE FROM SUPER 304 STEEL.

NUMERICAL SIMULATION AND WELD PROPERTIES

SPAWANIE LASEROWE KRÓCÓW RUROWYCH ZE STALI SUPER 304.
SYMULACJE NUMERYCZNE ORAZ WŁAŚCIWOŚCI ZŁĄCZA SPAWANEGO

Abstract

The laser welding process of test pipe stubs which were made from Super 304 stainless steel is usually used to produce components of a power infrastructure. It was numerically simulated and the obtained results are presented in this paper. For the laser welding method, the weldability of this steel is presented, as well as the results of strength and microstructure tests of a joint welded at the parameter settings selected from a numerical simulation. The chemical composition, including the increased content of alloying elements such as chromium and nickel, improves the strength characteristics of the welded steel, allowing for the production of components of superheaters and partition walls of boilers operating in supercritical parameters.

Keywords: laser welding, Super 304 austenitic steel, numerical simulation, SimufactWelding, properties of laser welded joints

Streszczenie

Artykuł przedstawia wyniki symulacji numerycznej procesu spawania laserowego króćców próbných z nierdzewnej stali kotłowej Super 304 przeznaczonej do wykonywania komponentów instalacji energetycznych. Przedstawiono spawalność stali z zastosowaniem metody spawania laserowego, a także wyniki badań wytrzymałościowych oraz mikrostruktury złącza spawanego wykonanego na podstawie parametrów dobranych w symulacji numerycznej. Skład chemiczny, a w tym zwiększona zawartość pierwiastków stopowych, takich jak chrom i nikiel poprawia charakterystyki wytrzymałościowe spawanej stali, umożliwiając wykonywanie z niej komponentów przegrzewaczy oraz ścian działowych kotłów pracujących w parametrach nadkrytycznych.

Słowa kluczowe: spawanie laserowe, austenityczna stal nierdzewna Super 304, symulacje numeryczne, SimufactWelding, właściwości wytrzymałościowe złączy spawanych laserowo

1. Introduction

Recently, in power plants and chemical and petrochemical industries, the use of new high-alloy steels such as Super 304 is considered. Due to the high corrosion resistance and creep resistance of these types of materials in structural applications, their weldability and new welding technology are being developed. The content of chromium and nickel alloys improves anti-corrosion parameters, which extends the operating time of welded elements [1–3].

Although Super 304 austenitic stainless steel is characterized as being well weldable, the laser beam welding (LBW) requires a careful control of a welding temperature [4] and obtaining a proper weld without welding defects is difficult to achieve. Conventional welding methods require the preparation of joining edges by chamfering [5]. Due to the narrowness of the fusion zone, proper fitting of joining edges is required (Fig. 1). The acceptable range of parameters, required to weld a material, could be estimated by using a numerical simulation with a dedicated welding process solver. The paper presents the results of a LBW-based joining method of Super 304 steel, a numerical simulation of the process and the obtained results of welded joint tests.

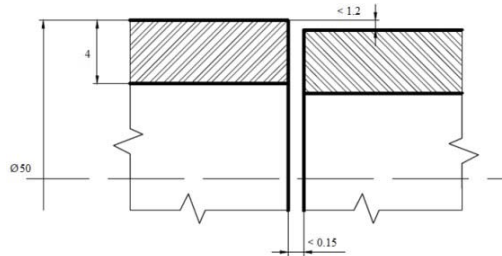


Fig. 1. Preparation of Super 304 pipes edges for laser welding

The Super 304 steel has been developed to replace the currently used 304 steel, which has good weldability due to a high content of chromium and nickel, but has a tendency for porosity at unfavorable operating parameters. The development of new generation materials, such as Super 304, as well as new welding technologies supported by a numerical simulation of the welding process, have contributed to numerous studies [6–8].

2. Material characteristics of Super 304 steel

High temperature resistance characteristic of Super 304 steel is caused by a high content of chromium and nickel elements (Tab. 1), which improves creep resistance. The 18% chromium content increases corrosion resistance and hardenability of the alloy. Niobium is another alloying element that improves creep resistance as well as hardenability. The low carbon content improves the weldability of Super 304 steel, while reducing the risk of hydrogen cracking. In turn, the occurrence of alloying elements, such as copper and manganese, improves the overall strength, and in particular fracture toughness [9].

Table 1. Chemical composition of Super304 steel

Element	C	Si	Mn	Ni	Cr	Cu	Nb	N
Content [%]	0.1	0.3	1.0	9.5	18.0	3.0	0.5	0.09

The traditional method of welding requires the use of an additional material, while the laser welding process is much faster, gives a narrow weld by melting the edge of the material, which also creates a narrow heat affected zone and therefore this process does not require any additional heat treatment.

3. Laser welding of Super 304 steel pipe stubs – numerical simulation

A numerical simulation of the welding process is a complex issue. The obtained computational results are only an estimation of actual test observations. An effective modeling of the welding process requires the use of many simplifications of physical phenomena which occur during welding. The SimufactWelding program uses the method of volumetric heat sources. The volume of a laser beam takes the melting point of a material. The energy fraction associated with the cylindrical heat source describes the energy fraction that will be carried out through a cylinder (Fig. 2), while the remaining energy – through surface heat sources. The parameters of a laser welding process assumed in the numerical simulation are shown in Tab. 2.

Table 2. Settings of heat source parameters assumed in the numerical simulation

Heat source parameters	Power [W]	Velocity [m/s]	Efficiency
Value	4000	0.03	0.8

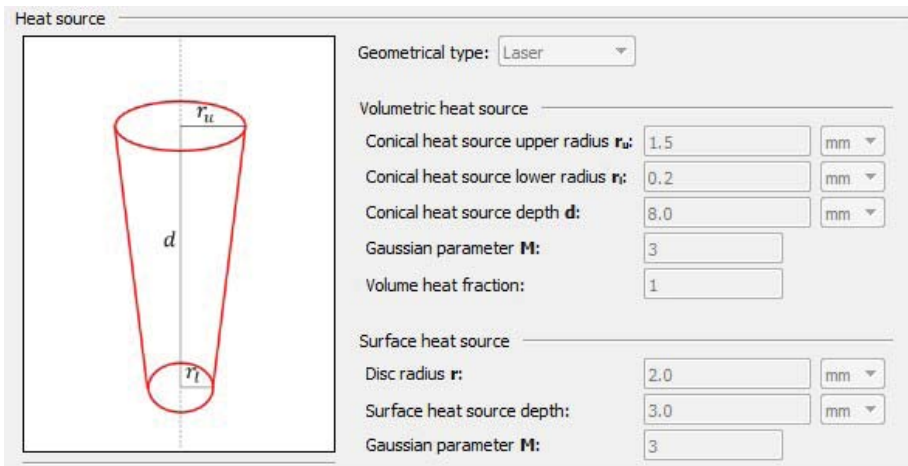


Fig. 2. Programmed volumetric heat sources geometry parameters

The simulated temperature distribution (Fig. 3) showed a correct form of the weld with the material melting through the entire thickness of the pipe. Obtained in the numerical simulation, the predicted shape of the weld shows that the parameters assumed for this simulation should be appropriate for a real laser welding of test pipe stubs made of Super 304 steel.

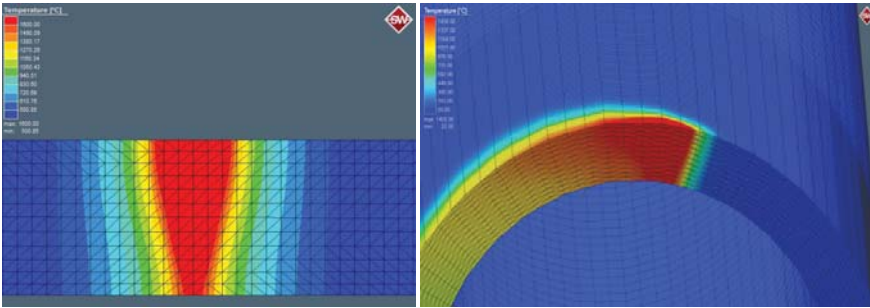


Fig. 3. The simulation of the temperature distribution in the cross and longitudinal section of laser welds

4. Laser welding of Super 304 steel stubs

A circumferential laser welding of pipes made from Super 304 steel with a thickness of 4mm, outer diameter of 50 mm and length of 150 mm was done at settings of parameters shown in Tab. 3.

Table 3. Welding parameters of Super304 steel pipes joints

Heat source parameters	Power [W]	Velocity [m/s]	Frequency [kHz]
Value	4000	0.03	50

The welding device used was a high power CO₂ laser Trumpf TruFlow 6000 with the maximum power of 6 kW mounted on the additional rotary axis of a TruLaser Cell 1005 work center. A welding head with a focal length of 200 mm was used. The pipes were fixed on a rotary axis. Inside the pipes, due to the protection of a weld root, shielding gas (argon with the efficient of 12 l/min) was conveyed. Due to the highest ionization potential, helium with coaxial-blown of 20 l/min was used to protect the face of the weld. The obtained results of weld tests refer to joints without a post-weld treatment [10, 11].

5. Non-destructive tests

The most frequently observed welding defects that may occur during a circumferential laser welding are incomplete welds, groove contraction, porosity (Fig. 5) or poor connection. The evaluation of weld quality requires several tests of welding methods. The results of visual tests (VT) and ultrasonic tests (UT) of welds are presented below.

Visual testing was conducted according to PN-EN ISO 17637 [12]. The acceptable quality level was identified according to PN-EN ISO 13919-1 [13]. The weld qualified to B quality level (stringent requirements) is shown in Fig. 4.

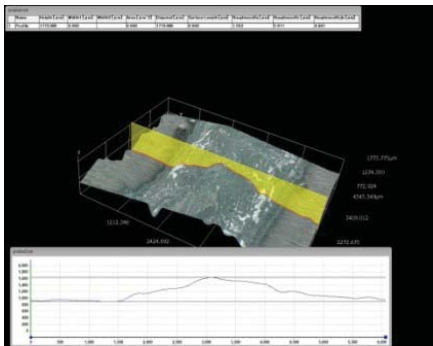


Fig. 4. Visual testing of a weld's face surface geometry for Super 304 steel

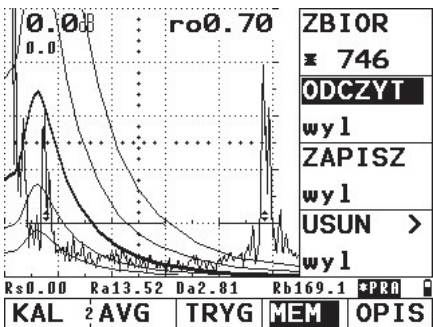


Fig. 5. Ultrasonic tests result – detection of gas pore inside weld

In the performed test, an ultrasonic flaw detector USM 35S of GE (Krautkramer) industry was used. The echo-sounding method was applied by front (MSEB-4) and side (MWB 70 4) measuring head using the DGS (DDSR = 0.7 mm) scale. A typical ultrasonic-based detection of a gas pore is shown in Fig. 5. The defect was recognized as the lack of the side fusion on the side of the weld edge, which might have been caused by a faulty crystallization process as well as a gas pore defect.

6. Destructive tests of welded joints

The austenitic structure and alloy elements increase the strength characteristics of Super 304 steel and, in addition, a reduction of the heat affected zone in the base material was obtained by using laser welding with optimized parameters selected by a numerical simulation. It should be noted that the strength characteristics of a weld are of decisive importance in determining the acceptance level of welded joints.

When considering the durability and safety of welded gas or boiler installations, it is important to ensure that the welded material and the heat affected zone (HAZ) have properties similar to the basic material (BM). To examine the quality of welded joints obtained without a post-heating treatment, the microhardness testing in cross-section was done. The hardness test was carried out in accordance with PN-EN ISO 6507-1 [14]. Fig. 7 shows the results of microhardness of the weld cross-section.

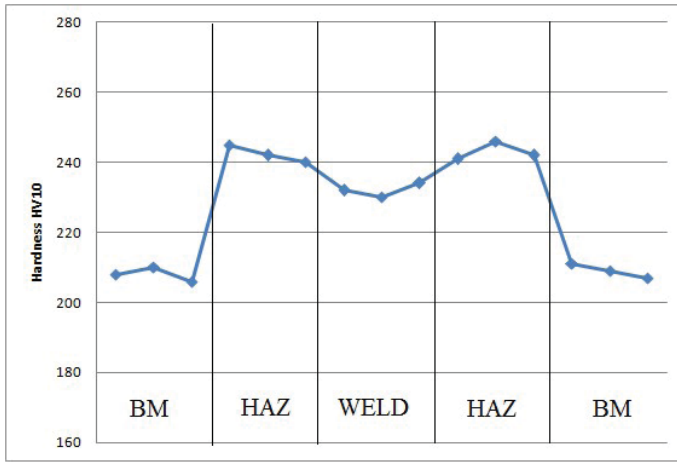


Fig. 6. The microhardness distribution in the weld cross-section

The results of the hardness test show an increase in the weld and HAZ. The hardness distribution is typical for the laser welding, with stronger reinforcement in the heat affected zone and slightly lower in the welding zone. According to PN-EN ISO 15614-11, the maximum allowable hardness limit for Vickers HV10 is 350 [15]. The obtained results do not exceed the value of 350 HV10 (maximum measured value – 247 HV10), so the obtained weld does not require any additional heat treatment.

7. Metallographic test

A metallographic study was carried out in accordance with PN-EN ISO 17639 [16]. Microscopic and macroscopic examinations were performed using a Hirox KH-8700 digital confocal microscope. The macrostructure was shown at a magnification of 35x (Fig. 8) and the microstructure with a magnification of 600x (Fig. 9). The macroscopic image of the weld cross-section shows properly formed joints. At the edge of the weld, a gas pore is visible, which was detected in the ultrasonic test.

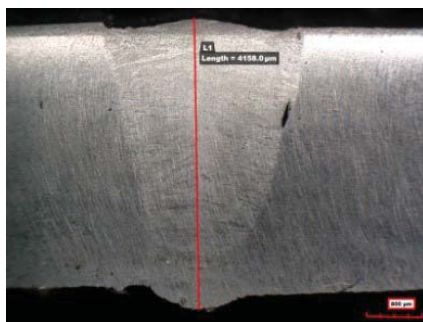


Fig. 7. Macrostructure of weld (Hirox confocal digital microscope, magnification 35x)

The obtained weld joints are characterized by the lack of welding defects except for a small pore of gas. Typical BM, HAZ and weld microstructures images for Super 304 austenitic stainless steel weld are shown in Fig. 9. The typical final weld structure of Super 304 steel is austenitic.

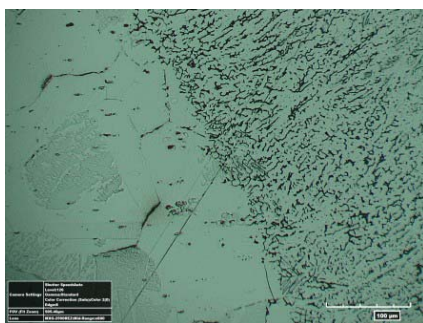


Fig. 8. Microstructure of weld (Hirox KH-8700 with magnification of 600x)

8. Conclusions

A study of laser welded pipe stubs was carried out. According to PN-EN ISO 13919-1 standard [13], stringent requirements of B quality level were obtained. Destructive and nondestructive tests confirmed proper strength characteristics and correct cross-section welds construction. According to PN-EN ISO 15614-11 standard [15], due to the obtained hardness values which do not exceed the limit of 350 HV10, post-weld treatment for joints welded by a laser is not required. The numerical simulation gave results similar to the real tests with samples welded by a laser.

The research was carried out in the NCBiR project of National Centre for Research and Development (NCBiR) No. LIDER/31/0173/L-8/16/NCBR/2017 „Technology of manufacturing sealed weld joints for gas installation by using concentrated energy source”.

References

- [1] Viklund P., Hjörnhede A., Henderson P., Stålenheim A., Pettersson R., *Corrosion of superheater materials in a waste-to-energy plant*, "Fuel Processing Technology", Vol. 105/2013, 106–112.
- [2] De Oliveira M.P., Zhang W., Yu H., Bao H., Xie X., *Recent developments in niobium containing austenitic stainless steels for thermal power plants*, [in:] Conf. Energy Materials 2014, Xi'an Shaanxi Province, China, 2014, 271–277.
- [3] Koscielniak B., Smola G., Grzesik Z., Hernas A., *Oxidation resistance of austenitic steels under thermal shock conditions in an environment containing water vapor*, "High Temperature Materials and Processes", Vol. 73(4)/2018, DOI: 10.1515/htmp-2016-0209 (access).
- [4] Danielewski H., Skrzypczyk A., Antoszewski B., Zowczak W., Zrak A., *Microstructures and properties of laser welded Super304 steel pipe joints using LNM304 filler wire as an additional material*, Proc. SPIE, Vol. 10974/2018, art.109740P.
- [5] Scendo M., Radek N., Trela J., *Influence of laser treatment on the corrosive resistance of WC-Cu electrospark coatings*, "International Journal of Electrochemical Science", Vol. 8/2013, 9264–9277.
- [6] Radek N., Konstany J., *Cermet ESD coatings modified by laser treatment*, "Archives of Metallurgy and Materials", Vol. 57/2012, 665–670.
- [7] Klimpel A., *Technologie laserowe. Spawanie, napawanie, stopowanie, obróbka cieplna i cięcie*, Wyd. Politechniki Śląskiej, Gliwice 2012.
- [8] Gątarek, M., Słania J., Rawicki Ł., Golański G., Krawczyk R., Urbańczyk P., *Spawanie złączy doczołowych jednorodnych ze stali Super 304H*, „Przegląd Spawalniczy”, Vol. 88(4)/2016, 31–34.
- [9] Zbroja P., Ziewiec A., Tasak E., *Słoność do pęknięć gorących austenitycznej stali Super 304H przeznaczonej do pracy w podwyższonej temperaturze*, „Przegląd Spawalniczy”, Vol. 84(1)/2012, 10–14.
- [10] Słania J., Urbańczyk P., *Technologia wytwarzania oraz plan kontroli jakości przegrzewacza pary kotła parowego wg PN-EN 12952-5*, „Przegląd Spawalnictwa”, Vol. 5/2012, 29–41.
- [11] Skrzypczyk A., Danielewski H., *Properties and Microstructure of Laser Welded VM12-SHC Steel Pipes Joints*, "Archives of Metallurgy and Materials", Vol. 61(2B)/2016, 1143–1149.
- [12] PN-EN ISO 17637:2011 – Badania nieniszczące złączy spawanych – Badania wizualne złączy.
- [13] PN-EN ISO 13919-1:2002 Spawanie – Złącza spawane wiązką elektronów i wiązką promieniowania laserowego – Wytyczne do określania poziomów jakości według niezgodności spawalniczych.
- [14] PN-EN ISO 6507-1:2007 Metale – Pomiar twardości sposobem Vickersa – Część 1: Metoda badań.

- [15] PN-EN ISO 15614-11:2005 Specyfikacja i kwalifikowanie technologii spawania metali. Badanie technologii spawania. Część 11: Spawanie wiązką elektronów i wiązką promieniowania laserowego.
- [16] PN-EN ISO 17639:2013 Badania niszczące spawanych złączy metali – Badania makroskopowe i mikroskopowe złączy spawanych.

Sylwia Kosecka-Żurek  orcid.org/0000-0001-7428-8834

skosecka-zurek@pk.edu.pl

Faculty of Mechanical Engineering, Cracow University of Technology

APPLICATION OF IT TOOLS IN OPTIMIZATION OF LOGISTICS PROBLEMS

WYKORZYSTANIE NARZĘDZI INFORMATYCZNYCH DO OPTIMALIZACJI PROBLEMÓW LOGISTYCZNYCH

Abstract

This paper presents IT tools supporting logistics processes. Such processes include, for example, planning the optimal route for the transport of packages or proper packing of these packages in the car. The paper discusses selected computer tools that can be successfully used to improve logistics processes.

Keywords: optimization, logistics, supply chain management

Streszczenie

W artykule przedstawiono narzędzia IT wspierające procesy logistyczne. Procesy te obejmują na przykład planowanie optymalnej trasy transportu paczek lub właściwe rozlokowanie tych paczek w samochodzie. W artykule omówiono wybrane narzędzia komputerowe, które z powodzeniem można wykorzystać do usprawnienia procesów logistycznych.

Słowa kluczowe: optymalizacja, logistyka, zarządzanie łańcuchem dostaw

1. Introduction

Optimal planning (e.g. time, resources) is very desirable in logistics because it gives real profits. Many complex logistics processes can be significantly improved by using IT tools. This is not only registration of these processes in the IT system, which seems indispensable nowadays, but one step further: supporting these processes in order to obtain optimal results in terms of time saving and good use of human and equipment resources.

The most common problem of deliveries – Vehicle Routing Problem – is to minimize transport costs from one warehouse to any number of customers [1].

The problem of determining the optimal plan for transporting products between suppliers and customers is an NP-difficult problem, which means that there is no algorithm solving this problem in polynomial time [1].

The Polish language dictionary PWN [4] defines optimization as follows: organizing some activities, processes, etc. in such a way as to give the greatest possible results with the least amount of effort; searching by the mathematical methods for the best, due to the selected criterion, solutions of a given economic issue, taking into account certain restrictions.

In the current computerized times, IT tools provide great opportunities to optimize logistic processes.

2. Materials and methods

Vehicle route planning is one of the main logistical problems. It is not easy to find the best solution with many restrictions, such as:

- ▶ – availability of points,
- ▶ – availability of drivers,
- ▶ – limiting drivers' working time,
- ▶ – availability of appropriate cars,
- ▶ – car load capacity and other car features (speed, equipment),
- ▶ – accessibility of roads for specific types of cars and
- ▶ – ban on the joint transport of certain products.

The expected result is the shortest sum of routes and the least used cars.

Michlowicz shows [1], among others, such variations of currently existing supply problems:

- ▶ – CVRP (Capacity Vehicle Routing Problem) – the problem of deliveries with defined load capacities of vehicles; all vehicles have identical loads,
- ▶ – OVRP (Open Vehicle Routing Problem) – the vehicle does not return to the initial warehouse,
- ▶ – VRPTW (Vehicle Routing Problem with Time Windows) – CVRP extension for time windows for each customer,
- ▶ – SDVRP (Site-Dependent Vehicle Routing Problem) – the problem of deliveries with different load capacities of vehicles,

- ▶ – MDVRP (Multi Depot Vehicle Routing Problem),
- ▶ – MDVRPTW (Multi Depot Vehicle Routing Problem with Time Windows).

The distribution of packages in the car is yet another problem which is crucial for optimization. In this case, the following factors should be taken into account, e.g.:

- ▶ – where to take the packages (order of loading),
- ▶ – package sizes,
- ▶ – package shape,
- ▶ – dimensions of the car,
- ▶ – the possibility of stacking packages and
- ▶ – ban on the joint transport of certain products (cannot be transported together).

The OptaPlanner open source tool [3] is useful to solve the first of the described problems. It contains many examples and its code is officially available. One can modify it for their own purposes. OptaPlanner includes an example called “Vehicle Routing”. For test purposes, one can also use the supplied example input data or prepare new data, modify restrictions and “reprogram” the operation way. OptaPlanner has a user-friendly interface (see Fig. 1).

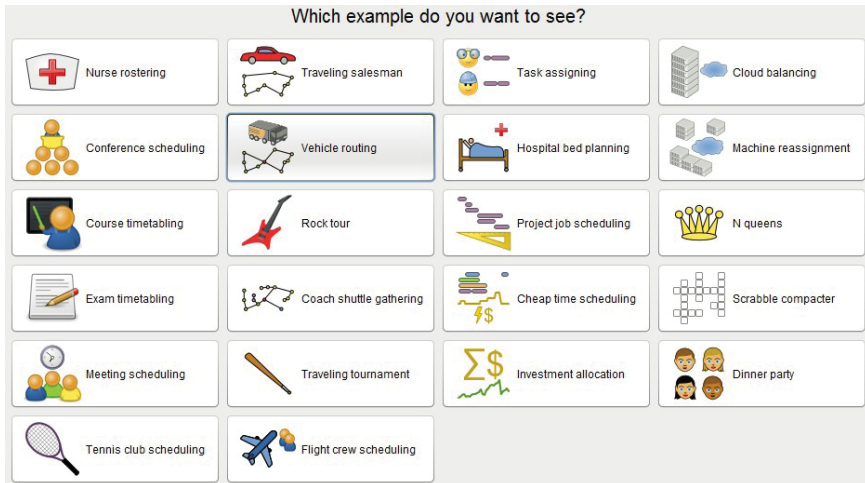


Fig. 1. OptaPlanner – sample GUI

The basic optimization task is as follows:

1. Input data:
 - ▶ a fleet of vehicles with a certain capacity,
 - ▶ points of delivery (coordinates),
 - ▶ customer service time and
 - ▶ time windows - in variant.
2. Problem:
 - ▶ Receipt of shipments from customers and transport to the warehouse.
3. Solution (optimization):
 - ▶ minimization of the total distance covered by all vehicles.

3. Results

Let's prepare simple input data:

```
TYPE : CVRP (basic case, without time windows)
DIMENSION : 3 (three points where the car stops)
EDGE_WEIGHT_TYPE : EUC_2D (euclidean distances)
CAPACITY : 50 (capacity of vehicle)
NODE_COORD_SECTION (points and coordinates)
  1 10 20 (the first point with coordinates 10, 20)
  2 40 70 (the second point with coordinates 40, 70)
  3 10 100 (the third point with coordinates 10, 100)
DEMAND_SECTION (points, three because "DIMENSION : 3")
  1 0 (ordinal number and load to be delivered, nothing is delivered
to the first point)
  2 1 (ordinal number and load to be delivered)
  3 1 (ordinal number and load to be delivered)
DEPOT_SECTION (depots)
  1 (the first point is depot)
  -1
VEHICLES : 2 (two vehicles)
```

The result is shown in a graphical form in Fig. 2. The figure is a screenshot, with the contrast enhanced and descriptions improved.

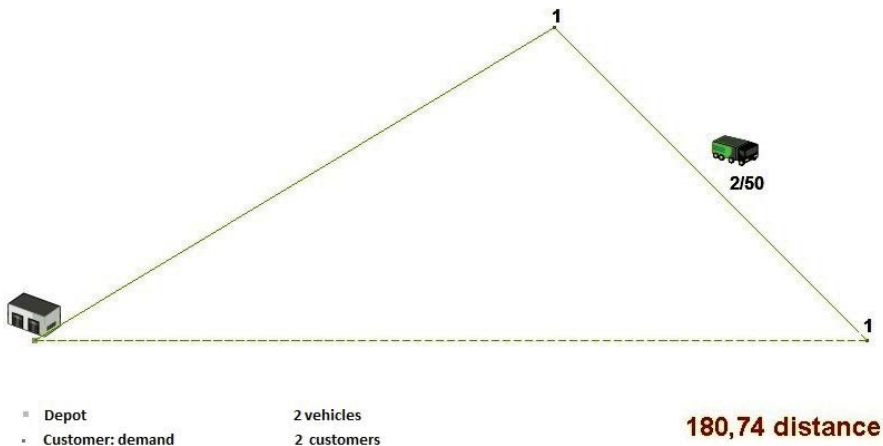


Fig. 2. OptaPlanner – the result of the planning for the example discussed

As shown in Fig. 2, one of the two available cars has been used. Description 2/50 is the reference of the load (2) to the capacity of the vehicle (50). The numbers next to the points indicate the load to be delivered to the point. Let's increase the load now:

1. Input data:

```
TYPE : CVRP
DIMENSION : 3
EDGE_WEIGHT_TYPE : EUC_2D
CAPACITY : 50
NODE_COORD_SECTION
  1 10 20
  2 40 70
  3 10 100
DEMAND_SECTION
  1 0
  2 40
  3 12
DEPOT_SECTION
  1
  -1
VEHICLES : 2
```

Result is shown in Fig.3. The illustration is a screenshot, with the contrast enhanced and descriptions improved.

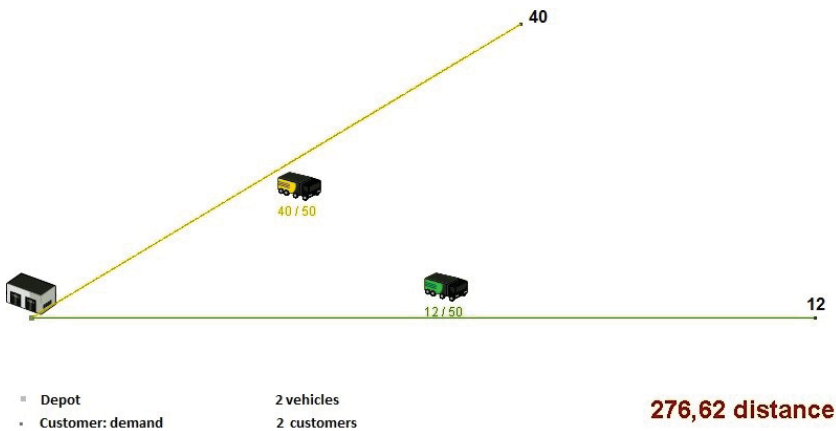


Fig. 3. OptaPlanner – the result of the planning after the modification of the first example (two vehicles)

Due to the load increase, the second car should be used. As shown in Fig. 3, both available cars have been used because the load exceeds the capacity of a single vehicle.

Let's consider another example: add a second depot, increase the number of locations and cars. The modified problem is shown in a graphical form in Fig. 4.

2. Input data:

```
DIMENSION : 10
EDGE_WEIGHT_TYPE : EUC_2D
CAPACITY : 50
NODE_COORD_SECTION
 1 10 20
 2 40 50
 3 10 100
 4 20 100
 5 25 80
 6 30 20
 7 35 40
 8 40 60
 9 45 65
10 50 100
DEMAND_SECTION
1 0
2 0
3 12
4 40
5 50
6 5
7 5
8 5
9 10
10 2
DEPOT_SECTION
 1 (the first point is depot)
 2 (the second point is depot)
-1
VEHICLES : 3
```

The obtained result is shown in Fig. 5. Let's now show a much more complicated example that the OptaPlanner can optimize: 100 customers, time windows (Fig. 6). The temporary solution obtained after interrupting the optimization a couple of seconds after launch is shown in Fig. 7. The final solution after optimization is presented in Fig. 8. One can easily notice that the total distance was decreased in comparison with the preliminary solution presented in Fig. 7.

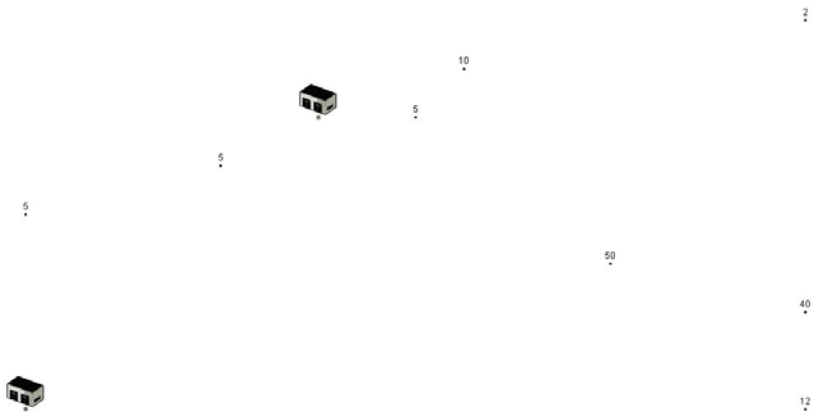


Fig. 4. OptaPlanner – planning problem: ten points, two depots, three vehicles.
This is a screenshot, with the contrast enhanced

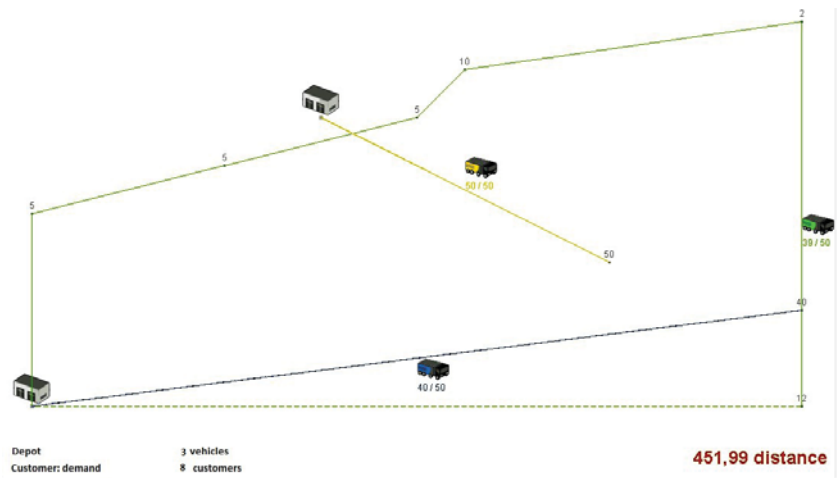


Fig. 5. OptaPlanner – the result of the planning: planned routes for three vehicles.
This is a screenshot, with the contrast enhanced and descriptions improved

Another problem that is crucial for optimization is the arrangement of packages in the car. It can be assumed that this is a typical optimization problem - knapsack problem. It is a problem of choosing objects so that their total value would be as large as possible and simultaneously fit in the backpack. In our case, the items are parcels and the car is a backpack. IT tools can also be used for this problem.

Additional restrictions which often occur are, for example:

- ▶ where to take the packages (order of loading),
- ▶ package shape,
- ▶ dimensions of the car,
- ▶ the possibility of stacking packages or
- ▶ packages cannot be transported together.



Fig. 6. OptaPlanner – planning problem which points time windows. This is a screenshot, with the contrast enhanced and descriptions improved

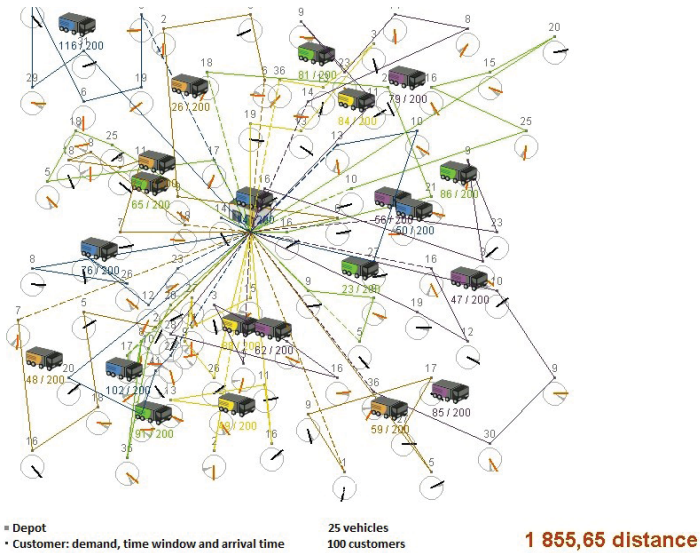


Fig. 7. OptaPlanner – the result of planning for problem which points time windows (an interrupted optimization with a temporary solution). This is a screenshot, with the contrast enhanced and descriptions improved

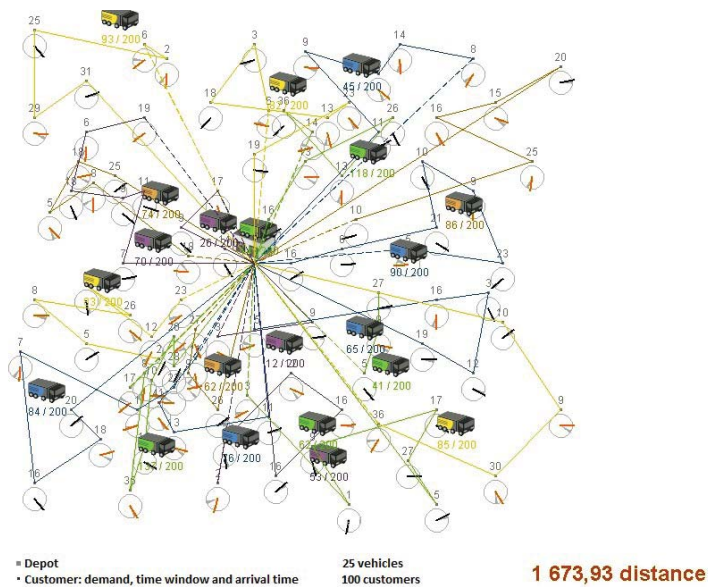


Fig. 8. OptaPlanner – result of planning for problem which points time windows (full optimization).
 This is a screenshot, with the contrast enhanced and descriptions improved

IT tools can also be used to solve such problems. An example is the freeware Goodloading application [7], which supports the optimal placement of cargo in the car. It optimizes positioning of cuboidal parcels of specified dimensions in a car (set) of specified dimensions. It also supports the situation of stacking packages.

4. Discussion/Conclusion

IT tools significantly contribute to improving the efficiency of logistics processes. The examples presented in this paper show that there are many problems in logistics that require optimization. There are different IT tools to cope with this task. The ones described here – OptaPlanner [3] and Goodloading [7] are commonly available. The former also allows one to create new solutions. This is a big advantage, because one can add a way of optimization for a specific situation.

Goodloading [7] gives a quick answer to how to optimally place the load in the car. However, there is a lack of planning packages with unusual shapes (one can only plan cuboids), taking into account the axle load or planning several cars at the same time (sets).

Logistics is a good domain to implement optimization algorithms and combine them with other solutions to achieve cost and time minimization. Simultaneously, this area seems to be excellent environment for testing efficiency of various optimization tools.

References

- [1] Michlowicz E., *Rozwiązywanie problemów dostaw w systemach dystrybucji*, "Logistyka", Vol. 4/2012, 557–564.
- [2] Michlowicz E. Smolińska K. Zwolińska B., *Optymalizacja dystrybucji w zadaniach transportowo – produkcyjnych*, "Logistyka", Vol. 4/2015, 4898–4905.
- [3] *OptaPlanner website*, <https://www.optaplanner.org> (access: 14.12.2018).
- [4] *Słownik języka polskiego PWN*, <https://sjp.pwn.pl> (access: 14.12.2018).
- [5] Piocha S., Dyczkowska J., *Zarządzanie łańcuchem dostaw – logistyka zaopatrzenia*, "Logistyka", Vol. 5/2012, 733–740.
- [6] Waściński T., *Procesy logistyczne w zarządzaniu łańcuchem dostaw. Logistics processes in supply chain management*, "Zeszyty Naukowe Uniwersytetu Przyrodniczo-Humanistycznego w Siedlcach Seria: Administracja i Zarządzanie", Vol. 103/2014, 25–38
- [7] *Goodloading website*, <https://goodloading.com/> (access: 14.12.2018).

Anna Kufel  orcid.org/0000-0002-5104-0630

Stanisław Kuciel  orcid.org/0000-0001-9244-7499

stask@mech.pk.edu.pl

Institute of Material Engineering, Faculty of Mechanical Engineering, Cracow University of Technology

COMPOSITES BASED ON POLYPROPYLENE MODIFIED WITH NATURAL FILLERS TO INCREASE STIFFNESS

KOMPOZYTY NA OSNOWIE POLIPROPYLENU MODYFIKOWANE NATURALNYMI NAPEŁNIACZAMI W CELU ZWIĘKSZENIA SZTYWNOŚCI

Abstract

Composites based on a polypropylene matrix with coffee ground powder, wood flour and tuff of a mass weight of 12.5wt% were produced by the method of injection moulding. Tests of tensile and bending strength properties were carried out and Charpy impact was determined at three temperatures: -24°C, 22°C and 80°C. Scanning electron microscopy (SEM) images were taken to assess the effects of reinforcement and homogenization of mixtures and to determine the characteristics of the microstructure. Composites with 12.5wt% coffee ground powder, wood flour and tuff were characterized by an increase the elastic modulus. Tensile strength slightly decreased for composites with ground coffee grains and tuff.

Keywords: polypropylene, natural fillers, mechanical properties, composites

Streszczenie

Wytworzono kompozyty na osnowie polipropylenu modyfikowane zmieloną kawą, mączką drzewną oraz tufem w ilości masowej 12.5%. Kompozyty zostały wytworzone metodą formowania wtryskowego. Została wykonana statyczna próba rozciągania oraz zginania, a także próba udarności w trzech temperaturach eksploatacji: -24°C, 22°C, 80°C. W celu określenia charakterystyki i zbadania wpływu wzmocnienia oraz homogenizacji mieszaniny wykonano zdjęcia na skaningowym mikroskopie elektronowym. Kompozyty z 12.5wag.% zawartością kawy, mączki drzewnej lub tufu charakteryzują się zwiększonym modulem sprężystości oraz nieznacznym spadkiem sztywności dla kompozycji z kawą i tufem.

Słowa kluczowe: polipropylen, napelniacze naturalne, właściwości mechaniczne, kompozyty

1. Introduction

Natural resources are increasingly used as reinforcements of thermoplastic polymers and provide an excellent alternative to synthetic fibres [1]. Natural raw materials added to polymeric materials increase the modulus of elasticity, which leads to increased stiffness of the products made on this basis. One of the problems of using natural fillers is their low compatibility with hydrophobic polymer matrices. To improve the adhesion between the hydrophilic fibres and the hydrophobic matrix, the fibres are usually surface-modified (silanization) or compatibilizing agents are added to the polymer matrix [2]. Polypropylene products are currently used in almost all fields. Polypropylene (PP) has become a widely used polymer material that possesses low density, but high thermal stability as well as a low cost of production.

Natural fillers (lignocellulosic and mineral) such as jute [3], abaca [4], kaolin [5], talc [6] etc. are commonly used to reinforce the polymer. One natural filler is volcanic tuff, which is a compact, porous sedimentary rock and consists of pyroclastic material, often with an admixture of another clastic material cemented with a siliceous or loamy binder. Tuff is a hard rock with a high porosity, and therefore has a relatively low density. It consists of aluminium, silicon, oxygen, potassium and trace amounts of carbon. The addition of tuff (3–5%) for recycled thermoplastic polymers becomes the mixing promoter that facilitates their processing and increases their deformation capacity and the stiffness of such mixtures [7]. Studies of composites based on thermoplastics using tuff as a filler have shown that such composites are characterized by higher rigidity and surface hardness; furthermore, they have a higher temperature resistance [8]. Tuff in quantities from 10wt% to 30wt% can be used to reduce material costs by replacing more expensive admixtures such as pigments, flame retardants and impact modifiers [9].

Coffee is one of the most consumed beverages in the world. In literature, there are different research papers focused on using spent coffee grounds (SCG). The research showed that adding SCG into a polypropylene matrix promotes a slight decrease in flexural strength and restricts deformation due to stress concentration phenomena provided by dispersed particles in the PP matrix. The flexural modulus increases as a consequence of the remarkable decrease in deformation ability [10].

Currently, there are numerous combinations of agricultural by-products used as fillers (such as coconut shell, rattan, durian seed, rice hush, banana fibre) [11]. Chun et al. [12] examined the utilization of cocoa pod husk (CPH) in polypropylene biocomposites. The increase in the CPH content decreased the tensile strength and the elongation at break of PP/CPH biocomposites but increased the tensile modulus. The addition of a compatibilizer improved the tensile strength and tensile modulus of PP/CPH biocomposites. In another study [13] it was found that SCG particles have a positive effect on the matrix (PP) properties, while these performances were improved by using a chemical treatment (silane, SESB-g-MA) resulting in stronger interactions with the matrix.

Compared with traditional glass fibre and mineral fillers, wood/natural fibre fillers are less expensive, lighter, sustainable, and less abrasive to processing machines. Natural fibre

composites may substitute PP- short glass fibre composites when a reduction in strength is acceptable. Wood plastic composites, on the other hand, may replace PP–talc composites, in applications where impact strength is not critical [14].

The aim of the study is to introduce natural fillers to the polypropylene matrix to increase stiffness, to change the colour and also, in the case of coffee, give a natural fragrance. For this purpose, three types of composite were produced by the injection moulding process to evaluate changes in strength properties in a wide temperature range as well as the influence of water absorption. In addition, the microstructure of the fillers and their effects on the polymer matrix were also evaluated.

2. EXPERIMENTAL PART

2.1. Materials

The polypropylene (PP) Moplen HP500N from Basell Orlen Polyolefins, Plock, Poland was used as a matrix. Tuff, wood flour and coffee ground were used as fillers. The particles of tuff (Filipowice mine, Poland) with a range of 5–20 μm were obtained by grinding on a Retsch ZM 200 mill. After grinding, the tuff was rinsed in 1molar hydrochloric acid and then calcined at 800°C. Ground coffee from grains (Tchibo Arabica – Guatemala Grande) were roasted at 250°C. The grains were ground using a Retsch ZM 200 mill to a grain size of 2–8 mm. Wood flour (Lignocel BK40/90), supplied by J. Rettenmaier & Söhne, with a fibre length of approximately 150 μm and a beam diameter of 20–30 μm , was used. As a compatibilizer, anhydride maleic PP SCONA TPPP 9112 GA (MAPP) supplied by Byk (Altana Group) was used. The standard dumbbell composites were previously mixed in a twin-screw co-rotating extruder and subsequently subjected to injection moulding. The samples (Fig. 1) were made by injection moulding on the Engel ES200/40 HSL machine at Zakłady Azotowe S.A in Tarnow (Poland). Table 1 shows the injection parameters of the produced composites in terms of temperature and injection speed.

Table 1. Injection parameters of the prepared composites

Sample	C1, °C	C2, °C	C3, °C	Nozzle temperature, °C	Holding time, s	Cooling time, s	Injection speed, mm/s	Injection pressure, bar	Injection time, s
PP	180	185	190	195	40	10	20	80	2.87
PP12M	175	180	185	190	40	10	15	80	3.38
PP12T	185	185	190	190	40	10	18	80	4.63
PP12K	175	180	185	187	40	10	17	80	3.69

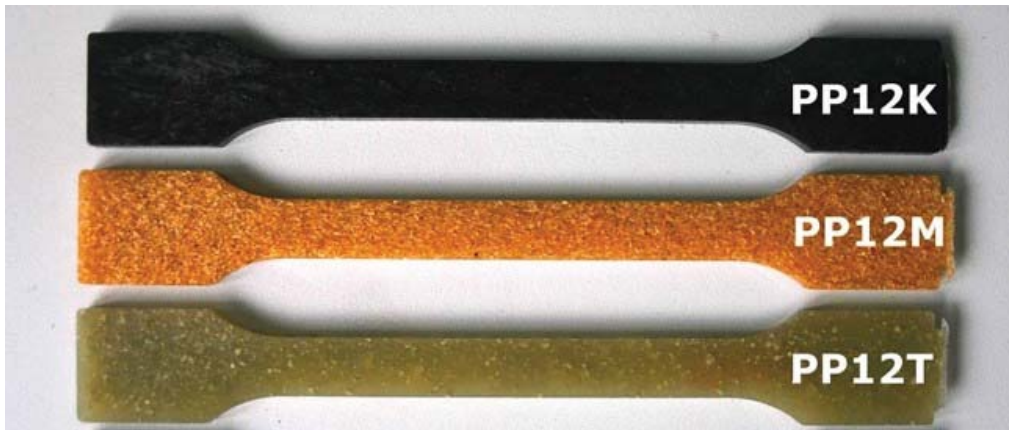


Fig. 1. Injection moulded samples with ground coffee grains, wood flour and tuff

2.2. Methods

The density of the materials was measured by a hydrostatic method. The mechanical properties were estimated by a tensile test with an universal testing machine Criterion 043 with an MTS axial extensometer. Tests for tensile modulus, tensile strength and strain at break were carried out according to the EN ISO 527 standard. The test speed was set to 10 mm/min. The three point flexural test was also conducted for the compositions according to PN-EN ISO 178. Flexural modulus and flexural strength were determined. The Charpy impact test (PN-EN ISO 179-1:2010) was carried out on unnotched specimens using a Zwick HIT5.5P. Fractured surfaces from impact tests were observed by scanning electron microscopy (SEM) in a JEOL JSN5510LV. Before observation, samples were covered with a thin layer of gold. To assess the influence of water absorption, all compositions were tested in a conditioned state and after 30 days of soaking in water. Measurements of water absorption were taken after an incubation period of 1, 7, 14 and 30 day/s.

3. EXPERIMENTAL PART

The tested materials are described in table 2 with the results of the density measurements. The fillers were introduced in the amount of 12.5wt%. The introduction of natural fillers in the amount above 10% usually results in improved strength parameters and gives favorable aesthetic effects. Furthermore, the high content of fillers also contributes to the increase of water absorption and the acceleration of aging processes. The addition of wood flour, coffee or tuff did not have a significant effect on the density of the obtained composites. The highest increase in density was observed for PP12M.

Table 2. Compositions of manufactured samples with their density

Samples	Composition	Density, g/cm ³
PP	Polypropylene (Moplen HP500N)	0.909 ± 0.002
PP12M	Polypropylene + 12.5wt% wood flour + 5wt% MAPP	0.946 ± 0.002
PP12K	Polypropylene + 12.5wt% ground coffee grains + 5wt% MAPP	0.932 ± 0.001
PP12T	Polypropylene + 12.5wt% tuff + 5wt% MAPP	0.948 ± 0.005

Analysing the results from the static tensile test (Table 3), it can be observed that the elastic modulus increased for all compositions. The best result was obtained by the composition with wood flour, for which the elastic modulus at room temperature increased by over 40% and the tensile strength increased by approximately 5%. The addition of 12.5wt% tuff and ground coffee grains led to respectively 5.8% and 3.5% increase in stiffness and a slight decrease in tensile strength (4.5% and 13.5%). Analysing the results from the static tensile test at the extreme operating temperatures of -24°C and 80°C; the tensile strength was higher at the lower temperature and the lowest at the highest temperature. The same tendency was indicated for elastic modulus. The addition of powder fillers led to lower impact strength.

Table 3. Mechanical properties of the tested samples

Samples	Temperature, °C	Tensile strength, MPa	Young modulus, MPa	Strain at break, %	Charpy impact strength, kJ/cm ²
PP	-24	52.5 ± 0.1	4837 ± 81	8.8 ± 1.3	22.1 ± 2.1
	22	31.0 ± 0.2	1691 ± 30	>200	unbroken
	80	21.1 ± 0.5	817 ± 64	>200	unbroken
PP12T	-24	42.9 ± 2.3	4898 ± 24	2.2 ± 0.3	6.8 ± 1.7
	22	29.6 ± 0.4	1789 ± 20	16.9 ± 4.6	10.5 ± 2.3
	80	18.5 ± 0.8	784 ± 7	28.7 ± 2.8	26.5 ± 1.8
PP12M	-24	53.3 ± 0.8	5754 ± 217	2.6 ± 0.3	9 ± 0.7
	22	32.8 ± 0.1	2414 ± 106	8.80 ± 0.4	14.3 ± 0.8
	80	22.6 ± 0.5	1291 ± 51	10.9 ± 2.0	28.2 ± 0.4
PP12K	-24	37.7 ± 2.7	4526 ± 184	1.6 ± 0.2	4.7 ± 0.9
	22	26.8 ± 0.8	1756 ± 52	10.6 ± 1.4	6.6 ± 1.0
	80	18.3 ± 0.5	746 ± 30	19.1 ± 3.4	25.4 ± 7.7

Figures 2 and 3 compare the flexural test results of PP and its composites at temperatures of -24°C +22°C and +80°C. The best results of flexural modulus were obtained at -24°C and led to an increase of over 50% compared to 22°C. The best flexural strength and modulus results were obtained for PP12M composites (with wood flour). This is probably related to the good adhesion of the filler to the matrix. The lowest results were recorded for PP12K composites – with ground coffee.

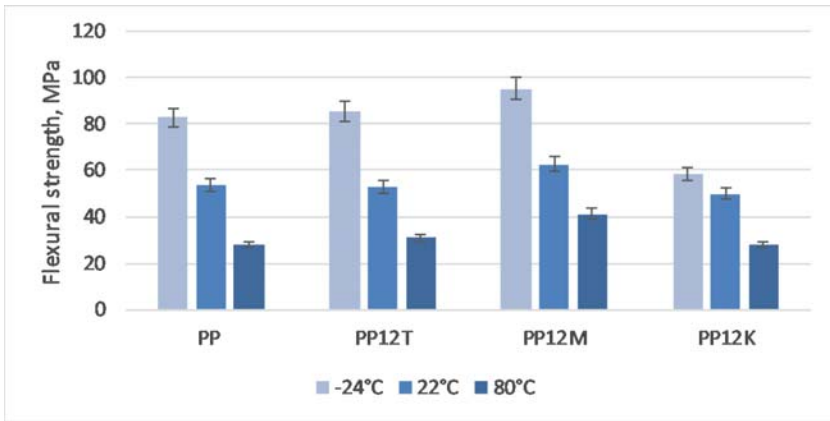


Fig. 2. The effect of temperature on flexural strength of tested composites

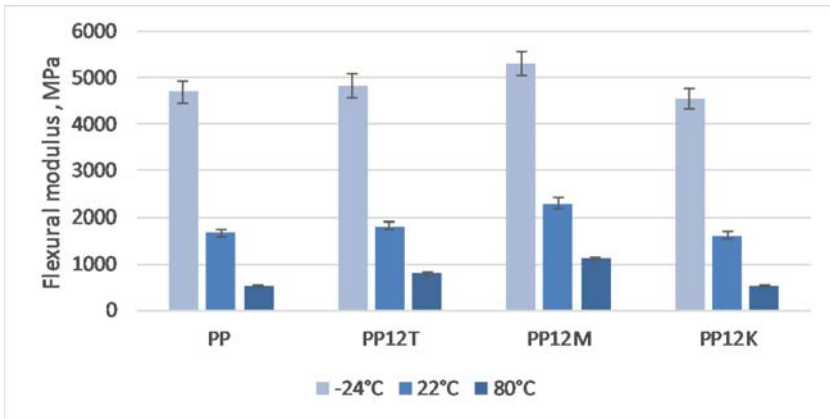


Fig. 3. The effect of temperature on flexural modulus of tested composites

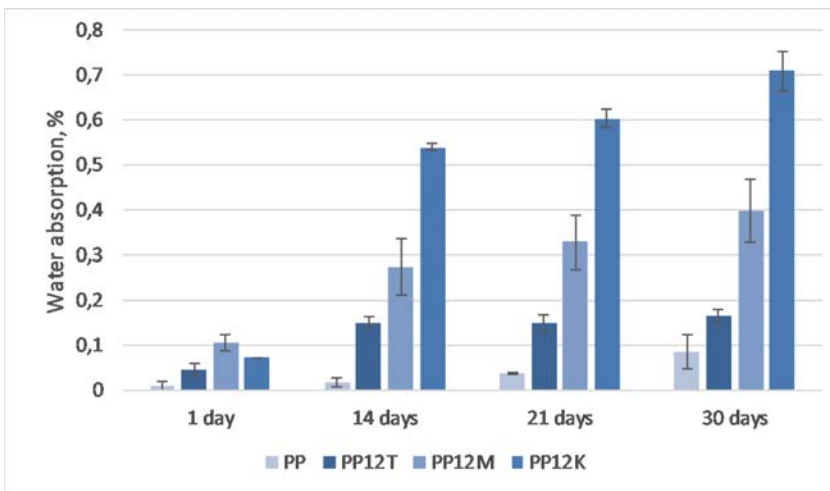


Fig. 4. Water absorption measured for the tested materials after 1, 14, 21 and 30 day/s of incubation in water

The addition of natural fillers, especially lignocellulose, increased the water absorption of all manufactured composites (Fig. 4). Initially, the composite with wood flour had the highest water absorption, however, after a few days the coffee composition absorbed the most water, probably due to the numerous micropores formed in this composite after the injection process, due to the evaporation of the remaining water from the coffee particles.

Table 4 presents the mechanical properties for the composites in the conditioned state and after incubation in water. After 30 days of incubation in water there was no significant effect on the strength properties. The tensile strength slightly decreased and the elastic modulus increased, especially for the composite containing wood flour. This phenomenon is known for lignocellulosic fillers. Slow soaking of water increased their volume and, consequently, shear stress occurred at the filler-polymer matrix border which led to an increase in stiffness. Hydrolytic degradation caused quite a significant decrease in strain at break, probably due to sorption on grain boundaries or composite fibres.

Table 4. Comparison of the mechanical properties of the samples in the conditioned state and after 30 days of incubation in water

Samples	Tensile strength, MPa		Young modulus, MPa		Strain at break, %	
	Conditioned state	After incubation	Conditioned state	After incubation	Conditioned state	After incubation
PP	31.0 ± 0.2	32.8 ± 0.3	1691 ± 30	1920 ± 26	>200	>200
PP12T	29.6 ± 0.4	26.5 ± 1.1	1789 ± 20	2131 ± 109	16.9 ± 4.6	5.6 ± 0.1
PP12M	32.8 ± 0.1	34.5 ± 0.5	2414 ± 106	2704 ± 52	8.80 ± 0.4	7.5 ± 0.9
PP12K	26.8 ± 0.8	26.9 ± 1.7	1756 ± 52	1762 ± 35	10.6 ± 1.4	9.6 ± 1.2

Figure 5 presents the microstructures of the tested materials. Tuff particles (5–20 µm) can be observed as well as ground coffee grains (2–8 mm). We can also see characteristic wood fibrils. Much smaller tuff particles with a developed surface are well embedded in the polymer matrix. Coffee particles have a diversified morphology and size and exhibit a limited adhesion to the polymer matrix.

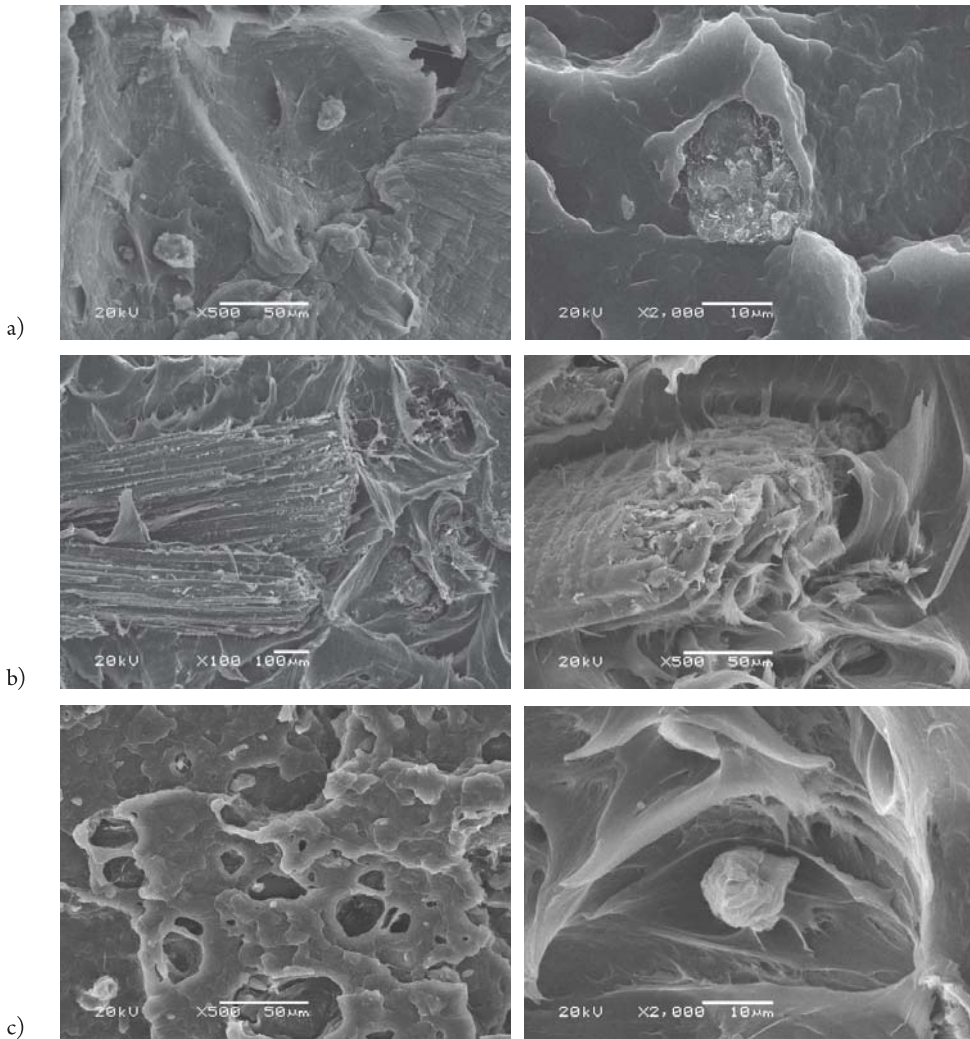


Fig. 5. SEM micrographs of tensile fractured surfaces of the tested composites

4. CONCLUSIONS

It is possible to produce good quality composites with both natural mineral and lignocellulosic fillers. The addition of ground coffee, wood flour or tuff increases the modulus of elasticity. Due to the small amount of fillers and their form (powder fillers – not fibrous), the effect of strength increase was not expected, but an improvement of stiffness was possible. Furthermore, the use of tuff to increase stiffness, gives an interesting green colour to applications and, as well as the addition of wood flour, increases resistance to aging or wear. In addition, the modification of the composite with natural fillers, facilitates the use of recyclates and the tuff, which is protected by a patent, is an addition which favors their mixing abilities.

References

- [1] Saba N., Jawaid M., Allothman O.Y., Paridah M.T., *A review on dynamic mechanical properties of natural fibre reinforced polymer composites*, Construction and Building Materials, vol. 106/2016, 149–159.
- [2] Yatigala N.S., Bajwa D.S., Bajwa S.G., *Compatibilization improves physico-mechanical properties of biodegradable biobased polymer composites*, Composites Part A: Applied Science and Manufacturing, vol. 107/2018, 315–325.
- [3] Righetti B., Mello R., Benedetto D., Hirayama D., De Andrade O., *Manufacturing and Characterization of Jute / PP Thermoplastic Commingled Composite 2. Experimental Procedures*, Materials Research vol. 20/2017, 458–465.
- [4] Vilaseca F., Valadez-Gonzalez A., Herrera-Franco P.J., Pèlach M.À., López J.P., Mutjé P., *Biocomposites from abaca strands and polypropylene. Part I: Evaluation of the tensile properties*, Bioresource Technology, vol. 101/2010, 387–395.
- [5] Zago D.M., Jikan S.S., Badarulzaman N.A., Nuhu A.H., *Effect of Additives on Polypropylene / Kaolin Composite Prepared via In-situ Process*, Journal of Science and Technology, vol. 9/2017, 19–23.
- [6] Qiu F., Wang M., Hao Y., Guo S., *The effect of talc orientation and transcrystallization on mechanical properties and thermal stability of the polypropylene/talc composites*, Composites Part A: Applied Science and Manufacturing, vol. 58/2014, 7–15.
- [7] Kuciel S., Kuźniar S., Mikuła J., *Tuf – nowy mineralny kompozybilizator recyklatów PHED przeznaczonych do wytwarzania wyrobów metodą rozdmuchiwania*, Przetwórstwo Tworzyw, 2013, 250–258.
- [8] Żmudka S., Budniak I., Kuciel S., Mikuła J., *Ocena możliwości zastosowań wulkanicznego tufu jako napelnacza polimerów termoplastycznych*, Czasopismo Techniczne, 1-M/2009, 421–428.
- [9] Tarverdi P.K., Madoyan Z., *Preparation and properties of polypropylene and pa 6 composites reinforced with armenian tuff stone*, European Scientific Journal, vol. 2/2014, 161–166.
- [10] García-García D., Carbonell A., Samper M.D., García-Sanoguera D., Balart R., *Green composites based on polypropylene matrix and hydrophobized spend coffee ground (SCG) powder*, Composites Part B: Engineering, vol. 78/2015, 256–265.
- [11] Nikmatin S., Syafiuddin A., Hong Kueh A.B., Maddu A., *Physical, thermal, and mechanical properties of polypropylene composites filled with rattan nanoparticles*, Journal of Applied Research and Technology, vol. 15/2017, 386–395.
- [12] Chun K.S., Husseinsyah S., Osman H., *Utilization of cocoa pod husk as filler in polypropylene biocomposites: Effect of maleated polypropylene*, Journal of Thermoplastic Composite Materials, vol. 28(11)/2015, 1507–1521.
- [13] Essabir H., Raji M., Laaziz S.A., Rodrique D., Bouhfid R., el kacem Qaiss A., *Thermo-mechanical performances of polypropylene biocomposites based on untreated, treated and compatibilized spent coffee grounds*, Composites Part B: Engineering, vol. 149/2018, 1–11.
- [14] Sobczak L., Lang R.W., Haider A., *Polypropylene composites with natural fibers and wood – General mechanical property profiles*, Composites Science and Technology, vol. 72(5)/2012, 550–557.

Marcin Noga orcid.org/0000-0002-3738-2220
noga@pk.edu.pl

Zdzisław Juda orcid.org/0000-0001-6795-4536
Institute of Automobiles and Internal Combustion Engines, Faculty of Mechanical
Engineering, Cracow University of Technology

THE APPLICATION OF NIMH BATTERIES IN A LIGHT-DUTY ELECTRIC VEHICLE

ZASTOSOWANIE AKUMULATORÓW NIMH W LEKKIM UŻYTKOWYM POJEŹDZIE ELEKTRYCZNYM

Abstract

This article presents the results of experimental tests and simulations of a light-duty electric vehicle, in which the original lead-acid battery pack was replaced with a lightweight pack of nickel-metal-hydride (NiMH) batteries, which enabled a significant increase to the vehicle's load capacity. The research was mainly focused on the aspect of electricity consumption and prediction of the range of the vehicle equipped with a new battery pack. The operation of a vehicle with total weights of 500 kg and 740 kg was analysed. Recorded vehicle speed waveforms were used to simulate vehicle motion in the Matlab/Advisor environment. The experiments showed a reduction in the specific energy consumption of a vehicle of lower weight, while simulation tests showed good compliance of the results of electricity consumption with experiments in relation to both the considered total vehicle weights.

Keywords: electric vehicle; NiMH battery; energy consumption; simulation; experimental research

Streszczenie

W artykule zaprezentowano wyniki badań eksperymentalnych i symulacyjnych lekkiego, elektrycznego pojazdu użytkowego, w którym oryginalny zestaw akumulatorów kwasowo-olowiowych został zastąpiony lekkim pakietem akumulatorów niklowo-metalowo-wodorkowych, co pozwoliło znacznie zwiększyć ładowność pojazdu. Badania skupiono głównie na aspekcie zużycia energii elektrycznej i predykcji zasięgu pojazdu wyposażonego w nowy zestaw akumulatorów. Analizowano zachowanie pojazdu o masie 500 kg oraz 740 kg. Przebiegi zmian prędkości zarejestrowane podczas jazd testowych użyto do przeprowadzenia symulacji ruchu pojazdu w środowisku Matlab/Advisor. Wyniki badań eksperymentalnych wskazały na ograniczenie jednostkowego zużycia energii przez pojazd o mniejszej masie, natomiast w badaniach symulacyjnych uzyskano dobrą zgodność zużycia energii z rezultatami eksperymentów w obu analizowanych przypadkach.

Słowa kluczowe: pojazd elektryczny, akumulatory NiMH, zużycie energii, symulacja, badania eksperymentalne

1. Introduction

1.1. Background

Electric vehicles are gaining more and more popularity as a form of road transport. Some experts estimate that in 2030, the share of electric vehicles will be average 25% of vehicles travelling on roads across the whole world[3]. According to the same prognosis, a significant proportion of the remaining vehicles will have hybrid propulsion systems, in which apart from the internal combustion engine, an electric motor can usually be found. Internal combustion engines are still being developed; however, it is clear that over the course of dozens of years, the electric drive will be a replacement for the internal combustion engine in automotive applications [12]. The basic advantage of replacing propulsion from combustion engines in the automotive sector with the electric drive is their zero emission of toxic gases at the place of their use. In the wider context, one should take into account not only the methods of producing electricity in the area of vehicle use [13] and aspects related to energy and emissivity of production processes but also the recycling of waste electric vehicle components [6]. Particular attention should be paid to energy storage systems consisting mostly of electrochemical batteries.

Of the less significant benefits of replacing the internal combustion engine with the electric motor, one should mention the simplification of the drive system by eliminating the gearbox. This is possible due to the convenient output characteristics of electric motors, although recently, solutions of two-stage transmissions for electric cars that enable the improvement of the traction characteristics of the vehicle have appeared [16]. Among the basic problems in the development of pure electric drives in automotive applications, the most important are the relatively low capacity of energy storage systems based on the currently available types of batteries resulting in a low vehicle range [17]. Another problem linked to the growing popularity of electric vehicles is also the limited electricity supply possibilities in some countries resulting from the limited abilities of the electricity production system. In some countries, the only remedy is, in principle, the development of nuclear energy [2].

1.2. Batteries in electric vehicles

In the first vehicles with electric drive, lead-acid batteries were used [9]. In the following years, nickel-cadmium batteries were also employed; these have now been eliminated from vehicle applications due to their use of toxic cadmium. In automotive applications, nickel-metal-hydride batteries similar to NiCd battery began to be used [25]. Among other applications, these were found in the famous second-generation GM EV1 electric vehicle. For various reasons, they have not yet been widely used in vehicles that have exclusively electric drive mechanisms. Some authors even see the collusion of a fuel lobby involving blocking the development of high-capacity NiMH batteries [28]. However, it should be noted that the energy density of nickel-metal-hydride batteries is lower than for dynamically developing

Li-ion batteries, and the price of 1 kWh stored energy is relatively higher. Information from the research and development sector regarding the development of NiMH batteries with extremely high performance forecasts a wider application of this technology in electric vehicles. [21]. However, NiMH batteries have found a very common use in vehicles with hybrid drive systems [7] as a mature, non-problematic technology. Nowadays, energy storage systems in vehicles with pure electric drives are usually in the form of various types of lithium-ion batteries. The objective of engineers is to find batteries characterized by high specific energy and specific power with an increased number of work cycles and a reduction in production costs.

Lead-acid batteries are commonly used in light-duty commercial vehicles. This is mainly due to their low price, simple operation and the fact that they do not require battery management systems, which lithium-ion batteries require for safe and trouble-free operation [18]. The latter has begun to be used in golf buggy type vehicles in recent years however, this significantly raises the price of such vehicles. In addition, lithium-ion batteries are a less safe solution than lead-acid or nickel-hydride batteries. This is due to the use of flammable, organic and usually liquid electrolytes. There are relatively frequent known cases of fires, even explosions in electric vehicles equipped with lithium-ion batteries [10]. Moreover, in the case of Li-ion batteries, there is the phenomenon of 'thermal runaway'. This consists of an uncontrolled increase in the temperature of the battery leading to its combustion, and initiated in the process in which the critical temperature of this type of cell has been exceeded [4]. This phenomenon is practically non-existent in the case of nickel-metal-hydride batteries, which is their unquestionable advantage. Nickel-metal-hydride batteries do not require the balancing of individual cells in a serial connection, which is mandatory for lithium-based batteries. Yet another advantage of NiMH batteries in relation to Li-ion batteries is the relatively trouble-free recycling process of used batteries, in which many rare earth metals are recovered [5].

In the case of lithium-ion batteries, the recycling process is more difficult than for other batteries due to the significant differences in the chemical composition of materials used for the production of particular types of Li-ion cells. In the case of NiMH batteries, there are also differences in the materials used, especially for the negative electrode, but they do not cause such problems in recycling as is the case with Li-ion batteries.

1.3. Comparison of the key parameters of the most important traction batteries

As mentioned earlier, during the development of electric vehicles, various types of batteries have been used. A comparison of the most important parameters of traction batteries used in the past and modern electric vehicles is presented in Table 1; lead-acid batteries were also compared. Nowadays, these batteries are no longer used in passenger electric vehicles. This is primarily due to their low energy density and low cycle life. However, they can still often be found in currently produced golf carts, forklifts and vehicles for transport inside workplaces. Low prices of storage systems and low maintenance requirements are the most important considerations.

In modern full-size vehicles with electric drives, various types of lithium-based batteries are mainly used; this is especially due to their high specific energy, specific power and cycle life. These parameters are crucial for an electric vehicle energy storage system. Nickel-metal-

-hydride batteries are currently used in vehicles with hybrid drives, but at the beginning of the present century they were used in small-series electric vehicles. Working in hybrid propulsion systems in the range of around 30-70% of the state of charge (SOC), nickel-metal-hydride batteries receive an exceptionally high durability, exceeding 10 years of operation.

Table 1. Parameters comparison of different type batteries used in electric vehicles [27]

Key parameter	Lead-Acid	Ni-MH	Li-ion
cell voltage [V]	2.0	1.2	3.2–3.7 1
specific energy [Wh/kg]	30–50	60–120	90–250
specific power [W/kg]	~180	up to 1300	even 2500
internal resistance [mΩ]	low	high	very low to moderate 1
cycle life (80% DoD)	200–300	300–500	500–2000
charge time [h]	8–16	2–4	1–4
self-discharge/month [%]	5	30	<5
peak load current	<5C	usually <5C 2	even >30
coulombic efficiency [%]	90	90 3	99
discharge temperature [°C]	–20 to 50	–20 to 65	–20 to 60
management system	simple	moderate	very complex 4
total cost of storage system	low	moderate	high
safety requirements	thermally stable	thermally stable, fuse protection	protection circuit mandatory

1 – depending on cell chemistry; 2 – special design for automotive purposes – even 20C; 3 – fast charging, at slow charging 70% max; 4 – precise control at the cell level

The comparison of batteries is not unambiguous in all aspects. This is due to the large number of Li-ion battery types and, to a lesser extent, the differences in the construction of NiMH batteries. They differ significantly in the materials used for construction, which results in differences in the obtained parameters. For example, LiCo_2 batteries have almost twice the specific energy as LiFePO_4 , but they are not suitable for use in vehicles due to the low allowable discharge current. Regarding NiMH batteries, those used in hybrid vehicles have low internal resistance and a relatively high allowable load current (up to 20C), which also gives them high power density; however, specific energy is also lower than in Table 1 – below 50 Wh/kg.

The key advantages and disadvantages of nickel-metal-hydride battery technology compared to Li-ion batteries in particular are listed below:

- ▶ NiMH batteries remain cheaper than batteries made with lithium technologies when considering the total cost of the energy storage system.
- ▶ The basic materials necessary for storing energy are hydrogen, nickel and titanium.
- ▶ They are characterised by high durability when used properly.
- ▶ The recycling of waste batteries is much easier than is the case with Li-ion batteries.
- ▶ They have high tolerance for increased temperature and a lack of propensity for self-ignition.

- ▶ Complex battery management systems that are mandatory for lithium-based batteries are not required for NiMH batteries.
- ▶ Nickel-metal-hydride batteries can be discharged to much lower SOC than lithium-based batteries to ensure a high cycle life.
- ▶ The memory effect is eliminated in modern NiMH batteries.
- ▶ The lower cell voltage of NiMH batteries requires higher number of cells connected in series to have the same voltage. This is not favourable in point of reliability.
- ▶ Currently, mass-produced NiMH batteries have a lower energy density in comparison to lithium-based batteries.
- ▶ Due to the intensive heat generation, an efficient battery cooling system is required.
- ▶ They have high self-discharge – up to 30% per month.

In summary, NiMH batteries have some advantages over Li-ion batteries; however, on key issues, such as e.g. specific energy, lithium-based batteries are currently preferred for application in battery-powered electric vehicles. The recent development in nickel-metal-hydride batteries which is described in next section can change this situation.

1.4. Recent developments in the field of NiMH batteries

The development of NiMH batteries is mainly based on the search for metal alloys with new structures that enable higher specific energy levels [22].

Alloys known under the names AB_5 and AB_2 are characterised by their ability to store hydrogen and their good working parameters [23]. Alloy AB_5 is a mixture of nickel (B) – as a metal that does not form hydrides – with other metals that do have a tendency to form hydrides, e.g. Ce, Nd, La (A). Nickel doped with other materials, e.g. Sn, Al, Co, shows greater stability. In turn, AB_2 alloys, called Laves phases, contain metals such as Hf, Zr or Ti on the A side and metals like Mn, Ni or Cr on the B side. AB_2 alloys are characterised by higher capacitances if used as negative electrodes in batteries. AB_2 alloys occur in three structures:

- ▶ hexagonal C14
- ▶ regular C15
- ▶ hexagonal C36

NiMH batteries using AB_2 alloys were used in the GM EV1 car in 1999. The specific energy in these batteries was 52 Wh/kg. Research and development work in the field of NiMH batteries focuses mainly on the search for new alloys for electrodes and new electrolytes. In general, materials for negative electrodes are called Ni-TM, where TM stands for transition metal; the following alloys are considered: Ni-Mn, Ni-Fe, Ni-Co and Ni-Zn. Due to the toxic effects of cadmium, the Ni-Cd alloy was abandoned. Of the batteries present on the market, the best parameters are characterised by those containing the Ni-Zn alloy [1, 22]. At a relatively low cost, they have a high energy density (about 70 Wh/kg) although they do not have a very long life, which limits their use in electric vehicles. They are mainly used in power backup systems (UPS). As part of a large grant funded by the US DoE, the RANGE (robust affordable next-generation energy storage system) project was created [22].

The global BASF company is performing intensive research on more efficient NiMH batteries – the goal is to obtain specific energy in the range of 600–1,200 Wh/kg, and prices in the range of 150 \$ for 1 kWh. As the main contractor, BASF conducted intensive research on the development of electrode and electrolyte materials for the next-generation Ni-MH batteries. The main goals are low cost and high specific energy. One of the tasks performed by BASF was the development of high-capacity MH alloys that contain MgNi, BCC (body-centred cubic) alloys and Si. The second task was to obtain a substitute for the electrolyte currently used to reduce corrosion and for the possible improvement of the redox reaction. Subsequent tasks include the development of active materials for positive electrodes and integration into the form of ready-made battery. The final goal is to commercialize the new EV Energy storage.

In the field of materials for the negative electrode, 5 alloys were tested: MgNi, Mg₂Ni, BCC-C14, BCC and Si. Of these, the BCC-C14 alloy was rated higher, which showed high capacity with correct cycle stability. The capacity the BCC-C14 alloy was 30% higher than the classic AB₃ alloy. In the research and development of the new electrolyte, many samples of the modified aqueous KOH were tested [20]. Research has shown that the way to increase energy density is to achieve higher cell voltage; therefore, the focus was on IL fluids (ionic liquid), consisting of only anions and cations and characterised by, among other features, high thermal stability, high ion conductivity and non-flammability. Finally, three variants of cells were made, of which the sealed pouch cell showed a specific energy of 127 Wh/kg [19].

2. Aim and scope of the work

The aim of the described work was to develop a new lightweight energy storage system basing on a nickel-metal-hydride battery for a light-duty electric vehicle for a golf cart type of vehicle which originally had a set of lead-acid flooded batteries. The motivation for the authors was the fact that examples of the use of a NiMH battery in a similar light-duty electric vehicle were not presented in the available sources.

The developed energy storage system was composed on the basis of a battery taken from a hybrid electric vehicle. This operation was aimed at significantly increasing the vehicle's loading capacity by reducing its weight (by around 200 kg). The expense of this approach was a reduction in the vehicle's range; however, in the case of transport within workplaces, there are applications in which the 10-km-range of the vehicle on a single charge is sufficient and the load capacity of the vehicle becomes the most important factor. In the discussed case, replacing batteries with a total weight of 240 kg for a nickel-metal-hydride battery with a weight of 40 kg allows increasing the loading capacity to 350 kg or up to over 400 kg if no passenger is carried. This is an increase of 130% compared to the original value.

The used nickel-metal hydride batteries have a power density of 1,000 W/kg, which makes it possible to draw high current from them while maintaining a high level of durability. Lead-acid batteries with a similar total weight (40 kg) and a nominal voltage of 48 V have a significantly lower current capacity. In addition, traction batteries of this size (with a capacity of 30 Ah) that

are resistant to deep-cycle discharge are not produced. It would be possible to use a pack of starter batteries, but such batteries used in an electric vehicle would be subject to rapid wear.

In the first stage of work, after development of the new storage system and composing of data acquisition system, it was possible to conduct experimental tests of the vehicle. Two test drives were performed – one without load and one with a load of 240 kg. During the test drives, the vehicle's speed, battery voltage, battery current and temperature were recorded. This primarily enabled calculation of the influence of weight on the energy consumption of the vehicle. The recorded vehicle's speed profiles were also needed in the simulation that followed.

The second stage of work was executed using the Matlab/ADVISOR environment. The aim was to develop a model of electric vehicle using a NiMH battery, which allows the fast simulation of energy consumption and estimation of the vehicle's range and how this is affected by its weight without the need for experimental tests.

3. Development of a new storage system

3.1. Tested vehicle

The object of the research was a light-duty vehicle with a Melex type 945DS electric drive. Vehicles of this kind are often used to transport goods within workplaces, as golf carts, or with increasing frequency to transport tourists in historical city centres. The vehicle is shown in Fig. 1.



Fig. 1. The tested electric vehicle

The tested vehicle was equipped with an electric system with a nominal voltage of 48 V and a DC drive motor. Such motors are still popular in new vehicles of this type, mainly due to the low price of a DC motor with a controller compared to an asynchronous motor with an inverter. The basic technical data of the test vehicle with the factory battery is presented in Table 2.

Table 2. Technical data of the Melex 945DS tested vehicle with a factory-type battery [8]

Parameter	Value	Parameter	Value
length x width; wheelbase	2660 x 1230; 1660 mm	rated armature current	100 A
net vehicle weight	380 kg	rated output power	3.9 kW at 4300 rpm
vehicle capacity	2 people + 150 kg load	rated torque	8.2 Nm
factory battery type	Trojan T-125 (6 V)	max. motor efficiency	75 %
nominal voltage	48 V	total gear ratio	16
battery capacity (10h)	221 Ah	tyre size	145/80 B10
motor type	DC, separately excited	maximum speed	~30 km/h
motor symbol	DV3-4006AA	vehicle range	~60 km

The motor was managed using a programmable Curtis 1266 controller designed for operation with a nominal voltage of 36 V or 48 V and with a maximum continuous armature current of 140 A. The controller was based on the MOSFET technology with the voltage, armature current, and excitation current adjustable by means of pulse width modulation (PWM). The frequency of PWM is 16 kHz. In the control circuit of the excitation winding, the transistors are connected in an H-bridge configuration, so that the polarity of the supply voltage can be changed, which allows changing the direction of motor rotation. There is the possibility of changing the number of configuration parameters, such as maximum speed, allowable motor armature and excitation currents, and generator operation. There is also the possibility to delay the start and intensity of the regenerative braking process. Changing of the controller settings is made using a dedicated Curtis 1311 programming tool.

The original electricity storage system is based on lead-acid batteries with a capacity of 221 Ah (10 hrs.). The energy stored in the original battery pack is 10.61 kWh, which allows driving a distance of about 60 km.

3.2. Applied NiMH modules and development of a new battery pack

For the work described in this article, a traction battery pack from a Toyota Prius NHW11 produced in 2000–2003 (MY '00) was used. The pack is composed of 38 modules with a nominal voltage of 7.2 V connected in series; this gives a nominal voltage of 273.6 V for the whole pack. The modules were manufactured by Panasonic, and in a slightly modified form, they were also used in the 2nd generation Prius (MY '03) and 3rd generation (MY '09) vehicles. The list of basic data of the NiMH battery modules used in the test vehicle is presented in Table 3.

As shown in Table 3, the applied batteries have a relatively low specific energy; however, they have a very high specific power, which allows drawing a high current. The nominal voltage of the electric system of a Melex commercial vehicle is 48 V. In order to match the voltage of the NiMH battery pack to the voltage of the Melex vehicle electric system five adjacent modules were connected in parallel. This resulted in there being seven sections of

Table 3. Basic technical data of Toyota Prius NHW11 battery modules [14, 15]

Parameter	Value/Description
cell type	NiMH
manufacturer	Panasonic
module shape	prismatic
width x length x height, mm	275 x 19.6 x 106
rated voltage, V	7.2 (6 cells in series)
module capacity, Ah	6.5
module weight, kg	1.05
specific energy, Wh/kg	44.6
specific power, W/kg	1000
C-rate during discharge (peak)	~20

five modules with an equivalent capacity of 32.5 Ah. The sections were connected in series, which allowed the obtaining of a nominal voltage of 50.4 V; this is a value very similar to the 48 V mentioned above. In this way, 35 of the 38 Prius batteries in the package were used. Figure 2 shows a fragment of the connection diagram of the NiMH battery of the Prius MY '00, as well as a battery pack after adapting the connections for use in the Melex vehicle.

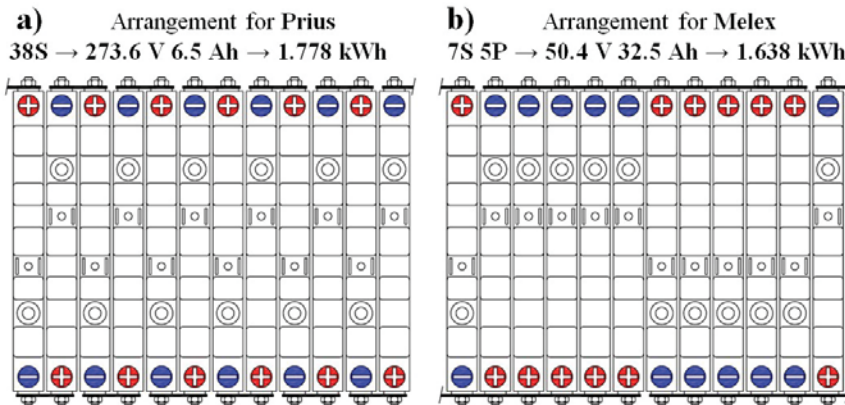


Fig. 2. A fragment of the Prius battery pack before (a) and after adaptation for use in a Melex electric vehicle (b)

A view of the rear part of the vehicle with the installed battery pack from the Prius is shown in Fig. 3. The combining of modules in sections was established using connectors made of 2-mm-thick copper sheeting.

During the tests, the battery was positioned as shown in Fig. 3. Currently work is underway to locate the battery in the place of the original battery (under the driver and passenger seats).

In the summary of this part of the work, Table 4 presents a comparison of the key parameters of both energy storage systems: the original lead-acid system; the newly-developed, lightweight system built on the basis of nickel-metal-hydride battery modules.

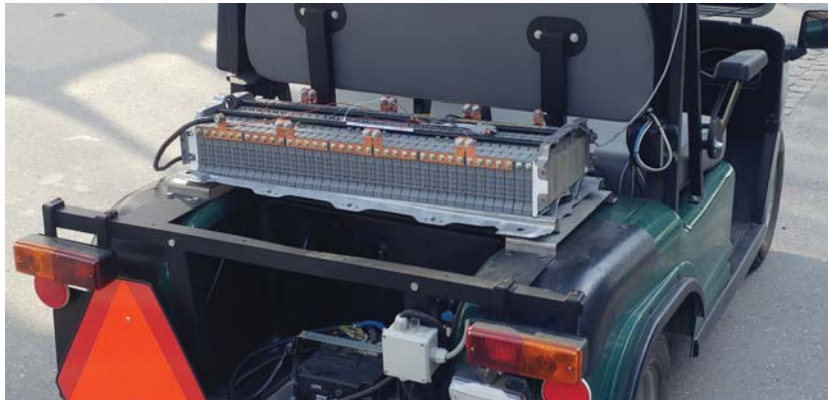


Fig. 3. Rear part of the tested vehicle with NiMH battery

Table 4. Comparison of key parameters of the original lead-acid and the newly-developed NiMH packs for a light-duty electric vehicle

Parameter	Lead-acid	NiMH
module rated voltage, V	6	7.2
connection type inside a module	3S	6S
module rated capacity, Ah	221	6.5
module weight, kg	30	1.05
number of modules used in the pack	8	35
type of connection of modules in the pack	8S	7S 5P
pack rated voltage, V	48	50.4
pack rated capacity, Ah	221	32.5
stored energy, kWh	10.61	1.638
pack weight, kg	240	40
specific energy for a pack, Wh/kg	44.2	41
specific power for a pack, W/kg	~180	920
allowable peak load, A	~1100	650
internal resistance of a pack, mΩ	21.0 at 99 % SOC 23.2 at 75% SOC 24.5 at 51% SOC	20.7 at 99% SOC 17.7 at 75% SOC 17.5 at 53% SOC

As mentioned earlier, 35 of the 38 NiMH modules were used in the newly-developed package. The remaining three unused modules remained in the package housing; to some extent, this reduces the specific energy and specific power of the pack. Leaving unused modules was necessary because, due to the expanding dimensions of modules during operation, they must work with appropriately small dilatations provided by the housing elements designed for 38 modules. Removal of three unnecessary modules would require designing a new housing or at least the laborious retrofitting of the existing housing, which was not needed at this stage. The initial value of the internal resistance of the NiMH battery pack obtained a very

similar value to the resistance of the lead-acid battery pack, even though the NiMH battery has a significantly lower capacity and a larger number of cells connected in series. This indicates the special construction of the used NiMH cells for automotive applications. As known, the energy losses dissipated on heat depend on the internal resistance values. At a high resistance value, there would also be the need for significantly more intensive cooling of the pack.

From the point of view of using low-capacity batteries in an electric vehicle, the allowable value of the peak load is a very important parameter. For a newly developed package it is around 650 A, which, with sufficient reserve, exceeds the value of the maximum current drawn by the motor of the tested vehicle, even at dynamic acceleration. This enables the use of the same settings of the vehicle motor controller with the original 48 V, 221 Ah lead-acid battery pack.

3.3. Measuring path

In order to conduct measurements of the energy consumption of the tested vehicle, it was necessary to record the current drawn and returned to the battery and the battery voltage. The voltage measurement was made using a resistive voltage divider with an attenuation of 1:6 (to match the input range of the acquisition card), while the current was measured using a contactless sensor using the Hall effect with a sensitivity of 0.625 V per 150 A. In addition, the temperature of the battery was also recorded using a thermistor sensor. The rotational speed of the motor was determined based on the Hall sensor signal giving five pulses per shaft revolution. The vehicle speed and the distance travelled were determined using a GPS device operating at a frequency of 10 Hz. All signals were recorded in the measuring system on the memory card. The diagram of the measuring path and the main power circuit used in the test vehicle is shown in Fig. 4.

The battery temperature sensor was placed in one of the modules close to the centre of the pack in the space provided for this purpose.

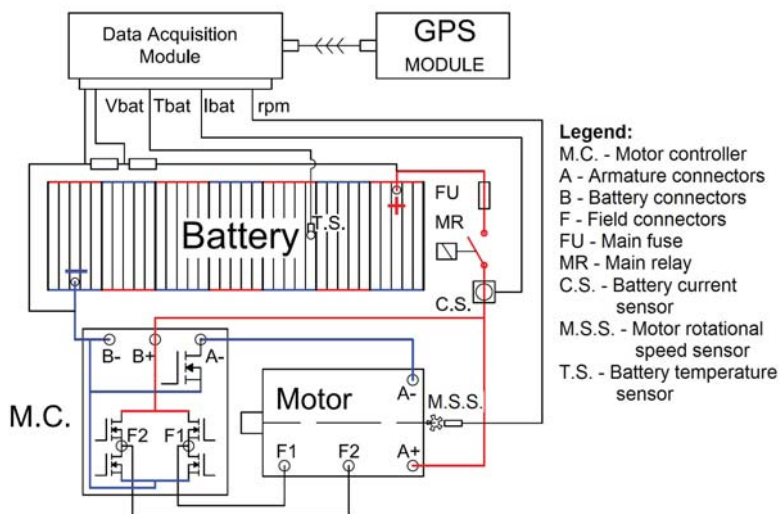


Fig. 4. Diagram of the measuring path with the main power circuit applied in the test vehicle

4. Results

4.1. Experimental tests

Two test drives were performed on a vehicle equipped with a NiMH battery pack. Both test routes were started with a battery charged to 100% SOC. In the first case, the lead-acid battery remained in the vehicle, which resulted in a total vehicle weight of 740 kg including the driver. In the second case, lead-acid batteries with a total weight of 240 kg were removed from the vehicle, so the gross weight of the vehicle was 500 kg. To have both speed profiles as similar as possible, the vehicle was driven by the same driver in both cases. Test drives were conducted at the *Czyżyny* campus of Cracow University of Technology in Krakow on roads with a flat and smooth surface, mainly asphalt, and with a shorter concrete section. In the area where the tests were performed, regular traffic has access (low to moderate intensity and at a speed limit of 30 km/h). In situations in which regular traffic was present, it was not possible to obtain two identical vehicle speed profiles for both tests. However, it was decided that the vehicle would be driven by one driver, maintaining the same driving style for both tests and the same average speed of movement across the entire ride. The same conditions produced very good results in earlier studies of the same vehicle equipped with lead-acid batteries (these results are the subject of a separate article). A linear dependence of the energy drawn from the battery on the distance travelled by the vehicle was reached.

The main goal of the research was to determine the energy consumption of a vehicle equipped with a set of NiMH batteries and the influence of its total weight on energy consumption. The amount of energy taken from the battery while driving E_{drv+} was determined by the equation (1):

$$E_{drv+} = \int_{t_0}^{t_1} V \cdot I dt, \text{ for } I > 0 \quad (1)$$

where:

V – battery voltage, V

I – battery current, A

t – time, s

t_0 – time of the start of driving, s

t_1 – time of the end of driving, s

The amount of energy delivered to the battery E_{drv-} during regenerative braking was determined by the equation (2):

$$E_{drv-} = \int_{t_0}^{t_1} V \cdot I dt, \text{ for } I < 0 \quad (2)$$

Finally, the balance of energy used during driving, including the energy returned to the battery during regenerative braking, was calculated using formula (3):

$$E_{drv} = E_{drv+} + 0.8 \cdot E_{drv-} \quad (3)$$

The value of 0.8 refers to the coulombic efficiency of the used battery. This means that on average, 80% of the charge returned to the battery raises its charge, the rest is dissipated to heat. The obtained value was determined using a diagnostic tester based on the registration of the battery charging current and the SOC increment in a hybrid-drive management system. The examined vehicle uses NiMH batteries with parameters very similar to those used in this work. Coulombic efficiency values adopted in the hybrid vehicle manufacturer's calculation model are also confirmed in other written materials, e.g. [24].

Figure 5 shows plots of the current and voltage of the battery while driving a vehicle with a gross weight of 740 kg.

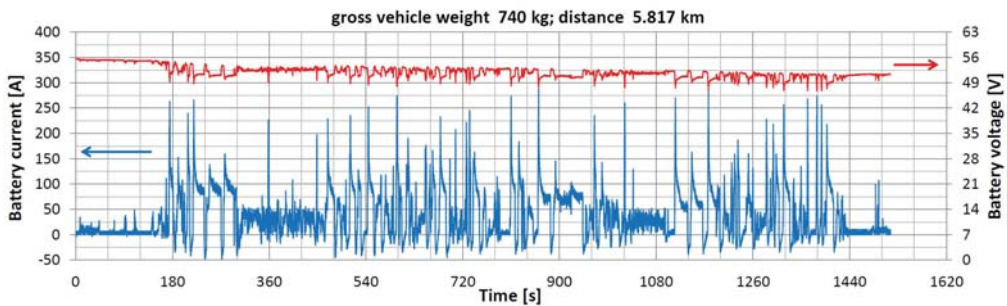


Fig. 5. Battery current and battery voltage as a function of time during the test drive of vehicle with a weight of 740 kg

The open-circuit battery voltage V_{oc} at the beginning of the measurement was 55.6 V. After finishing the drive, the V_{oc} voltage was 51.4 V. The lowest recorded voltage during the acceleration of the vehicle with a partially discharged battery was 46.71 V. The battery current during the acceleration of the vehicle often exceeded 250 A, reaching a maximum value of 287.1 A. The highest value of the current during regenerative braking was 48.4 A.

Figure 6 shows the plot of vehicle speed and battery temperature over time while driving a vehicle with a total weight of 740 kg.

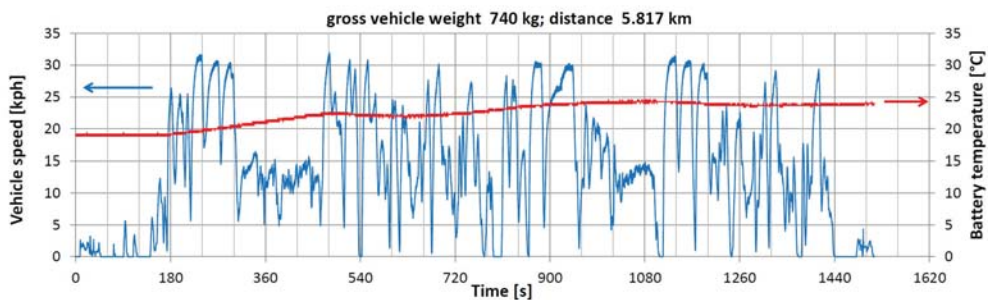


Fig. 6. Vehicle speed and battery temperature as a function of time during the test drive of vehicle with a weight of 740 kg

The maximum vehicle speed was 31.9 km/h and the temperature of the battery increased from an initial value of 19°C to a maximum value of 24.5°C obtained around 1,080 seconds after the start of the test drive.

Figure 7 shows the current and voltage course of the battery when driving a vehicle with a weight of 500 kg.

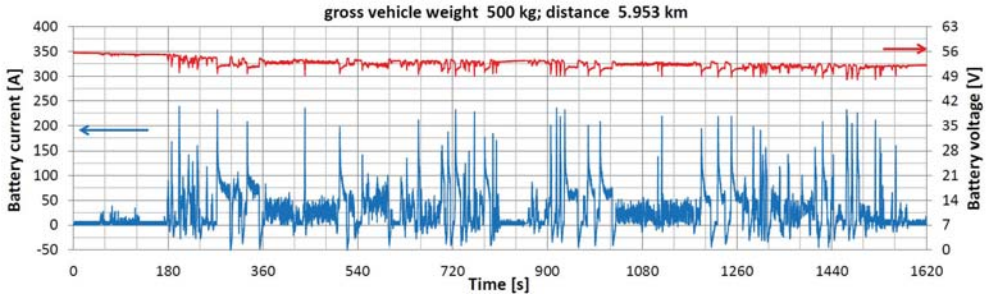


Fig. 7. Battery current and battery voltage as a function of time during the test drive of vehicle with a weight of 500 kg

The open-circuit battery voltage V_{oc} at the beginning of the measurement was 55.59 V. Following completion of the route, the V_{oc} voltage was 52.05 V. The lowest recorded voltage during the acceleration of the vehicle was 47.91 V. Battery current during the acceleration of the vehicle did not exceed 250 A reaching the maximum value of 238.6 A. The highest value of current during regenerative braking was 51.9 A.

Figure 8 shows a plot of vehicle speed and battery temperature over time while driving a vehicle with a weight of 500 kg.

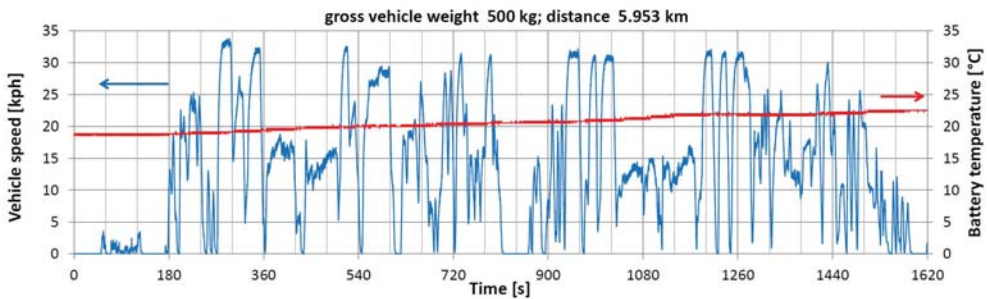


Fig. 8. Vehicle speed and battery temperature as a function of time during the test drive of vehicle with a weight of 500 kg

The maximum vehicle speed reached 33.84 km/h and the temperature of the battery increased from an initial value of 18.9°C to a maximum value of 22.8°C at the end of the test drive.

A summary of the most important results obtained for both test drives is shown in Table 5.

Table 5. Results of both of the test drives

Experimental test results	Vehicle weight 740 kg	Vehicle weight 500 kg
test duration, s	1512.1	1600.7
distance travelled, km	5.817	5.953
maximum current drawn from the battery, A	287.1	238.6
maximum regenerative braking current, A	51.9	48.4
minimum battery voltage under load, V	46.71	47.91
energy drawn from the battery E_{drv+} , kWh	0.856	0.707
energy of regen. braking measured on the battery E_{drv-} , kWh	-0.061	-0.051
energy of regen. braking stored in the battery, kWh	-0.049	-0.041
energy balance E_{drv} , kWh	0.807	0.666
specific energy consumption, kWh/km	0.139	0.112
specific energy consumption per 1 t of vehicle weight, kWh/(km·t)	0.187	0.224
maximum vehicle speed, km/h	31.9	33.84

As can be seen in Table 5, the specific energy consumption for a vehicle with a 32% lower weight is lower by only 20%; thus, specific energy consumption related to one ton of vehicle weight is significantly higher in the case of the lower-weight vehicle.

4.2. ADVISOR software and vehicle model

The simulation model of the tested vehicle was executed in the Advisor program [11]. The Advisor environment, in this case release r0116, uses the power of the Matlab/Simulink scientific calculation package [26]. The Advisor environment allows, among other features, the evaluation of an energy management strategy for an electric vehicle's propulsion system. The subsystem models used in the program are based on test data and are quasi-static, assuming constant values in a given calculation step. The user must provide measured or estimated data that define the vehicle and its components. The program's construction is modular, which enables the easy modification of components. Figure 9 shows the course of simulation calculations with separated blocks which correspond to individual vehicle components. Additionally, the main test vehicle parameters used in the developed model are presented in red boxes. Blue arrows indicate the modules in which appropriate parameters are defined.

As can be seen in Fig. 9, in each block, the required values of vehicle speed and torque are converted, taking into account the available values. In the first block (drive cycle), the required vehicle speeds are defined for each second of the cycle. In each subsequent block, up to the electric motor that produces the drive torque, losses of energy at this stage conversion are taken into account. Finally, the values of the torque required in a given step are calculated. This information is then passed to the preceding blocks in which the real values are determined, taking into account input data and losses on the energy conversion path. Finally, the 'veh'

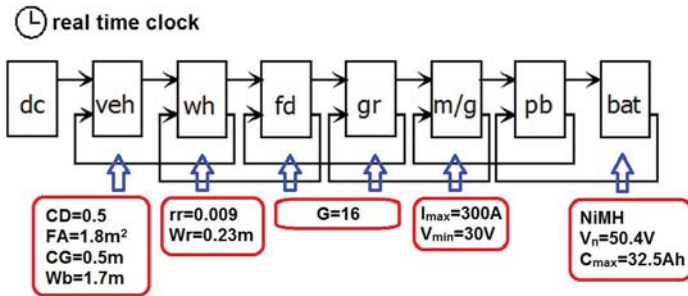


Fig. 9. Data flow in the Advisor model of the electric vehicle with test vehicle parameters used in the developed model

Abbreviations in Fig. 9:

dc – drive cycle	CG – centre of gravity height
veh – vehicle	Wb – wheelbase
wh – wheel	rr – rolling resistance coefficient
fd – final drive	Wr – wheel radius
gr – gear	G – gear ratio (total for gr and fd)
m/g – motor, generator, controller	Imax – motor maximum current
pb – power bus	Vmin – motor minimum voltage
bat – energy storage system	Cmax – battery capacity
CD – drag coefficient	Vn – battery nominal voltage
FA – vehicle frontal area	

block calculates the vehicle speed after taking into account the traction force; the result is used to determine the acceleration value in the next step.

The simulation uses a simple thermal model of a NiMH battery in connection with parallel air cooling. The operating parameters of the battery are characterised by the serial connection of the internal resistance of the battery and voltage at the terminals of the battery being treated as an ideal voltage source. The battery power is limited by the maximum value that can be supplied by the system on the one hand and by the maximum power that the motor can take on the other. The model uses a parallel cooling air flow along each battery module. This approach ensures a fairly even temperature distribution between the modules and the individual cells. The simulation model of the NiMH battery used for the tested vehicle is based on the data obtained in the laboratory tests of NREL [26]. The internal resistance of the cells is shown in the form of a look-up table indexed by the level of the battery cells SOC. Separate tables are valid for the charging mode and for the discharging mode. Based on this data, an open circuit voltage V_{OC} is obtained for a module composed of six cells connected in series. The V_{OC} values are also presented in the model in the form of an array indexed with the SOC level. The value of the available power is the result of the model's operation. The electrical parameters calculated in the model are given as follows:

Battery power P is calculated using formula (4):

$$P = (V_{OC} \cdot I) - RI^2 \quad (4)$$

where:

- V_{OC} – open-circuit voltage of battery, V
- R – battery internal resistance, Ω
- I – battery current, A

After transformation, the following formula (5) is obtained:

$$RI^2 - (V_{OC} \cdot I) + P = 0 \quad (5)$$

From the two possible solutions, one rejects the solution in which the same power is obtained through extremely high currents and low voltages.

The SOC calculation provides the present amount of charge in the battery and is calculated using formula (6) based on values of battery capacity C_{MAX} and battery charge used up to the moment of SOC calculation C_{US} :

$$SOC = \frac{C_{MAX} - C_{US}}{C_{MAX}} \quad (6)$$

The electric motor model is based on an efficiency look-up table, which is indexed by the rotational speed of the rotor and the motor torque. The available motor torque is calculated on the basis of the available power. The model takes into account the power losses in the form of heat excreted externally through convection, radiation and heat exchange in the cooling system. The vehicle model used in the simulation is based on classic vehicle dynamics equations and takes into account the rolling resistance, aerodynamic drag and the strength necessary to climb a gradient. First, the traction force for a given acceleration is calculated, and then the acceleration achieved at a given traction force. During the calculation step (1s), the vehicle speed is the mean value of the speed at the end of the previous calculation step and the speed required at the end of the current step.

Creation of the calculation model consists of setting the required parameters, e.g. motor parameters, vehicle weight, gear ratio and, motor efficiency map. A model of the applied Prius modules was implemented in Advisor; this simplified creating the vehicle model. The remaining required parameters were adopted from the technical data set of the tested vehicle – the most important of these are presented in Fig. 9.

4.3. Simulation results

Both of the actual test drives were characterised by a similar style of driving and distance covered. The speed profiles of both test runs were registered and used to prepare driving tests for simulations. For driving cycles in the simulations, digitised speed profiles of real vehicles registered during road tests were used. In the same way as in the case of experiments, two simulation tests were carried out:

1. Test drive of a vehicle with a total weight of 740 kg
2. Test drive of a vehicle with a total weight of 500 kg

The simulation results for the case of the vehicle with a total weight of 740 kg are shown in Fig. 10.

Similarly, Fig. 11 shows the results for the vehicle with a total weight of 500 kg.

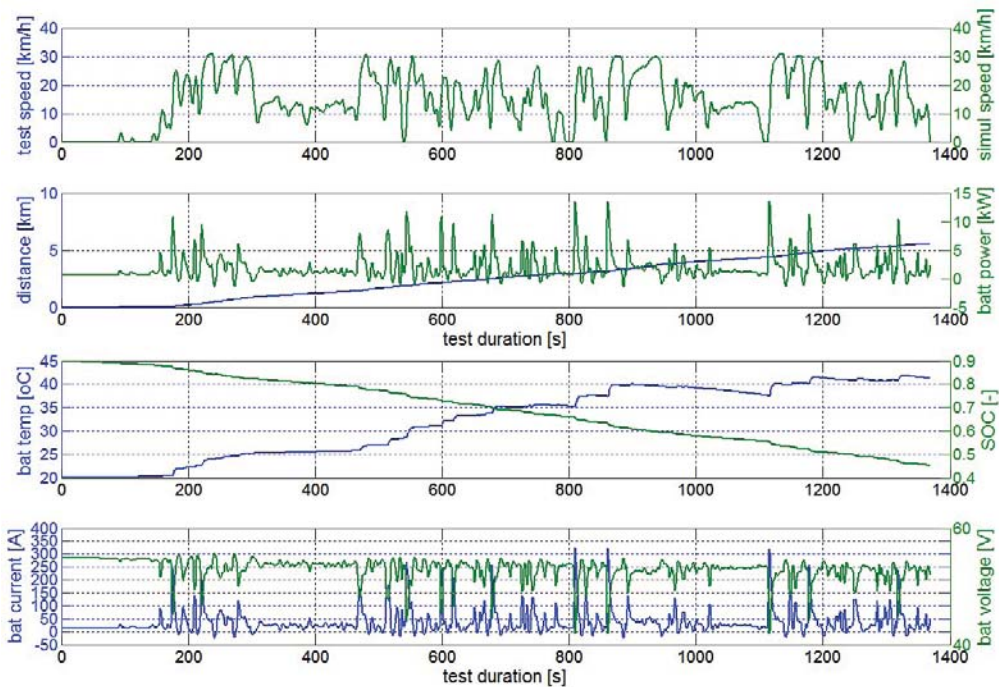


Fig. 10. Results of the simulation of EV with a total weight of 740 kg

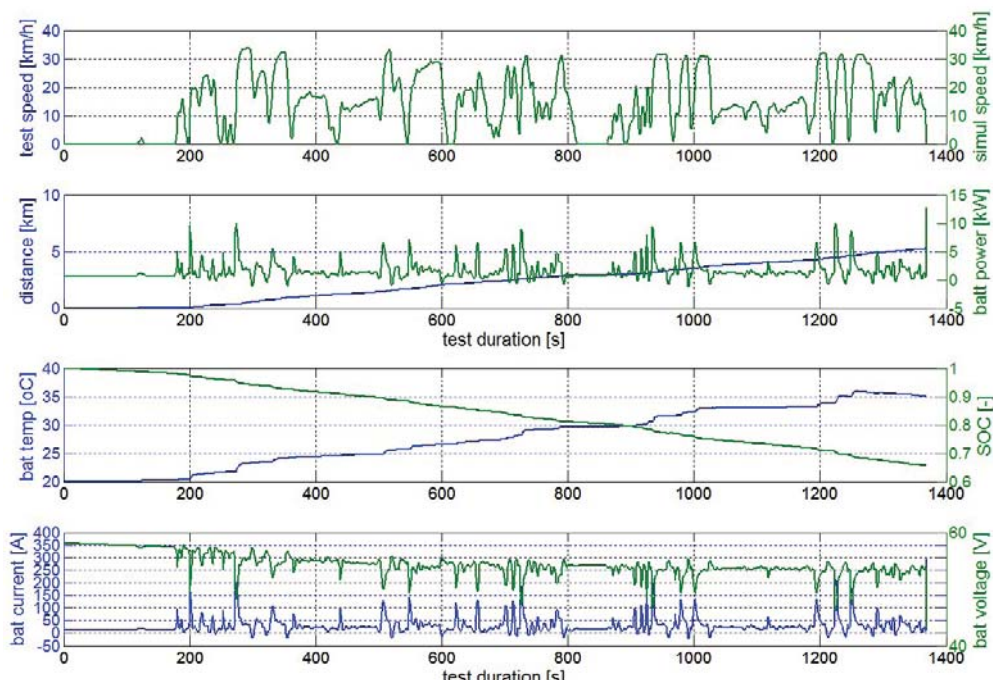


Fig. 11. Results of the simulation of EV with a total weight of 500 kg

Due to the slightly different speed profiles, a shorter distance for the vehicle weighing 500 kg was achieved. The lighter vehicle used a little less energy – the specific energy consumption was 0.14 kWh/km for the vehicle with a weight of 740 kg and 0.12 kWh/km for the vehicle with a weight of 500 kg. The maximum values of the current drawn from the batteries reached 322.7 A and 294.85 A and occurred during fast acceleration values of the vehicle. Table 6 shows the main results of the driving test simulation in both cases – the vehicle with a total weight of 740 kg and the vehicle with a total of weight 500 kg.

Table 6. Driving test simulation results for both cases of total vehicle weight

Simulation test results	Vehicle weight 740 kg	Vehicle weight 500 kg
drive test duration, s	1370	1370
distance travelled, km	5.57	5.23
used battery charge, % SOC	45	35
maximum current drawn from the battery, A	322.7	294.85
maximum regenerative braking current, A	25.13	22.5
maximum battery voltage under load (at start), V	55.7	55.5
minimum battery voltage under load (end of test), V	42.0	42.89
energy consumed during the test, kWh	0.79	0.62
specific energy consumption, kWh/km	0.14	0.12
maximum motor torque, Nm	26.73	22.91
maximum vehicle speed, km/h	31.15	33.7

The results of the vehicle driving simulation using the same conditions as the actual test drives indicated strong conformity of the specific energy consumption between simulation and reality. Therefore, in the next step, further simulations were performed to estimate the range of the vehicle equipped with a newly developed lightweight energy storage system. It was assumed that the vehicle would travel starting from 100% SOC down to 10% SOC, which is a safe value for NiMH batteries. Unlike lead-acid batteries, as well as most lithium-based batteries, this value does not significantly reduce the NiMH battery life cycle. Figure 12 presents the result of the simulation aimed at showing the maximum range of the vehicle with a total weight of 740 kg using 90% SOC. The test was conducted until 10% of the initial charge remained in the battery. To estimate the range, a multiplied, the same real speed profile was used.

After 2960 s and 90% of battery charge consumed, the tested vehicle travelled 10.92 km. At the end of the simulation, as a result of the degradation of the electrical parameters of the battery, an increasing discrepancy between the required speed and the resultant simulation began to appear. The maximum discrepancy reached 6 km/h. Figure 13 presents the result of a similar simulation aimed at showing the maximum range of the vehicle with a total weight of 500 kg using 90% SOC.

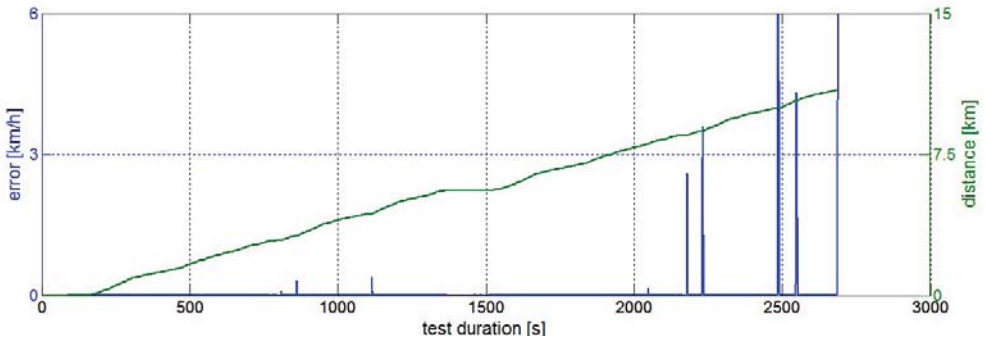


Fig. 12. EV range with a weight of 740 kg after using 90% of the charge

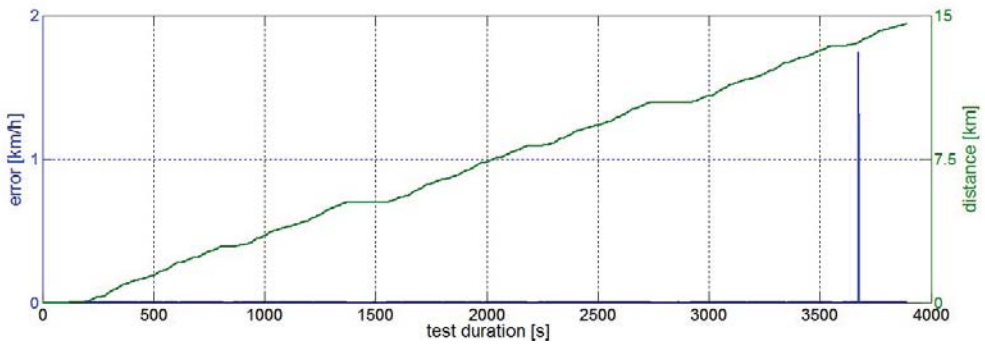


Fig. 13. EV range with a weight of 500 kg after using 90% of the charge

Similar to the previous case, as a result of the degradation of the electrical parameters of the battery, an increasing discrepancy between the required speed and the resultant simulation began to appear at the end of the simulation. The maximum discrepancy reached 1.7 km/h. Non-compliance of the real speed in relation to the required speed is not high and occurs incidentally. The results obtained in both cases (total vehicle weights of 740 kg and 500 kg) are listed in Table 7.

Table 7. Vehicle range and energy parameters after using 90% of battery energy

Test results after using 90% of battery energy	Vehicle weight 740 kg	Vehicle weight 500 kg
vehicle range, km	10.92	12.98
test duration, s	2,960	3,469
energy consumed, kWh	1.56	1.56
specific energy consumption, kWh/km	0.14	0.12
regenerative braking energy, kWh	0.03	0.022

The estimated vehicle range was slightly below 11 km for the vehicle with the higher weight, and almost 13 km for the vehicle without load; this is as predicted. However, it should be remembered that this relates to a new pack of batteries. In the case of used batteries, it will undeniably be lower, depending on the degree of battery wear.

5. Discussion

Analysing the results of experimental studies, it can be concluded that:

- ▶ When driving with a higher load, the battery current has higher peak values during acceleration; this is due to the increased motor load and the higher inertia forces of the heavier vehicle.
- ▶ During braking, slightly higher peak battery currents were obtained for the vehicle with the lower weight; this results from the slightly higher maximum speed of the vehicle without an additional load.
- ▶ The specific energy consumption of the vehicle with the higher weight is slightly higher than that of the vehicle without an additional load; this is caused by the high participation of the motion resistance of the vehicle independent of load, such as parasitic frictional losses in the drivetrain or and air resistance force.
- ▶ The temperature of the battery in the vehicle with a higher weight obtained a higher value at the end of the test drive; this is due to the higher average battery current when driving with an additional load.

The results of the simulations performed on the vehicle model in the Advisor program indicated that a good convergence of the results of specific energy consumption depending on the vehicle weight was obtained. This was the overriding goal of the simulation research and this goal should be considered as having been achieved. The results for the less important parameters, i.e. peak currents and battery voltage, show some discrepancies in relation to the results of measurements on the real vehicle. This is due to the inevitable simplifications adopted in the model resulting from a lack of complete data regarding, for example, the motor efficiency map. An improvement in this matter would require a series of tedious motor tests. Discrepancies between the battery temperature results obtained in the experiment and the results of simulations from the difference in the place where the battery temperature is determined in the simulation and where it is measured in the vehicle. The temperature obtained by simulation refers to the inside of the battery; however, it is in fact only possible to measure the temperature in the hollow of the module housing made of plastic. Simulations carried out in the Advisor program also provide results that may be problematic to obtain in real-world measurements. This applies, for example, to the curve of motor torque during the test. The maximum values of this parameter are included in Table 6. It should also be noted that the simulation with the used tool also has some limitations. It is not possible to take into account the variable slope of the road or external factors such as wind. In the presented situation, this is not a serious problem, because the place of application of the vehicle under consideration (e.g. in a factory) significantly limits the possibility of vehicle exposure to such variable factors.

Using the acquired experience, further work in this topic will be executed in the direction of developing a system that determines the actual state of charge of the battery and the estimated range of the vehicle. It is important to note that the test vehicle is also used in the work of the student scientific association, in which a prototype of a range-extender with a low-emission internal combustion engine powered with hydrogen is being developed.

6. Summary and conclusions

The newly-developed lightweight energy storage system based on NiMH batteries has fulfilled its task in the light-duty electric vehicle. The drive system of the vehicle functions properly. The assumed goal of the work has been achieved. It was possible to significantly increase the loading capacity of the vehicle at the expense of reducing the range. The other main traction parameters of the vehicle were retained. From the user perspective, the vehicle operates no worse than it did when equipped with the original lead-acid battery. Due to slightly higher rated voltage of the newly-developed battery pack and the lower weight of the unloaded vehicle, the maximum speed increases by 2 km/h compared with a vehicle equipped with the factory lead-acid batteries. Determining the behaviour of a new battery in the long term would require more extensive exploitation tests.

Simulation tests confirmed that the vehicle and battery model developed in the Advisor program meets the main expectations, i.e. it allows estimating the vehicle's range depending on the load or style of the vehicle with satisfactory accuracy. It should be remembered that the driving methods (speed profile) was not exactly the same during both test drives; however, the authors made every effort to reach the greatest possible similarity of profiles using the available resources. A sufficient development of the mathematical model of the vehicle created in the Matlab/Advisor environment allows conducting other more extensive predictive research in the future, especially regarding the range of the vehicle depending on its load. This can be achieved in a short time, without conducting additional experimental tests.

The vehicle range estimated by way of simulation with battery levels from full charge to 10% SOC was approximately 13 km for a vehicle with a new battery and no load. For a vehicle with a 240 kg load, a range of around 11 km was obtained, which confirmed the initial predictions about the range of the vehicle with a NiMH battery of lower capacity – about 10 km. Real-world full-load vehicle tests will be possible after the integration of a new battery in the space provided for the mounting of the original lead-acid battery and the installation of a cargo box.

During the experimental tests, the minimum intensity of regenerative braking was defined in order to minimise the impact of this process on the obtained results of energy consumption by the vehicle. NiMH batteries can tolerate high-current charging well (unlike lead-acid batteries), hence the possibility to adjust the generating braking parameters to a higher intensity. This would certainly increase the braking energy recovery rate, reducing the energy consumption of vehicle motion. The next works in this topic will be conducted in this area.

In summary, in special applications of light-duty electric vehicles, the nickel-metal-hydride battery originally foreseen for a hybrid vehicle can be an interesting alternative to not only the commonly used lead-acid batteries, but also to the recently increasingly appearing lithium-ion batteries. However, recent developments in large-capacity NiMH batteries described in the first part of this work give hope that this technology may also appear once again in full-size electric vehicles.

This research was conducted in the framework of task No. M-4/443/2017/DS, which was a subsidy for research granted by the Ministry of Science and Higher Education of the Republic of Poland.

The authors of the article would like to thank the Head of the Institute of Automobiles and Internal Combustion Engines of Cracow University of Technology, Prof. Marek Brzeżański for acquiring the Prius battery pack from the Toyota Motor Poland Company for research purposes, who was represented in this process by Dr. Andrzej Szalek, to whom the authors are also grateful.

References

- [1] Aditya J.P., Ferdowski M., *Comparison of NiMH and Li-ion batteries in automotive applications*, Proceedings of 2008 IEEE Vehicle Power and Propulsion Conference, Harbin, China, 3–5 September 2008, 10.1109/vppc.2008.4677500.
- [2] Bazaras Z., Timofeev B., Vasilieva N., Vilkauskas A., Raslavicius L., Keršys R., *Current state of the global electric power engineering*, Proceedings of 16th International Scientific Conference Transport Means 2012, Kaunas, Lithuania, 25–26th October 2012, 267–269.
- [3] Brooke L., *Not dead yet: The resilient ICE looks to 2050*, Automotive Engineering, vol. 5(4), 2018, 22–23.
- [4] Feng X., Ouyang M., Liu X., Lu L., Xia Y., He X., *Thermal runaway mechanism of lithium ion battery for electric vehicles: A review*, Energy Storage Materials, vol. 10, 2018, 246–267, 10.1016/j.ensm.2017.05.013.
- [5] Gaines L., *The future of automotive lithium-ion battery recycling: Charting a sustainable course*, Sustainable Materials and Technologies, 1–2, 2014, 2–7, 10.1016/j.susmat.2014.10.001.
- [6] Hao H., Mu Z., Jiang S., Liu Z., Zhao F., *GHG Emissions from the Production of Lithium-Ion Batteries for Electric Vehicles in China*, Sustainability, vol. 9(4), 2017, 504, 10.3390/su9040504.
- [7] Johnson N.M., *Battery technology for CO₂ reduction*, [in:] Folkson, R., (Ed.): *Alternative Fuels and Advanced Vehicle Technologies for Improved Environmental Performance*, Woodhead Publishing, Sawston, 2014, 582–631, 978-0-85709-522-0.
- [8] Juda Z., Noga M., *The influence of battery degradation level on the selected traction parameters of a light-duty electric vehicle*, IOP Conf. Ser.: Mater. Sci. Eng., vol. 148, 2016, 012042, 10.1088/1757-899x/148/1/012042.
- [9] Karden E., *Development trends for future automobiles and their demand on the battery*, [in:] Garche J., Karden E., Moseley P. T., Rand D.A.J., (Eds.): *Lead-Acid Batteries for Future Automobiles*, Elsevier, Amsterdam, 2017, 3–25, 978-0-44463-700-0.
- [10] Luo W., Zhu S., Gong J., Zhou Z., *Research and Development of Fire Extinguishing Technology for Power Lithium Batteries*, Procedia Engineering, vol. 211, 2018, 531–537, 10.1016/j.proeng.2017.12.045.

- [11] Markel T., Brooker A., Hendricks T., Johnson V., Kelly K., Kramer B., O'Keefe M., Sprik S., Wipke K., *ADVISOR: A systems analysis tool for advanced vehicle modeling*, J of Power Sources, vol. 110(2), 2002, 255-266, 10.1016/s0378-7753(02)00189-1.
- [12] Noga M., *Various aspects of research of the SI engine with an additional expansion process*, MATEC Web of Conferences, vol. 118, 2017, 00017, 10.1051/mateconf/201711800017.
- [13] Noga M., Juda Z., *Energy Efficiency of a Light-Duty Electric Vehicle*, Proceedings of 21st International Scientific Conference Transport Means 2017, Juodkrantė, Lithuania, 20-22 September 2017, 78–85.
- [14] Onomura Y., Inazu M., Ito M., Minohara T., Nozaki K., *Secondary Battery Development for Hybrid Vehicles at Toyota*, Toyota Technical Review, vol. 57(2), 2011, 9–18.
- [15] Saga K., *Development of Powertrain Technology for Even Better Fuel Efficiency*. Toyota Technical Review, vol. 60, 2014, 4–12.
- [16] Shin J.W., Kim J.O., Choi J.Y., Oh S.H., *Design of 2-speed transmission for electric commercial vehicle*, International Journal of Automotive Technology, vol. 15(1), 2014, 145–150, 10.1007/s12239-014-0016-8.
- [17] Ślaski G., Ohde B., *A statistical analysis of energy and power demand for the tractive purposes of an electric vehicle in urban traffic – an analysis of a short and long observation period*, IOP Conf. Ser.: Mater. Sci. Eng., vol. 148, 2016, 012027, 10.1088/1757-899X/148/1/012027.
- [18] Xing Y., Ma E.W., Tsui K.L., Pecht M., *Battery Management Systems in Electric and Hybrid Vehicles*, Energies, vol. 4(11), 2011, 1840-1857, doi:10.3390/en4111840.
- [19] Yan S., Meng T., Young K., Nei J., *A Ni/MH Pouch Cell with High-Capacity Ni(OH)₂*, Batteries, vol. 3(4), 2017, 38, 10.3390/batteries3040038.
- [20] Yan S., Nei J., Li P., Young K., Ng, K., *Effects of Cs₂CO₃ Additive in KOH Electrolyte Used in Ni/MH Batteries*, Batteries, vol. 3(4), 2017, 41, 10.3390/batteries3040041.
- [21] Young K.H., *Research in Nickel/Metal Hydride Batteries 2016*, Batteries, vol. 2(4), 2016, 31, 10.3390/batteries2040031.
- [22] Young K.H., Ng K.Y.S., Bendersky L.A., *A Technical Report of the Robust Affordable Next Generation Energy Storage System-BASF Program*, Batteries, vol. 2(1), 2016, 2, 10.3390/batteries2010002.
- [23] Zhu J.H., Liu C.T., Pike L.M., Liaw P.K., *A thermodynamic interpretation of the size-ratio limits for laves phase formation*, Metallurgical and Materials Transactions A, vol. 30(5), 1999, 1449–1452, 10.1007/s11661-999-0292-5.
- [24] Zhu W.H., Zhu Y., Davis Z., Tatarchuk B.J., *Energy efficiency and capacity retention of Ni–MH batteries for storage applications*, Applied Energy, vol. 106, 2013, 307-313, 10.1016/j.apenergy.2012.12.025.
- [25] *20 Truths About the GMEV1 Electric Car*, <http://web.archive.org/web/20090123001021/http://www.greencar.com:80/features/gm-ev1/> (access: 30.06.2018).
- [26] *ADVISOR Documentation*, http://adv-vehicle-sim.sourceforge.net/advisor_doc.html (date of access 2018-06-30).

- [27] *BU-107: Comparison Table of Secondary Batteries*, https://batteryuniversity.com/learn/article/secondary_batteries (access: 15.05.2018).
- [28] *Patent encumbrance of large automotive NiMH batteries*, https://en.wikipedia.org/wiki/Patent_encumbrance_of_large_automotive_NiMH_batteries (access 30.06.2018).

Norbert Radek  orcid.org/0000-0002-1587-1074

Piotr Kurp  orcid.org/0000-0002-1001-5033

Faculty of Mechatronics and Mechanical Engineering, Kielce University of Technology

Jacek Pietraszek  orcid.org/0000-0003-2851-1606

jacek.pietraszek@mech.pk.edu.pl

Institute of Applied Informatics, Cracow University of Technology

LASER FORMING OF STEEL TUBES

KSZTAŁTOWANIE LASEROWE RUR STALOWYCH

Abstract

The paper presents a study on microstructure and microhardness changes obtained in the spun carbon steel tube after shaping by a laser beam. The surface of a pipe was machined circumferentially using a 1500 W CO₂ laser beam at various diameters (distance from the focus). As a result, plastic deformations such as convex and narrowing shape changes were observed. The conducted research, including microhardness measurements, shows that, in comparison to the unprocessed material, the microstructure was significantly changed, both in the convex and narrowed layer.

Keywords: laser forming, tube, carbon steel

Streszczenie

W pracy przedstawiono badania zmian mikrostruktury i mikrotwardości warstwy wierzchniej wyoblonej i przewężonej rury ze stali węglowej po laserowym kształtowaniu. Powierzchnia rury była skanowana po obwodzie wiązką lasera CO₂ o mocy 1500 W przy różnych średnicach (odległościach od ogniska). W efekcie uzyskano odkształcenia plastyczne, takie jak wyoblenie i przewężenie rury. Przeprowadzone badania, w tym pomiary mikrotwardości, wykazują, że mikrostruktura uległa istotnej zmianie w stosunku do materiału rodzimego, zarówno w warstwie wyoblonej, jak i przewężonej.

Słowa kluczowe: kształtowanie laserowe, rura, stal węglowa

1. Introduction

Laser technologies are currently extensively utilized in manufacturing, technology and healthcare. In technical practice, a laser technology is used mainly for cutting, welding and surface modification [1–3]. However, there is another technology that is relatively weakly known and it is an advantageous utilization of a laser beam to shape materials, known as the laser forming [4].

The current typical industrial practice of material shaping requires the use of a press equipment and high-strength tools for pressing and bending. The production of these tools requires materials of much higher quality and very high accuracy, which results in their high price and, finally, a large cost of the whole forming process. Bending tools are usually specific, not universal, and can be used cost-effectively only in large series processes, whereas the laser forming process is completely different, as changing the shape of a workpiece requires only a change of the control program, not the machining equipment. It means that laser-based bending is suitable for a small-lot production or almost single-unit production. Additionally, the laser forming process may be used to create shapes that cannot be obtained by other technologies.

The laser forming process creates thermal stresses on the surface of a workpiece. Internal stresses cause plastic deformation, bending or shortening of a material. A laser beam hits the surface of a part, making the material heat up locally at the point of the impact. The heat from the laser beam causes thermal expansion of the material, which in turn causes a change in the shape of the part. The key issue, which has to be resolved to achieve the desired shape changes in the laser forming technology is to determine the path and technological parameters of a laser beam.

This technology may be used in various ways. The power of a laser beam, its wavelength, the diameter of a laser spot on the surface of a material and the path feed rate are basic parameters of the laser forming process. By hitting the surface of a workpiece, a laser beam initiates three different deformation mechanisms which can be active separately or in combination:

- ▶ the temperature gradient mechanism (TGM) [5], mainly used to produce precise small bend angles in thick sheets,
- ▶ the buckling mechanism (BM) [6, 7], usually used for bending of thin metal sheets,
- ▶ the upsetting mechanism (UM) [7, 8], also called a shortening mechanism, used to form a plane sheet into a specially formed part, the shortening of small frames or aligning in microparts operations.

Rarely, more controversial phase transition mechanism [9, 10] is considered.

2. Materials and treatment parameters

The pipes used in the experiment were made from the S235 carbon steel. The tube dimensions were the following: the length of 300 mm, the diameter of 45 mm and the wall thickness of 1.5 mm. Before the experiment, the sample was checked to be free of dirt and next the surface of the pipe was coated with a thin film of a special absorber to increase the absorption coefficient.

A CO₂ laser TLF 6000 TURBO was used for the experiment with the following parameter settings:

- ▶ continuous mode,
- ▶ wavelength $\lambda = 10.6 \mu\text{m}$,
- ▶ efficiency $\eta = 7\%$,
- ▶ maximum power $P = 6000 \text{ W}$ (power used for the experiment 1500 W).

A stationary unfocused laser beam with a power of 1500 W was set perpendicularly to the surface of the tube. The tube was rotated at 5 rpm (Fig. 1). Simultaneously, the laser-heated material was cooled by water spraying (water temperature 18°C) to maintain the proper temperature distribution. The distance from the focus of the beam was systematically increased to achieve a gradually increased laser spot. The thermal stresses, created inside heated tube, caused the shape change.

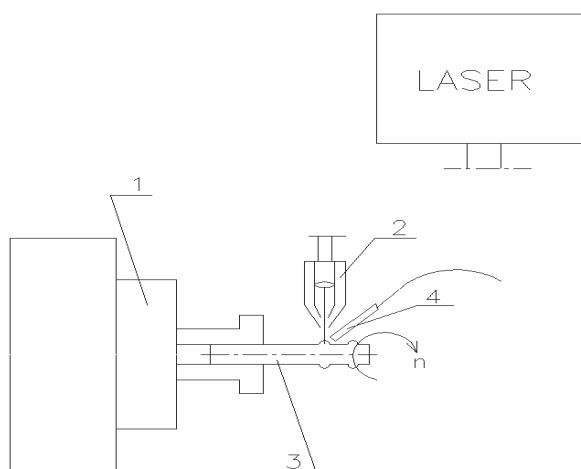


Fig. 1. The scheme of the tube laser forming: 1 – a spindle, 2 – a laser head, 3 – a tube, 4 – a pipe with a cooling liquid

The tube shaping led from the original diameter of $\phi 45 \text{ mm}$ to the reduced one of $\phi 44.2 \text{ mm}$ in the neck and to the increased one of $\phi 51.45 \text{ mm}$ in the greatest widening. Three specimens were taken from the mentioned places for hardness measurements and the evaluation of the metallographic microstructure:

- ▶ the first sample is an unprocessed material (unaffected by the laser beam action),
- ▶ the second sample is from the neck (diameter of $\phi 44.2 \text{ mm}$; a distance from the focus – 50 mm),
- ▶ the third sample from the greatest widening (diameter of $\phi 51.45 \text{ mm}$; a distance from the focus – 150 mm).

The metallographic evaluation was performed on a JOEL JSM-5400 device. The hardness measurements were carried out according to the Vickers method with a load of 0.1 kG . A microstructure analysis was conducted for specimens using a Joel JSM-5400 scanning electron microscope.

3. Results and discussion

The microstructure of the unprocessed carbon steel consisted of ferritic and pearlitic grains (Fig. 2). It is characteristics of the eutectoid steel microstructure. In the processed material, the growth and orientation of the granular homogeneous cylindrical grains (Fig. 3) refer to the direction of heat transfer and the activation of many mechanisms of the laser forming.

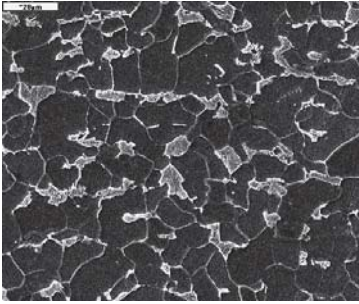


Fig. 2. The microstructure of the carbon steel

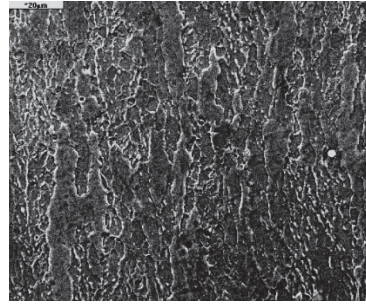


Fig. 3. The grain orientation caused by heat dissipation

Micro cracks with the length of about 0.17 mm were also observed (Fig. 4) in the lower layer. They may have been caused by:

- ▶ the occurrence of tensile stresses in the final stage of the process at the bottom of the layer,
- ▶ large temperature gradients and the low coefficient of a thermal conductivity ($k = 50 \text{ W/m}^{\circ}\text{K}$ for S235 carbon steel, decreases with the increasing temperature).

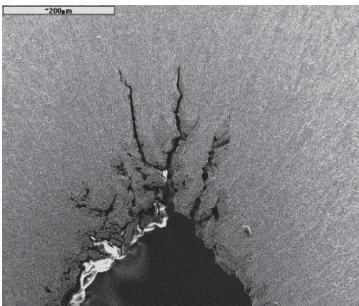


Fig. 4. Microcracks after laser forming

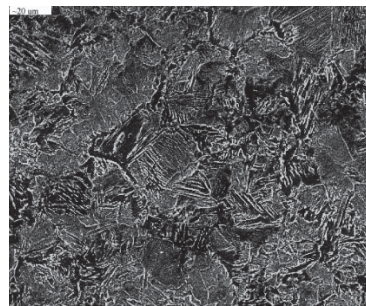


Fig. 5. Bainite microstructure

In the heat affected zone (HAZ), the following microstructures were observed: bainite, ferrite-bainite and pearlite. The bainite detection in HAZ (Fig. 5) is an indication of rapid heating and cooling of the material, because bainite creation is associated with them.

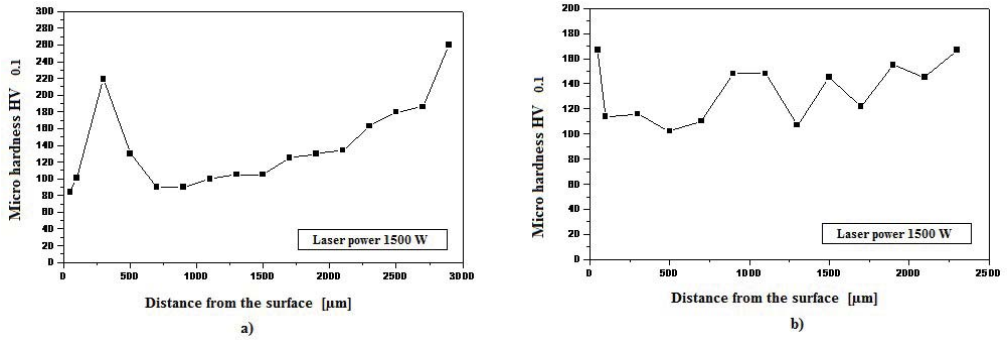


Fig. 6. Microhardness measurements for the tube after laser forming

The second set of microhardness measurements was made on both sides of the bent parts. The analysis of the obtained dataset showed that the microhardness of the concave layer (Fig. 6a) is higher than the microhardness of the convex layer (Fig. 6b).

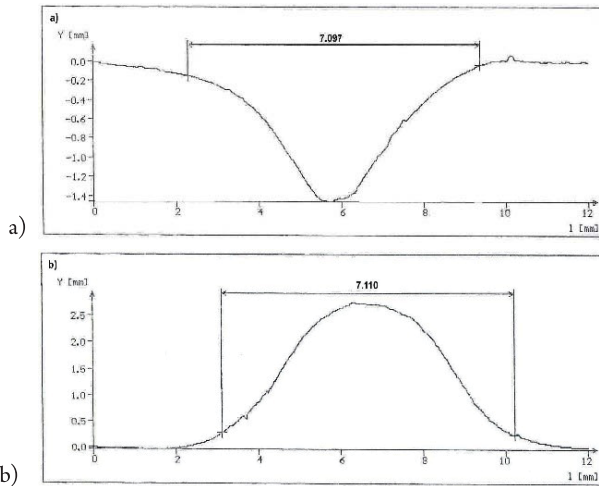


Fig. 7. Changes of the pipe dimension as versus of the laser diameter: a) contracted layer, b) spun layer

The maximum measured microhardness was approx. 260 HV0.1, while the microhardness of the base material equaled 80 HV0.1. The changed shape of the spun tube was precisely measured by a PG2/200 shape analyzer. It allowed for the determination of the following dimensions of the formed tube:

- ▶ the radius of spinning,
- ▶ the angle of spinning,
- ▶ the width of the spun zone.

The geometry of the tube areas changed in the process and is presented in the formograph (Fig. 7), which shows a lack of the symmetry in the cross-section. One-sided fixing of the tube was a probable cause of this phenomenon.

4. Summary

The laser forming process affects the structure and the hardness of a material. The experiment showed that the structure changes of the S235 carbon steel occurred at the location affected by a laser beam. The microhardness measurements found that the increased hardness of the material is a result of a combined laser-based heating and simultaneous liquid-based cooling. This phenomenon seems to be similar to induction hardening – in both situations heating and cooling rates are high. The ability to manage structural and phase changes should allow for the formation of tubes with the desired mechanical properties. The laser forming process appears to be a promising technology for a small series production, but its use in industry will depend on eliminating its adverse effects, particularly microcracks. The simplest solution to prevent microcracks is the process is to slow down, but it reduces the competitiveness of the process compared to traditional methods of metal forming.

The research reported herein was supported by a grant from the National Centre for Research and Development (No. PBS3/A5/47/2015).

References

- [1] Pietraszek J., Radek N., Bartkowiak K., *Advanced statistical refinement of surface layer's discretization in the case of electro-spark deposited carbide-ceramic coatings modified by a laser beam*, "Solid State Phenomena", Vol. 197/2013, 198–202.
- [2] Radek N., Pietraszek J., Antoszewski B., *The average friction coefficient of laser textured surfaces of silicon carbide identified by RSM methodology*, "Advanced Materials Research", Vol. 874/2014, 29–34.
- [3] Radek N., Antoszewski B., *Influence of laser treatment on the properties of electro-spark deposited coatings*, "Kovove Materialy-Metallic Materials", Vol.47/2009, 31–38.
- [4] Geiger, M., Vollertsen, F., *The Mechanisms of Laser Forming*, "CIRP Annals", Vol. 42(1)/1993, 301–304.
- [5] Shi Y., Shen H., Yao Z., Hu J., *Temperature gradient mechanism in laser forming of thin plates*, "Optics and Laser Technology", Vol. 39(4)/2007, 858–863.
- [6] Hsieh H.-S., Lin J., *Study of the buckling mechanism in laser tube forming with axial preloads*, "International Journal of Machine Tools and Manufacture", Vol. 45(12/13)/2005, 1368–1374.
- [7] Che Jamil M.S., Sheikh M.A., Li L., *A finite element study of buckling and upsetting mechanisms in laser forming of plates and tubes*, "International Journal of Manufacturing, Materials, and Mechanical Engineering", Vol. 1(1)/2011, 1–17.
- [8] Radek N., Mesko J., Zrak A., *Technology of laser forming*, "Manufacturing Technology", Vol. 14(3)/2014, 428–431.

- [9] Wang X.F., Takacs J., Krallics G., Szilagyi A., Markovits T., *Research on the thermo-physical process of laser bending*, “Journal of Materials Processing Technology”, Vol. 127(3)/2002, 388–391.
- [10] Gou R., Dan W.-J., Yu M., Zhan, W.-G., *Effect of laser forming on mechanical properties of multiple-phase steels by using a thermal–microstructure–mechanical model*, “International Journal of Materials Research”, Vol. 109(10)/2018, 922–929.

Małgorzata Stojek  orcid.org/0000-0002-6037-195X

mstojek@pk.edu.pl

Faculty of Civil Engineering, Cracow University of Technology

ENGINEERING SAFETY- AND SECURITY-RELATED QUALITY REQUIREMENTS

INŻYNIERSKIE WYMAGANIA JAKOŚCIOWE ZWIĄZANE Z BEZPIECZEŃSTWEM I OCHRONĄ

Abstract

Safety- and security-related problems for software intensive systems are often due to poor or missing relevant engineering requirements. Although there is nothing really new in our presentation, specified problems and methods are well worth revisiting because they are still far from being widely recognized and put into industrial practice.

Keywords: safety, security, software-intensive systems

Streszczenie

W przypadku systemów intensywnie korzystających z oprogramowania problemy związane z bezpieczeństwem i ochroną są często wynikiem złych lub brakujących odpowiednich wymagań technicznych. Choć w niniejszym artykule nie ma poruszanych nowych zagadnień, określone problemy i metody są warte ponownego przeanalizowania, ponieważ wciąż są dalekie od powszechnego uznania i przeniesienia ich do praktyki przemysłowej.

Słowa kluczowe: bezpieczeństwo, ochrona, systemy intensywnie wykorzystujące oprogramowanie

1. Introduction

Nuseibeh and Easterbrook [1] advocate for the following definition of the requirements engineering (RE) previously proposed by Zave [2]: “Requirements engineering is the branch of software engineering concerned with the real world goals for, functions of, and constraints on software systems. It is also concerned with the relationship of these factors to precise specifications of software behavior, and to their evolution over time and across software families”.

Such broad understanding of RE obviously encompasses safety and security related problems. Despite the fact that Boehm and Papaccio recognized in 1988 that “reworking a software requirements problem once the software is in operation typically costs 50 to 200 times what it would take to rework the problem in the requirements stage” [3], it still remains the fact that requirements engineers often fail to pay sufficient attention to security concerns [4]. In addition, given the fact that software-related accidents are almost all caused by flawed requirements, it is somehow surprising that safety concerns of stakeholders could be mostly restricted to comply with basic standards or legal requirements.

In what follows, we revisit requirements issues related to safety and security engineering [5, 6] and discuss their quality aspects for the development and maintenance of cost effective and secure software dependent systems.

2. Safety and security as quality factors

2.1. Safety and security related definitions

Traditionally, safety, security and requirements engineering have been separate research fields with different backgrounds, journals, and conferences. Safety engineering ensures that a system is sufficiently safe to operate (i.e. free from accidental harm to someone or something); security deals with privacy, authentication, and integrity as immune to their intentional breach. Both have common limitations since they usually address rather prevention of the harm than its detection and proper reaction to its occurrences. Nowadays, safety/security engineering is defined as “the engineering discipline within systems engineering concerned with lowering the risk of unintentional/intentional unauthorized harm to valuable assets to a level that is acceptable to the system’s stakeholders by preventing, detecting, and reacting to accidental/malicious harm, mishaps/misuses (i.e., accidents/attacks and incidents), hazards/threats, and safety/security risks” [6].

Let us now see RE as “the discipline consisting of the cohesive collection of all tasks that are primarily performed to produce the requirements and other related requirements work products for an endeavor” [6]. Seeing that safety and security related requirements are included, common collaborative methods are to be established and implemented. Taking into account different cultural engineering backgrounds, such cooperation is with no doubts challenging and requires the right staffing and project management.

2.2. Quality characteristics of requirements

When one thinks about standard requirements engineering tasks, they are usually undertaken after a thorough business analysis and vision statement including capabilities and goals (not requirements yet). A software requirements specification (SRS) is modeled after business (stakeholders) requirements specification (Concept of Operations, CONOPS) by means of the following tasks: requirements identification, analysis, specification, management and validation. The major difficulty is known [7]: “The hardest single part of building a software system is deciding precisely what to build. No other part of the conceptual work is too difficult as establishing the detailed technical requirements, including all the interfaces to people, to machines, and to other software systems. No other part of the work so cripples the resulting system if done wrong. No other part is more difficult to rectify later”.

It is important to make a distinction between goals and operational cases driven by them vs product requirements. The former implies functional requirements while the latter also includes non-functional requirements that are not necessarily driven by operational functionality of the engineering system. The non-functional product requirements cover quality, data, interface requirements as well as system constraints. All requirements are documented and stored in relevant repositories and should have the following characteristics: cohesiveness, completeness, consistency, correctness, currency, customer/user orientation, external observability, feasibility, lack of ambiguity, mandatory, metadata, relevance, usability, validatability, verifiability [8].

By quality requirement one understands a specification of a mandatory amount of a type of product quality. Thus, safety and security requirements fall into minimum acceptable quality consideration. To avoid ambiguity attached to the term ‘quality’, the quality model defining its meaning must be introduced [9]. A quality model consists of quality characteristics (defining the meaning of a specific type of a quality of a system or its part), quality attributes and quality measurements (scales and methods) [10], where safety and security considerations are parts of external quality characteristics related to the system defensibility (see [10, p. 35]).

2.3. Safety and security as quality characteristic

Safety/security subclass of defensibility seizes control of the following problems [6]:

- ▶ accidental/malicious harm to valuable assets;
- ▶ safety/security abuses (mishaps/misuses such as accidents/attacks and safety/security incidents);
- ▶ safety abusers (people, systems, and the environment);
- ▶ security abusers (attackers and malware – systems, software, and hardware);
- ▶ safety/security vulnerabilities;
- ▶ safety/security dangers (hazards/threats) including the existence (conditions) of non-malicious/malicious abusers who unintentionally exploit/can exploit system vulnerabilities to accidentally/intentionally harm vulnerable valuable assets;
- ▶ safety/security risks

and have safety/security solutions: prevented (eliminated, mitigated, keep acceptable low), detected, reacted to, adapted to. The aforementioned defensibility characteristics lead to problem and solution type defensibility attribute, respectively.

We have four types of safety/security defensibility-related requirements: general safety/security defensibility requirements, defensibility significant requirements with four safety/security assurance levels (SAL), defensibility function/subsystem requirements and defensibility constraints. Safety and security requirements are generally negative ones since they specify what the system shall not cause, enable or allow to occur and/or exist.

Quality requirements, as critically important drivers of the architecture and testing, should be based on a quality model defining the specific types of quality and how their measurements scales. By restricting our attention to safety and security requirements, we have the following models [11]:

- ▶ safety models: asset models, accident models, hazard models and safety risk models;
- ▶ security models: asset models, attacker models, attack models, threat models, security risk models.

It is of utmost importance to ensure that safety and security requirements are adequately complete at any given point in time. Poor and/or missing quality requirements have their negative consequences. For their list and suggestion how to avoid them see e.g. a very comprehensive paper of Firesmith [12].

3. Conclusion

To be more effective, safety and security engineering should be integrated in the architecture design process at a very early stage as necessary for the completeness of project engineering requirements. Although these problems have been already addressed many times, they are well worth revisiting because the associated industry best practices are still far from being widely put into practice. For the recent integration between requirements engineering and safety analysis, see a systematic literature review in the paper of Vilela et al. [12].

References

- [1] Nuseibeh B., Easterbrook S., *Requirements engineering: A roadmap*, [in:] Proc. Conf. ICSE '00 The Future of Software Engineering, ACM New York, 2000, 35–46.
- [2] Zave P., *Classification of research efforts in requirements engineering*, “ACM Computing Surveys”, Vol. 29(4)/1997, 315–321.
- [3] Boehm B., Papaccio P., *Understanding and controlling software costs*, “IEEE Transactions on Software Engineering”, Vol. 14(10)/1988, 1462–1477.
- [4] Mellado D., Blanco C., Sánchez L., Fernández-Medina E., *A systematic review of security requirements engineering*, “Computer Standards & Interfaces”, Vol. 32(4)/2010, 153–165.

- [5] Firesmith D., *Common concepts underlying safety, security, and survivability engineering*, Technical Note CMU/SEI-2003-TN-033, Carnegie Mellon University 2003.
- [6] Firesmith D., *Engineering safety- and security-related requirements for software-intensive systems*, [in:] Proc. ICSE'10 32nd ACM/IEEE Int. Conf. on Software Engineering, Vol. 2, 2010, 489–490.
- [7] Brooks F., *No silver bullet – essence and accident in software engineering*, “IEEE Computer”, Vol. 20(4)/1987, 10–19.
- [8] Firesmith, D., *Specifying good requirements*, “Journal of Object Technology”, Vol. 2(4)/2003, 77–87.
- [9] Firesmith, D., *Using quality models to engineer quality requirements*, “Journal of Object Technology”, Vol. 2(5)/2003, 67–75.
- [10] Firesmith, D., *Engineering safety requirements, safety constraints, and safety-critical requirements*, “Journal of Object Technology”, Vol. 3(3)/2004, 27–42.
- [11] Firesmith D., *Are your requirements complete?*, “Journal of Object Technology”, Vol. 4(1)/2005, 27–43.
- [12] Firesmith D., *Common requirements problems, their negative consequences, and industry best practices to help solve them*, “Journal of Object Technology”, Vol. 6(1)/2007, 17–33.
- [13] Vilela J., Castro J., Martins L., Gorschek T., *Integration between requirements engineering and safety analysis: A systematic literature review*, “The Journal of Systems and Software”, Vol. 125/2017, 68–92.

